Karl-Franzens University Graz

Institute for Physics

Universitätsplatz 5, A-8010 Graz, Austria

Methodology Development for the Reconstruction of the ESA Huygens Probe Entry and Descent Trajectory

A thesis submitted in partial fulfillment of
the requirements for the degree

Dr.rer.nat.
in
Natural Sciences Physics

by

Dipl.-Ing. Mag.rer.nat.
Bobby Kazeminejad

January 2005

Committee:

Univ.-Prof. Dr. David H. Atkinson
Department of Electrical and Computer Engineering
University of Idaho
Moscow, ID 83844-1023
United States of America

Univ.-Prof. Dr. Helmut O. Rucker
Space Research Institute
Austrian Academy of Sciences
Schmiedlstrasse 6
A-8042 Graz
Austria

Univ.-Prof. Dr. Reinhart Leitinger
Institute for Physics
Universitätsplatz 5
Karl-Franzens University
A-8010 Graz
Austria

Scientific Advisors:

Dr. Jean-Pierre Lebreton
Research and Scientific Support Department
European Space Agency
Keplerlaan 1, 2200 AG Noordwijk
The Netherlands

Dr. Olivier Witasse
Research and Scientific Support Department
European Space Agency
Keplerlaan 1, 2200 AG Noordwijk
The Netherlands

Miguel Pérez-Ayúcar
Research and Scientific Support Department
European Space Agency
Keplerlaan 1, 2200 AG Noordwijk
The Netherlands

Präambel

Hiermit bestätige ich, Bobby Kazeminejad, dass die vorliegende Dissertation eine eigenständige Originalarbeit darstellt, die von mir selbst angefertigt und abgefasst worden ist.

Datum: Unterschrift:

Abstract of the Dissertation

Methodology Development for the Reconstruction of the ESA Huygens Probe Entry and Descent Trajectory

by

Bobby Kazeminejad

The European Space Agency's (ESA) Huygens probe performed a successful entry and descent into Titan's atmosphere on January 14, 2005, and landed safely on the satellite's surface.

A methodology was developed, implemented, and tested to reconstruct the Huygens probe trajectory from its various science and engineering measurements, which were performed during the probe's entry and descent to the surface of Titan, Saturn's largest moon. The probe trajectory reconstruction is an essential effort that has to be done as early as possible in the post-flight data analysis phase as it guarantees a correct and consistent interpretation of all the experiment data and furthermore provides a reference set of data for "ground-truthing" orbiter remote sensing measurements.

The entry trajectory is reconstructed from the measured probe aerodynamic drag force which also provides a means to derive the upper atmospheric properties like density, pressure, and temperature. The descent phase reconstruction is based upon a combination of various atmospheric measurements such as pressure, temperature, composition, speed of sound, and wind speed. A significant amount of effort was spent to outline and implement a least-squares trajectory estimation algorithm that provides a means to match the entry and descent trajectory portions in case of discontinuity.

An extensive test campaign of the algorithm is presented which used the Huygens Synthetic Dataset (HSDS) developed by the Huygens Project Scientist Team at ESA/ESTEC as a test bed. This dataset comprises the simulated sensor output (and the corresponding measurement noise and uncertainty) of all the relevant probe instruments. The test campaign clearly showed that the proposed methodology is capable of utilizing all the relevant probe data, and will provide the best estimate of the probe trajectory once real instrument measurements from the actual probe mission are available.

As a further test case using actual flight data the NASA Mars Pathfinder entry and descent trajectory and the space craft attitude was reconstructed from the 3-axis accelerometer measurements which are archived on the Planetary Data System. The results are consistent with previously published reconstruction efforts.

Acknowledgements

I would like to thank Jean-Pierre Lebreton (ESA Research and Scientific Support Department, The Netherlands) and the European Space Agency for supporting and funding this research.

Many thanks also to my supervisors David H. Atkinson (University of Idaho, USA) and Helmut O. Rucker (Space Research Institute of the Austrian Academy of Sciences, Austria) for their patient guidance.

I would also like to thank Paul Withers (Boston University, USA) for his cooperation and help in the reconstruction of the Mars Pathfinder entry and descent trajectory, and Vincent Gaborit (University of Paris VII, France) for providing his model of the Huygens probe heat-shield mass ablation.

I am very grateful to Miguel Pérez-Ayúcar (ESA Research and Scientific Support Department, The Netherlands) for putting so much effort into the development of the Huygens Synthetic Dataset, without which the development, implementation, and validation of the Huygens trajectory reconstruction algorithm would not have been possible.

I would also like to thank Kai Clausen and Luitjens Popken (ESA Project Department) for their exceptional contributions to the Huygens Recovery Task Force, without which the Huygens mission would not have been as successful.

Many thanks also to Gérardine Meishan Goh. Last, but by no ways least, I would like to thank my parents Judith and Hamid, my sister Natascha, and my brother Shahin, who have helped in so many ways.

Contents

Chapter 1

Introduction

1.1 General Aspects of Trajectory Estimation

Postflight data analysis is a vital part of all scientific space missions. The success of any planetary space mission depends on the quality of information retrieved from the measurements taken. Certainly the enormous costs required to design, construct, instrument, fly, and support the necessary flight operations justifies a significant expenditure of efforts in analyzing the measurements taken.

The problem addressed herein is the accurate determination of the trajectory (i.e., the position and velocity at any given instant) of a flight vehicle as well as the characteristics of the planet's atmosphere that the spacecraft enters using data that was acquired during the flight. The process of using these measured data to perform the reconstruction is called *trajectory estimation*. How well this approximation agrees with the vehicle's actual position and velocity can never be exactly known, but may be estimated. Thus, the second approximate calculation concerns the accuracy of the trajectory estimate.

Planetary probes enter atmospheres at typical velocities ranging from 6–48 km/s and are rapidly decelerated due to aerodynamic drag. This entry phase is characterized by hypersonic and supersonic velocities, which imply enormous heating rates at the spacecraft's external surface due to aerodynamic friction. The vehicle is therefore protected by a heat shield, which precludes any communication with Earth or an orbiter, as well as any measurement that has to be done using an external sensor. The only available information during the entry phase is therefore the measured accelerations. As the gravitational force acting on the spacecraft's center of mass cannot be detected by measurements made in a frame fixed with respect to the spacecraft (the spacecraft, accelerometer instrument, and test mass are all free falling at the same rate) the measured acceleration can be fully interpreted as aerodynamic drag that is directly related to the atmospheric density. The spacecraft accelerometers are therefore very often part of a scientific instrument package dedicated to investigate the structure of the planet's upper atmosphere (Atmospheric Structure Instruments or ASI). The technique to derive the atmospheric structure from entry probe accelerometer measurements was first demonstrated by the Planetary Atmosphere Experiments Test Probe (PAET), which entered Earth's atmosphere in June, 1971 and demonstrated the reliability of the reconstruction procedure by comparing the derived atmospheric structure with nearly simultaneous acquired standard meteorological soundings (Seiff *et al.*, 1973). This technique was also applied in a variety of other

planetary missions such as the Viking Landers (Seiff and Kirk, 1977), the Mars 6 mission (Kerzhanovich, 1977), the Mars Pathfinder Lander (Magalhães *et al.*, 1999; Withers *et al.*, 2003), the Mars Exploration Rovers (Desai *et al.*, 2004), the Pioneer Venus Probes (Seiff *et al.*, 1980), and the Jupiter Galileo probe (Seiff *et al.*, 1996).

The atmospheric structure determination is not only important from a planetary science point of view but is also an important part in the trajectory estimation process. The reconstructed temperature profile is used to calculate the speed of sound and determine the aerodynamic regime the probe is moving in (e.g., Mach number, Knudsen number, etc.). This is used together with the ratio of the measured normal and axial accelerations to interpolate the probe angle-of-attack profile from a preflight aerodynamic database.

When the spacecraft is decelerated to close to the speed of sound, it enters the descent phase that is characterized by the deployment of a sequence of parachutes[1] and the dropping of the heat shield. Only at that stage can a communication link be achieved, and instrument sensors exposed directly to the ambient atmosphere, in order to measure pressure, temperature, composition, etc. The deployment of parachutes introduces some oscillatory motions into the spacecraft (and hence into the measured accelerations) that will severely limit the accelerometer based trajectory reconstruction. The ability of the spacecraft to immerse sensors directly into the atmosphere (and therefore to measure the time dependency of the measurements) provides a new source of information that can be used to derive a descent altitude and descent speed profile. The horizontal vehicle motion can be derived from the measurement of the radio link frequency shift due to the Doppler effect or, alternatively, from optical instruments that sense the relative position (and the change of that position) with respect to a fixed point such as the Sun or the horizon.

It is clear that even if there is only one spacecraft trajectory, the reconstruction must be done in two separated steps, the entry phase and the descent phase. Both are based on different sets of sensor measurements with different sampling rates, measurement ranges, and accuracy. The reconstructed trajectory portions will have error bars that stem from both measurement errors (noise) and systematic errors such as the limited accuracy of certain model parameters (e.g., the gravitational constant of the planet, initial state vector dispersions, etc.), or a systematic inaccuracy of an instrument (e.g., calibration error, relative location of the spacecraft center of mass to the accelerometer instrument, etc.). It is therefore necessary to try to estimate these uncertainties and provide this information with the reconstructed trajectory. Furthermore these uncertainties could lead to a situation where the entry portion and descent portion of the reconstructed trajectory do not match. It is therefore useful to implement a statistically weighted batch or a sequential estimation algorithm (e.g., weighted least-squares with or without a priori knowledge, recursive least-squares, Kalman filter, etc.), which provides the capability to adequately correct model parameters (typically the initial conditions) and merge the two trajectory portions together.

[1]The number of parachutes can range from one to three or more, each of a different size in order to adapt the descent time as required by the mission.

1.2 Huygens Trajectory Estimation

The Huygens trajectory estimation effort differs from previous probe trajectory estimation efforts mainly in two respects. First, the amount of available sensor measurements (5 scientific instruments and the probe housekeeping data) and, second, the uniqueness of Titan's physical environment (described in Chap. 4), which will be explored *in situ* for the first time. An accurate reconstruction of the probe entry and descent trajectory is therefore needed to ensure a consistent interpretation and correlation of results from all the probe science experiments, and to provide confidence in ground-truth calibrations of the Cassini orbiter remote sensing measurements. Without a common and consistent descent profile, each probe experiment team would need to develop a profile independently thereby causing a significant duplication of effort and expenditure of resources, and making correlation and comparison of results from different experiments somewhat suspect and therefore less meaningful. Furthermore, direct atmospheric sampling by the probe provides "ground truth" verification of orbiter observations of Titan. Without a means to tie the measured atmospheric properties to the probe altitude, location, and velocity at specific times, the value of ground-truth support for orbiter science at Titan would be significantly compromised. The goal of the Huygens trajectory reconstruction effort is therefore (Atkinson and Kazeminejad, 2004)

1. to provide a common trajectory for all experiment teams to use when interpreting their respective data sets. This eliminates the need for each team to perform the task independently and thereby offers a more economical use of limited resources;

2. to provide a common basis for interpretation and correlation of data from different experiments. For example, the existence of atmospheric turbulence and wind shear, evident from the unique signatures in the HASI accelerometer data can only be correlated with other atmospheric properties such as temperature gradients, winds, and cloud decks if a common probe trajectory profile is utilized by all the experiment teams;

3. to provide the atmospheric properties along the probe entry and descent path for use by the orbiter experiment teams as a means of "ground-truthing" remote sensing measurements;

4. to provide precise measurements of the probe position and velocity throughout descent, which is required for the Doppler Wind Experiment (DWE) recovery of the zonal winds by Doppler tracking of the Huygens probe.

The responsibility of developing analysis techniques by which the Huygens entry and descent trajectory will be reconstructed from the official NASA/ESA hand-off point at the interface altitude of 1270 km to the surface was given to the Huygens Descent Trajectory Working Group (DTWG)[2], chartered in 1996 as a subgroup of the Huygens Science Working Team (HSWT) (Atkinson and Kazeminejad, 2004). The membership of the DTWG includes the Huygens and Cassini project scientists, the Huygens Operations Scientist, and representatives from each of the probe science instrument teams and contributing orbiter teams. The DTWG aims to

[2]The author is Co-chair of the DTWG.

- develop a framework between experiment teams and the Huygens Mission Team for sharing and exchanging data relevant to the descent trajectory analysis and modelling;

- develop methodologies by which the probe descent trajectory and attitude can be accurately reconstructed from the probe and orbiter science and engineering data; and

- provide a single, common descent profile that is consistent with all the available probe and orbiter engineering and science data, and that can be utilized by each instrument team for analysis of experiment measurements and correlation of results between experiments.

The development of a proper reconstruction methodology, its computational implementation, and its testing are the main goals of this work and therefore fully support the DTWG in achieving its objectives.

The Huygens mission and the probe design are described in Chapters 2 and 3. As the development, implementation, and testing of the algorithm was aimed to be ready prior to the actual probe mission on January 14, 2005, extensive effort was put into the development of a clear interface between the DTWG and the instrument teams. This interface defines which data would be needed for the reconstruction (Atkinson and Kazeminejad, 2004) and the format in which it would have to be provided (Kazeminejad, 2004). Furthermore the ESA project scientist team put extensive effort into the development of a synthetic data set of the Huygens sensors (HSDS) (Pérez-Ayúcar *et al.*, 2004), which served as a testbed for the reconstruction algorithm. The HSDS is described in Chap. 5. The reconstruction methodology and its utilization of the HSDS is described in Chap. 6 and Chap. 7 for the entry phase, and Chap. 8 and Chap. 9 for the descent phase, respectively. For both portions of the trajectory certain test case scenarios were identified that not only reflect the nominal mission scenario with all the data sources being available as expected but also a variety of contingency situations with the loss or malfunction of one or more trajectory relevant instruments.

The trajectory fitting methodology and its use of the HSDS is finally described in Chap. 10.

The developed algorithm was also applied to the 3-axis Mars Pathfinder entry accelerometer measurements, and the results were compared to previous reconstruction efforts (see Chap. 12).

In the concluding remarks (see Chap. 13) the capabilities and performance of the reconstruction tool is summarized. More important the reconstruction experiences, challenges, and solutions to fix certain problems are summarized. This will be useful for the reconstruction process using the actual flight data in January, 2005.

Chapter 2

The Cassini/Huygens Mission

2.1 Mission Overview and Objectives

The Huygens probe is the ESA-provided element of the joint NASA/ESA/ASI[1] Cassini/ Huygens mission to Saturn and Titan. The scientific objectives of the Cassini/Huygens mission can be summarized as follows (Matson *et al.*, 2002; Lebreton and Matson, 2002):

- Determination of the atmospheric composition;
- Investigation of energy sources driving the atmospheric chemistry;
- Investigation of aerosol properties and cloud physics;
- Measurement of global winds and temperature;
- Determination of surface properties and internal structure; and
- Investigation of the upper atmosphere and ionosphere.

Huygens' goals are to make a detailed *in situ* study of Titan's atmosphere and to characterize the surface of the satellite along the descent ground track and near the landing site. After a descent of about 137 min, the Probe will impact the surface at about 5-6 m/s (Kazeminejad *et al.*, 2004). As it is hoped that Huygens will survive after impact for at least a few min, the payload includes the capability of making *in situ* surface measurements for a direct characterization of the landing site (nominal mission duration). If everything functions nominally, the Probe batteries can provide half an hour or more of electrical energy for an extended surface science phase. The current mission scenario foresees the orbiter listening to the probe for a full 3 hours, which includes at least a 30 min surface phase, as the maximum descent time is expected to be 2.5 hours. An extended surface phase will allow a detailed analysis of a surface sample and meteorological studies of the surface weathering and atmosphere dynamics.

The Cassini/Huygens spacecraft was launched on October 15, 1997. Saturn orbital insertion (SOI) occured on July 1st, 2004. The Huygens probe will be released on December 25, 2004 and will enter the atmosphere of Titan on January 14, 2005. With a launch mass of 5650 kg, the Cassini/Huygens spacecraft was too heavy for a direct injection to Saturn.

[1]Italian Space Agency

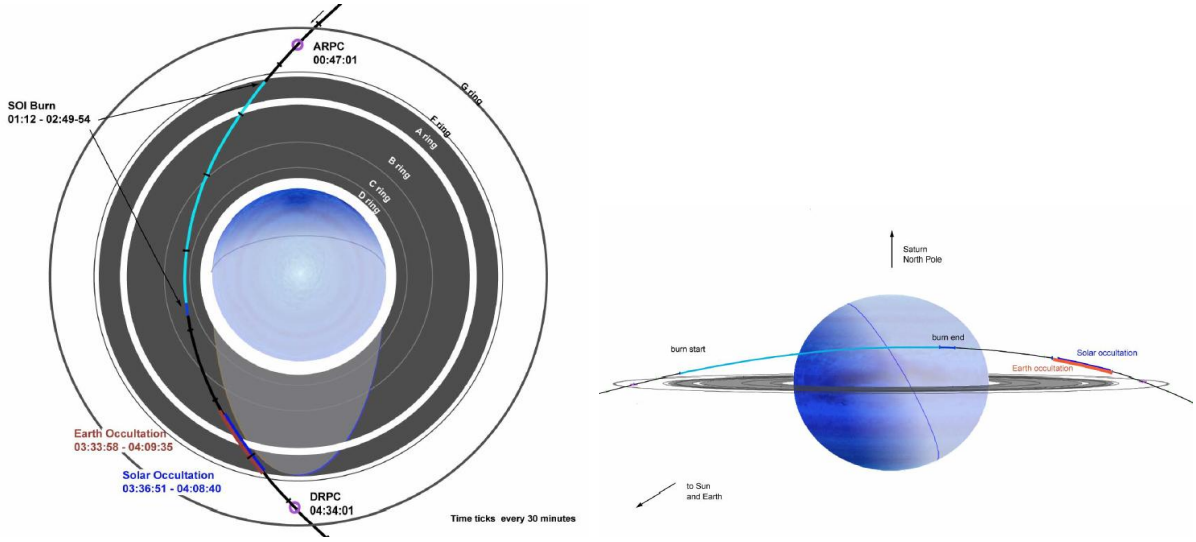

Figure 2.1: *Cassini Saturn Orbit Insertion (SOI) trajectory as seen from Saturn's north pole (left) and equator viewing direction (right). The period of main engine burn is indicated, and the ascending and descending ring plane crossing locations are designated with ARPC and DRPC respectively (Seal, 2004).*

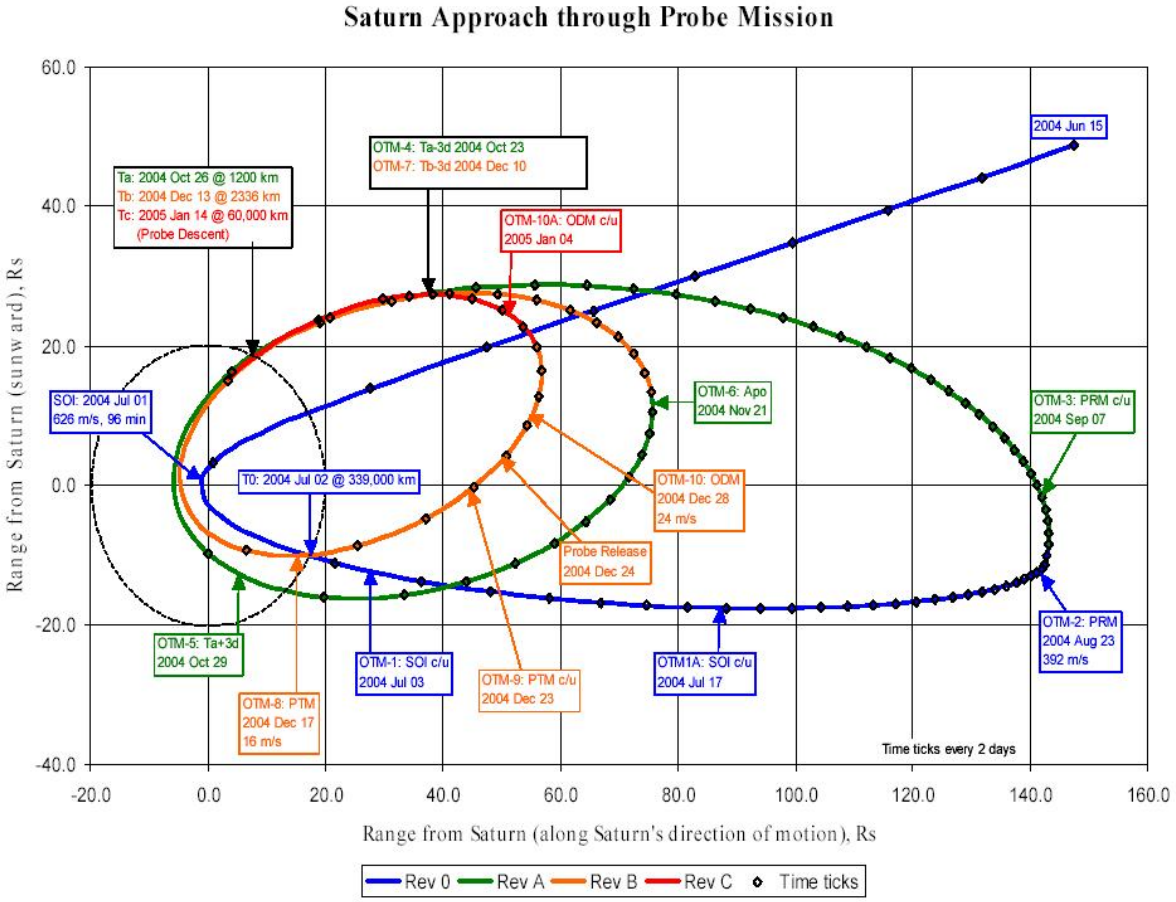

Figure 2.2: *First three Cassini orbits after SOI (Schipper, 2003). The Huygens probe is released on Rev C on December 25, 2004 and enters Titan's atmosphere on January 14, 2005.*

(In order to fly directly to Saturn from Earth in 1997 requires a $C_3 > 108$ km^{2}s^{-2}.[2] A Jupiter gravity-assist (JGA) reduces this value to $C_3 > 83$ km^{2}s^{-2} (Lorenz, 1994).) To optimize C_3 the Cassini/Huygens spacecraft therefore utilized gravity assists from Venus (April 1998 and June 1999), Earth (August 1999) and Jupiter (December 2000).

Cassini arrived at Saturn on July 1, 2004 (UTC) and entered the most critical phase of the mission after launch, the Saturn Orbit Insertion (SOI). The SOI time period represented the closest Saturn flyby of the Cassini orbital tour and, therefore, provided a unique opportunity to study the planet and rings from extremely close range. Cassini passed a mere 20,000 km above the cloud tops of the planet (closer than any previous spacecraft) and only 15,000 km above Saturn's main rings (Seal, 2004). The inbound trajectory was inclined to the ring plane, and crossed it in the gap between the F and G rings in order to minimize the danger of colliding with a ring particle at 2.6 R_S (see Fig. 2.1). The Saturn orbit insertion maneuver started approximately 89 min prior to periapsis and lasted for 97.465 min (Strange, 2001) providing a ΔV of 633.3 m/s. At periapsis the spacecraft was closer to Saturn and the inner rings than at any time during the entire tour (approximately 1.3 R_S). At (rev A) apoapsis a Periapsis Raise Maneuver (PRM) was performed (23 August 2004), which targeted the spacecraft to Titan and reduced the Titan approach speed.

After two subsequent Titan encounters (i.e., Ta and Tb) the probe separated from Cassini on December 25, 2004 (see Fig. 2.2). Five days after Probe release (December 29, 2004) the Orbiter performed an Orbiter Delay Maneuver (ODM) which delayed its arrival at Titan relative to the probe (thereby allowing it to relay the probe's signal) and generate the required Titan miss distance. The size of this maneuver was dictated by the required Orbiter Delay Time (ODT)[3], and by the length of the coast phase: while a shorter coast would decrease the entry point uncertainty and coast energy requirements, it would lead to a larger ΔV requirement of the ODM. The ODM placed the orbiter into a trajectory which flies over the probe landing site, 60 000 km above the surface of Titan. After a coast phase of approximately 23 days the probe arrived at the NASA/ESA interface point (defined as an altitude of 1270 km above the planet's surface) on January 14, 2005 and started its atmospheric entry and descent to the surface. The Huygens probe transmitted its data at a constant 8 kbit/s to the overflying Cassini spacecraft, which pointed its High Gain Antenna (HGA) to a pre-defined location on Titan until it passed the horizon of the probe's landing site. Due to the retrograde Titan flyby of the orbiter during the probe mission (see Fig. 2.3), the prograde rotation and prograde winds shortened the time for the communication link.

[2]Launch energy is typically defined as C_3, i.e., the energy per kg of spacecraft mass, once it gets away from the Earth's gravitational field.

[3]The Orbiter Delay Time is defined as the time from interface epoch to orbiter periapsis epoch.

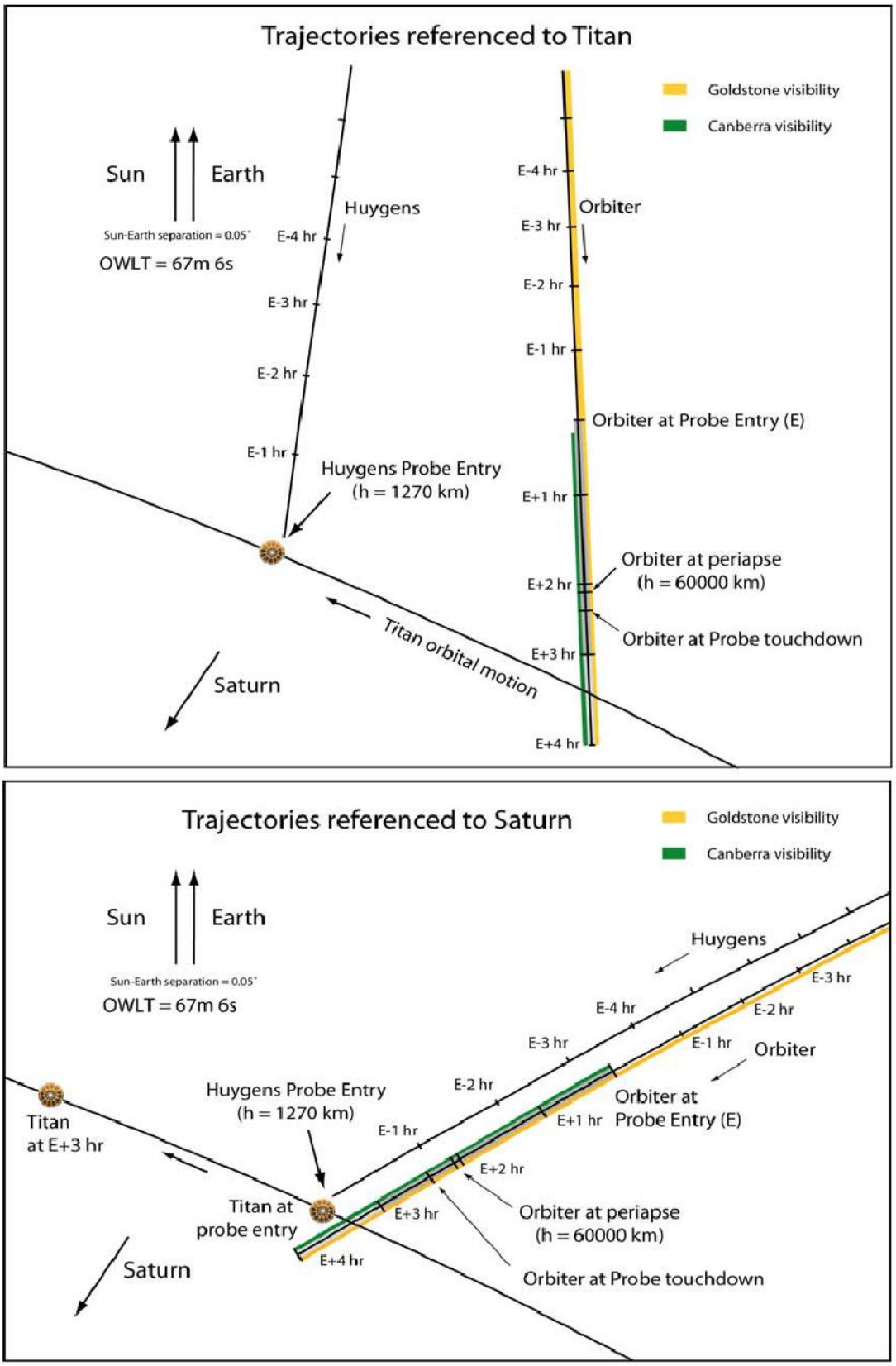

Figure 2.3: *Huygens approach trajectory referenced to Titan (upper panel) and to Saturn (lower panel). The orbiter will pass Titan at an altitude of 60,000 km on its retrograde side. The relative position of the Sun, the Earth, and Saturn are indicated. The green and yellow lines indicate the visibility of Cassini from the Goldstone and Canberra Deep Space Network antennas respectively. The trajectory tick marks are given in hours with respect to the interface epoch (Schipper, 2003).*

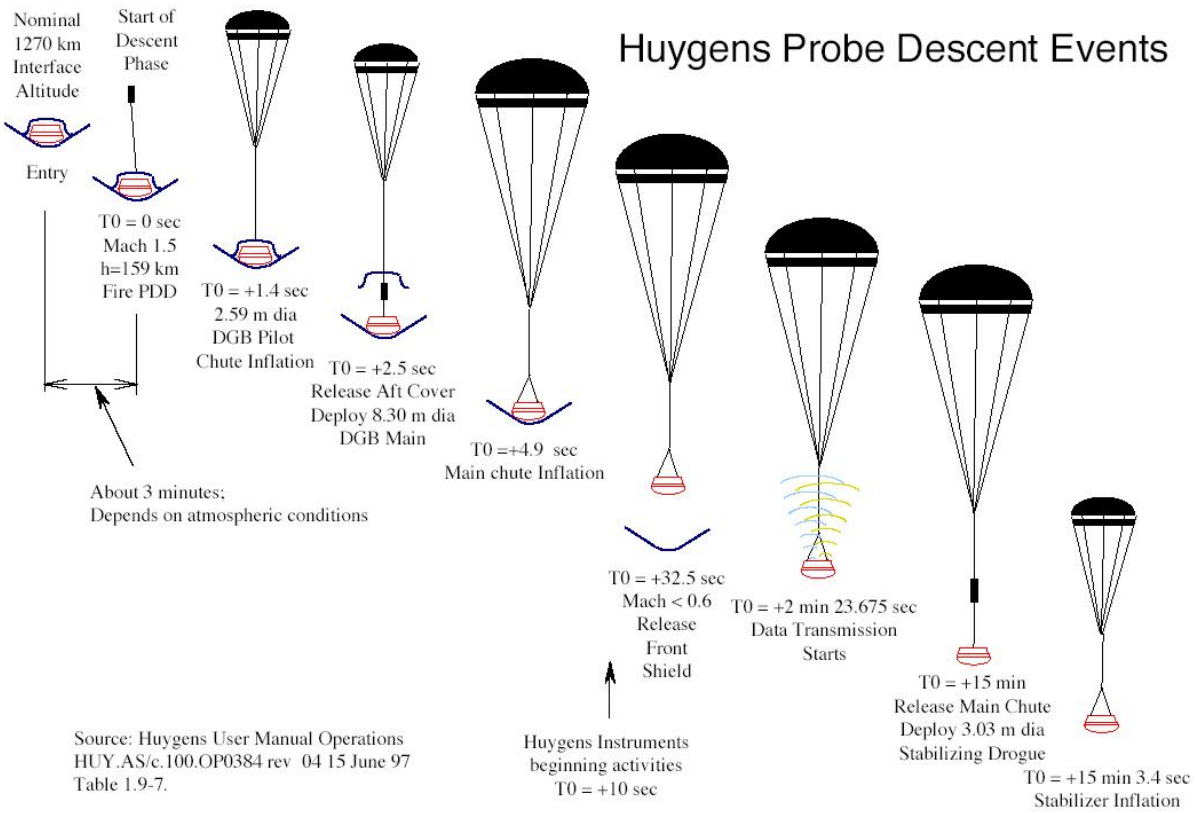

Figure 2.4: *The Huygens probe entry and descent mission sequence.*

2.2 Huygens Probe Mission Timeline

The Huygens mission sequence is schematically depicted in Fig. 2.4 and can be divided into the following parts:

- the entry phase sequence with the so called pre-T_0 timeline; and
- the descent phase with the so called post-T_0 timeline.

The pre-T_0 timeline has to ensure the correct activation of the parachute deployment (i.e., the firing of the pilot chute) at T_0. This comprises the detection and enabling of two important events in the entry phase, the probe onboard software (POSW) mission timer start S_0 and the triggering of the parachute sequence arming timer T_A. Both detections are driven by deceleration measurements with the acceleration limits specified in Table 2.1. The descent phase starts with the initiation of the parachute sequence at T_0 and the corresponding timeline is also listed in Table 2.1. The parachute design and dimensions are described in Chap. 3. It is important to note that the detection of S_0 and T_A can only occur after the detection process has been *enabled*, which happens when the measured deceleration reaches the corresponding thresholds on the raising edge of the deceleration profile (i.e., 50 m/s^2 and 80 m/s^2 for S_0 and T_A respectively). The detection event itself is declared when the corresponding deceleration limits on the trailing edge of the profile are measured (i.e., 10 m/s^2 and 9.484 m/s^2 for S_0 and T_A respectively).

Phase	Time	Event
Entry-phase	acc. $>$ 50 m/s^2 (RE)	S_0-detect. enabled
	acc. $>$ 80 m/s^2 (RE)	T_A-detect. enabled
	acc. $<$ 10 m/s^2 (TE)	S_0-detect.
	acc. $<$ 9.484 m/s^2 (TE)	T_A-detect.
Descent with Main Chute and front shield	$T_0 = S_0 + 6.375$ s	PDD firing
	T_0+1.47 s	Pilot chute inflated
	T_0+2.50 s	Back-cover release
	T_0+4.95 s	Main parachute deployed
	T_0+32.50 s	Front-shield jettison
Descent with main chute	T_0+45.455 s	Probe relay link switch on
	T_0+900 s	Main parachute separation
Descent with stabilizing drogue	T_0+901.02 s	Stabilizing drogue deployed

Table 2.1: *Timing of important events in the probe mission timing sequence (Kazeminejad* et al.*, 2004). acc. = measured acceleration value; RE= rising edge of the deceleration profile; TE= trailing edge; T_A = triggering of the parachute sequence arming timer, S_0 = probe onboard software (POSW) mission timer start, and T_0 = starting time of the parachute deployment sequence.*

Chapter 3

Huygens Probe Design and Instruments

The probe system comprises two principal elements: the Huygens probe, which will enter Titan's atmosphere once it is separated from the Cassini spacecraft after Cassini is inserted into an orbit around Saturn, and the probe support equipment, which remains attached to Cassini to establish a communication link during the probe mission (Clausen *et al.*, 2002).

The Probe (see Fig. 3.1) consists of two elements: the aeroshell and the Descent Module. The aeroshell is wrapped in a multi-layer thermal protection for the cruise phase. It is made of two parts: the front shield subsystem (FRSS) and the Back Cover. The 79 kg, 2.7 m diameter, 60-degree half-angle coni-spherical front shield is designed to decelerate the probe in Titan's upper atmosphere from about 6 km/s at entry to a velocity equivalent to about Mach 1.5 ($\sim$400 m/s) at around 160 km altitude. Tiles of "AQ60" ablative material (a felt of phenolic resin reinforced by silica fibres) provide protection against the atmospheric induced radiative and convective heat fluxes up to 1.4 MW/m^2. The Back Cover protects the Descent Module during entry, and carries a multi-layer insulation (MLI) for the cruise and coast. A hole in it ensures depressurization during launch and re-pressurization during entry. As the Back Cover does not have stringent aerothermodynamic requirements, it is a stiffened aluminium shell of minimal mass (11.4 kg) protected by Prosial (5 kg). The Descent Module comprises two platforms, a fore-dome and an after-cone and is enclosed in the aeroshell like a cocoon.

The Descent Control Subsystem (DCSS) is activated nominally at Mach 1.5, at about 160 km altitude (Kazeminejad *et al.*, 2004). The parachute sequence (see Fig. 3.2) begins by firing the Parachute Deployment Device (PDD) to eject the pilot chute pack through a break-out patch in the Back Cover, the attachment pins of which shear under the impact. The 2.59 m diameter Disk Gap Band (DGB) pilot chute inflates behind the Descent Module and pulls the Back Cover away from the assembly. As it goes, the Back Cover pulls the 8.30 m diameter DGB main parachute from its container. This canopy inflates during the supersonic phase in order to decelerate and stabilize the probe through the transonic regime. The Front Shield is released at about Mach 0.6. In fact, the main parachute is sized by the requirement to provide sufficient deceleration to guarantee a positive separation of the Front Shield from the Descent Module. The main parachute is too large for a nominal descent time shorter than 2.5 hours, a constraint imposed by battery capacity,

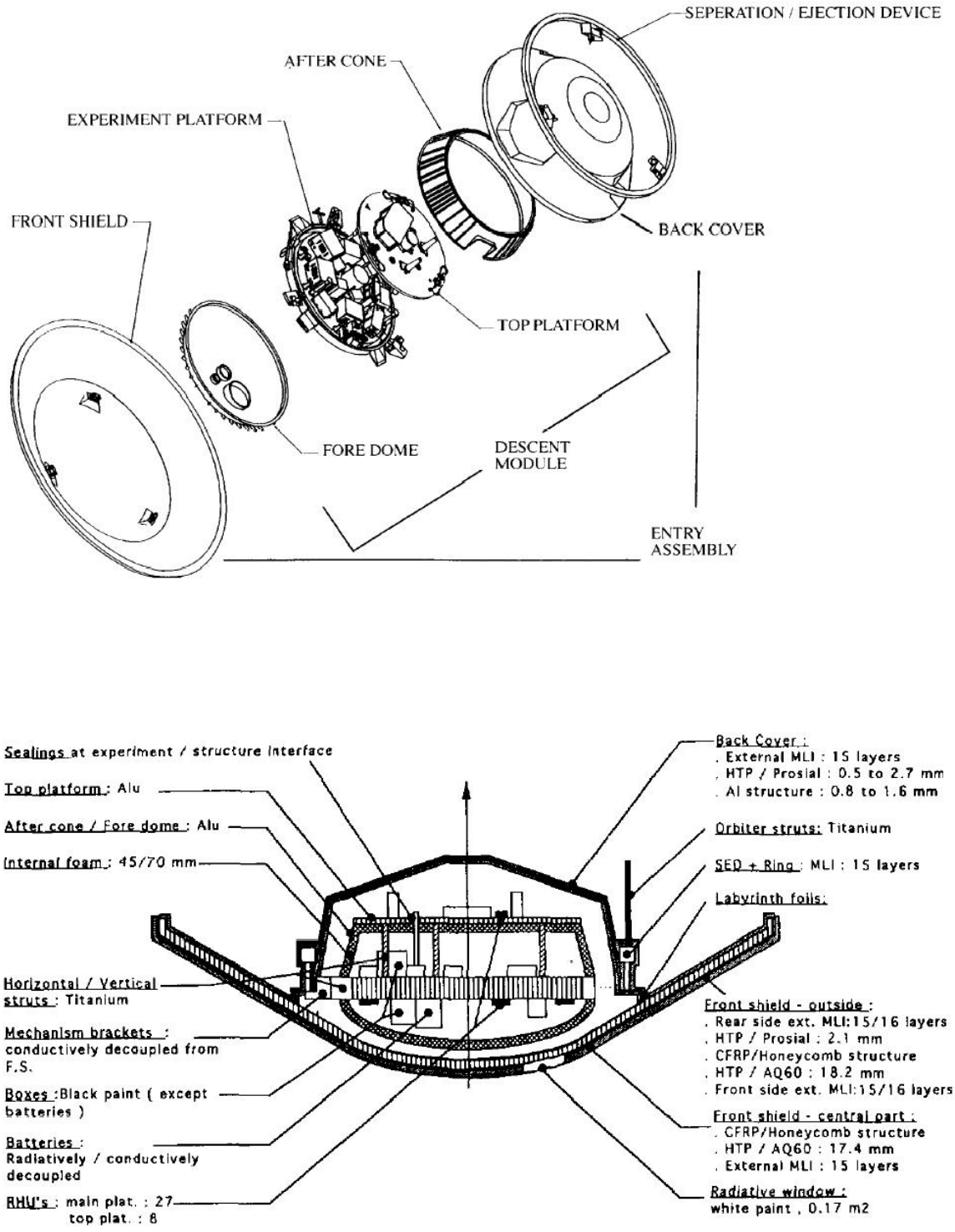

Figure 3.1: *Huygens Probe Design (Clausen* et al.*, 2002).*

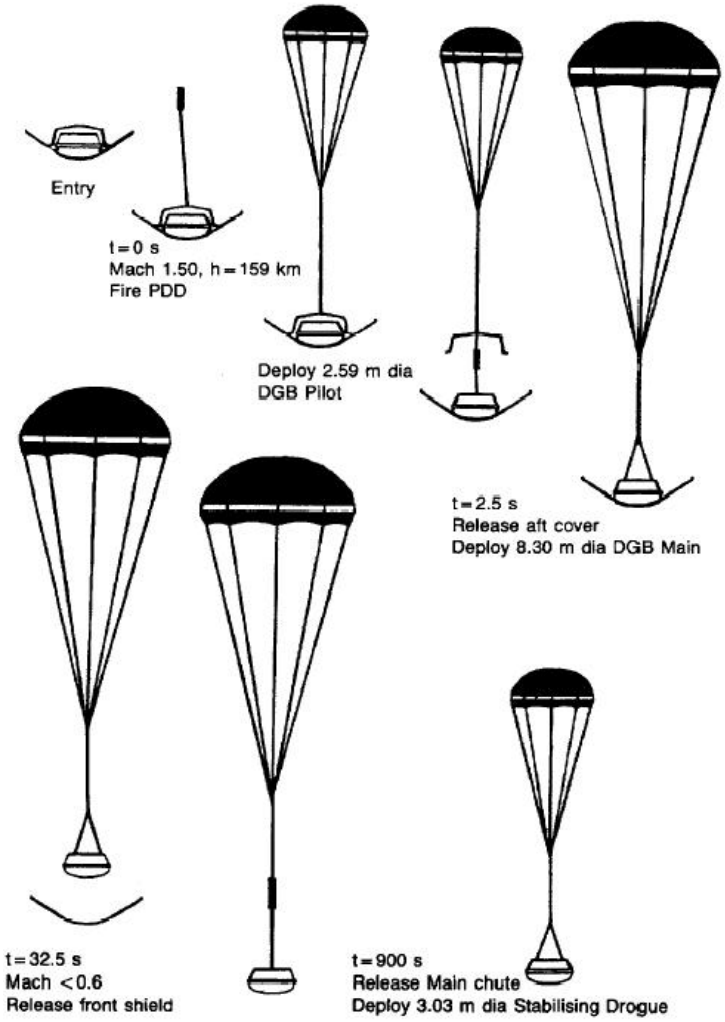

Figure 3.2: *Huygens parachute system (Clausen* et al.*, 2002).*

communication geometry between the probe and the orbiter, and thermal performances of the Descent Module in Titan's atmosphere. It is therefore jettisoned after 15 min and a 3.03 m diameter DGB stabilizing parachute is deployed. All parachutes are made of kevlar lines and nylon fabric. The main and the stabilizer chutes are housed in a single canister on the Descent Module's top platform. Compatibility with the probe's spin is ensured by incorporating a swivel using redundant low-friction bearings in the connecting riser of both the main and stabilizer parachutes.

After the probe impacts on Titan's surface it continues its measurements and transmits its data at a constant 8 kbit/s to the overflying Cassini spacecraft, which points its High Gain Antenna to a predefined location on Titan until it goes below the horizon of the probe's landing site. Due to the retrograde Titan flyby of the orbiter during the probe mission, the planned landing point had to be moved from the northern hemisphere to the southern and from the afternoon to the morning sector.

3.1 Mass Budget and Cross-Sectional Area

The probe mass and its aerodynamic cross section change during the various mission phases. During the entry phase the probe loses mass due to the heat shield ablation. The total ablation mass loss is predicted to be ∼9.7 kg. The mass loss profile as a function of probe velocity can be modelled from the two first order differential equations (Gaborit, 2004a,b)

$$\frac{dm_s}{dt} = -\frac{\eta_{eff}}{2\,L_{\rm abl}}\,\rho\,v_{\rm rel}^3 S_0 \tag{3.1}$$

and

$$\frac{dv_{\rm rel}}{dt} = -\frac{\rho\,v_{\rm rel}^2\,S_0\,C_D}{2\,m_s} \tag{3.2}$$

where $L_{\rm abl}$ can be considered as an ablation enthalpy that takes into account all the physical interactions of the ablation process (e.g., fusion, sublimation, ionization etc.), η_{eff} is a factor that characterizes the effectiveness of the energy transfer of the incoming flow particles into the heating of the probe shield. S_0 is the probe cross section (which can be considered as constant during the ablation process), m_s is the probe mass at the time t, and $v_{\rm rel}$ is the relative velocity between spacecraft and flow field. C_D is the aerodynamic drag coefficient and ρ is the flow field density. Combining Eq. (3.1) and Eq. (3.2) yields

$$\frac{dm_s}{dt} = \sigma\,v_{\rm rel}\,dv_{\rm rel} \tag{3.3}$$

with $\sigma = \frac{\eta_{eff}}{C_D\,L_{abl}}$. Integrating Eq. (3.3) gives

$$m(t) = m_0\,\exp\left\{0.5\,\sigma\,(|v_{\rm rel}|^2 - |v_0|^2)\right\} \tag{3.4}$$

with the initial mass m_0. v_0 is the relative velocity of the probe at the time of the start of the ablation process and is taken as the maximum probe velocity. The σ value can be adjusted to fit the entire ablation mass loss (9.7 kg) during the entry phase and was determined as $\sigma \simeq 4.18 \times 10^{-10}$ m^{-2} s^2. Table 3.1 provides the mass and cross-section for the main four probe configurations during the mission.

Configuration	Probe Mass [kg]	Probe equivalent cross-section [m^2]
Entry phase conf.	320.0	5.73
Descent conf. with main chute and front shield	288.677	59.83
Descent conf. with main chute only	207.64	55.44
Descent conf. with stab. drogue	202.423	8.57

Table 3.1: *Probe mass and equivalent cross-section for the various probe configurations.*

3.2 Probe Aerodynamic Database

The preflight aerodynamic database of the Huygens entry and descent modules as well as the main parachute has been obtained from various wind tunnel campaigns executed between 1991 and 1995. Those tests focused on module scale tests in the subsonic, transonic and supersonic regions. The database consists of static and dynamic force coefficients as a function of Mach number Ma and angle-of-attack α for the entry module (see Fig. C.1) and as function of the Reynolds number Re and α for the descent module (P. Couzin, Alcatel Space/France, private communication).

3.3 Science Instruments and Relevance

This section summarizes important facts about the various probe instruments their measurements as well as their relevance to the entry and descent trajectory reconstruction (cf. Atkinson and Kazeminejad, 2004).

Doppler Wind Exeriment

The Huygens Doppler Wind Experiment (DWE) (Bird *et al.*, 2002) is designed to measure the vertical profile of zonal (east/west) winds in the atmosphere of Titan from link lock (beneath 160 km) to the surface. The DWE is the only Huygens investigation with hardware on both the probe and the orbiter (within the Probe Support Avionics in the orbiter-mounted Probe Support Equipment). The Doppler wind hardware comprises two ultrastable oscillators. The Transmitter Ultrastable Oscillator (TUSO) is the primary signal generator[1] used to drive the Probe Relay Link (PRL) of transmitter A. The 10 MHz output of the TUSO is upconverted to the PRL A frequency of 2.040 GHz and is amplified for transmission through the probe transmitting antenna to the Cassini orbiter High Gain Antenna. All timing and signal generator requirements for receiver A on the orbiter are controlled by the second DWE ultrastable oscillator, the Receiver Ultrastable Oscillator(RUSO).

The RUSO will receive a signal that is frequency shifted due to the relative motion of the orbiter and the probe. By measuring the frequency shift of the probe telemetry and removing known Doppler contributions from the orbiter trajectory and the known modelled probe descent velocity, the assumption of the dominance of the zonal winds allows the shear in the east/west winds to be found. To convert the frequency data to an absolute zonal wind profile, it is required that either 1) the absolute transmitted frequency or 2) a single known wind measurement be known. Near the surface (or on the surface if the probe survives impact), it is likely that the winds will diminish to zero thereby providing the required wind reference point. The DWE measurements of zonal wind allow the constraining of the probe longitude drift during its descent phase.

[1] In the event of TUSO failure, PRL A can be switched to a temperature compensated crystal oscillator (TCXO) creating a radio link with a frequency stability that is approximately 1000 times poorer than the TUSO over 3 hours.

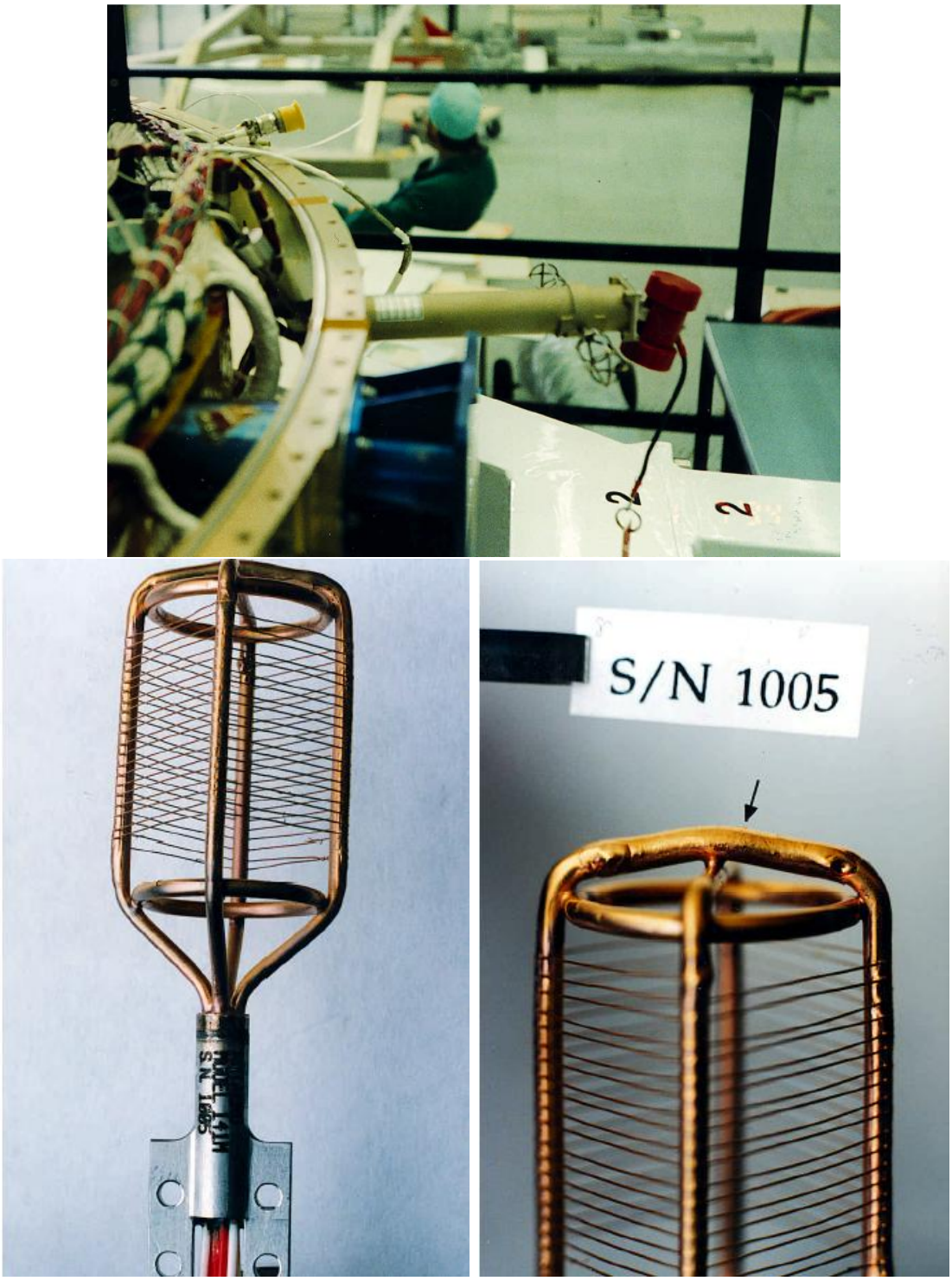

Figure 3.3: *Huygens probe scientific instruments; upper panel: HASI STUB with the TEM units and the PPI Kiel probe; lower panels: HASI TEM S1 fine (left) and S2 coarse (right) sensor. (Fulchignoni* et al.*, 1997)*

Huygens Atmospheric Structure Instrument

The Huygens Atmospheric Structure Instrument (HASI) (Fulchignoni *et al.*, 2002) is designed to measure the physical quantities characterizing Titans atmosphere. HASI measures profiles of atmospheric pressure and temperature as well as the electrical properties of the atmosphere. Furthermore atmospheric turbulences along the descent path are characterized. The Huygens Atmospheric Structure Instrument comprises several subsystems: 1) Deployable Boom System (DBS) with the Permittivity, Wave, and Altimetry (PWA) electrodes; 2) the fixed stem (STUB) with the temperature sensors, Pressure Profile Instrument Kiel probe (PPI), and acoustic sensors; 3) the accelerometers (ACC); and 4) the Data Processing Unit (DPU).

The HASI accelerometers comprise one highly sensitive single axis servo accelerometer and three piezoresistive accelerometers. The piezoresistive accelerometers are aligned parallel or orthogonal to the Huygens probe symmetry (X) axis. To improve the accuracy of accelerations along the probes symmetry axis the servo accelerometer is mounted near the Huygens probes center of mass. The Servo accelerometer operates by sensing the displacement of a seismic mass. The current required to drive the mass from its displaced position back to its null position is a direct measurement of acceleration. The piezoresistive accelerometers consist of a suspended seismic mass supported by a cantilever whose displacement is determined by two strain-dependent resistances. Part of a Wheatstone bridge, the variation in output voltage produced when an external voltage is applied is therefore dependent on the acceleration.

The HASI temperature sensors (see lower panels of Fig. 3.3) are dual element platinum resistance thermometers, each unit comprising a platinum-rhodium truss cage frame exposing the two sensing elements to the atmospheric flow. The two redundant temperature sensor units (fine and coarse) are mounted on the STUB, which is shown in the upper panel of Fig. 3.3. The Pressure Profile Instrument (PPI) includes sensors for measuring the atmospheric pressure during descent and on the surface. The transducers and the related electronics are located in the HASI Data Processing Unit (DPU). The atmospheric flow is conveyed to the DPU through a Kiel-type pressure probe accommodated within a pitot tube that is mounted on the STUB stem end. The Kiel probe provides accurate measurements of the total (environmental plus kinetic) pressure for flow inclination angles up to 45 deg. The pressure transducers are silicon capacitive absolute pressure sensors known as Barocaps. The Barocap consists of a small sensor head with associated transducer electronics. The varying ambient pressure deflects a thin silicon diaphragm in the sensor head. This causes a change in the separation of two capacitive plates. The variation in capacitance is converted into an oscillation frequency in the PPI electronics.

The Huygens Atmospheric Structure Instrument is nominally switched on during the coast phase approximately 5.5 min prior to arrival at the entry interface altitude. Accelerometer (ACC) sampling starts 2 min after the HASI is powered on and continues for four minutes as the probe altitude decreases from 1300 km to about 160 km. Following the release of the front shield at about 160 km, the HASI booms are deployed and direct measurement of temperature, pressure (T0 + 1min) and electrical properties (T0 + 2.5min) commences.

The HASI accelerometers are the primary source to reconstruct the probe entry phase and also provide the time of probe impact. The pressure and temperature measurements are essential to reconstruct the descent phase.

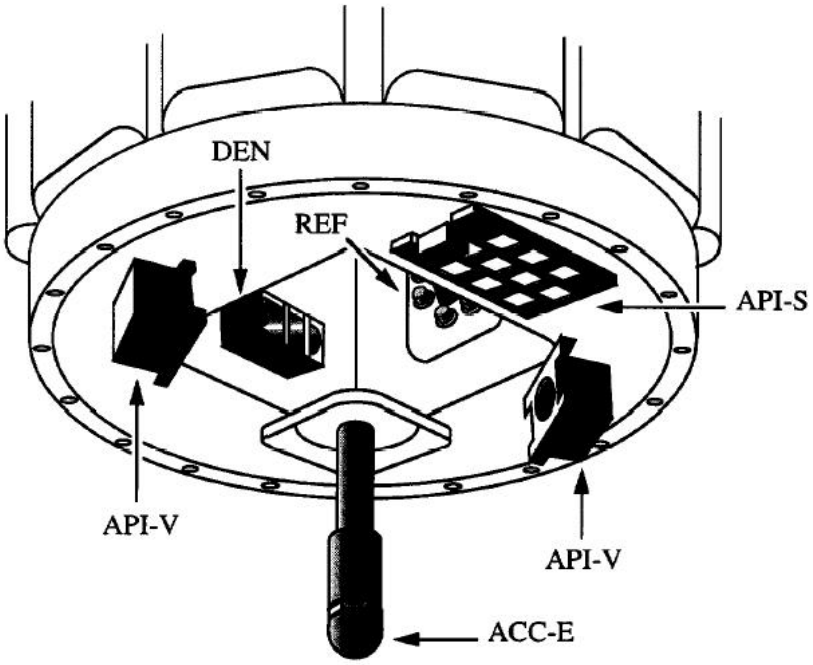

Figure 3.4: *SSP instrument layout (upper panel) and DISR Sensor Head location on the Huygens probe (lower left) and as seen from above (lower right).*

Surface Science Package

The Huygens Surface Science Package (SSP) (Zarnecki *et al.*, 2002) is a collection of nine instrument subsystems (see Fig. 3.4) designed primarily to study the surface properties of Titan.However, a number of measurements are conducted during the descent and support the descent trajectory analysis. Seven of the measurement subsystems are exposed to the atmosphere and surface of Titan. These include sensors to measure the force of the surface impact (external accelerometer, ACC-E), the acoustic properties of the surface (speed of sound, API-V, and the depth of an ocean if the probe lands on a liquid surface using the acoustic sounder, API-S), and the density, permittivity, temperature and thermal conductivity, and refractive index of an ocean (DEN, PER, THP, and REF). Additionally, the SSP experiment has two internally mounted measurement subsystems - an internal accelerometer (ACC-I) and a tilt meter (TIL), both mounted on the SSP electronics box. While the measurements have been optimized for surface operations, several subsystems operate during the probe descent and, within different regions of the atmosphere, contribute data important to the reconstruction of the descent trajectory.

Gas Chromatograph and Mass Spectrometer

The Gas Chromatograph Mass Spectrometer (GCMS) (Niemann *et al.*, 2002) measures the chemical composition of Titan's atmosphere from 170 km altitude (∼1 hPa) to the surface (∼1500 hPa) and determine the isotope ratios of the major gaseous constituents. The GCMS is a quadrupole mass filter with a secondary electron multiplier detection system and a gas sampling system providing continuous direct atmospheric composition measurements and batch sampling through three gas chromatographic columns. The mass

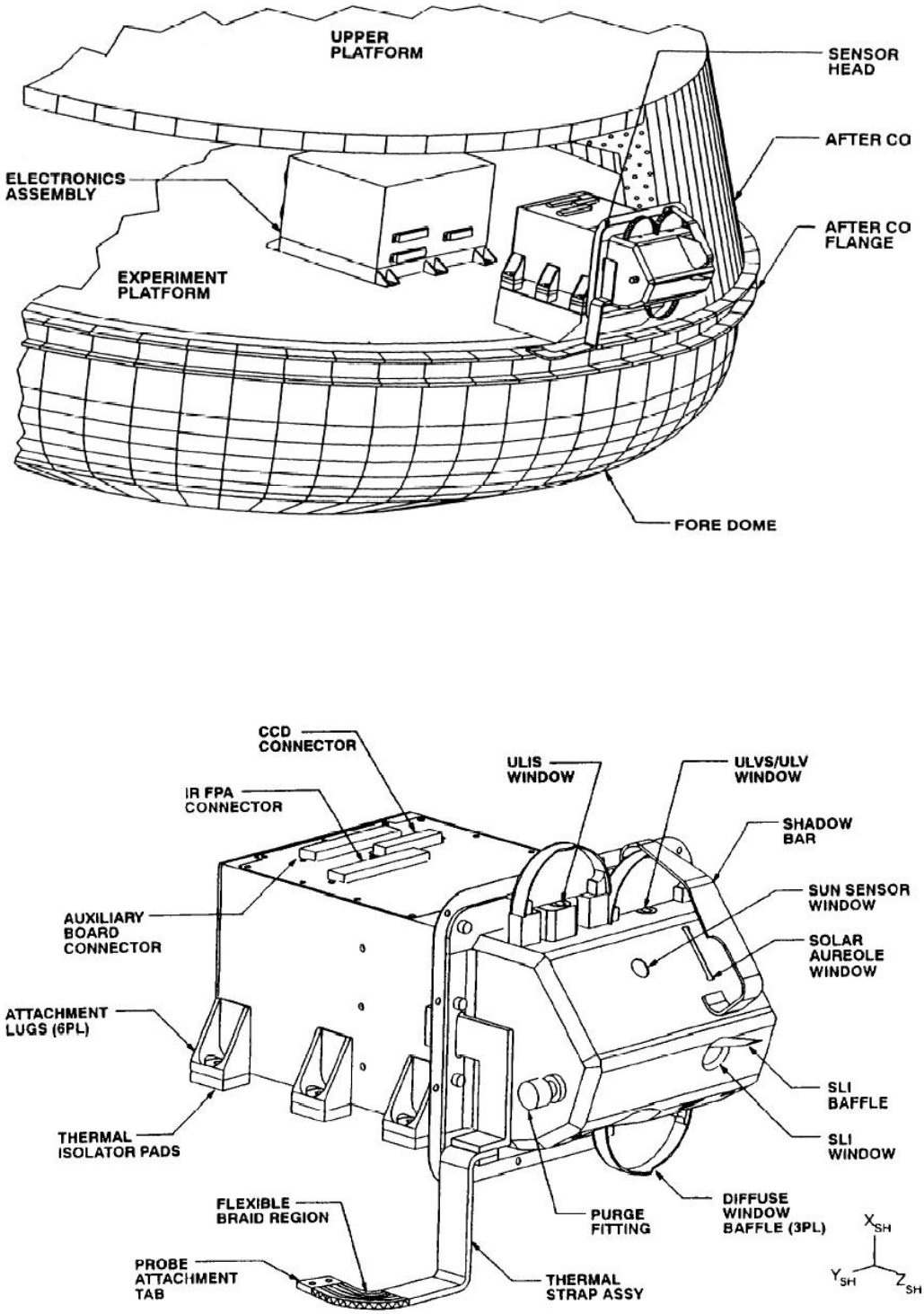

Figure 3.5: *DISR Sensor Head location on the Huygens probe (upper panel) and as seen from above (lower panel) (Tomasko* et al.*, 1997).*

spectrometer employs five ion sources sequentially feeding the mass analyzer. The GCMS measurements of the concentration of the major atmospheric constituents will provide the possibility to derive the mean molecular mass and its changes during the entire descent phase.

Aerosol Collector and Pyrolizer

The Aerosol Collector and Pyrolizer (ACP) (Israel *et al.*, 2002) has an internal pressure sensor that indicates the external pressures during several periods of the probe descent. However, the resolution is low (approximately 1 mVolt per 35 mbar) and is not competitive with the pressure sensors on HASI. Therefore, ACP pressure measurements is only considered as a backup and cross check for the HASI pressure sensor.

Descent Imager and Spectral Radiometer

The Descent Imager/Spectral Radiometer (DISR) (Tomasko *et al.*, 2002) is the optical instrument aboard Huygens that measures the brightness of the sunlight in Titan's atmosphere with several different spatial fields of view, in several directions, and with various spectral resolutions. The location of the DISR Sensor Head is shown in the upper panel of Fig. 3.5 and the Sensor Head itself is depicted in the lower panel. Especially important from a trajectory reconstruction point of view is the DISR Sun Sensor which will measure the Solar Zenith Angle (SZA). The SZA can be used to derive the probe longitude drift during the descent phase.

3.4 Engineering Instruments and Relevance

Radar Altimeter Units

The Proximity Sensor/Radar Altimeter Unit (RAU), comprising two completely redundant radar altimeters (unit A, 15.4 to 15.43 GHz and unit B, 15.8 to 15.83 GHz), is responsible for measuring probe altitude from about 25 km to the surface. Each altimeter transmits a swept frequency modulated continuous wave (FMCW) in which the sweep period is adjusted so that the frequency of the return signal differs by 200 kHz from that of the transmitted signal. Since the transmitted frequency is swept, the sweep period is directly related to the propagation time and, therefore, to altitude.

The RAU units provide a means to derive a surface elevation profile during the last 25 km by comparing the surface altitude measurements to the reconstructed altitude profile derived from the atmospheric pressure and temperature measurements.

Central Acceleration Sensor Unit

The Central Acceleration Sensor Unit (CASU) comprises three axial accelerometers, each of which supplies analog signals to the Command and Data Management Units (CDMU). Designed to measure accelerations in the range of 0 to +10g (with a sampling rate of 1 Hz) the CASU is used primarily for triggering of events during entry and descent. As the CASU performance is inferior to that of the HASI accelerometers (in terms of

range, resolution, and sampling rate) it will be mainly used as a backup device in case of malfunction or data gaps in the HASI data.

Chapter 4

Titan's Physical Properties and Atmosphere

4.1 Physical Properties

For purposes of the Huygens entry and descent trajectory reconstruction, the most relevant physical parameters of Titan are the satellite's gravitational constant (GM), its radius R_P, its rotational period ω_P, and its pole coordinates at the epoch of J2000. These parameters and the corresponding references are provided in Table 4.1.

Parameter	Unit	Value	Uncertainty	Reference
Gravitational Parameter GM	km^3/s^2	8978.2	0.2818	Cassini Navigation Team
Radius R_P	km	2575	0.5	NAIF PCK00007
Rotation period ω_P	days	15.9454	–	(Davies *et al.*, 1995)
Pole α_0	deg	36.41-0.036 T	–	(Davies *et al.*, 1995)
Pole δ_0	deg	83.94-0.004 T	–	(Davies *et al.*, 1995)
Prime Meridian angle W	deg	189.64+22.5769768 d	–	(Davies *et al.*, 1995)

Table 4.1: *Titan's physical properties: α_0 and δ_0 are standard equatorial coordinates with equinox J2000 at epoch J2000 (JD2451545.0 TDB), T is the interval in Julian centuries (36525 days) from the standard epoch, and d is the interval in days from the standard epoch.*

4.2 Titan Atmosphere Models

The first close-up remote sensing and radio sounding measurements from Titan's atmosphere were performed by the Voyager 1 spacecraft during its flight through the Saturnian

system in November 1980. Two sets (ingress and egress) of refractivity data from a radio occultation experiment were used by Lindal *et al.* (1983) to infer two vertical pressure and temperature profiles between the ground and an altitude of 200 km assuming a pure N_2 composition. Two independent additional datasets are available from the Voyager 1 infrared spectroscopy experiment (IRIS) constraining the stratospheric thermal profile and the ultraviolet spectrometer (UVS) (Broadfoot *et al.*, 1977) designed to optimize the information from an ultraviolet absorptive occultation and provide information on the composition and abundance of UV absorbers in Titan's atmosphere (Smith *et al.*, 1982; Strobel *et al.*, 1992).

Three atmosphere models are currently available for Titan: The LH90 model (Lellouch and Hunten, 1987; Lellouch *et al.*, 1990) is based on a reanalysis of the radio occultation measurements of Lindal *et al.* (1983) for the altitudes lower than 200 km. The Y97 model (Yelle *et al.*, 1997) is also based on the radio occultation data from Lindal *et al.* (1983) but is further constrained by Voyager 1 IRIS measurements (Coustenis *et al.*, 1989; Coustenis and Bezard, 1995; Lellouch *et al.*, 1989, 1990) and, at altitudes above ∼1000 km, by the UVS solar occultation experiment from Smith *et al.* (1982) and Strobel *et al.* (1992). To predict the physical properties of Titan's atmosphere and provide an engineering model for the Huygens project mission analysis efforts, Yelle *et al.* (1997) considered the following three uncertainties: uncertainties in the analysis of the Voyager data, uncertainties due to temporal and/or spatial (i.e., latitudinal) variations of the atmospheric structure and composition (these could impact the atmosphere's temperature profile), and finally uncertainties due to the variations in the surface pressure (topography and/or weather systems). To take into account these three categories of uncertainties, Yelle *et al.* (1997) provided three versions of the Y97 model: a recommended model, a model for maximum mass density, and a model for minimum mass density. The three density profiles are shown together with their corresponding temperatures in Fig. 4.1. Note that the minimum and maximum model have temperature differences of roughly 30 K.

Recently Vervack *et al.* (2004) reanalyzed the Voyager 1 UVS solar occultations by Titan to expand upon previous analysis and to resolve inconsistencies that have been noted in the scientific literature. The proposed V04 engineering atmosphere model assumes an atmosphere composed of N_2 and CH_4 and is well-mixed at all altitudes (i.e., no diffusive separation). Below the reference "surface" level at 330 km, the V04 model is identical to the Y97 model. The most striking difference with respect to the Y97 model is the lack of a mesosphere.

The Y97 model assumes three different compounds for the molecular composition: nitrogen (N_2), methane (CH_4) and argon (Ar)[1]. The relative abundance of CH_4 and argon will vary with altitude in the upper atmosphere (i.e., above ∼600 km) because of diffusive separation and can be calculated analytically (see Sec. 4.3).

[1]Note that there is a theoretical expectation that argon is present in the atmosphere of Titan, but there has been no direct detection of this atom.

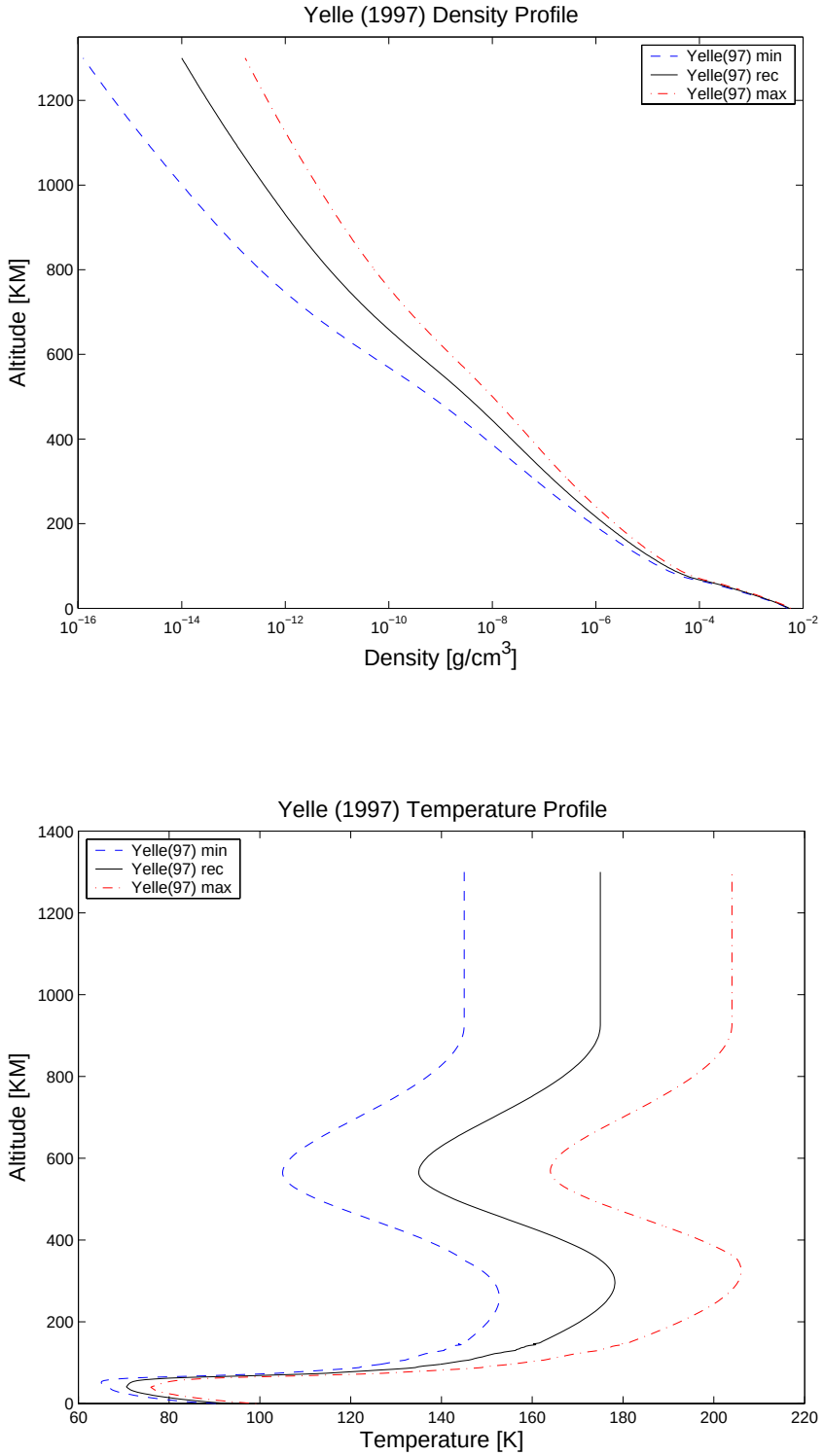

Figure 4.1: *Minimum, recommended, and maximum Yelle* et al. *(1997) Titan density (upper panel) and temperature (lower panel) profile.*

Species	Yelle minimum	Yelle recommended	Yelle maximum
CH_4	5.00E-2	3.007E-02	1.0013E-02
Ar	0.0	1.99573E-02	9.98933E-02

Table 4.2: *CH_4 and Ar mole fractions for Titan's heterosphere according to the three versions of the Y97 model (Yelle* et al.*, 1997). Note that the third compound is assumed to be N_2.*

4.3 Titan's Atmosphere Composition

Planetary atmospheres can be divided in terms of their composition into the *homosphere* and the *heterosphere*, which are separated by the *homopause*.

The homosphere region is characterized by turbulent mixing and the mole fractions of the various compounds are therefore constant which also implies a constant molecular mass. Table 4.2 provides the heterosphere mole fractions of the major species as assumed in the Y97 model.

In the heterosphere the mole fractions of the various compounds (and therefore also the molecular mass of the gas mixture) vary with altitude due to diffusive separation. The homopause is defined as the altitude where the *eddy diffusion* (mixing) coefficient is equal to the molecular diffusion coefficient (Bauer and Lammer, 2004). For Titan the homopause is estimated at an altitude of ∼600 km (Yelle *et al.*, 1997). Diffusive separation will therefore only become significant above 600 km and will require an evaluation of the altitude dependent molecular weight[2]. The methane and argon mole fractions can be modelled using analytical expressions provided by Strobel *et al.* (1992) and Steiner and Bauer (1990). The CH_4 mole fraction for the three Y97 profiles is shown in Fig. 4.2 and was calculated from

$$f_{CH_4} = A_1 \left(1 + \mathrm{e}^{(1-\nu)\,h}\right)^{\frac{3}{7\,(1-\nu)}} + A_2 \tag{4.1}$$

and the Argon mole fraction from

$$f_{Ar} = A_3 \left(1 + \mathrm{e}^{(1-\nu)\,h}\right)^{\frac{-0.3}{(1-\nu)}} \tag{4.2}$$

where h is the normalized geopotential height measured relative to the homopause given by

$$h = 1.67 \times 10^5 \frac{z - z_H}{(R_T + z_H)\,(R_T + z)} \tag{4.3}$$

z_H defines the altitude of the homopause and R_T the radius of Titan. A_1, A_2, and A_3 are integration constants used to match conditions deep in the atmosphere. The parameter ν describes the altitude of the eddy diffusion coefficient. Numerical values for the model parameters ν, A_1, A_2, A_3, and z_H are provided by Yelle *et al.* (1997) for the recommended Titan atmosphere model as 0.625, 0.024, 0.006, 0.020, and 1050.0 km respectively. The molecular weight of the gas mixture can then be calculated from

[2]Direct measurements of the molecular mass by the GCMS instrument will only be available during the entry phase below ∼160 km.

$$\mu = \sum_i f_i \, \mu_i \tag{4.4}$$

where μ_i is the molecular weight of the species i with the mole fraction f_i.

4.4 Titan Wind Models

The bulk of the information on the horizontal structure of temperature was derived from observations by the infrared spectroscopy experiment (IRIS) on Voyager 1 in 1981, just after Titan's northern spring equinox. IRIS made observations covering most latitudes within 60° N and S, with some zonal (i.e., east-west) coverage at ceratin latitudes (Coustenis and Bezard, 1995). The *gradient wind equation* relates the vertical gradient in the zonal wind to the meridional gradient in temperature and is given by

$$u \left\{ 2\,\Omega \, \sin\Lambda + u \, \frac{\tan\Lambda}{r} \right\} = - \left(\frac{1}{r} \, \frac{\partial \Phi}{\partial \Lambda} \right)_p \tag{4.5}$$

with the geopotential

$$\Phi = \int_0^z g \, dz\prime \tag{4.6}$$

g denotes the gravitational acceleration, z the altitude, u the zonal wind velocity (positive in the eastward direction), $\Omega = 2\,\Pi/16$ days the surface rotation rate, Λ the latitude, r the distance from the planet's center, and p the pressure. Using Eq. (4.5) and three IRIS equator-to-pole (meridional) temperature gradients (i.e., $\Delta T \sim 20$ K in the upper stratosphere, $\Delta T \sim 3$ K in the lower stratosphere near the surface), Flasar *et al.* (1981) derived a zonal wind height profile for $\Lambda = 45°$ and assuming a meridional temperature variation scaled as cosine of latitude. This profile increases monotonically to ∼111 m/s in the upper stratosphere. To account for the uncertainties due to the limited coverage in latitude and altitude and the errors in the retrieved temperatures, a maximum wind envelope was derived with doubled equator-to-pole temperature gradients, which implied a zonal wind velocities increased by a factor of $\sqrt{2}$. Lunine *et al.* (1991) expressed the maximum wind envelope in form of a simple engineering model that could be easily used for mission analysis efforts by the Huygens prime contractor *Aerospatiale* (now *Alcatel Space* in Cannes, France):

$$|v - v_s| \leq v_0 \left[1 + \frac{1}{8} \ln \left(\frac{0.5\,\mathrm{mbar}}{p} \right) \right] \cos\Lambda \tag{4.7}$$

with $v_0 = 200$ m/s. v_s is the velocity of the surface that which can be neglected due to surface friction. This engineering model, referred to as the *Aerospatiale Model*, implies a maximum wind speed (at 0° latitude and for pressures ≤ 0.5 mbar) of 200 m/s. Note that the latitudinal dependence in Eq. (4.7) corresponds to superrotation at constant angular velocity (rigid rotation).

During the redesign of the Huygens mission in the framework of the Huygens Recovery Task Force (Huygens Recovery Task Force, 2001; Kazeminejad, 2002) Eq. (4.7) was reduced by a factor of $\sqrt{2}$ which results in a maximum wind speed of ∼140 m/s and is

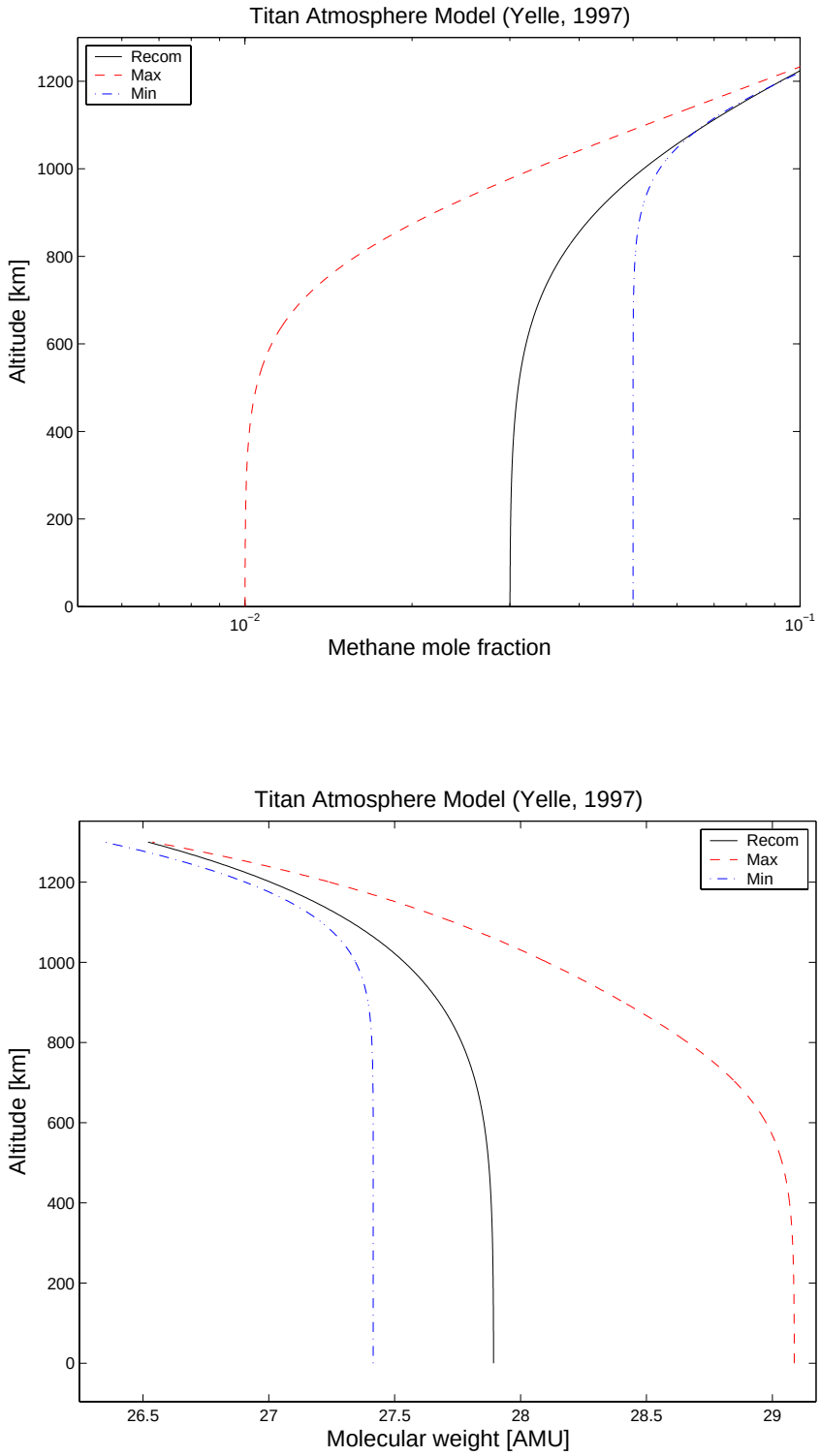

Figure 4.2: *CH_4 mole fraction (upper panel) and corresponding N_2-CH_4-Ar mixture molecular weight for the minimum, recommended, and maximum Yelle* et al. *(1997) Titan atmosphere model.*

consistent with the value suggested by the nominal Flasar model in the upper atmosphere (Lebreton, 2001). However, since two solutions to the gradient wind equation are possible (one with prograde and one with retrograde winds) the IRIS measurements do not fully constrain the atmospheric dynamics. However, recent earth-based direct observations have provided strong indications (i.e., with 94 % confidence) of a prograde global wind direction (Kostiuk *et al.*, 2001). The HRTF zonal wind model therefore assumes a prograde wind direction and was the standard model for all mission analysis efforts undertaken by the HRTF. It is also the standard model for ongoing analysis efforts by the Huygens Implementation Team (HIT).

4.5 Wind Gust and Gravity Wave Models

A wind gust model was developed by *Aerospatiale* during the Huygens Phase C/D based on experience on Earth models (Lebreton, 2003). The wind gust model was essentially used to study the dynamics of the probe-parachute swing during the descent phase that impacts the probe stability and its capability to maintain its radio link to the orbiter. The same model was used in various test simulations in the mission geometry redesign phase.

A Titan hydrostatic gravity wave model was developed by Strobel and Sicardy (1997), which is based on a linear saturation theory (the wave amplitude at all heights was set equal to the saturation limit) and constrained by observations of the Sgr 28 occultation (Hubbard *et al.*, 1993). The model is used to assess the maximum expected perturbations of Titan's atmospheric properties (i.e., density, pressure, and thermal structure). Although the validity of this model has been subject of many debates within the Cassini/Huygens science community, it was used by the Huygens project to investigate the performance of the Huygens entry subsystem (Lebleu, 2003).

4.6 Real Gas Equation

An ideal gas behaves as if its molecules were infinitely small and interact only by perfectly elastic collisions at the instant of collision. Its behavior can be described by the equation of state for an ideal gas. A real gas differs from this behavior for two reasons:

1. the force of attraction between the particles in a gas is not quite zero (van der Waals forces);

2. the volume of the particles in a gas is not quite zero.

Even if all gases behave like real gases they can be approximated by an ideal gas behavior in conditions of high temperature and/or low density. If the density increases and the temperature decreases (e.g., close to the surface of Titan) the assumption of an ideal gas will not be valid anymore and the equation of state for real gases has to be used. This equation can be represented by the series

$$\frac{P}{RT} = \frac{\rho}{\mu} + B_2(T)\left(\frac{\rho}{\mu}\right)^2 + B_3(T)\left(\frac{\rho}{\mu}\right)^3 + ... + B_n(T)\left(\frac{\rho}{\mu}\right)^n \tag{4.8}$$

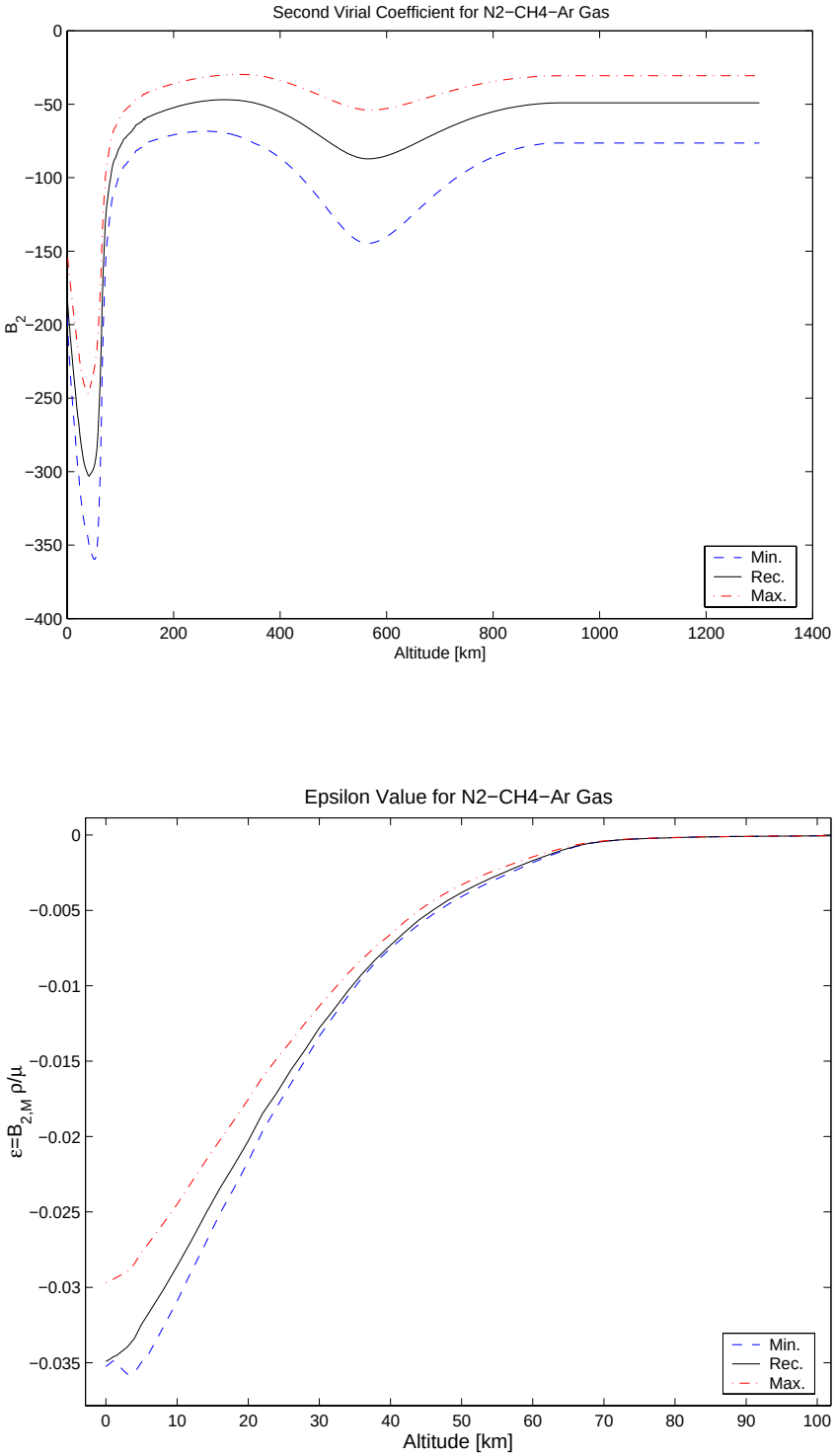

Figure 4.3: *Second virial coefficient $B_{2,M}$ (upper panel) and $\epsilon = B_{2,M}\rho/\mu$ in percent (lower panel) of a N_2-CH_4-Ar gas mixture with constant mole fractions according to the minimum, recommended, and maximum Yelle* et al. *(1997) Titan atmosphere model.*

where $B_2(T)$, $B_3(T)$, and $B_n(T)$ are respectively termed the second, third, and nth virial coefficients (Dymond and Smith, 1992). For calculations at pressures not much greater than 1 atm, the knowledge of the second virial coefficient is sufficient to describe the behavior of a real gas. Eq. (4.8) can then be simplified to

$$\frac{P\,\mu}{\rho\,R\,T} = \zeta \tag{4.9}$$

where ζ is termed the *compressibility factor* and is given by

$$\zeta \equiv 1 + \epsilon = 1 + \frac{B_2(T)\,\rho}{\mu} \tag{4.10}$$

Note that ϵ expresses the percentage of deviation from an ideal gas. If the gas is a mixture of more than one species then the second virial coefficient of the gas mixture $B_{2,M}$ has to be composed in the following manner

$$B_2 = \sum_x f_x^2\, B_{2,x}(T) + \sum_{x<y} f_x f_y B_{2,x-y}(T) + \sum_y f_y^2\, B_{2,y}(T) \tag{4.11}$$

where f_x and f_y are the mole fractions of species x and y, $B_{2,x}$ and $B_{2,y}$ are the corresponding second virial coefficients (for pure components), and $B_{2,x-y}$ is the so-called interaction virial coefficient (also referred to as the cross virial coefficient).

To calculate the second virial coefficient in Eq. (4.10) for Titan's atmosphere according to Eq. (4.11) a gas mixture of N_2, CH_4, and Ar was used with constant mole fractions as specified in Table 4.2. The B_2 coefficients for the pure gas components were evaluated using polynomial fits of laboratory measurement data as provided by Dymond and Smith (1992). Fig. 4.3 shows the calculated B_2 coefficient (upper panel) and the ϵ value (lower panel) for an altitude range of 0-200 km. One can see that a deviation from the ideal gas situation will only occur at altitudes lower than $\sim$80 km and will increase up to 3.5 % on the planet's surface.

Chapter 5

The Huygens Synthetic Dataset

5.1 Description of Simulated Sensor Data

In order to test the reconstruction algorithm a simulated synthetic dataset, i.e., the Huygens Synthetic Dataset (HSDS), was developed by the Project Scientist Team (PST) at ESA/ESTEC and was validated by the various probe instrument teams. The file format and content is fully consistent with the interface conventions between the DTWG and the instrument teams and therefore provides a perfect test case for the capabilities of the reconstruction algorithm. The development and validation of the HSDS comprises the following four steps (Pérez-Ayúcar *et al.*, 2004):

1. the definition of an atmosphere profile and a mission scenario (e.g., initial state vector and various simulation parameters);
2. the simulation of the Huygens probe entry and descent trajectory using the official Huygens 3 degrees-of-freedom (3DOF) trajectory simulation software DTAT (Castillo and Sánchez-Nogales, 2004);
3. the proper modeling of the sensor measurement ranges, sampling rates, and operational modes;
4. the simulation of sensor outputs on the basis of the simulated trajectory; and
5. the validation of the sensor outputs by the various instrument teams (PIs).

There have so far been four deliveries of the HSDS from the PST, with a continuous refinement and implementation of new features in order to better simulate the expected instrument sensor output during the actual mission in January 2005. The latest version of the HSDS (i.e., ver. 1.5) comprises the following sensor models

- HASI (3-axis) accelerometer measurements during the entry phase, pressure and temperature (corrected and uncorrected for dynamical effects) during the descent phase;
- SSP speed of sound, acoustic sounder and impact time measurements;

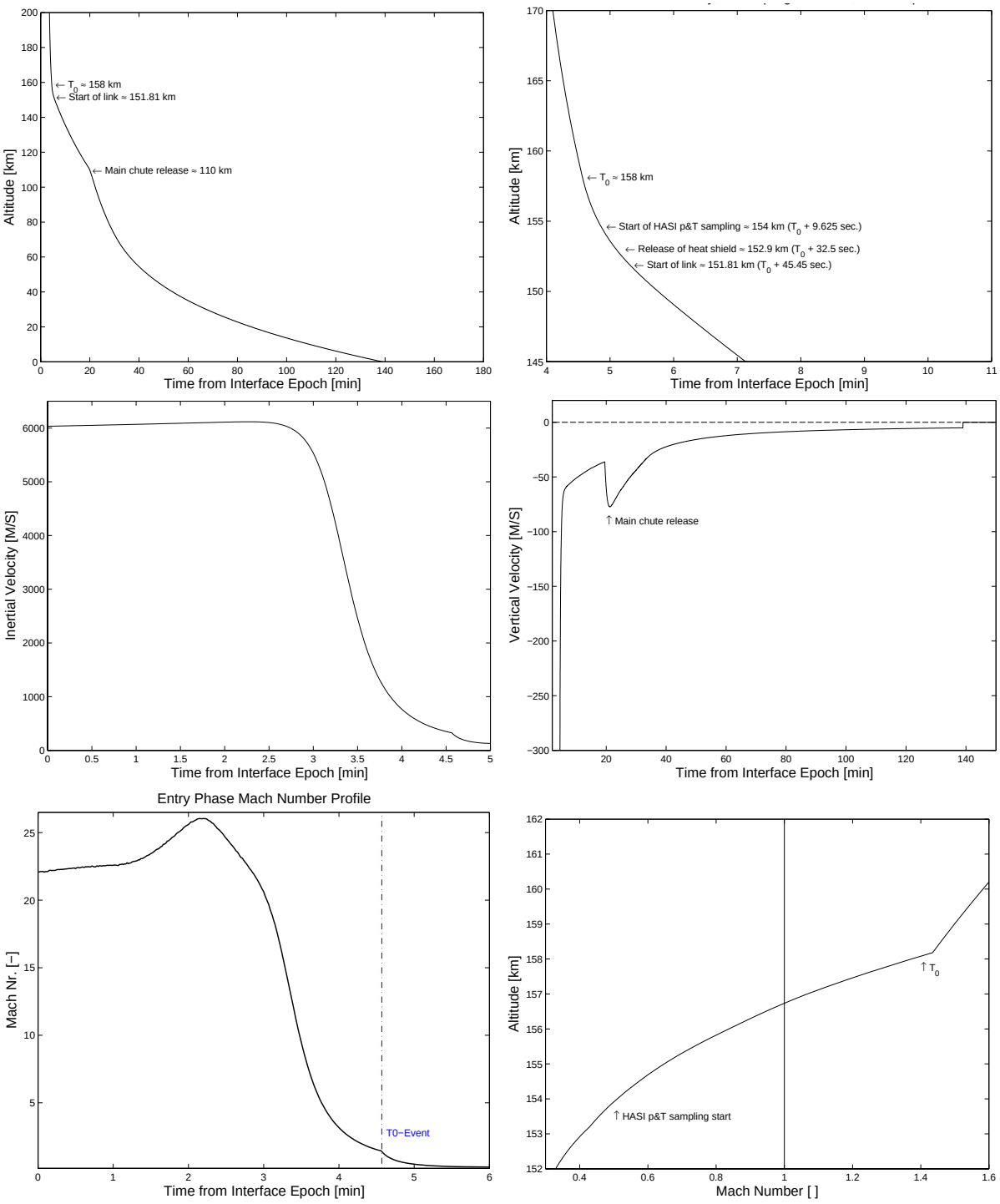

Figure 5.1: *Simulated Huygens entry and descent trajectory used for the simulation of the various sensor data; the time is given relative to the interface epoch (UTC JAN 14, 2005 08:58:55.816); upper panels: altitude profiles with important events, middle panels: entry inertial (left) and descent vertical (right) speed; lower panels: probe Mach number vs. altitude profile.*

- GCMS mole fraction measurements of the major compounds (i.e., N_2, CH_4, Ar) during the descent phase;
- DWE zonal wind measurements during the descent phase;
- DISR Solar Zenith Angle (SZA) and altitude and descent speed (derived from optical images) during the descent phase; and
- probe housekeeping data: engineering accelerometer, and Radar Altimeter Unit (RAU) measurements.

All sensor models are provided with and without simulated zonal (prograde) wind[1]. Both the wind and the no wind scenario datasets are also provided with and without simulated measurement noise. Furthermore the simulated Huygens probe entry and descent trajectory (which served as a basis for all the sensor simulations) is provided in a dedicated file in order to assess the performance of the reconstruction process.

HSDS v.1.5 is based upon the JPL040225 trajectory delivery[2] state vector and is provided in Tables 5.2 and 5.1. The wind dataset assumes a prograde zonal wind according to Lebreton (2001). The Y97 (see Sec. 4.2) nominal atmosphere profile is used for both the wind and the no wind scenarios. Fig. 5.1 depicts various parameters of the simulated probe entry and descent trajectory (wind scenario) which was used to derive the simulated sensor data of HSDS v.1.5. The upper panels show the probe altitude profile as a function of elapsed time from the interface altitude (1270 km above Titan's surface) and indicate important mission events as specified in Table 2.1. The start of the parachute sequence T_0 takes place at an altitude of ∼160 km. The heatshield is released at ∼153 km ($T_0 + 9.652$ sec.) and the communication link is established at ∼151.8 km ($T_0 + 45.45$ sec.). This also corresponds to the start of the DWE zonal wind measurements, which are derived from the Doppler shift of the probe relay signal due to the relative probe-orbiter motion. The main chute is released at ∼110 km (T_0+900 sec.) and the nominal surface impact time is 139 minutes past interface epoch. The start of the HASI atmospheric pressure and temperature measurements is scheduled at T_0+9.625 sec., which corresponds to an altitude of ∼154 km. The middle panels of Fig. 5.1 show the inertial velocity during the probe entry phase (left panel) and the vertical descent speed during the descent phase (right panel). The lower panels of Fig. 5.1 show the dimensionless Mach number and the start of the HASI pressure and temperature sampling at ∼ Mach 0.5.

Fig. 5.3 depicts the HASI X-servo accelerometer sensor output as a function of elapsed seconds past the interface epoch. The lower panel is a zoom of the entry phase measurements and shows the peak deceleration of more than 12g and the starting time of the parachute sequence T_0. The table in the lower panel of Fig. 5.7 summarizes the range, resolution and 1σ uncertainty of the HASI X-servo accelerometer.

The upper panel of Fig. 5.4 shows the measurements of the HASI X-piezo accelerometer which will be also switched on during the entry phase and at the end of the descent phase

[1]At the time of writing the HSDS is available online at `ftp://ftp.rssd.esa.int/pub/HUYGENS/DTWG_Simulated_Data_Set/`.

[2]The NASA-JPL Cassini navigation team provides the Huygens project with the estimated initial state vector of the Huygens probe at the defined interface altitude and epoch as well as its dispersion ellipse and planetary constants in form of a defined set of files, which are named according to the date of delivery.

to measure the time of probe impact. The expected impact deceleration profile is also simulated and is depicted in the sub-panel. The lower panel of Fig. 5.4 shows the probe housekeeping CASU accelerometer profile, which saturates at $10g$ as it is used only for the initialization of the parachute sequence.

Fig. 5.5 shows the HASI Y- and Z-piezo accelerometer measurements. HSDS v.1.5 assumes a zero angle-of-attack during the entire entry phase, which implies no acceleration measurements in the normal direction apart from measurement noise.

The HASI pressure and temperature measurements are performed by the Pressure Profile Instrument (PPI) and two temperature sensing units (i.e., TEM#1 and TEM#2) (Fulchignoni *et al.*, 2002). All three units are mounted on a fixed stub (see Fig. 3.3), which is long enough to protrude into the free flow. Each of the TEM units is a dual element (S1 and S2) platinum resistance thermometer. TEM's main sensing element, designated as S1 is a fine-wire platinum resistance thermometer. The S2 secondary sensing element (coarse sensor) is attached to the top of the S1 support frame and will guarantee temperature measurements even if S1 is damaged. The HASI instrument team will analyze the measurements of all four temperature sensors and provide the best one for the reconstruction of the descent trajectory. The HSDS therefore comprises only one data file. The TEM units have two measurement ranges: 60 – 110 K (high resolution range with an accuracy of 0.5 K and 0.8 K for respectively S1 and S2), and 100 – 330 K (low resolution range with an accuracy of 2 K for both units S1 and S2). The switching temperature is 105 K. The HSDS TEM simulated data set and the low and high resolution switching temperature (including noise) is shown in the upper panel of Fig. 5.6.

The HASI-PPI sensor has three operational modes that comprise three different measurement ranges, 0–0.4 bar (low pressure range), 0-1.16 bar (medium pressure range), and 0-1.6 bar (high pressure range). During the probe descent the atmospheric pressure will increase exponentially and the PPI will therefore switch from low, to medium, and finally to high pressure mode whenever the limit of one mode is reached. The PPI measurement uncertainty is 1% of the full range and the measurement uncertainty therefore changes from one mode to the next. The simulated PPI profile is shown in the lower panel of Fig. 5.6. It should be kept in mind that both the TEM and the PPI instrument units will be switched on at T_0+10 seconds and will therefore sample data with the heat shield attached for 22.5 seconds[3]. The local flow surrounding the sensors will very likely be disturbed by the heat shield, which implies that TEM and PPI data measured during the first 22.5 seconds will not be reliable and are flagged accordingly in both the HSDS and the actual measurement file that will be provided by the HASI instrument team for the DTWG reconstruction effort. Fig. 5.7 summarizes the various HASI instrument modes and sampling rates.

The upper panel of Fig. 5.8 shows the altitude measurements of the SSP acoustic sounder instrument (SSP-APIS) and the speed of sound measurements of the SSP-APIV sensor (lower panel). Note that SSP-APIS will only be able to measure the altitude profile briefly before the probe impacts (i.e., 400 m to $\sim$ 20 m) and the speed of sound will only be measured for pressures higher than 100 mbar, which corresponds to altitudes lower than $\sim$175 km.

Fig. 5.9 shows the simulated DISR Solar Zenith Angle (upper panel) and the DWE zonal wind speed measurements (lower panel).

[3]The probe heat shield is jettisoned at T_0+32.5 seconds.

Parameter	Probe	Orbiter
Interface Time (ET)	14-JAN-2005-09:00:00.000	
B-Plane Angle [deg]	-190	-180.3
B-Modulus [km]	1730.81	62888.58
Entry angle γ [deg]	-65.15	-
V_{inf} [km/s]	5.63	5.39
$\alpha - V_{inf}$ [deg]	-13.26	-12.22
$\delta - V_{inf}$ [deg]	5.79	5.97
Orbiter Delay Time [h]	-	2.1
Semimajor axis (1σ) [km]	50.17	13.36
Semiminor axis (1σ) [km]	9.37	2.98
Orientation angle Θ [deg]	179.71	69.19
S/C Altitude [km]	1270	60,000
East Lon. [deg]	173.81	143.25
South Lat. [deg]	9.52	3.46

Table 5.1: *Probe and orbiter interface parameters (T2002-01 reference trajectory/JPL-040225 Delivery);*

x [km]	-1.312458638E+02
y [km]	-3.824933072E+03
z [km]	-3.697321588E+02
vx[km/s]	-2.346112519E+00
vy [km/s]	5.539336275E+00
vz [km/s]	4.588600223E-01
Titan GM [km^3/s^2]	8.978200000E+03
Saturn GM [km^3/s^2]	3.794062976E+07
Sun GM [km^3/s^2]	132712440041.940

Table 5.2: *Huygens probe state vector at interface epoch UTC JAN 14, 2005 08:58:55.816 (inertial Titan centered EME2000 coordinate system) and primary and perturbing body gravitational constants;*

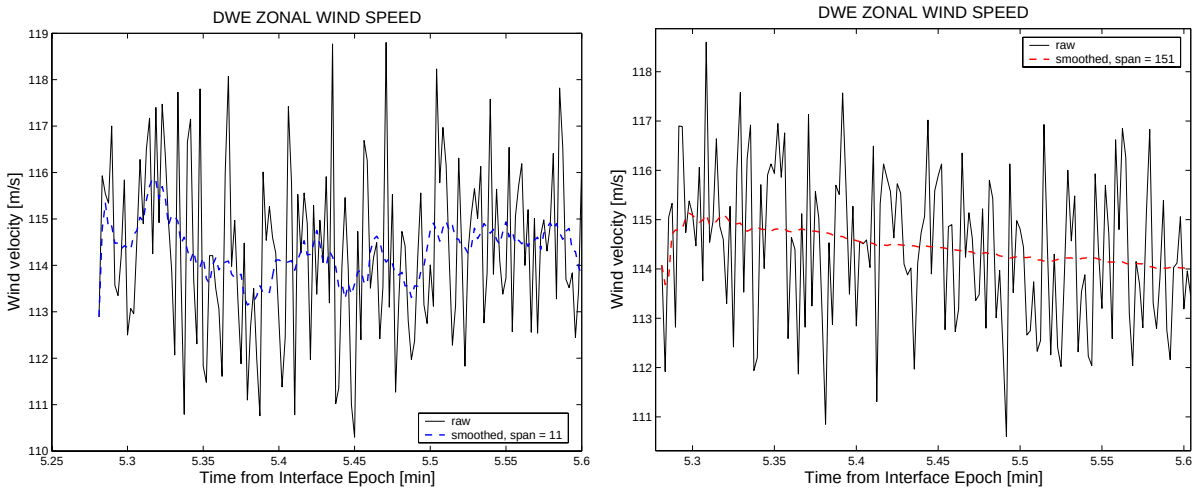

Figure 5.2: *Example of the application of the data smoothing algorithm to the noisy DWE data set. A span of 11 data point was used in the left panel and a span of 151 in the right panel. One can clearly see the capability of the algorithm to reduce the data noise, but care must be taken not to lose small scale information in the filtering process.*

The upper panel of Fig. 5.10 summarizes the GCMS measurement resolution, uncertainties, and sampling rates and the lower panel shows the simulated mole fraction profiles for the three constituents, N_2, CH_4, and Ar.

Fig. 5.11 shows the Radar Altimeter Unit (RAU) measurements and the simulated surface elevation profile (lower panel). Note that the RAU unit will only work for altitudes lower than ∼30 km. Beneath 150 m the RAU units are likely to saturate and the only measurements of altitudes and velocity will likely be from the SSP-APIS sensor.

5.2 Smoothing Data

All the instrument data will be affected to some extent by measurement noise that was simulated (according to the estimations provided by the instrument specifications) in the HSDS. Too much noise in the input data will not only decrease the reconstruction quality but can even make a reconstruction impossible. It is therefore necessary to apply a data smoothing algorithm. There are two common types of smoothing methods: filtering (averaging) and local regression. Each smoothing method requires a *span*, which defines a window of neighboring points to include in the smoothing calculation for each data point. This window moves across the data set as the smoothed response values is calculated for each predictor value. A large span increases the smoothness but decreases the resolution of the smoothed data set, while a small span decreases the smoothness but increases the resolution. The optimal span value depends on the data set and the smoothing method. A *Moving Average Filtering* method was used which smooths data by replacing each data point with the average of the neighboring data points defined within the span. This process is equivalent to lowpass filtering with the response of the smoothing given by the difference equation

$$y_s(i) = \frac{1}{2N+1}\{y(i+N) + y(i+N-1) + ... + y(i-N)\} \tag{5.1}$$

where $y_s(i)$ is the smoothed value for the ith data point, N is the number of neighboring data points on either side of $y_s(i)$, and $2N+1$ is the span. The moving average smoothing method follows the following rules:

- The number of points within the span must be odd.
- The data point to be smoothed must be at the center of span.
- The span is adjusted for data points that cannot accommodate the specified number of neighbors on either side.
- The end points are not smoothed because a span cannot be defined.

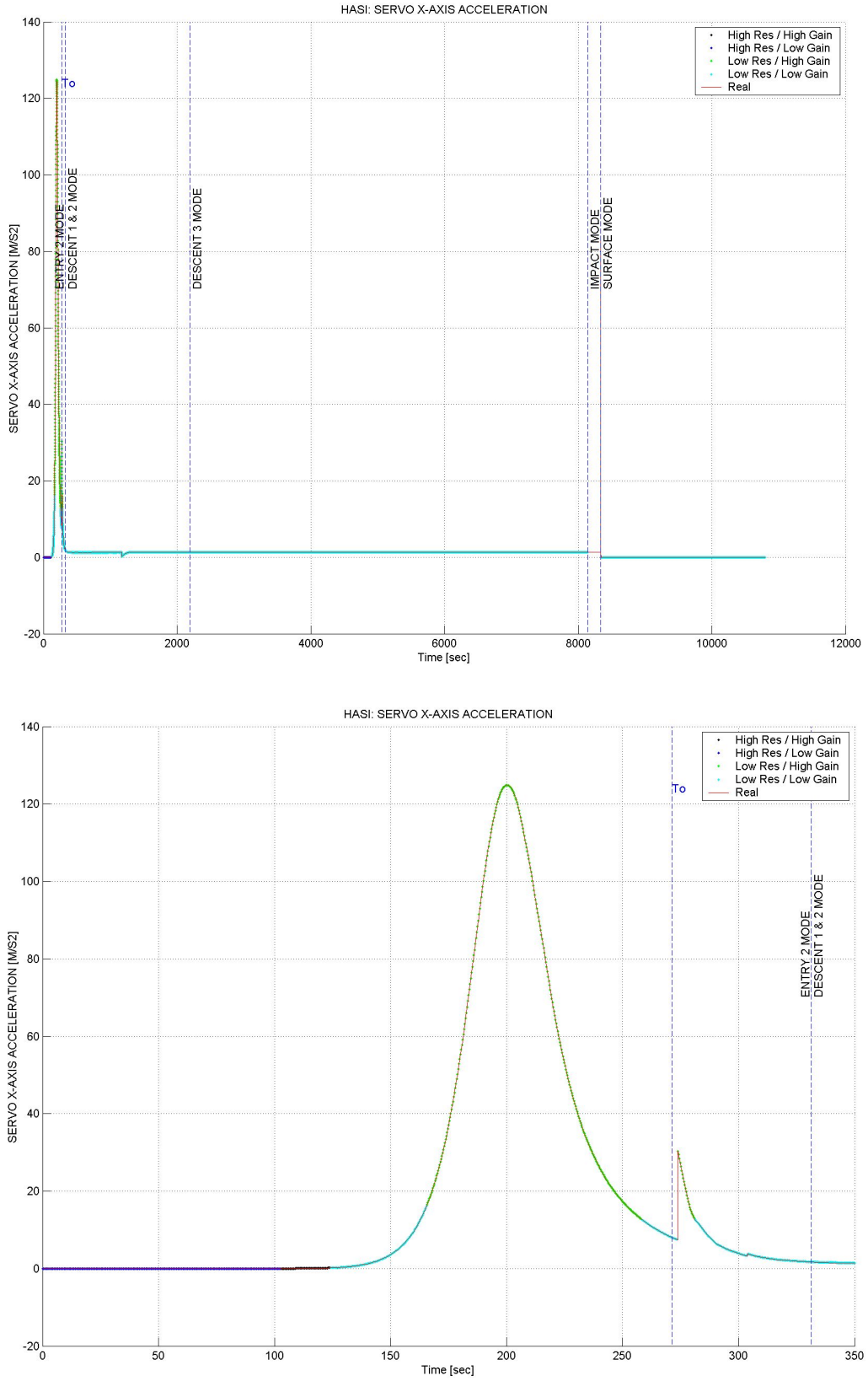

Figure 5.3: *HSDS v.1.5: HASI X-servo accelerometer measurements; the lower panel is a zoom of the entry phase measurements.*

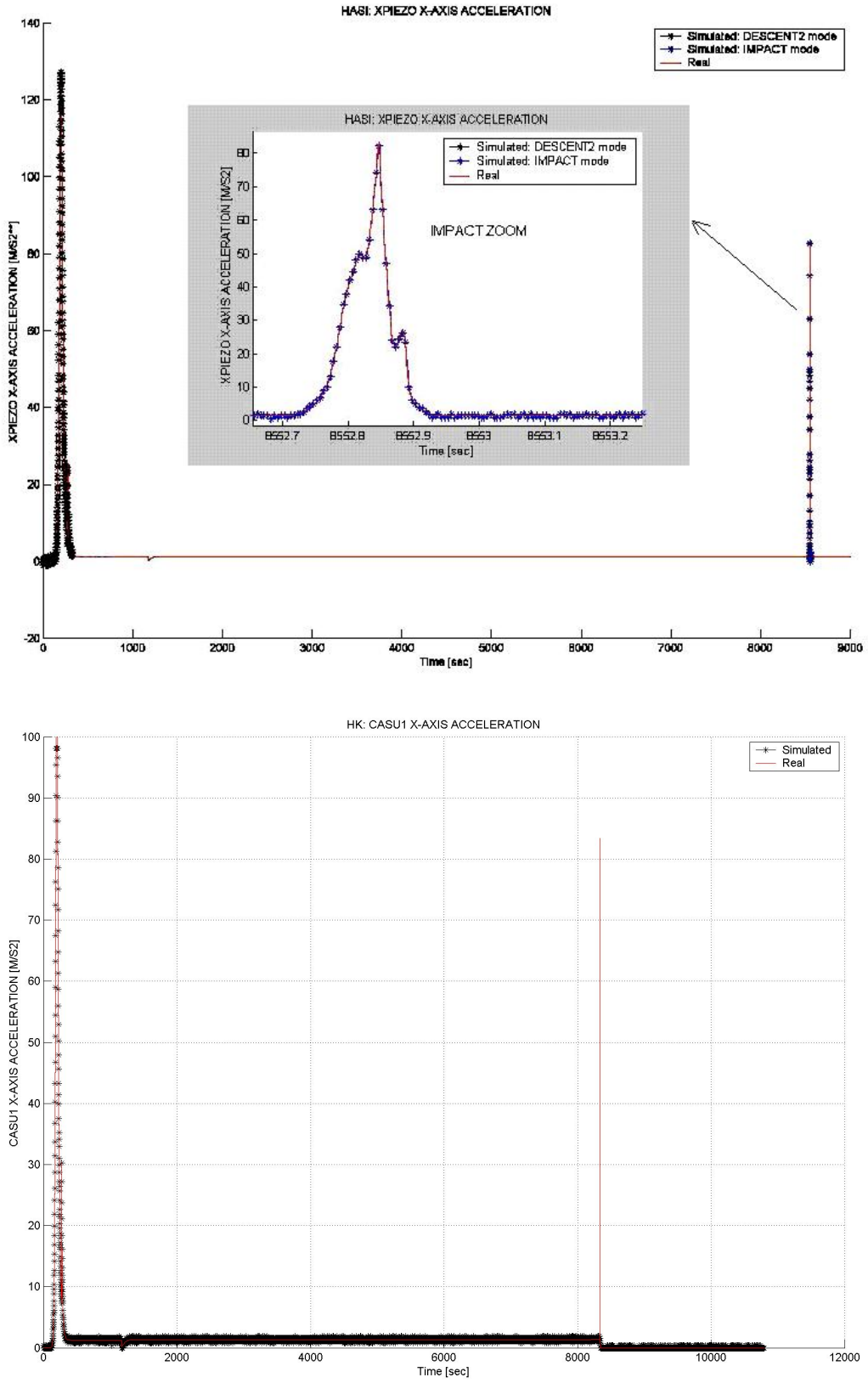

Figure 5.4: *HSDS v.1.5: HASI X-piezo (upper panel) and housekeeping Central Acceleration Sensor Unit (CASU) data (lower panel). Note that the CASU maximum measurement range is 10g.*

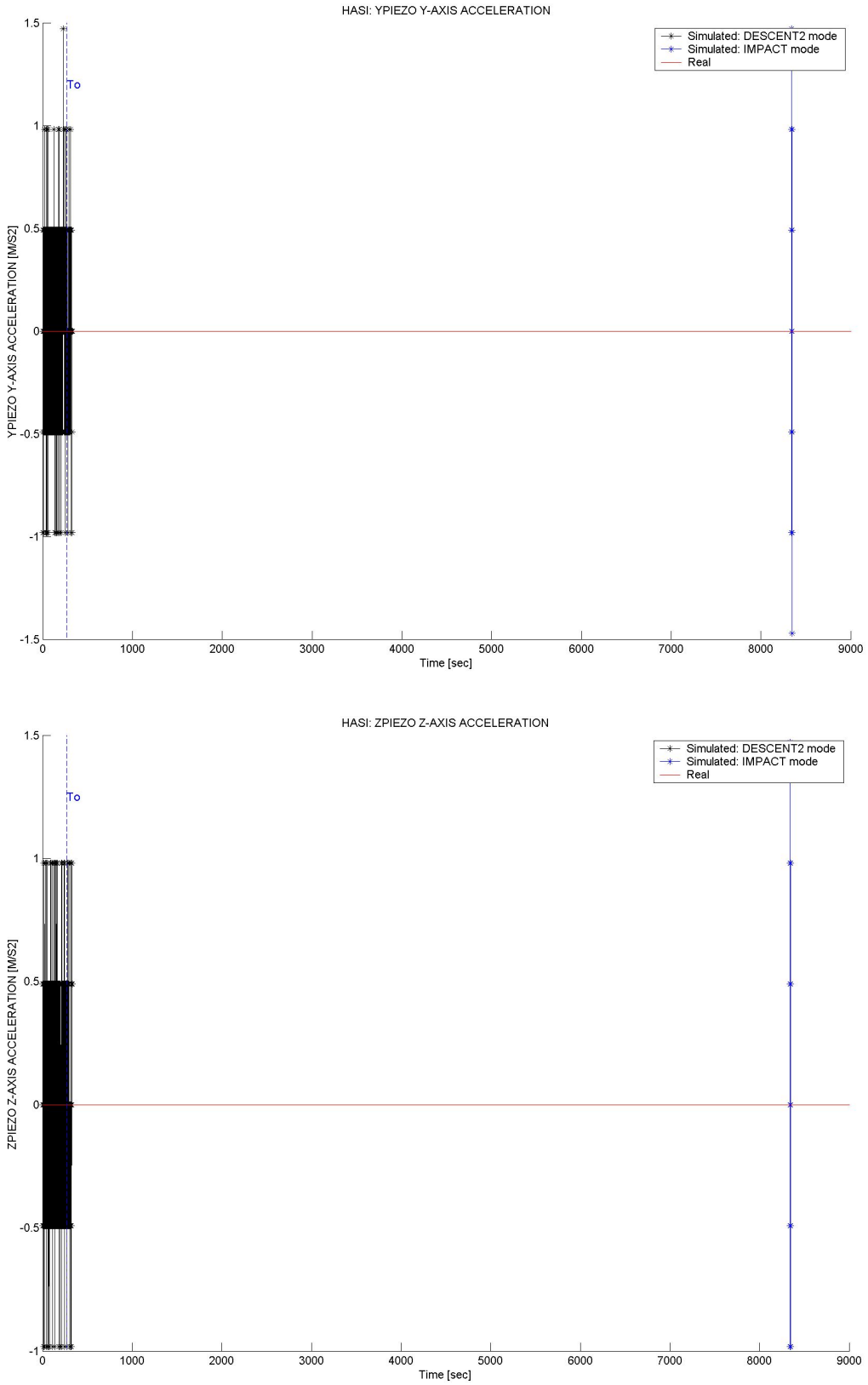

Figure 5.5: *HSDS v.1.5: HASI Y-piezo and Z-piezo accelerometer meausurements. Due to the assumed zero angle-of-attack profile the simulated measurements represent noise centered around 0 m/s^2.*

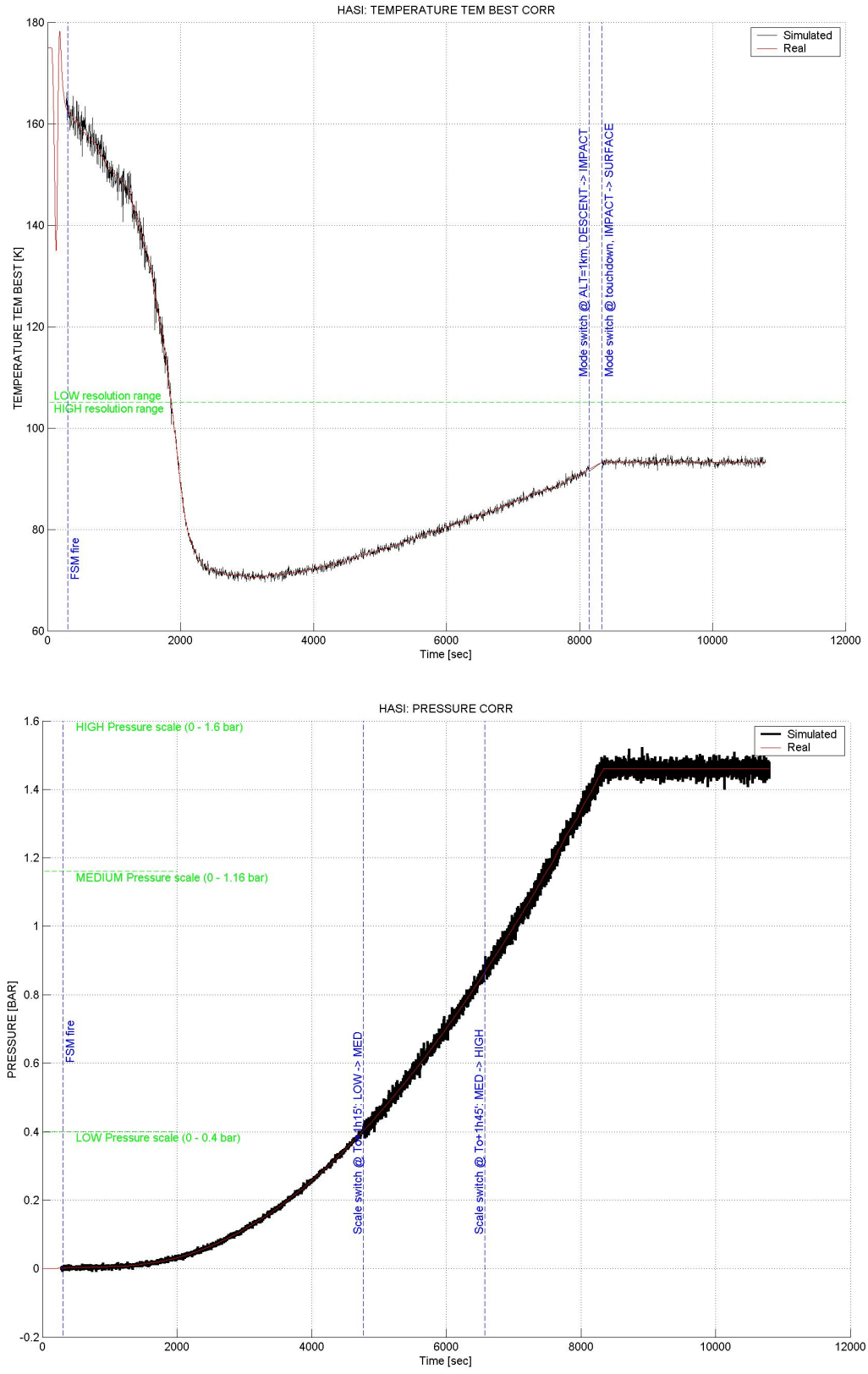

Figure 5.6: *HSDS v.1.5: HASI temperature (upper panel) and pressure (lower panel) profiles.*

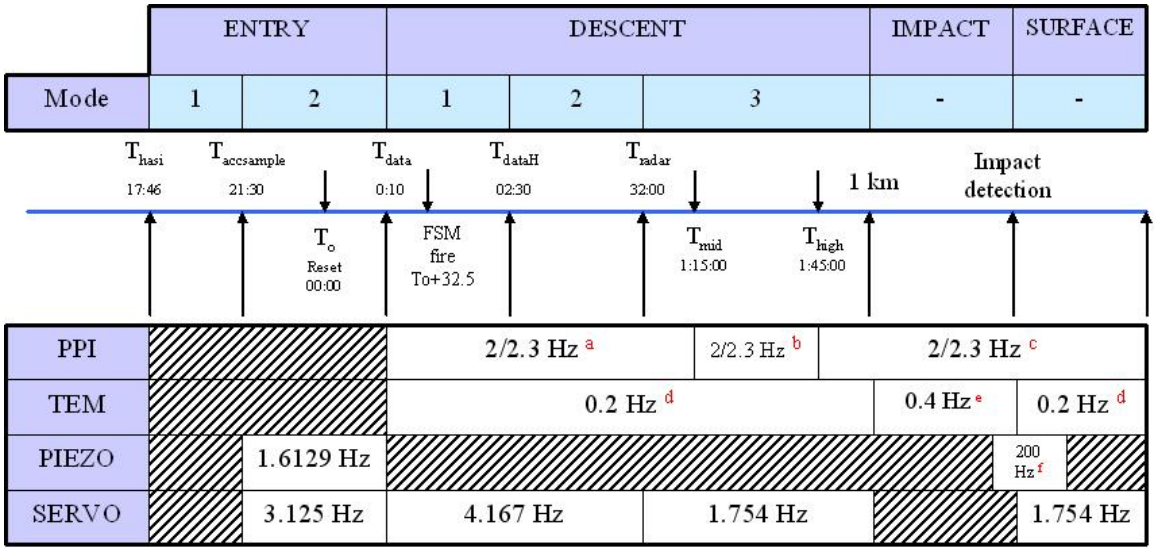

Range / resolution / uncertainty	HIGH x10	LOW x1
FINE	2 mg / 0.3 µg / 0.3 µg	20 mg / 3 µg / 3 µg
COARSE	1.85 g / 0.3 mg / 0.3 mg	18.5 g / 3 mg / 3 mg

Figure 5.7: Upper panel: *HASI instrument sampling rates and operation modes;* ***PPI****: (a) Low pressure phase (0–0.4 bar), (b) Medium pressure phase (0–1.16 bar), (c) High pressure phase (0–1.6 bar);* ***TEM****: (d) TEM 1F, TEM 1C, TEM 2F, TEM 2C (F=fine, C=coarse), (e) TEM 1F, TEM 2F (only Fine sensors);* ***PIEZO ACC****: (f) special impact buffer at 200 Hz from time of impact -0.5 sec. to time of impact +5.5 sec.* **Lower panel**: *HASI X-Servo range, resolution, and uncertainties (1σ) for the high and low gain mode (Fulchignoni* et al.*, 1997).*

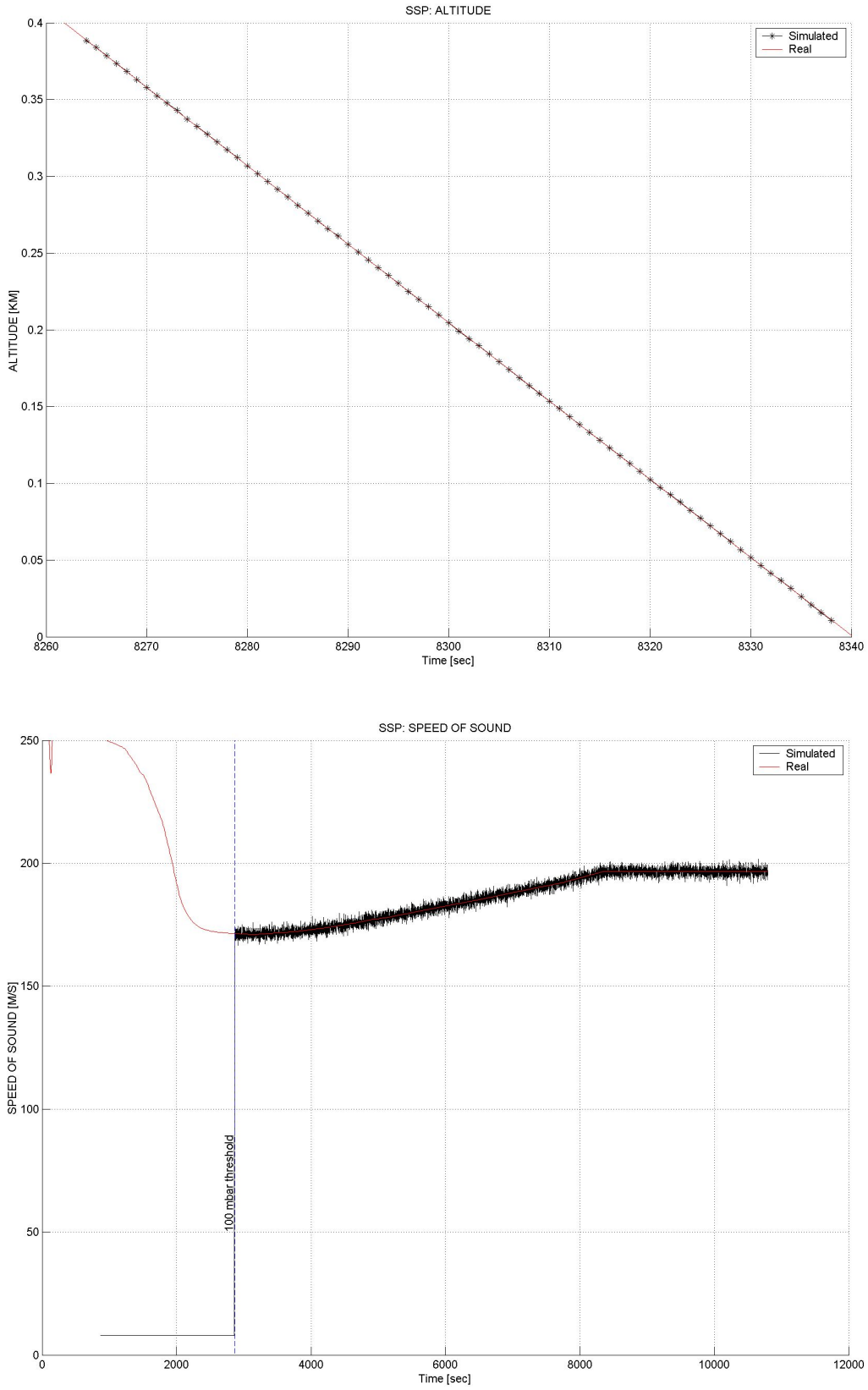

Figure 5.8: *HSDS v.1.5: SSP acoustic sounder altitude (upper panel) and speed of sound (lower panel) measurements.*

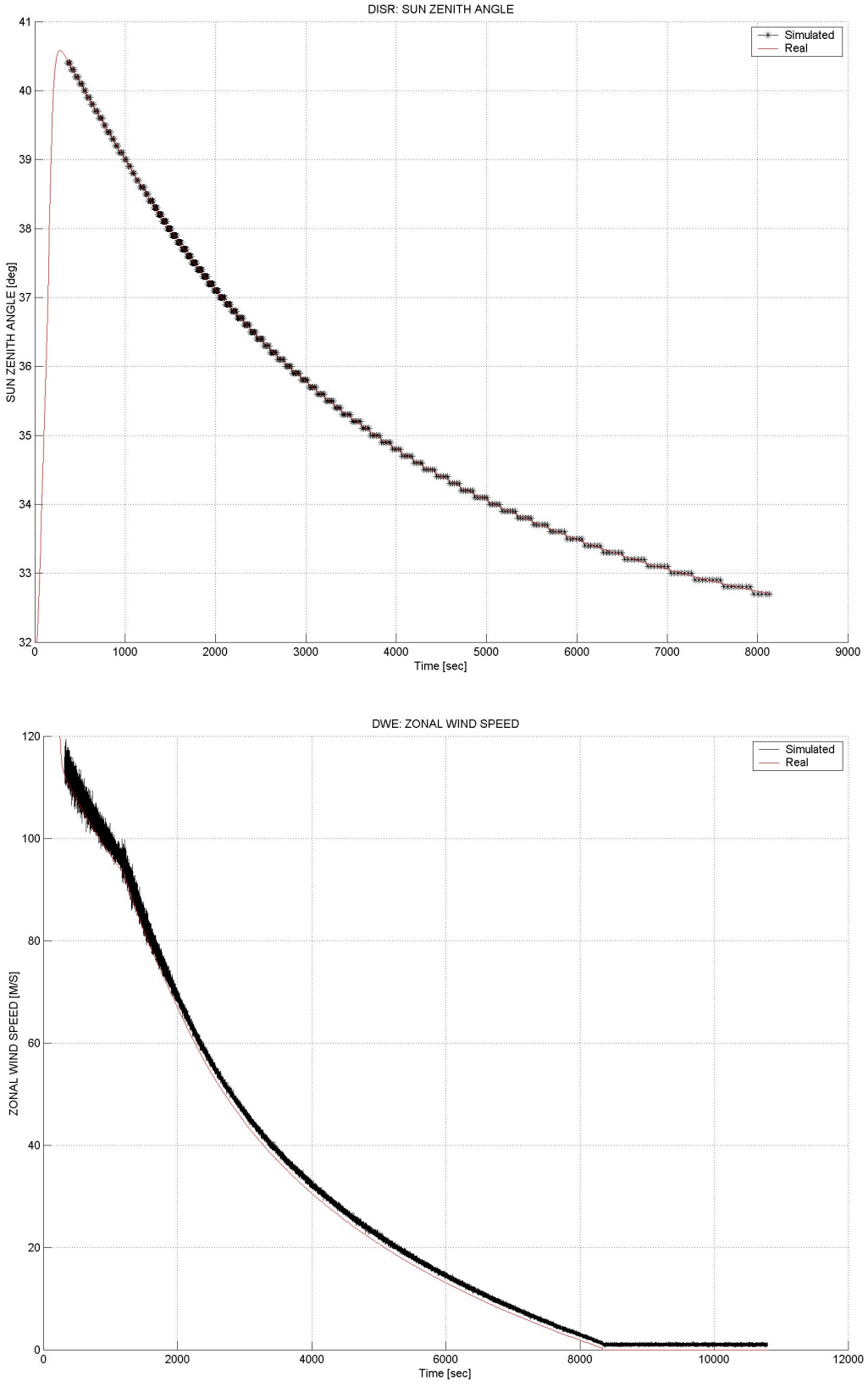

Figure 5.9: *HSDS v.1.5: DISR Solar Zenith Angle (upper panel) and Doppler Wind Experiment zonal wind profile (lower panel).*

Exp	Uncertainty (as 1 sigma)	Resolution	Range	Sampling rate [Hz]	Alt/time range [km / sec]	modes
GCMS mol fractions	1%	0.1	No limits	1 Hz or 0.2-0.25 Hz	To+50sec	

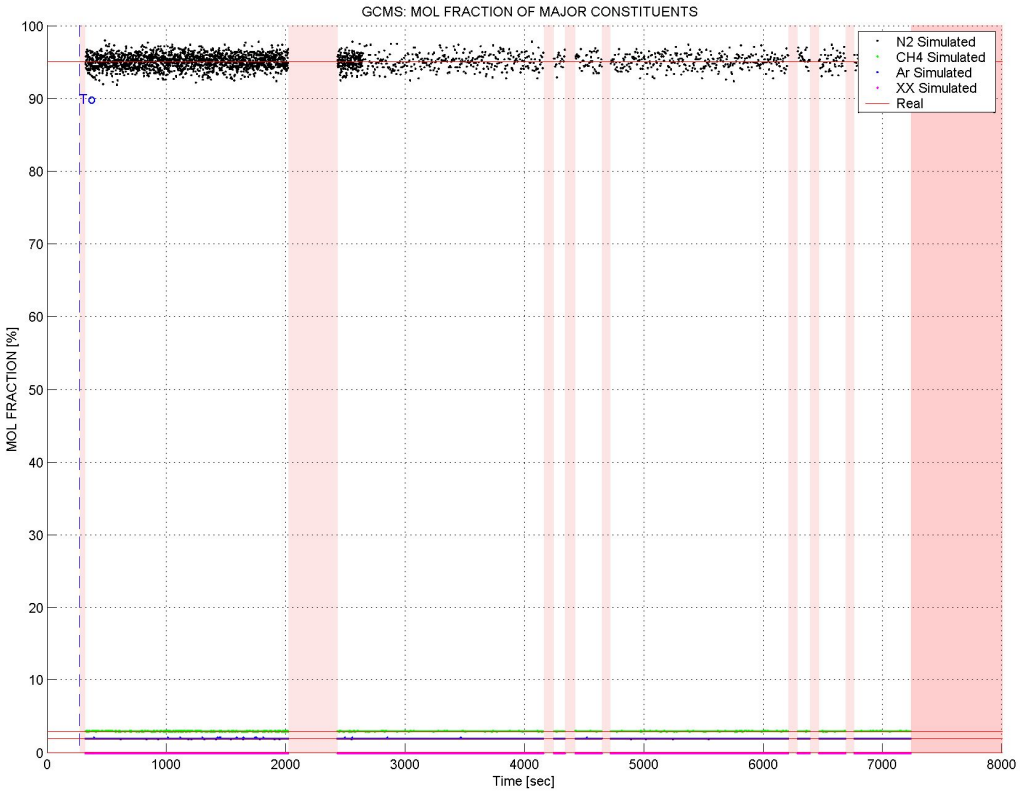

Figure 5.10: *GCMS instrument modes (upper panel) and HSDS v.1.5 simulated mole fractions of N_2, CH_4, and Ar (lower panel).*

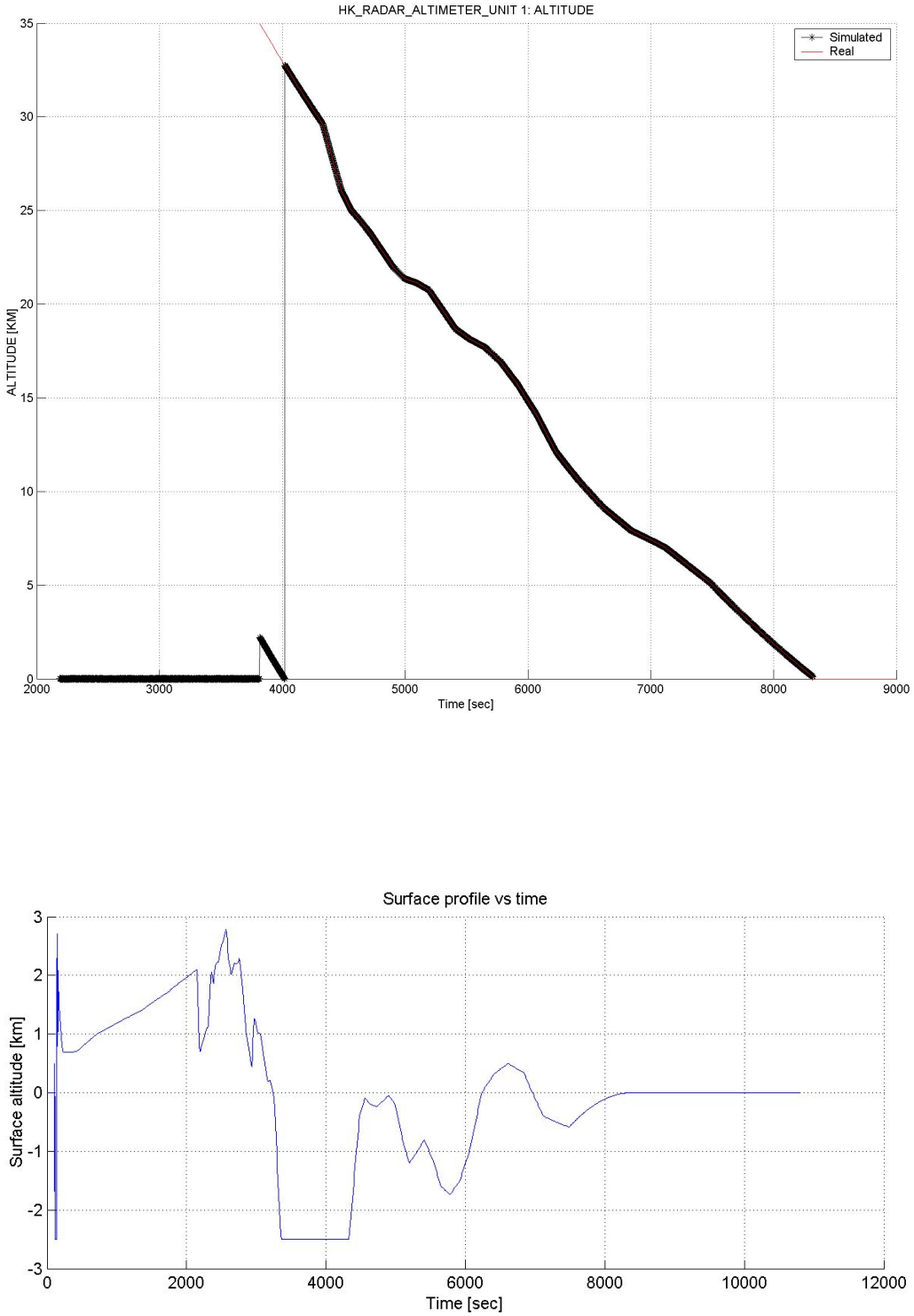

Figure 5.11: *Simulated Radar Altimeter Unit measurements (upper panel) and corresponding simulated surface elevation profile (lower panel).*

Chapter 6

Entry Phase Reconstruction

The probe entry phase is defined as the portion of the trajectory starting from the official NASA/ESA interface point at 1270 km altitude down to T_0, the firing of the Parachute Deployment Device (PDD) at an altitude of ∼160 km. The Cassini Navigation team will provide ESA with the 6 dimensional state vector (i.e., probe position and velocity in a Titan centered inertial EME2000 coordinate system), the estimated interface epoch (in Ephemeris Time), and the corresponding uncertainties in the form of a covariance matrix.

6.1 Relevant Data for the Entry Phase

The probe possesses three sets of accelerometers: the Central Acceleration Sensor Unit (CASU), the Radial Acceleration Sensor Unit (RASU) and the HASI 3-axis science accelerometers. The CASU comprises three axial accelerometers (directed along the probe x-axis) designed to measure accelerations in the range of 0 to $+10g$. Note that the deceleration pulse is expected to exceed $10g$ and will therefore not be fully detected by the CASU unit. The CASU is primarily used for the correct timing and triggering of events during the entry and has therefore a low sampling rate of 1 Hz.[1] The RASU is designed to measure spin accelerations in the range of 0 to 120mg. Both the CASU axial accelerations and the RASU spin acceleration measurement are part of the probe housekeeping data.

The HASI accelerometer subsystem is located at the probe center of mass[2] (Fulchignoni *et al.*, 1997). The HASI accelerometer suite comprises one servo accelerometer with switchable range and three piezo accelerometers. The servo accelerometer is aligned with the probe x-axis (the spin axis or axial direction). One piezoresistive accelerometer is aligned with the x-axis, and the other two with the y- and z-axis (normal) directions. The servo accelerometer (Sundstrand QA-2000-030) senses the displacement of a seismic mass and drives it back to a null position. The required current is proportional to the acceleration. The accelerometer temperature is measured by a dedicated sensor included

[1]Due to the limited gain and sampling rate the CASU acclerometers will only be use as a backup dataset for the entry phase reconstruction in case the HASI science accelerometer fails.

[2]Note that as the probe mass distribution changes the center of mass shifts. The location of the accelerometers is however fixed. During the entry phase only a minor change of the probe mass distribution due to heat shield ablation is expected. During the descent phase the mass distribution will however change more significantly due to the release of the back cover, the parachute deployment, the heat shield release, and the release of the parachutes. If the accelerometer measurements are done outside of the center of mass, the probe spin and pendulum motion will also be sensed.

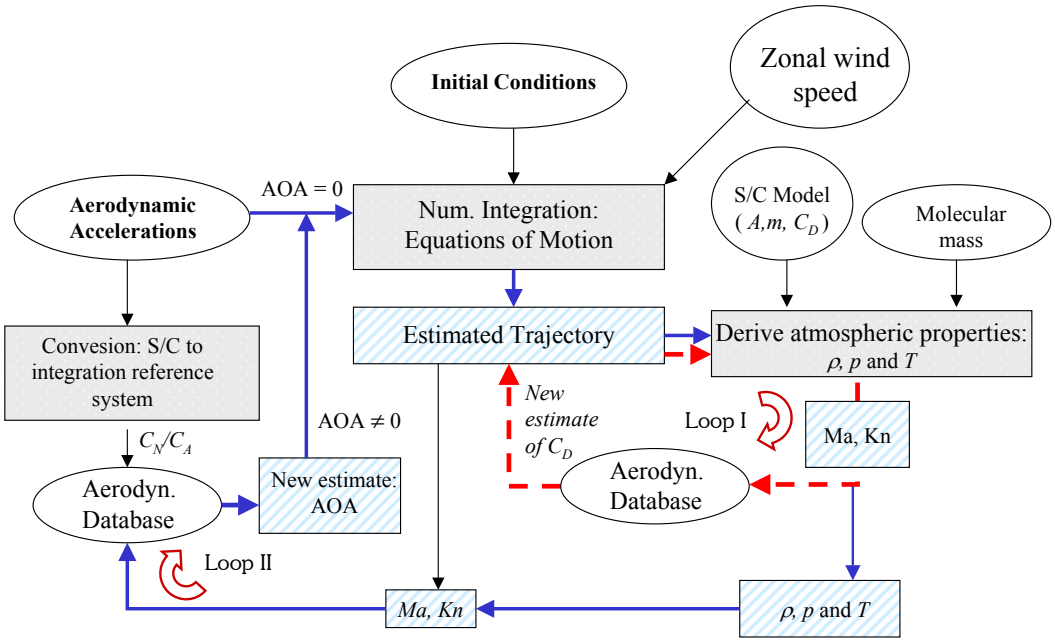

Figure 6.1: *Computational flow of entry phase reconstruction. Two internal loops need to converge: Loop I assumes a zero angle-of-attack (AOA). From the derived atmosphere property the aerodynamic regime can be determined and the drag coefficient C_D interpolated. Loop II uses the ratio of normal to axial acceleration (C_N/C_A) and Ma from Loop I to interpolate the AOA from the aerodynamic database. The new AOA can then be used for a new iteration of Loop I.*

in the servo package. The x-axis servo accelerometer's output is conditioned and amplified by two non-inverting amplifiers, one with gain of 1 and the other with gain of 10. They provide the two x-axis servo channel outputs. Besides these two channels, the servo's range is switchable between high resolution and low resolution ranges, achieved by switching the output of the servo accelerometer between two load resistors. The HASI servo accelerometer characteristics are summarized in Tables 6.1 - 6.3.

The piezoresistive accelerometer (ENDEVCO 7264A-2000T) consists of a suspended silicon seismic mass supported by two strain-dependent resistances, which produce a small output voltage depending on the applied acceleration. The sampling rate of the piezoresistive accelerometers is 1.6129 Hz for the entire entry phase (i.e., from probe wake-up+21.5 minutes to the start of data probe data transmission at T_0+45.45 seconds) and 200 Hz during a short period (i.e., 6 seconds) around probe surface impact. Further characteristics of the three piezoresistive accelerometers are given in Table 6.4.

6.2 Reconstruction Methodology and Strategy

The reconstruction of the probe entry phase is done by numerically integrating the equations of motion in a clearly specified reference system (referred to as the *integration*

reference system). The integration of the equations of motion requires the knowledge of the full probe state vector (i.e., the cartesian position and velocity vector specified in the integration reference system) at a starting or initial epoch. The gravitational forces acting on the spacecraft's center of mass cannot be detected by the onboard accelerometers as those measurements are made in a frame fixed with respect to the spacecraft (referred to as the *spacecraft reference system*. In other words the spacecraft and the accelerometers are both free falling at the same rate. The gravitational forces therefore have to be modeled at each step of the reconstruction process. For the proper transformation of the measured accelerations from the spacecraft reference system (see Sec. 6.3) into the integration reference system the probe angle-of-attack α is required, which can be estimated from the ratio of normal to axial accelerations a_N/a_A, or equivalently, the ratio of the normal and axial drag coefficients C_N/C_A. One can therefore write

$$\frac{a_N}{a_A} = \frac{C_N}{C_A} = f(\alpha, Ma) \tag{6.1}$$

which is a function of the angle-of-attack α and the Mach number Ma. The computation of Ma [given by Eq. (6.23)] requires the speed of sound c_s, which itself depends on the atmospheric temperature profile. The reconstruction of the entry trajectory therefore demands the reconstruction of the atmospheric properties. It can be seen that the entry trajectory must be reconstructed in an iterative process, which is shown in a flowchart in Fig. 6.1. Assuming a zero angle-of-attack the reference entry trajectory (including the entry velocity profile) can be integrated. The atmospheric properties (with an initial guess for the drag coefficient C_D) can then be derived as outlined in Sec. 6.6. This allows the derivation of the Ma number profile which is then used in a subsequent iteration to reevaluate the C_D from the aerodynamic database (Loop I). Once Loop I has converged, the Ma number profile and the C_N/C_A ratio can be used to interpolate α from the aerodynamic database. The updated α can then be used for a subsequent iteration of the trajectory integration (Loop II). The optimum trajectory (and atmosphere) are obtained once both Loop I and Loop II have converged.

During the probe entry phase, accelerations are the only measurements performed by the probe instruments. The deployment of the parachute will most likely introduce some oscillatory motions into the spacecraft, and hence into the measured accelerations as well, as it swings around on the end of its parachute. A probe trajectory that is based entirely on the numerical integration of the measured and calculated accelerations must therefore be restricted to the entry phase, whereas the descent phase reconstruction effort will be based on additional instrument measurements that are performed once the parachute sequence has been initiated (see Chap. 8).

6.3 Definition of Coordinate Systems

The exact and unambiguous definition of the coordinate systems is essential for the proper mathematical formulation of the various forces and integration of the equations of motion. Very often the integration reference system, the reference system of the input data, and the reference system used for the presentation of the reconstruction effort results differ from each other. A correct transformation between the systems is therefore very important.

The EME2000 Coordinate System

In the EME2000 Coordinate System a position vector is designated $\vec{r} = (r_1, r_2, r_3)$ and the coordinate axes are x, y, and z. The EME2000 system is aligned with the Earth *mean* equator and equinox at the reference epoch J2000 (i.e., 1.5 January 2000 = JD 245145.0) and has its origin at the center of the planet. The z axis is parallel to the mean rotation axis of the Earth and the x axis points in the direction of the mean vernal equinox, i.e. the ascending node of the Earth's mean orbital plane on the mean equator at the fixed epoch J2000. The y axis fills out an orthogonal right-handed system. Here the term "mean" indicates that only secular (or long-periodic) changes in the orientation of the Earth's rotation axis (or its equator) and the ecliptic are considered. The Cassini Navigation team will provide the initial state vector of the probe and the corresponding covariance matrix in a Titan-centered EME2000 coordinate system.

The Equatorial Coordinate System (Q-System)

We introduce the coordinates $\vec{r}' = (r'_1, r'_2, r'_3)$ in an equatorial system by rotating the coordinate axes of the EME2000 system by $90° - \delta_0$ around x-axis and $\alpha_0 + 90°$ about the z axis (see Fig. 6.2), where α_0 and δ_0 are the right ascension and declination of the planet's north pole. In that equatorial system the x' axis points to the intersection of the earth mean equator of the epoch J2000 and the planet's equator, the z' axis points to the planet's north pole (and is parallel with its rotation axis), and y' axis fills out an orthogonal right-handed system. The main difference between the Q-system and the Rotating Coordinate System (R-Frame) is that the Q-system is an inertial (non-rotating) system with the x' axis fixed to the direction of the node Q (i.e., the intersection point of the standard Earth equatorial plane with the planet's equatorial plane, see Fig. 6.2). The transformation of a vector $\vec{r}$ given in the EME2000 system to the corresponding vector in the Q-system can be done using the relation

$$\vec{r}' = \mathbf{E}\,\vec{r} \tag{6.2}$$

where $\mathbf{E}$ is a rotation matrix given by

$$\mathbf{E} = \begin{pmatrix} -\sin\alpha_0 & \cos\alpha_0 & 0 \\ -\cos\alpha_0\,\sin\delta_0 & -\sin\alpha_0\,\sin\delta_0 & \cos\delta_0 \\ \cos\alpha_0\,\cos\delta_0 & \sin\alpha_0\,\cos\delta_0 & \sin\delta_0 \end{pmatrix} \tag{6.3}$$

The Rotating Coordinate System (R-System)

In the Rotating Coordinate System a position vector is designated $\vec{r}^* = (r_1^*, r_2^*, r_3^*)$ and the coordinate axes x^*, y^*, and z^*. The Rotating Coordinate System is planet-centered and rotates with the planet. Any stationary point in the R-system is specified relative to the surface. The definition of rotational elements follows the IAU conventions (Davies *et al.*, 1995). The north pole lies on the north side of the invariable plane of the solar system. The direction of the north pole is specified in standard equatorial coordinates (i.e., right ascension α_0 and declination δ_0) with equinox J2000 at the standard epoch J2000 (JD 2451545.0). The location of the prime meridian is specified by the angle W

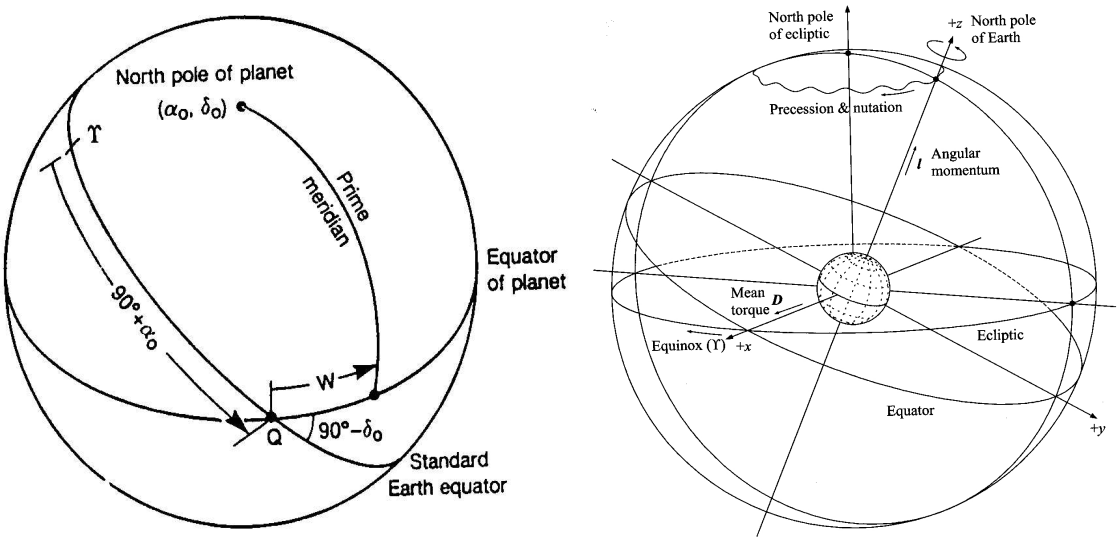

Figure 6.2: *Definition of the body fixed (left) and the EME2000 (right) coordinate system.*

that is measured *along* the planet's equator in an eastern direction with respect to the planet's north pole from the node Q (located at right ascension $90° + \alpha_0$) of the planet's equator (see Fig. 6.2). The right ascension of the point Q is $90° + \alpha_0$ and the inclination of the planet's equator to the standard equator is $90° - \delta_0$. The prime meridian is assumed to rotate uniformly with the planet. Therefore, the angle W varies linearly with time and specifies the ephemeris position of the prime meridian. The x^* axis points to the intersection of the prime meridian and the equatorial plane of the planet, the z^* axis points to the north pole and the y^* axis fills out an orthogonal right-handed system.

The Spacecraft Coordinate System (S/C-System)

The Cassini coordinate system is schematically shown in Fig. 6.3 (NASA-JPL, 1996). It is an orthogonal, right-handed system with its origin at the center of the field joint in between the Bus and the Upper Equipment Module Upper Shell Structure Assembly (USSA). The +Z-axis is perpendicular to the plane generated by the mating surfaces of the Bus at this origin, extending through the propulsion module in a direction that is downward when the spacecraft is mounted on the launch vehicle and forming an axis that can be thought of as the longitudinal axis of the spacecraft. The +X-axis extends perpendicular to the +Z-axis and parallel to a line through the centers of two bolt holes (A and H) at the Bus/USSA interface. The +Y-axis is mutually perpendicular to the +X- and +Z-axes in a right-handed sense. The remote sensing pallet is mounted on the +X side of the orbiter with the primary remote sensing bore sight in the -Y direction. The Huygens Probe is mounted on the -X side of the orbiter and will be separated in the -X direction. The magnetometer boom extends in the +Y direction. The HGA boreside is in the -Z direction, and the main engine exhaust is generally in the +Z direction.

The Huygens coordinate system is also shown in Fig. 6.3. It is an orthogonal, right-handed system with axes parallel to the orbiter system and its origin in the plane of the

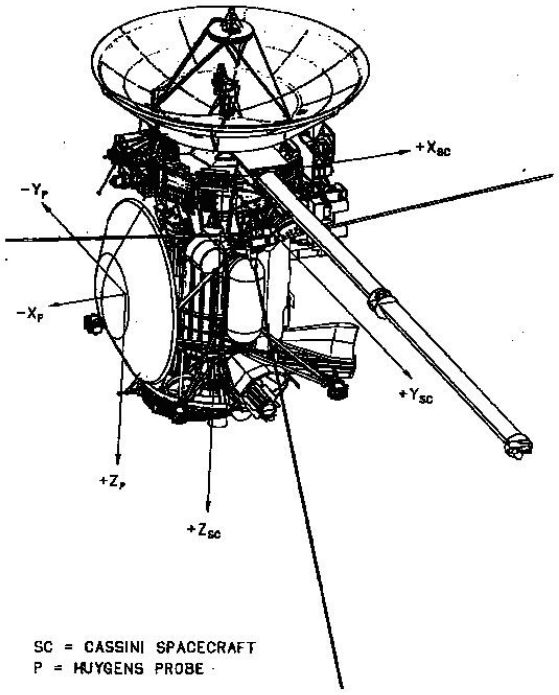

Figure 6.3: *Cassini orbiter and Huygens probe coordinate definition (NASA-JPL, 1996).*

interface attachment points at a point defined by the centerline of the probe. The probe will be separated in the -X direction and with a rotation that is anti-clockwise as seen from the orbiter (positive rotation in a right-handed sense about the X axis). The origin of the Probe coordinate system in orbiter coordinates is (-36.91362, 0, 161.14776) cm.

6.4 Probe Initial Conditions

As the Cassini/Huygens project is a collaboration between NASA and ESA, it is essential that an interface for the exchange of the necessary operational data between the two agencies be clearly defined. It is the responsibility of the NASA Jet Propulsion Laboratory (i.e., the Cassini Navigation Team) to deliver the Huygens probe to the prescribed target interface altitude, which is (per definition) 1270 km above the surface of Titan. The interface data that will be provided by the Cassini Navigation team to ESA can be divided into three groups (European Space Agency, 2001):

- **Environment Data** comprising the ephemeris of Saturn with respect to the solar system barycenter and Titan and Saturn's major satellites with respect to the Saturn barycenter in the EME2000 reference system, a leap seconds file for the conversion between Ephemeris Time (ET)[3] and Coordinated Universal Time (UTC), and finally a planetary constant file (PcK) with specifications for Titan's and Saturn's gravitational constants and rotational parameters for Titan (i.e., spherical

[3]The acronym ET is used here only for Ephemeris Time, which corresponds to Barycentric Dynamical Time (TDB). ET should not be confused with Eastern Time.

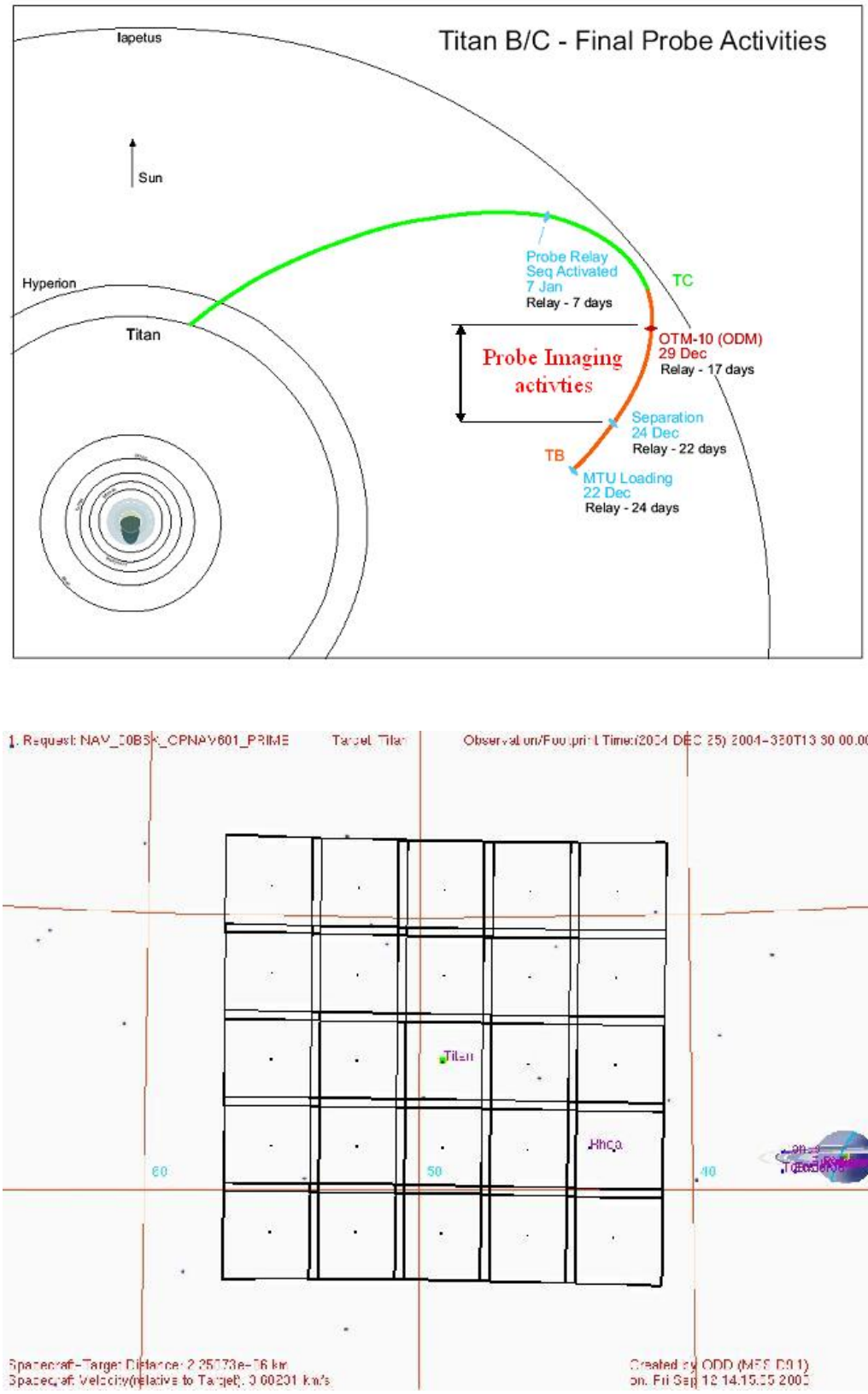

Figure 6.4: *Upper panel: probe imaging activity period shown on the Rev B/C orbit; Lower panel: example of WAC mosaic on release plus 1 day (Huygens Implementation Team, 2004)*

coordinates of Titan's north pole, rotational period, specification of the location of Titan's prime meridian).

- **Operational Data** comprising the *Probe/Orbiter - Delivery File* (PODF) with the interface time (in ET) and the state vectors of both the Huygens probe and the Cassini orbiter, including a full (14 × 14) covariance matrix for the state vectors and the Saturn and Titan gravitational parameters (i.e., GM) in a planetocentric reference system with an Earth mean equator and equinox of J2000.

- A **Verification Data Package** in order to cross check the correct understanding of the different coordinate systems, ephemerides and rotational models (Belló-Mora and Sánchez-Nogales, 2000).

Both the Environment data package and the Operational data package are essential for the reconstruction of the Huygens entry and descent trajectory. The relevant information will be extracted by the Project Scientist Team (PST) at ESTEC and provided to the DTWG in the form of a NAIF SPICE kernel, also referred to as the Huygens Event Kernel. This kernel has a predefined format, which was specified in the DTWG Interface Document (Kazeminejad, 2004) and is shown in Appendix D.

In order to narrow down the probe position uncertainty at the interface altitude, the Cassini cameras will attempt to image the probe after it is released from the orbiter and begins its 21 day coast to Titan. The purpose of probe imaging is to apply optical navigation techniques to improve the knowledge of probe delivery to the interface point. The probe images (opnavs) will be unable to improve the probe delivery accuracies, since the images are to be obtained after separation after, which there is no longer an opportunity to affect the probes trajectory. However, opnavs will improve estimates of the post-separation probe trajectory and therefore decrease the delivery dispersion ellipse at the NASA/ESA interface point.

There are three imaging opportunities, one each day between probe release and the Orbiter Deflection Maneuver (ODM) (see upper panel of Fig. 6.4). The strategy is to attempt to image the probe by taking a 5 × 5 mosaic on either the first or second day after probe release through the Wide Angle Camera (WAC) as shown in the lower panel of Fig. 6.4. Assuming the probe is located in the images, a subsequent image would be taken on the second or third day using the Narrow Angle Camera (NAC). On the first day, the probe image could be as large as 3-9 pixels across through the WAC, dropping to less than 2 pixels on the second day. With a focal length 10× that of the WAC, the NAC would provide an image of the probe that is 15 pixels across on the second day (approximately release + 30 hours), and 8 pixels across on the third day (release + 55 hours).

The benefit of probe optical navigation is to significantly improve (i.e., reduce) the (1σ) delivery uncertainties. A dedicated study by Kazeminejad and Atkinson (2002) showed that with imaging the probe 1σ delivery dispersion error could be decreased by a factor of $\sim$1.7 in the radial direction and, in the B-plane, by a factor of $\sim$2.1 along the semi-major axis and $\sim$1.6 along the semi-minor axis.

6.5 Formulation of the Equations of Motion

In the framework of Newtonian physics the acceleration $\vec{a}$ of a satellite under the influence of a force $\vec{F}$ is described by the differential equation

$$\vec{a} = \ddot{\vec{r}} = \vec{F}(t, \vec{r}, \vec{v})/m \tag{6.4}$$

where $\vec{r}$ and $\vec{v}(= \dot{\vec{r}})$ are the position and velocity vectors of the body in a non-rotating planet-centered coordinate system, and m denotes the mass of the body. For an atmospheric entry probe we have to consider mainly two types of acceleration that will determine its trajectory: an acceleration due to the gravitational attraction of the primary and secondary (perturbing) planets, $\vec{a}_{\mathrm{g}}$, and an acceleration due to the aerodynamic forces produced by the atmosphere of the primary planet, $\vec{a}_{\mathrm{Ad}}$. Eq. (6.4) can therefore be rewritten as

$$\vec{a} = \vec{a}_{\mathrm{g}} + \vec{a}_{\mathrm{Ad}} \tag{6.5}$$

Gravitational Probe Acceleration

The gravitational acceleration $\vec{a}_{\mathrm{g}}$ of a spacecraft due to the primary point mass M_0 (e.g., Titan in our special case) and N perturbing masses (e.g., the Sun and Saturn) in the planet centered (inertial) EME2000 coordinate system is given by

$$\vec{a}_{\mathrm{g}} = -G\,M_0\,\frac{\vec{r}}{|\vec{r}|^3} + \sum_{j=1}^{N} G\,M_j\left[\frac{\vec{p}_j - \vec{r}}{|\vec{p}_j - \vec{r}|^3} - \frac{\vec{p}_j}{|\vec{p}_j|^3}\right] + \vec{\nabla}U \tag{6.6}$$

where $\vec{r}$ and $\vec{p}_j$ are the position vectors of the spacecraft and the jth perturbing body ($j = 1...N$) respectively, G the gravitational constant, and $\vec{\nabla}U$ the gradient of the disturbing function due to the dynamical flattening of the planet

$$U = -G\,M_0\sum_{k=2}^{\infty} J_k\,\frac{R_{\mathrm{P}}^k}{|\vec{r}|^{k+1}}\,P_k(\sin\Theta)\ . \tag{6.7}$$

R_{P} is the equatorial radius of the planet, Θ the latitude of the spacecraft above the planet's equatorial plane, and J_k the coefficient of the kth zonal harmonic[4]. P_k is the Legendre polynomial of degree k. The spherical latitude Θ can be calculated from the r_3' component of the probe position vector in the so called Equatorial Coordinate System (see Sec. 6.3 for detailed definition of the various coordinate systems) by

$$r_3' = |\vec{r}|\,\sin\Theta \tag{6.8}$$

Using Eq. (6.2), $\sin\Theta$ can equally be expressed in EME2000 coordinates $\vec{r} = (r_1, r_2, r_3)$:

$$\sin\Theta = \frac{r_3'}{|\vec{r}|} = \frac{1}{|\vec{r}|}(r_1\,\cos\alpha_0\,\cos\delta_0 + r_2\,\sin\alpha_0\,\cos\delta_0 + r_3\,\sin\delta_0) \tag{6.9}$$

One can now see that

[4]Note that so far no harmonic coefficients for Titan have been determined. However, gravitational disturbances due to flattening of the planet are taken into account in the mathematical formulation of the problem to make the algorithm easily applicable to other solar system bodies (e.g., Mars).

$$\begin{aligned}
\frac{\partial \sin\Theta}{\partial r_1} &= -\frac{\sin\Theta\, r_1}{|\vec{r}|^2} + \frac{\cos\delta_0\, \cos\alpha_0}{|\vec{r}|} \\
\frac{\partial \sin\Theta}{\partial r_2} &= -\frac{\sin\Theta\, r_2}{|\vec{r}|^2} + \frac{\cos\delta_0\, \sin\alpha_0}{|\vec{r}|} \\
\frac{\partial \sin\Theta}{\partial r_3} &= -\frac{\sin\Theta\, r_3}{|\vec{r}|^2} + \frac{\sin\delta_0}{|\vec{r}|}
\end{aligned} \tag{6.10}$$

where α_0 and δ_0 are the right ascension and declination of the planet's north pole. With the Legendre polynomial $P_2(x)$ given by

$$P_2(x) = \frac{3}{2}x^2 - \frac{1}{2} \tag{6.11}$$

$\vec{\nabla}U$ in Eq. (6.6) developed to degree 2 reads (Kazeminejad, 2000)

$$\begin{aligned}
\frac{\partial U}{\partial r_1} &= \kappa \left\{ \frac{r_1}{|\vec{r}|^5}\, \chi(\Theta) - \frac{3}{|\vec{r}|^4} \sin\Theta\, \cos\alpha_0\, \cos\delta_0 \right\} \\
\frac{\partial U}{\partial r_2} &= \kappa \left\{ \frac{r_2}{|\vec{r}|^5}\, \chi(\Theta) - \frac{3}{|\vec{r}|^4} \sin\Theta\, \sin\alpha_0\, \cos\delta_0 \right\} \\
\frac{\partial U}{\partial r_3} &= \kappa \left\{ \frac{r_3}{|\vec{r}|^5}\, \chi(\Theta) - \frac{3}{|\vec{r}|^4} \sin\Theta\, \sin\delta_0 \right\}
\end{aligned} \tag{6.12}$$

where κ is a constant given by

$$\kappa = G\, M_0\, J_2\, R_{\mathrm{P}}^2 \tag{6.13}$$

and χ a function defined by

$$\chi(x) = \left(\frac{15}{2}\, \sin^2 x - \frac{3}{2} \right) \tag{6.14}$$

Aerodynamic Probe Acceleration

As an object moves through a fluid, the velocity of the fluid varies around the surface of the object. The variation of velocity produces a variation of pressure on the surface of the object. The effect of a fluid medium on a body moving within it therefore consists of pressure forces continuously distributed over the surface of the body, as well as shear forces due to the viscosity of the medium. All of these forces can be reduced to one principal vector $\vec{F}_{\mathrm{Ad}}$ of aerodynamic forces and to a principal vector $\vec{M}_{\mathrm{Ad}}$ of the moment of these forces about any designated point. If s_1, s_2 and s_3 define the coordinate system of the spacecraft then the components of the aerodynamic force vector $\vec{F}_{\mathrm{Ad}}$ projected onto those axis are defined as the axial force A, the normal force N, and the side force Z_1 (see Fig. 6.5, note that Z_1 is directed out of the plane). In our case s_1 also defines the symmetry axis of the body. If w_1, w_2, and w_3 define the wind (or relative atmosphere) coordinate system, where the w_1 direction is by definition opposite to the direction of the relative flow velocity vector $\vec{v}_{\mathrm{rel}}$, then the components of $\vec{F}_{\mathrm{Ad}}$ projected onto those axes

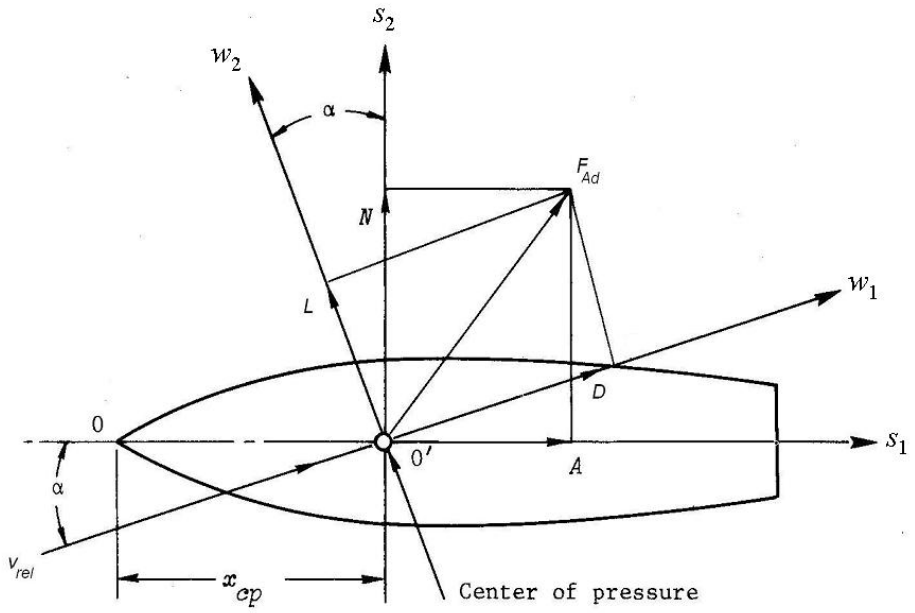

Figure 6.5: *Aerodynamic forces on a body of revolution in wind (w_1, w_2, w_3) and spacecraft (s_1, s_2, s_3) coordinate system; $\vec{F}_{\mathrm{Ad}}$ = aerodynamic force vector, α=angle of attack, $\vec{v}_{\mathrm{rel}}$ = relative flow velocity vector; L, D, A, and N = respectively lift, drag, axial and normal component of $\vec{F}_{\mathrm{Ad}}$; the side force Z_1 and lateral force Z components are directed out of the page (cf. Krasnov, 2000).*

are defined as the drag D, the lift L, and the lateral force Z. The angle between $\vec{v}_{\mathrm{rel}}$ and s_1 is called the angle of attack α. Note that $\vec{v}_{\mathrm{rel}}$ is assumed to be in the s_1, s_2 plane (i.e., the side slip angle[5] is zero), which implies that Z and Z_1 are 0.

The onboard accelerometers will measure the aerodynamic accelerations parallel to the spacecraft axes s_1, s_2 and s_3. Due to the rotational symmetry of the probe (with s_1 as the symmetry axis), the acceleration components in the s_2 and s_3 direction can be combined to get the normal acceleration a_N:

$$a_N = \left(a_{s_2}^2 + a_{s_3}^2\right)^{1/2} \tag{6.15}$$

The axial (i.e., parallel to s_1) is simply obtained from

$$a_A = a_{s_1} \tag{6.16}$$

It can be easily seen that the corresponding accelerations in the wind or atmosphere coordinate system can be calculated if the angle of attack α is known:

$$\begin{aligned} a_D &= a_A \cos\alpha + a_N \sin\alpha \\ a_L &= a_N \cos\alpha - a_A \sin\alpha \end{aligned} \tag{6.17}$$

[5]The side slip angle is the angle between the $\vec{v}_{\mathrm{rel}}$ vector and the s_1 axis measured in the w_2, w : 3-plane.

To first order the lift force can be neglected[6], and the aerodynamic acceleration in the inertial coordinate system of Eq. (6.5) can therefore be written as

$$\vec{a}_{\mathrm{Ad}} = -a_D \frac{\vec{v}_{\mathrm{rel}}}{|\vec{v}_{\mathrm{rel}}|} \tag{6.18}$$

where $\vec{v}_{\mathrm{rel}}$ is the relative velocity vector of the fluid (i.e., the atmosphere) and the spacecraft in the inertial coordinate system. $\vec{v}_{\mathrm{rel}}$ can be calculated using the relation

$$\vec{v}_{\mathrm{rel}} = \vec{v} - \vec{\omega}_{\mathrm{p}} \times \vec{r} - \vec{v}_w \tag{6.19}$$

where $\vec{r}$ and $\vec{v}$ are again the probe position and velocity vector in the inertial frame, $\vec{\omega}_{\mathrm{p}}$ the angular velocity vector of the planet, and $\vec{v}_w$ the velocity vector of the atmospheric wind. Note that Eq. (6.19) assumes that the (static) atmosphere co-rotates with the planet.

6.6 Atmospheric Structure Reconstruction

The atmospheric drag acceleration vector $\vec{a}_D$ is given by

$$\vec{a}_D = \frac{1}{2} C_D \frac{A}{m} \rho \, v_{\mathrm{rel}} \, \vec{v}_{\mathrm{rel}} \tag{6.20}$$

where m, A, and C_D are the spacecraft mass, cross-section area, and drag coefficient respectively. $\vec{v}_{\mathrm{rel}}$ is the relative velocity as given by Eq. (6.19) and ρ the atmospheric density, which is a function of the spacecraft altitude. Rearranging Eq. (6.20) yields

$$\rho = -\frac{2\,m}{C_D\,A} \frac{|\vec{a}_{\mathrm{Ad}}|}{|\vec{v}_{\mathrm{rel}}|^2} \tag{6.21}$$

It is important to note that m will change during the entry phase as the probe will lose mass due to heat shield ablation as described in Sec. 2.2. The cross section A changes during the descent phase (due to the jettison of the heat shield and the subsequent deployment of the various parachutes during the descent sequence) but can be considered as constant during the entire entry phase. The aerodynamic drag coefficient C_D is a dimensionless number that reflects the interaction of the atmospheric constituents with the satellite surface. This interaction is strongly dependent on the aerodynamic flow regime, which in return depends on the fluid composition, the fluid temperature, the body shape and orientation, and the fluid velocity. The axial and normal force coefficient C_A and C_N are measured in wind tunnel tests and provided as function of the Mach number Ma and the spacecraft orientation in the aerodynamic database (see Sec. 3.2). C_D can be derived from the relation

$$C_D = C_A \cos\alpha + C_N \sin\alpha \,. \tag{6.22}$$

The Mach number Ma is given by

$$Ma = \frac{|\vec{v}_{\mathrm{rel}}|}{c_s} \tag{6.23}$$

[6]Due to the spin of the probe the lift force vector will rotate with the probe and average to zero if it is constant over the spin period.

where c_s is the speed of sound given by

$$c_s = \sqrt{\frac{\gamma\, R\, T}{\mu}}\ . \tag{6.24}$$

with atmospheric temperature T and the molecular weight μ. γ is the ratio of specific heats, and $R = 8.314$ J K^{-1} mol^{-1} is the universal gas constant. Note that neither T nor μ are directly measured during the entry phase. μ in Titan's upper atmosphere depends on the relative abundance of methane and argon, which are not constant in altitudes above 600 km due to diffusive separation (Yelle *et al.*, 1997) and require therefore to be modelled as described in Sec. 4.3. Note that during the descent phase (i.e., the altitude range from ∼160 km down to the surface) μ will be measured by the GCMS experiment, and indirectly by the SSP experiment. From the density profile and an initial pressure estimation $p(z_0)$ the atmospheric pressure profile $p(z)$ can be derived by integrating the equation of hydrostatic equilibrium

$$\begin{aligned} p(z) &= p(z_0) - \int_{z_0}^{z} \rho\, g\, dz \\ p(z_0) &= -\rho(z_0)\, g(z_0)\, \left(\frac{d}{dz} \ln \rho\right)^{-1}_{z_0} \end{aligned} \tag{6.25}$$

The initial pressure $p(z_0)$ can be either directly provided in Eq. (6.25) or estimated from the density gradient. The temperature T is determined from the ideal gas law with knowledge of the mean molecular weight μ using the relation

$$T(z) = \frac{p(z)\, \mu}{\rho(z)\, R} \tag{6.26}$$

6.7 Entry Phase Error Analysis

The reconstructed entry phase trajectory is affected by a multitude of different error sources. The effects of these errors and uncertainties on the accuracy of the trajectory reconstruction can be estimated (Peterson, 1965; Withers *et al.*, 2003). The spacing in time Δt of points along the reconstructed trajectory is controlled by the accelerometer sampling rate. The uncertainty of each data point will be affected by the following error sources:

Accelerometer Errors

The accelerometer measurement uncertainty Δa is due to the limited instrument resolution, noise, changes in gain and offset since calibration, any systematic offset, corrections for off-center instrument position etc. The implied error of the reconstructed altitude h at the end of the time increment Δt can be estimated by

$$\Delta h_{acc} = \frac{1}{2}\, \Delta t^2 \times \Delta a \tag{6.27}$$

and the altitude error due to accelerometer uncertainties at the end of the integration span is simply

$$\Delta H_{acc} = \sqrt{\sum_i \Delta h_{acc}^2} \tag{6.28}$$

Gravitational Force Errors

The gravitational acceleration of the primary body (perturbing gravitational forces can be neglected in the error analysis) has an uncertainty due to the limited accuracy of its GM value. The altitude error at the end of the time increment Δt can be estimated by

$$\Delta h_g = \frac{1}{2}\,\Delta t^2 \times \Delta a_g + \Delta h \times \frac{2\,a_g}{(R_P + h)^2} \tag{6.29}$$

with

$$\Delta a_g = \frac{\Delta G\,M}{(R_P + h)} \tag{6.30}$$

and the altitude error due to gravitational force uncertainties at the end of the integration span is again given by

$$\Delta H_{acc} = \sqrt{\sum_i \Delta h_g^2} \tag{6.31}$$

Initial Conditions Errors

The initial conditions uncertainties are provided in the form of the 6×6 covariance matrix $\mathbf{P}_0$. The covariance matrix can be propagated together with the spacecraft state vector by computation of the system transition matrix $\mathbf{\Phi}_i = \mathbf{\Phi}(t_i)$ according to

$$\mathbf{P}_i = \mathbf{\Phi}_i\,\mathbf{P}_{i-1}\,\mathbf{\Phi}_i^T \tag{6.32}$$

The transition matrix $\mathbf{\Phi}$ [see Eq. (10.26)] can be obtained from the numerical integration of the Variational Equations, which are outlined in Sec. 10.2. From $\mathbf{P}_i$ the 1σ position vector can be obtained and then be converted into errors of altitude, longitude, and latitude (see Appendix C.3.

Mode	Sampling Rate [Hz]
Entry Mode	3.125
Descent Mode 1	4.167
Descent Mode 3 and Impact	1.754

Table 6.1: *HASI servo accelerometer sampling rates.*

Mode	Range	Resolution	Uncertainty (1σ)
High Gain	$\pm$ 2 mg	0.3 μg	0.3 μg
Low Gain	$\pm$ 20 mg	3 μg	3 μg

Table 6.2: *HASI x-servo accelerometer characteristics for* ***High Resolution (Fine) Mode****.*

Mode	Range	Resolution	Uncertainty (1σ)
High Gain	$\pm$ 1.85 g	0.3 mg	0.3 mg
Low Gain	$\pm$ 18.5 g	3 mg	3 mg

Table 6.3: *HASI x-servo accelerometer characteristics for* ***Low Resolution (Coarse) Mode****.*

Mode	Sampling [Hz]	Range	Resolution	Uncertainty (1σ)
Entry Mode	1.6129	$\pm$ 20 mg	50 mg	200 mg
Impact Mode	200	$\pm$ 20 mg	50 mg	200 mg

Table 6.4: *HASI x/y/-piezoresistive accelerometer characteristics.*

Chapter 7

Entry Phase Test Cases

The entry phase test campaign is based on the noise and no noise datasets of the HSDS v.1.5 with the simulated HRTF prograde wind model (see Sec. 4.4). The probe initial conditions and uncertainties are summarized in Tables 5.1 and 5.2 and are provided together with the planetary constants (e.g., gravitational constants, planetary pole coordinates etc.) in the EVENT_FILE (see Appendix D). The probe entry phase trajectory and Titan's upper atmosphere are reconstructed as described in Chap. 6. Even if the entry phase ends (per definition) at the initiation of the parachute sequence T_0 (i.e., nominally at 158 km altitude) the entry phase reconstruction is continued down to an altitude of 150 km. This allows the assessment of the ability of the accelerometer based reconstruction effort beyond T_0. This is essential for the entry phase and descent phase fitting process which we will describe in Chap. 10 as it requires an overlap of the entry and descent phase portions in order to build residuals in altitude and descent speed.

The various test cases for the entry phase were derived from the various combination of input accelerometer measurements and instrument noise. Table 7.1 summarizes the various test cases and their assumptions. For the quantitative comparison of the reconstruction efforts the residuals between the HSDS trajectory[1] and the reconstructed one (i.e., HSDS trajectory minus reconstructed trajectory) are shown. In addition a figure of merit defined as

$$\chi^2 = \sum_i \{X_{HSDS}(i) - X_{Rec.}(i)\}^2 \tag{7.1}$$

is calculated, where X_{HSDS} and X_{Rec} are the respective values of the synthetic dataset trajectory (provided in a separate file as part of the HSDS) and the results of the reconstruction effort at the time t_i. It should be noted however that this number is not always the best way to assess the reconstruction quality as it comprises the residuals from the altitude range of 1270 km down to 150 km, i.e., the entire entry phase and the very beginning of the descent phase. It is therefore necessary to also observe the exact shape of the residual profiles. The χ^2 figure of merit should be mainly used to assess the difference when this cannot be easily done by comparing the profiles with the naked eye.

An important input parameter for the entry phase reconstruction is the magnitude (and direction) of *high altitude winds*, defined as winds in the altitude range from the

[1]This is the trajectory that was used to produce the HSDS measurements and is provided as part of the HSDS dataset.

probe interface altitude at 1270 km down to the altitude where they would be measured by the Doppler Wind Experiment (DWE), which is at the start of the probe relay link at a nominal altitude of ∼152 km. High altitude winds play an important role in the reconstruction of the entry phase as they influence both the magnitude and the direction of the relative velocity vector, given by

$$\vec{v}_{\text{rel}} = \vec{v} - \vec{\omega}_p \times \vec{r} - \vec{v}_w \tag{7.2}$$

The relative velocity vector $\vec{v}_{\text{rel}}$ is derived from the inertial velocity vector $\vec{v}$ corrected by the atmospheric motion, which itself consists of the atmosphere co-rotation term $\vec{\omega}_p \times \vec{r}$ and a position dependent wind speed term $\vec{v}_w$. The probe accelerometers can only measure the magnitude (norm) of the aerodynamic drag vector. However, it is necessary to convert this value into a force vector to be able to introduce this force into the equations of motion as given by Eq. (6.5). This is done using the simple fact that the drag force vector is always pointing into the opposite direction of the relative velocity vector $\vec{v}_{\text{rel}}$. If the exact direction of $\vec{v}_{\text{rel}}$ is not properly modeled a systematic error is introduced into the numerical integration of the probe state vector. In other words, inexact knowledge of the $\vec{v}_{\text{rel}}$ results in exactly the same incorrect direction of the aerodynamic force vector in the equations of motion.

The high altitude winds cannot be directly measured as the DWE instrument depends on the probe relay signal, which is not transmitted during the entry phase. In the reconstruction of the real probe data, the high altitude winds will therefore have to be either guessed or estimated from orbiter or ground-based observations (e.g. Kostiuk *et al.*, 2001). The simulated dataset used the HRTF wind model, which has a constant prograde wind speed of 140 m/s above 219 km[2] and is pressure and latitude dependent below this altitude (Lebreton, 2001; Kazeminejad *et al.*, 2002). Three test cases of the campaign (i.e., ETC4, ETC4a, and ETC4b) are dedicated to evaluate the effect of high altitude winds and, even more important, the implications of the lack of proper knowledge on the reconstruction effort.

7.1 No Noise Test Cases

The no noise test cases represent an ideal scenario that is based upon simulated instrument data with the proper sampling times but without any measurement noise. The purpose of these test cases is to evaluate the accuracy of the implemented reconstruction methodology. One can therefore consider the reconstructed trajectory (and upper atmosphere) as a lower limit in the reconstruction error (i.e., the deviation from the reconstructed to the HSDS simulated trajectory). Any instrument noise will most likely increase this error. It should be noted that for all the test cases that assume a zero angle-of-attack α the normal accelerometer measurements (HASI Y- and Z-piezo) are either zero in the no noise input files or filled with simulated noise centered around zero in the noise input files.

[2]This altitude corresponds to the 0.5 mbar limit in the Yelle *et al.* (1997) recommended atmosphere profile.

Test Case	X-axis	Y-axis	Z-axis	Noise	Wind: Entry/Descent	α	Notes
ETC1	X-servo	Y-piezo	Z-piezo	No	140/DWE	0	Optimum
ETC2	X-piezo	Y-piezo	Z-piezo	No	140/DWE	0	Servo failure
ETC3	CASU	Y-piezo	Z-piezo	No	140/DWE	0	Servo + X-piezo failure
ETC1_N	X-servo	Y-piezo	Z-piezo	Yes	140/DWE	0	see ETC1
ETC2_N	X-piezo	Y-piezo	Z-piezo	Yes	140/DWE	0	see ETC2
ETC3_N	CASU	Y-piezo	Z-piezo	Yes	140/DWE	0	see ETC3
ETC4	X-servo	Y-piezo	Z-piezo	Yes	0/0	0	incorrect high alt. wind est. + DWE failure
ETC4a	X-servo	Y-piezo	Z-piezo	Yes	0/DWE	0	incorrect high alt. wind est.
ETC4b	X-servo	Y-piezo	Z-piezo	Yes	70/DWE	0	50% error on high alt. wind est.

Table 7.1: *Summary of test cases for the entry phase. Note that the X-axis corresponds to the axial (spin axis) direction and the Y- and Z-axes to the normal direction on the Huygens probe. α is the angle-of-attack. The "Wind" column specifies the magnitude (in m/s) of a prograde high altitude wind as first value, and the second value for the beginning of the descent phase. "DWE" means that the (zonal) wind speed measurements from the Doppler Wind Experiment are used as soon as they are available.*

Entry Test Case 1 (ETC1)

ETC1 is based upon accelerometer data from the HASI X-servo for the axial component and the HASI Y- and Z-piezo accelerations for the normal component. The reconstruction effort assumes a constant (prograde) high altitude wind speed of 140 m/s prior to the start of measurements from DWE. Fig. 7.1 shows the reconstruction results compared to the simulated HSDS trajectory. The upper panels show an overlay of the altitude and descent speed profiles, and the middle panels depict the corresponding residuals (synthetic trajectory minus reconstructed trajectory). It is seen that the altitude residuals peak at about -150 m at a relative interface time of 3.8 min and go back to zero at T_0. The peak residual corresponds very well to the time of peak deceleration (see lower panel of Fig. 5.3) and can therefore be attributed to the interpolation error of the accelerometer measurements in the integration of the equations of motion. After T_0 a linear increase is observed. The descent speed residuals (right middle panel of Fig. 7.1) show a positive peak of about 3.5 m/s at 3 min followed by a linear decrease. At T_0 the descent speed residual is approximately 2.5 m/s. Both the longitude and latitude residuals (lower panels) stay very low throughout the entire time span.

Figure 7.2 shows the results of the upper atmosphere reconstruction effort. The upper panels show the reconstructed density (left) and derived pressure profile (right) compared to the Y97 recommended, minimum, and maximum profiles. One can clearly see that the

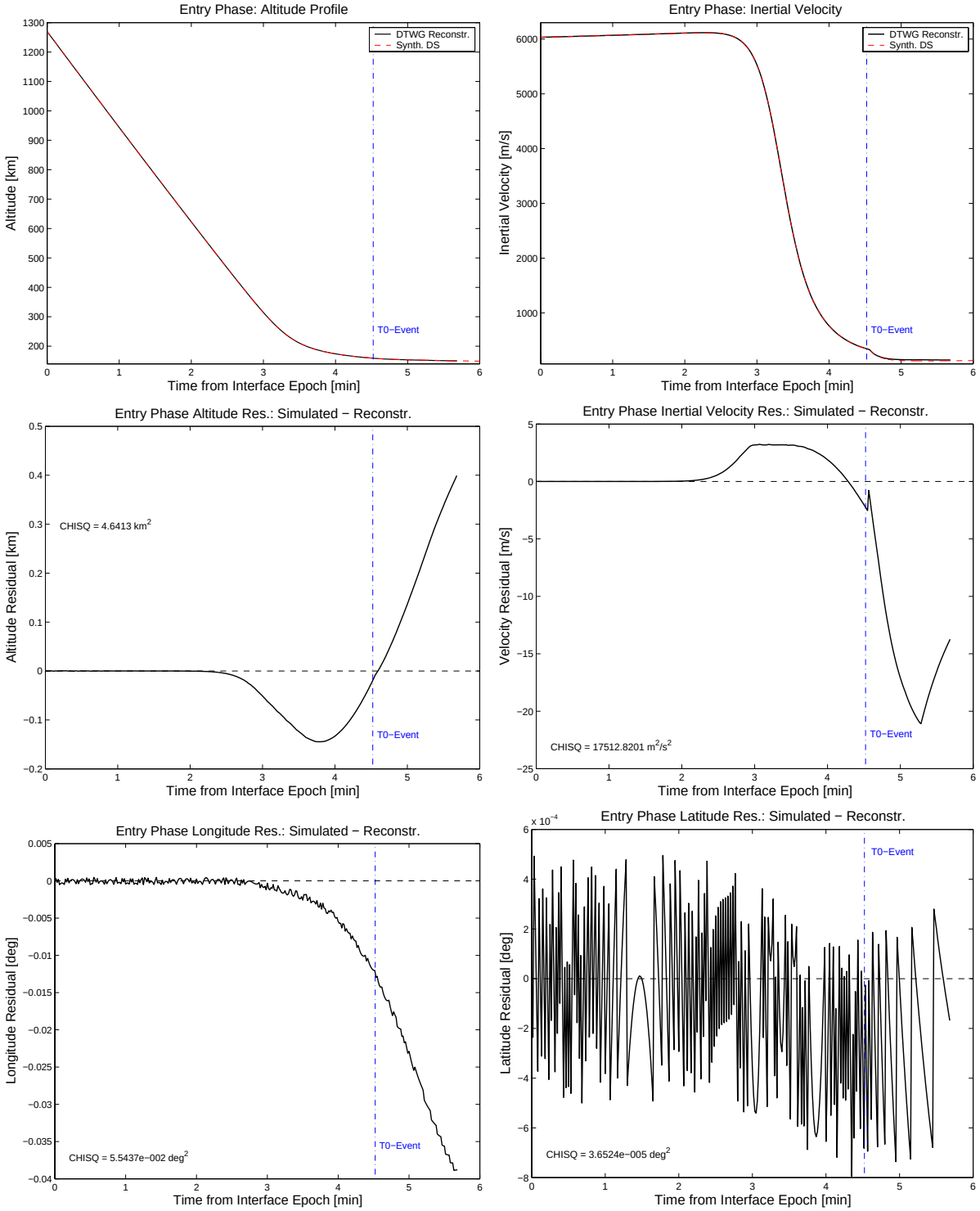

Figure 7.1: ***ETC1*** *entry trajectory reconstruction results: Upper panels: comparison of probe altitude (left) and descent speed (right) profiles from the HSDS (dashed line) and the reconstructed ones; Middle panels: corresponding altitude (left) and descent speed (right) residuals (HSDS trajectory minus reconstructed one); Lower panels: longitude (left) and latitude (right) residuals of synthetic and reconstructed trajectories. The vertical dashed line depicts the* T_0 *time, i.e., the initiation of the parachute sequence (see Sec. 2.2).*

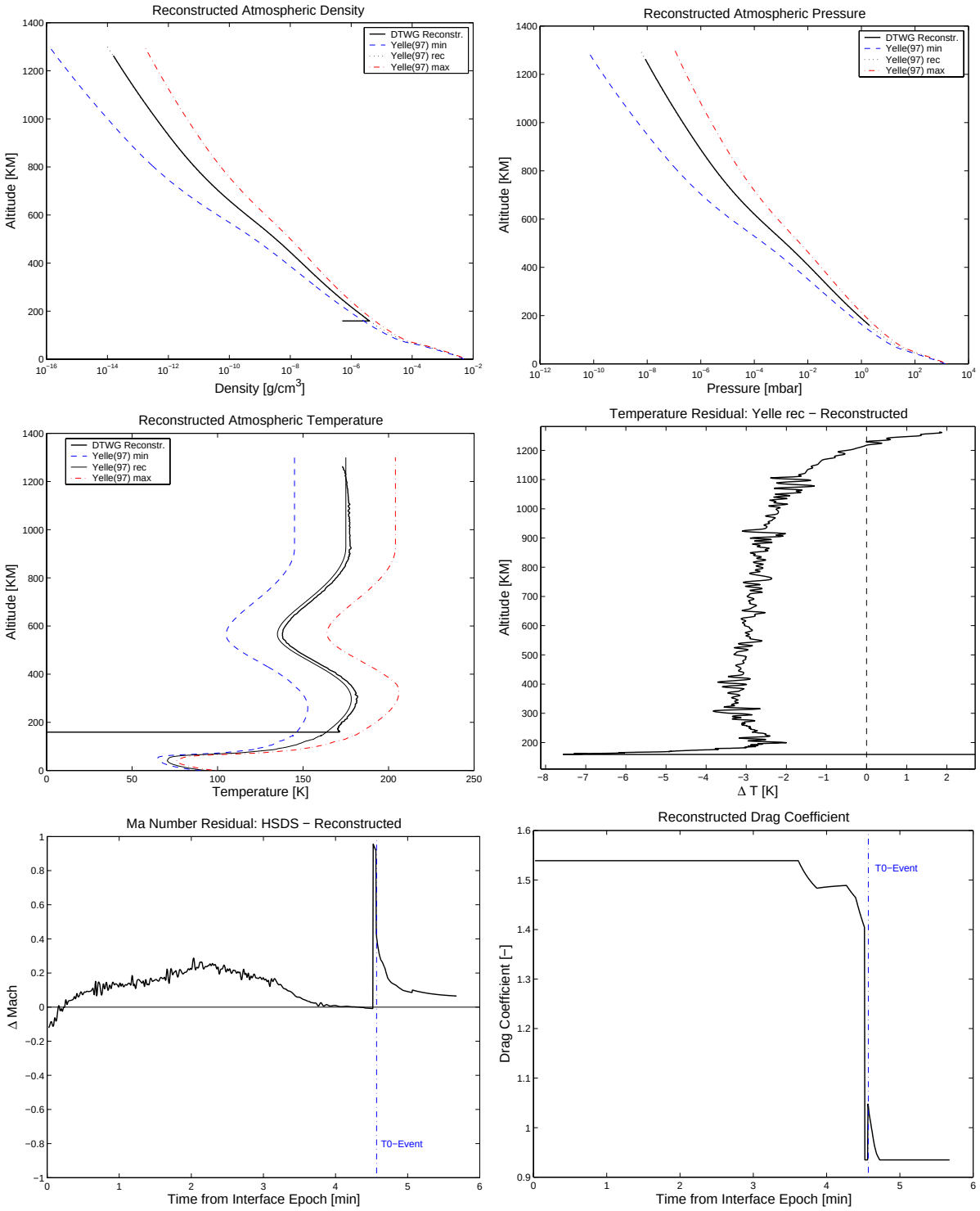

Figure 7.2: ***ETC1*** *upper atmosphere reconstruction results. Upper panels: reconstructed density (left) and pressure (right) profile compared to the Yelle* et al. *(1997) recommended, minimum, and maximum profiles; Middle panels: reconstructed temperature profile compared to the Yelle* et al. *(1997) recommended, minimum, and maximum profile and temperature residual (right) of the recommended minus the reconstructed profile; Lower panels: Mach number residuals HSDS minus reconstructed (left) and reconstructed aerodynamic drag coefficient (right).*

nominal profile was used for the simulation of the HSDS. The pressure profile reconstruction was done according to Eq. (6.25) with the initial pressure value of p_0=8.3080E-07 Pa at a starting altitude of 1263 km. This value was interpolated directly from the Y97 model and is therefore a fairly accurate starting point. In the actual mission scenario (with the upper atmosphere only constrained by remote sensing measurements from the orbiter) p_0 must be assumed, which will introduce a systematic error in the reconstructed pressure profile. The temperature profile can be derived from the density and pressure according to Eq. (6.26) and is shown together with the Y97 model profiles in the left middle panel. The corresponding residuals are shown in the right middle panel. It can be seen that even the very accurate starting pressure p_0 implies a temperature residual of almost +2 K. The temperature residual decreases through zero at 1200 km and then increases to positive values. The residuals remain at the approximately constant value of -3 K in the altitude range from 1100 km down to about 160 km when the parachute sequence starts. The T_0 event causes a peak deviation of almost 8 K. The lower left panels of Fig. 7.2 shows the residuals in Mach number, which stay below $\pm$ 0.2 . The interpolated drag coefficient C_D is shown in the lower right panel. A sudden jump in the C_D value at T_0 introduces a sudden jump in the reconstructed density, temperature and temperature residual, as well as the Mach number. It is also seen that the reconstruction of the atmospheric properties from accelerometer measurements is only possible prior to T_0.

It should be recalled that the reconstruction of the temperature profile during the entry phase is important for two main reasons

- To derive the Mach number which constrains the aerodynamic regime the spacecraft is in and allows to interpolate the drag coefficient from a preflight aerodynamic database;
- From an atmospheric science point of view the upper atmosphere temperature profile provides the exosphere temperature and the shape of the thermosphere.

For both purposes it is important to keep in mind the various uncertainties that are involved in the derivation of the temperature profile which requires a stepwise approach starting from the reconstruction of the density according to Eq. (6.25), integrating the pressure according to Eq. (6.25), and deriving the temperature according to Eq. (6.26).

1. The probe mass m will change during the entry phase due to heat shield mass ablation (see Sec. 3.1). This effect was not taken into account in the HSDS and neither in the ETC1 reconstruction effort. This effect will however be taken into account in later test cases using a simple model otlined in Sec. 3.1.
2. In the numerical integration of the entry trajectory the aerodynamic drag is derived from the conversion of measured axial and normal coefficients using the angle-of-attack α which itself has to be reconstructed and is therefore only known with limited accuracy. A further uncertainty is introduced from the interpolation error of the accelerations in the integration process. If α is zero only the later error source is effective.
3. The aerodynamic coefficient C_D is interpolated from the aerodynamic database as a function of α and Ma. The used C_D value therefore combines the errors of α, Ma, the uncertainty of the aerodynamic database, and the interpolation error.

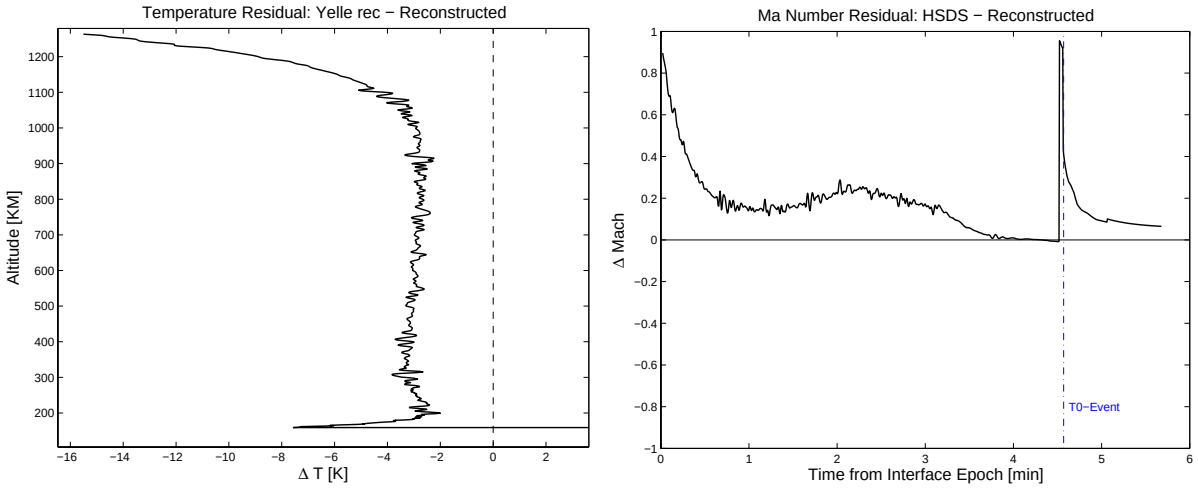

Figure 7.3: ***ETC1*** *upper atmosphere reconstruction results with* $p_0 = p_0 + 10\%$.

4. The molecular mass in the upper atmosphere is not constant due to diffusive separation of the various species (see Sec. 4.3 and Fig. 4.2). The atmosphere composition is not measured during the entry phase, and the mean molecular weight μ therefore needs to be modeled. In the test case campaign the modeling of μ was done in the same way as in the Y97 atmosphere model. This error source is therefore not effective in the test case campaign but will play a role when real flight data are used and the actual mean molecular mass profile is unknown.

5. The computation of the pressure from the reconstructed density requires an initial pressure value p_0 which must be assumed and will therefore introduce a systematic error in both the pressure and the temperature profile.

In order to estimate the impact of the p_0 estimation error, a biased value of $p_0' = p_0 + 0.10\,p_0$ is used and the temperature is reconstructed from ETC1. The new temperature residuals and derived Mach number profile are shown in the left and right panel of Fig. 7.3 respectively. It can be seen that the temperature residuals start from -16 K at 1263 km (which introduces a Mach number residual of almost 1 Mach) and decrease to the approximately constant 3 K in the altitude range of 1100 – 160 km. This shows that the temperature profile is only sensitive to initial pressure value errors at an altitude range above 1100 km.

Entry Test Case 2 (ETC2)

ETC2 assumes a failure of the HASI X-servo accelerometer and therefore uses the HASI X-piezo measurements only. The HASI X-piezo accelerometer has both a lower sampling rate (i.e., 1.6129 Hz, see Table 5.7) and a lower resolution (i.e., 50 mg). It is also important to note that the X-Servo sensor switches from its entry phase sampling rate of 3.125 Hz to an even higher rate of 4.167 Hz shortly after T_0 in order to better capture the parachute dynamics. Fig. 7.4 shows the reconstruction results for ETC2. The difference can be seen by comparing the ETC2 results shown in Fig. 7.4 to the corresponding ETC1 results in Fig. 7.1. No striking differences can be seen from the comparison of the two test case χ^2

values. ETC2 has higher values for the longitude and latitude residuals (as expected) but lower values for the altitude and velocity residuals. This would mean that the superior servo accelerometer provides a better reconstruction quality in the horizontal plane (i.e., longitude and latitude) but a slightly lower quality in the vertical direction and the probe dynamics. No clear explanation has so far been found for this behavior.

Entry Test Case 3 (ETC3)

ETC3 assumes a complete failure of both the HASI X-servo and the HASI X-piezo accelerometer. The entry trajectory reconstruction bases therefore on the CASU accelerometer. ETC3 also uses the HASI Y-piezo and the Z-piezo accelerations but due to the zero degree angle-of-attack and the no noise assumption, the two sensor inputs are zero. The ETC3 test case therefore simulates also a complete failure of the Y-piezo and the Z-piezo accelerometers as the reconstruction is only based on the CASU measurements.

The CASU was essentially designed to detect specific g-limits for the arming and initiation of the parachute sequence. It has therefore a limited measurement range of only 0-10g (note that the deceleration pulse exceeds 10g) and a fairly low sampling rate of only 1 Hz. Fig. 7.5 shows the ETC3 trajectory reconstruction results. A steady increase of the altitude, descent speed, latitude, and longitude residuals briefly after 3 minutes past interface epoch can be seen. Comparing this to the deceleration pulse of the probe (see Fig. 5.3) it can be seen that this corresponds to the time when the deceleration surpasses the 10g limit. The lack of the CASU to measure accelerations beyond this limit has a severe impact on the trajectory reconstruction effort. The altitude residuals increase up to 16 km and the probe reaches the 150 km altitude about 1.6 minutes too early. The inertial velocity residuals go up to -377 m/s. As expected the CASU accelerometer measurements also have a negative affect on the atmosphere reconstruction process. The ETC3 temperature residuals have an offset of 15 K at 1270 km (similar to ETC1 and ETC2) but also have offsets in the range of 4 – 10 K at lower altitudes (plots not shown). It should be noted that the reconstruction results from the CASU only test case could very likely be enhanced if the deceleration pulse beyond the 10g limit would be modeled. This approach has however not been further pursued in this test campaign.

7.2 Noise Test Cases

In test cases ETC1_N, ETC2_N, and ETC3_N the same instrument sensor combinations are used as for ETC1, ETC2, and ETC3, respectively, with the only difference that the instrument data are affected by the simulated sensor noise.

A comparison of the ETC1_N (noisy HASI X-servo, Y-piezo, and Z-piezo data) reconstruction results in Fig. 7.6 with the results from ETC1 (Fig. 7.1) shows only minor differences mainly in the descent velocity residuals. These are also reflected in a slightly higher χ^2 value. The altitude, longitude, and latitude values are very similar. This result proves the high quality of the X-servo instrument, as the introduced instrument noise is so little, that it affects the reconstruction effort only marginally.

Fig. 7.7 shows the test results for ETC2_N, i.e., the combination of noisy HASI X-piezo, Y-piezo, and Z-piezo accelerometer data. Comparing these results with ETC2 (Fig. 7.4) one can clearly see that the higher X-piezo noise has a more severe effect on the entire

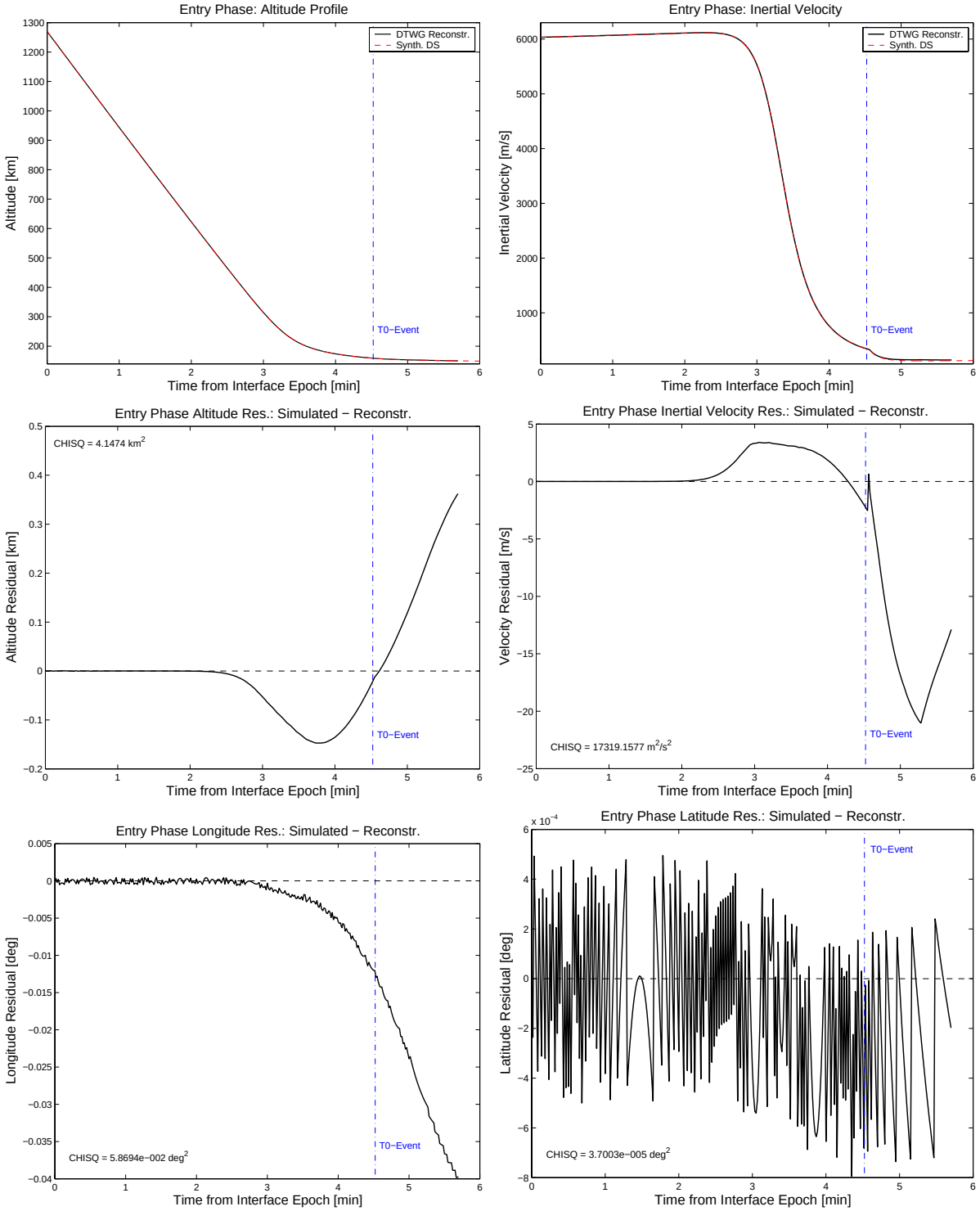

Figure 7.4: ***ETC2*** *entry trajectory reconstruction results. Upper panels: comparison of probe altitude (left) and descent speed (right) profiles from the HSDS (dashed line) and the reconstructed ones; Middle panels: corresponding altitude (left) and descent speed (right) residuals; Lower panels: longitude (left) and latitude (right) residuals of synthetic and reconstructed trajectories. The vertical dashed line depicts the* T_0 *time, i.e., the initiation of the parachute sequence (see Sec. 2.2).*

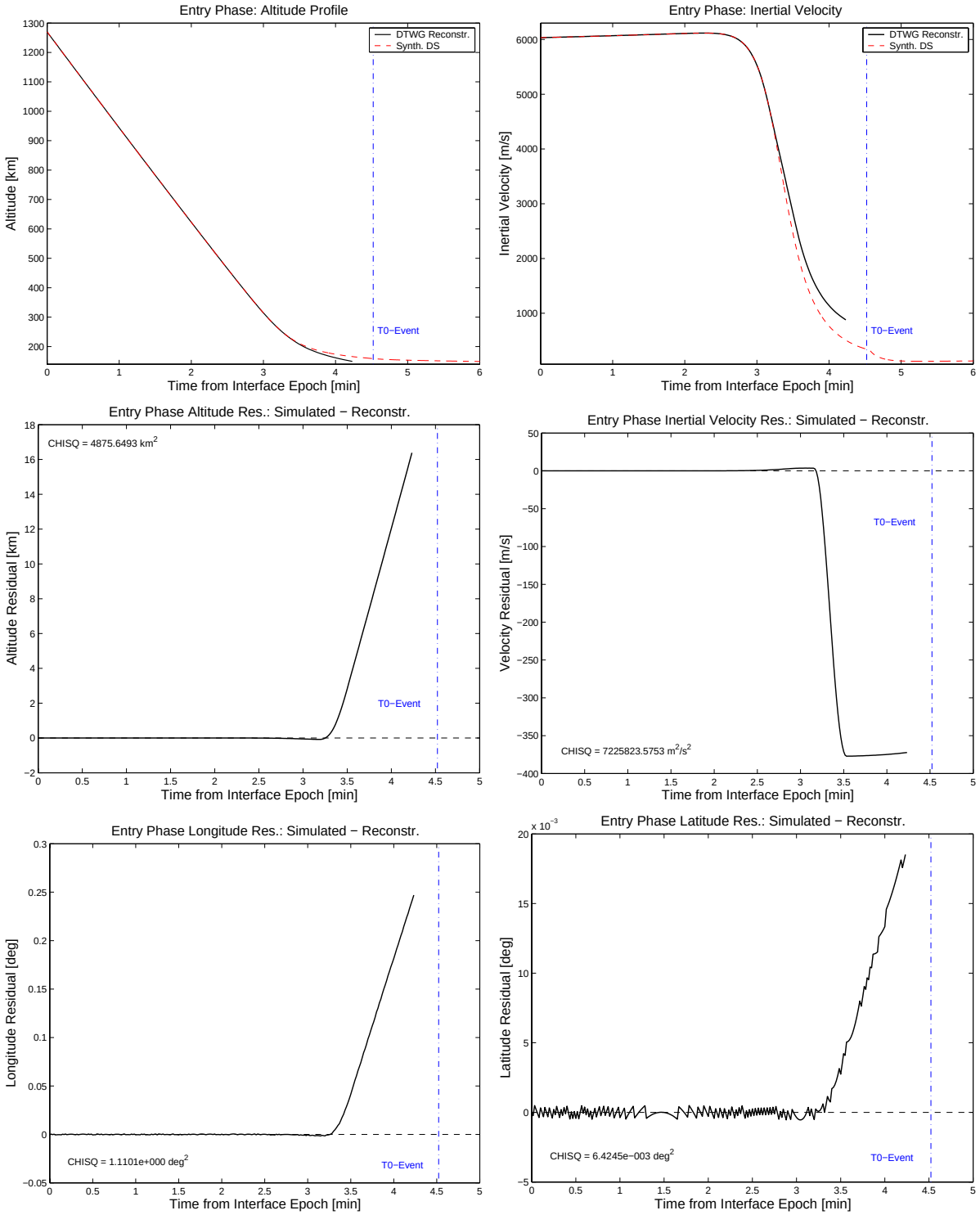

Figure 7.5: ***ETC3*** *entry trajectory reconstruction results: upper panels: comparison of probe altitude (left) and descent speed (right) profiles from the HSDS (dashed line) and the reconstructed ones; middle panels: corresponding altitude (left) and descent speed (right) residuals; Lower panels: longitude (left) and latitude (right) residuals of synthetic and reconstructed trajectories. The vertical dashed line depicts the* T_0 *time, i.e., the initiation of the parachute sequence (see Sec. 2.2)*

trajectory reconstruction. The altitude, longitude and latitude χ^2 values are respectively about 10, 3, and 4.4 times higher compared to the ETC2 values. The ETC2_N descent velocity χ^2 value is slightly lower but from the shape of the residual profile one can see that this is only due to lower residuals at the very end. The velocity residuals during the entire entry phase are definitely better for the no noise ETC2 case.

Fig. 7.8 shows the test results for ETC3_N, i.e., the combination of noisy CASU, Y-piezo, and Z-piezo accelerometer data. The CASU noise impact can be seen in all residual profiles as a continuous downward (i.e., to negative values) drift. The reconstruction effort however is comparable to that in ETC3, which shows that ETC3 is in error to such an extent that noise does not affect it much.

7.3 High Altitude Wind Studies

In the test cases ETC4, ETC4a, and ETC4b the impact of an inaccurate high altitude wind estimation and/or a lack of DWE measurements on the reconstruction effort is assessed.

Fig. 7.9 compares the altitude and inertial velocity residuals of the 3 test cases. ETC4 fully ignores high altitude winds and assumes that no DWE data would be available. ETC4a also ignores high altitude wind but assumes that the DWE would be fully operational, and ETC4b assumes a 70 m/s high altitude wind (i.e., an error of 50% as the actual simulated wind above 219 km is 140 m/s) and DWE wind measurements. It can be seen that ETC4 provides the worst reconstruction results. The velocity residuals (upper right panel) reach almost 30 m/s at T_0 and go beyond 100 m/s after 5 minutes from interface epoch. The altitude residuals (upper left panel) also grow continuously. For ETC4 the integrator stopped prior to the predefined integration span of 150 km due to the high systematic error.

The middle panels of Fig. 7.9 show the corresponding residuals for ETC4b. As expected a similar behavior up to about 5.5 minutes integration time can be seen. Once the DWE data are taken into account the slope of the altitude residuals profile decreases however. The velocity residuals decrease significantly once the DWE data are used.

The lower panels of Fig. 7.9 show the ETC4b results. The 70 m/s high altitude wind estimation provide a much better reconstruction results compared to the 0 m/s estimation in ETC4 and ETC4b. The altitude residual at T_0 are reduced by a factor of 2.7.

One can conclude from this analysis that an accurate estimation of the high altitude winds on Titan is an essential input parameter for the reconstruction of the entry trajectory. These simulation results show that even an inaccurate guess still provides a better reconstruction result than any approach that would entirely ignore the high altitude wind speeds.

7.4 Ablation Mass Impact

The probe loses a certain mass during the entry phase due to the ablation of the heat-shield. A simple model for the mass loss profile as function of probe velocity is implemented as outlined in Sec. 3.1. The probe mass development throughout the entire mission can be described by 4 phases with corresponding mass numbers provided in Table 3.1.

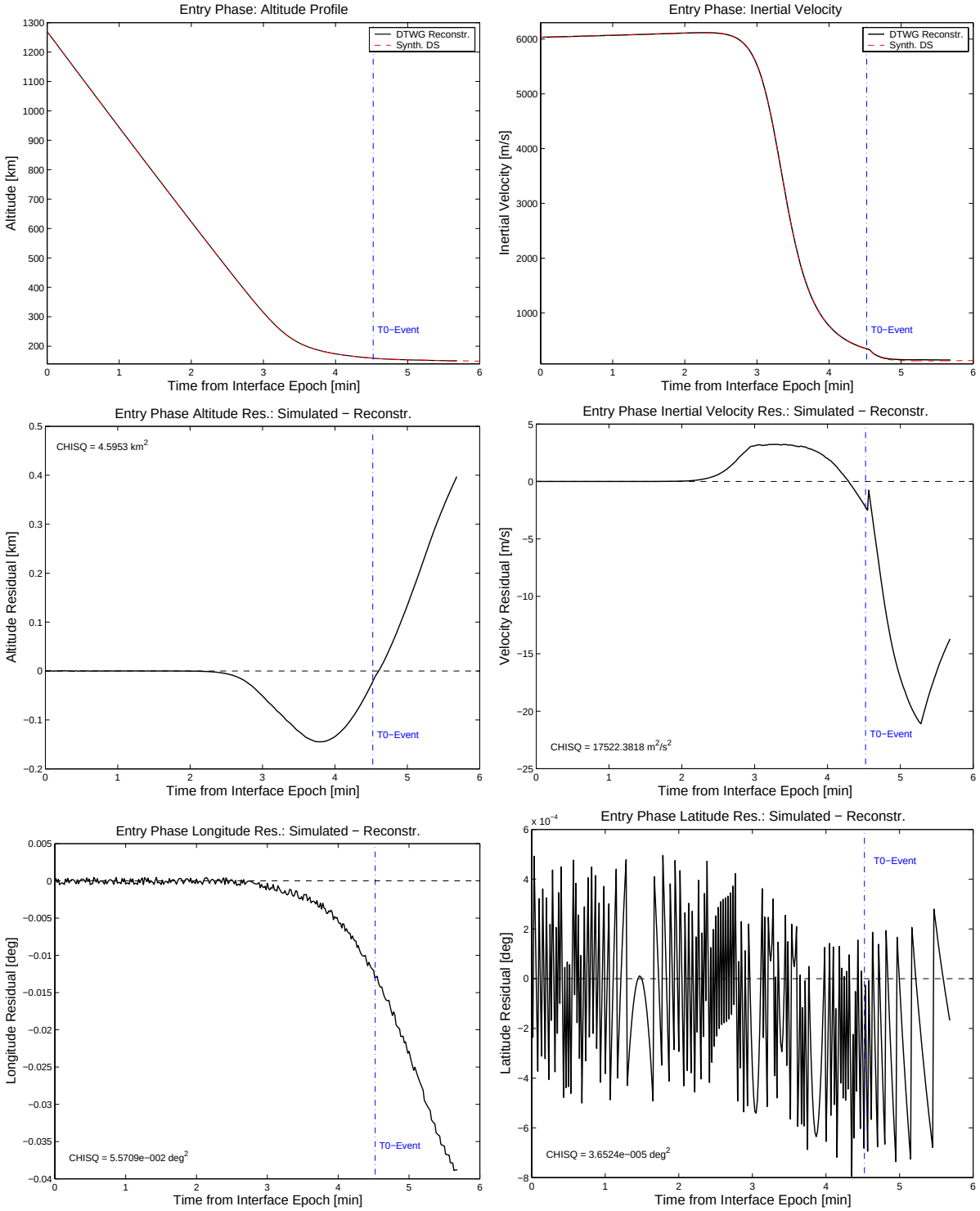

Figure 7.6: ***ETC1_N*** *entry trajectory reconstruction results. Upper panels: comparison of probe altitude (left) and descent speed (right) profiles from the HSDS (dashed line) and the reconstructed ones; Middle panels: corresponding altitude (left) and descent speed (right) residuals; Lower panels: longitude (left) and latitude (right) residuals of synthetic and reconstructed trajectories. The vertical dashed line depicts the* T_0 *time, i.e., the initiation of the parachute sequence (see Sec. 2.2).*

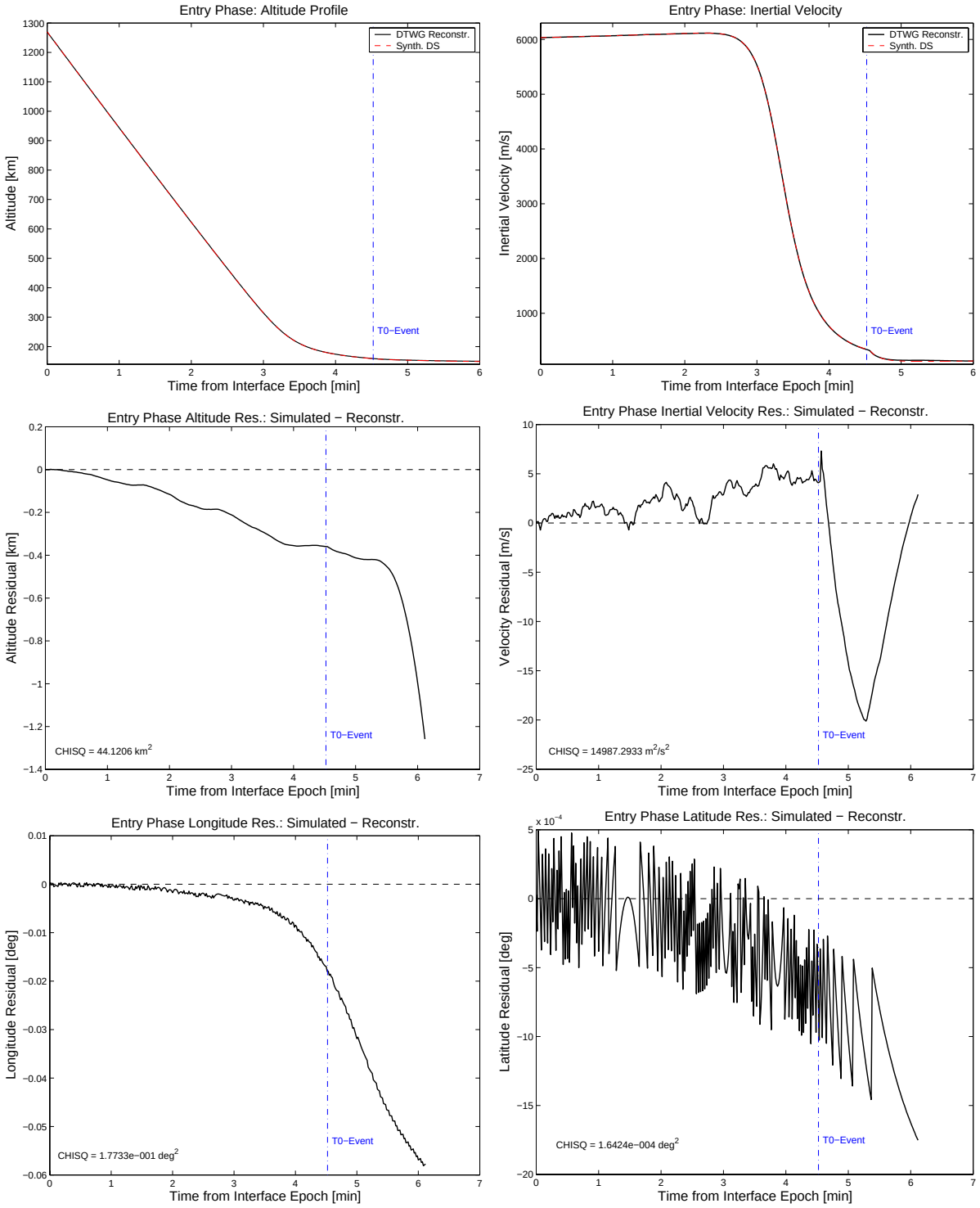

Figure 7.7: ***ETC2_N*** *entry trajectory reconstruction results. Upper panel: comparison of probe altitude (left) and descent speed (right) profiles from the HSDS (dashed line) and the reconstructed ones; Middle panels: corresponding altitude (left) and descent speed (right) residuals (synthetic dataset trajectory minus DTWG reconstruction); Lower panels: longitude (left) and latitude (right) residuals of synthetic and reconstructed trajectories. The vertical dashed line depicts the* T_0 *time, i.e., the initiation of the parachute sequence (see Sec. 2.2).*

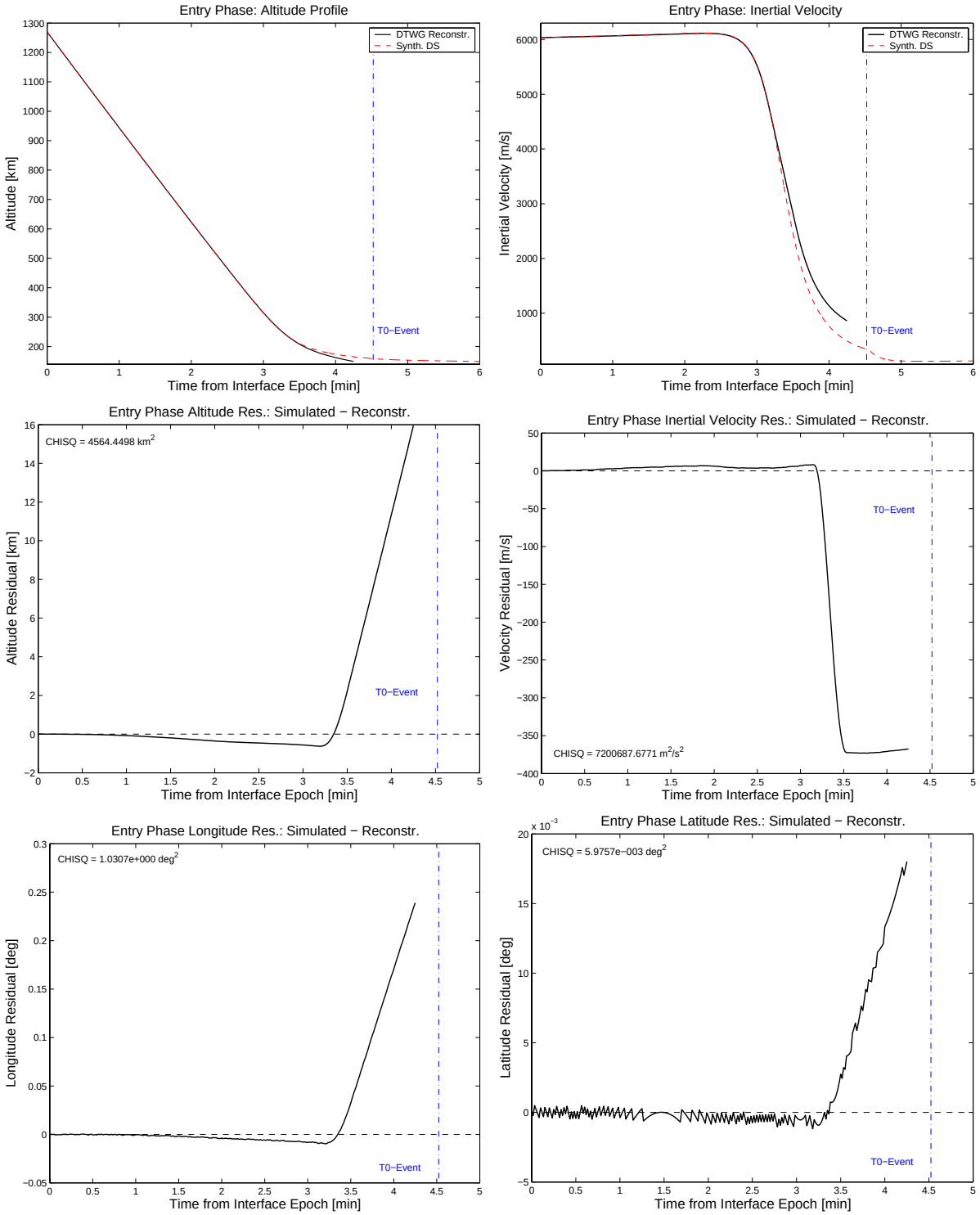

Figure 7.8: ***ETC3_N*** *entry trajectory reconstruction results. Upper panels: comparison of probe altitude (left) and descent speed (right) profiles from the HSDS (dashed line) and the reconstructed ones; middle panels: corresponding altitude (left) and descent speed (right) residuals); Lower panels: longitude (left) and latitude (right) residuals of synthetic and reconstructed trajectories. The vertical dashed line depicts the* T_0 *time, i.e., the initiation of the parachute sequence (see Sec. 2.2)*

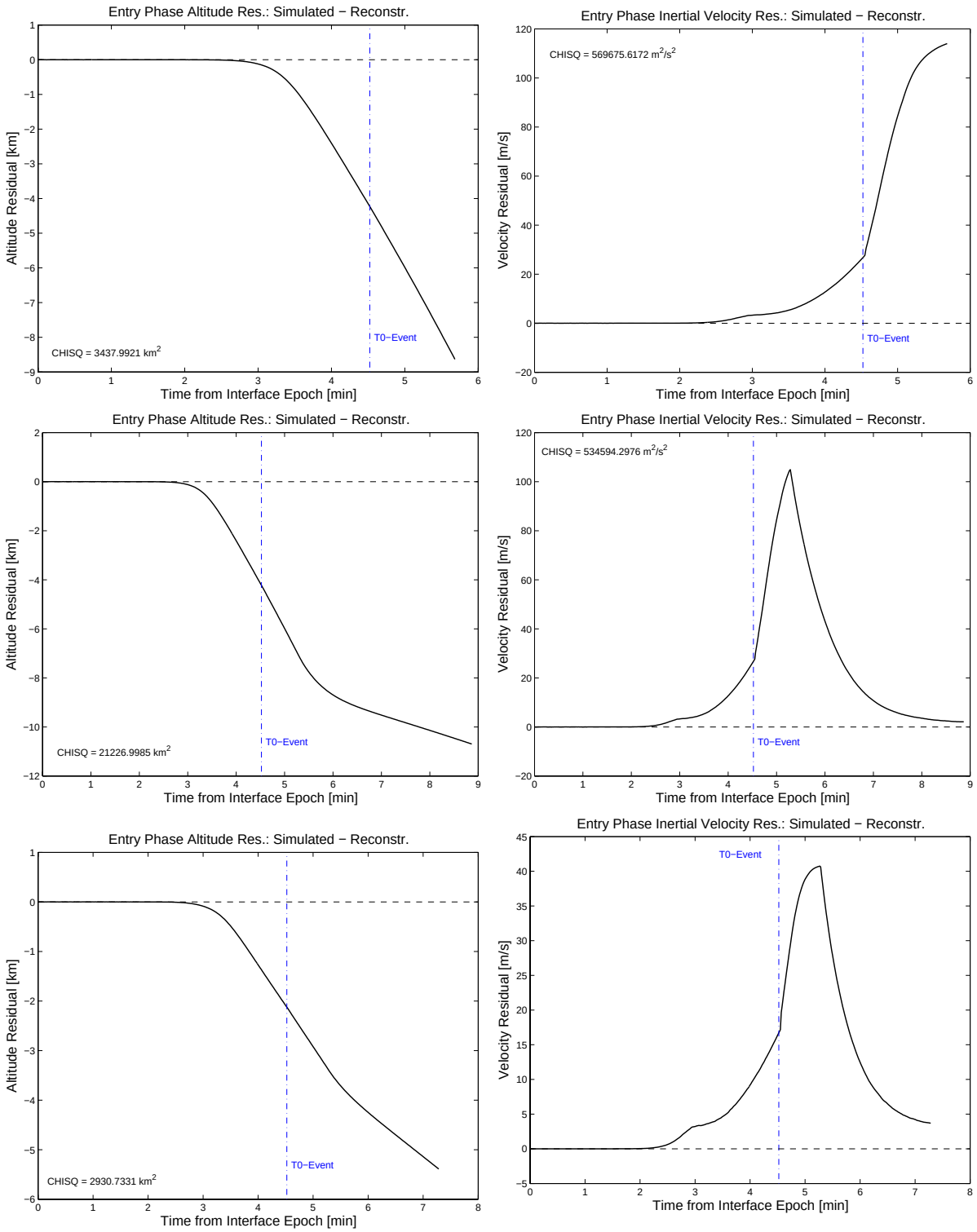

Figure 7.9: ***ETC4*** *(upper panels),* ***ETC4a*** *(middle panels), and* ***ETC4b*** *(lower panels) entry trajectory reconstruction results: the left panels show the altitude residuals and the right panels the inertial velocity residuals.*

The upper panels of Fig. 7.10 compare the mass profile ignoring the mass ablation effect (left panel) and using the ablation model (right panel) as provided by Eq. (3.4).

The middle panels compare the altitude (left) and descent speed (right) residuals simulating mass ablation (solid line) and ignoring the ablation effect (dashed line). One can see that the mass ablation has little effect on the reconstruction of the trajectory.

The lower panel of Fig. 7.10 shows the results of the upper atmosphere temperature reconstruction as residuals to the Y97 recommended atmosphere model, which was used for the computation of the HSDS. The dashed line shows the temperature residuals ignoring the mass ablation and the solid lines results using the ablation model. It can be seen that the change in mass due to ablation will mainly impact the reconstructed temperature profile in an altitude range of 160 to roughly 400 km (where the peak probe deceleration takes place) and can influence the temperature up to 3 K. The ablation simulation test case implies a higher temperature residual due to the fact that the HSDS did not take into account the effect of heat-shield mass ablation.

7.5 Entry Phase Error Results

Figure 7.11 shows the results of the altitude error calculation. The altitude error is composed of the error due to accelerometer uncertainties (upper left panel), gravitational force uncertainties (upper right panel), and initial conditions uncertainties derived from the propagation of the covariance matrix (lower right panel). The lower right panel shows the rss of all these error sources. One can see that the altitude error due to gravitational force increases steadily but remains very low even at the end of the entry phase ($\sim$1.2 m). The error contribution due to accelerometer measurement error is proportional to the range of measured acceleration. One can therefore see a steep increase in the time of peak deceleration. After the deceleration impulse this error remains constant. The maximum accelerometer error contribution is about 160 m. The highest error contribution comes from the uncertainty of the initial conditions. The initial altitude error at 1270 km is $\sim$86.5 km and decreases to about 84 km at the end of the integration interval.

Fig. 7.12 shows the longitude (left panel) and latitude (right panel) errors that result from the propagation of the covariance matrix. The initial longitude and latitude errors at 1270 km are 0.7 and 0.4 deg respectively. Both errors increase and reach values of respectively 1.1 and 0.6 deg at T_0.

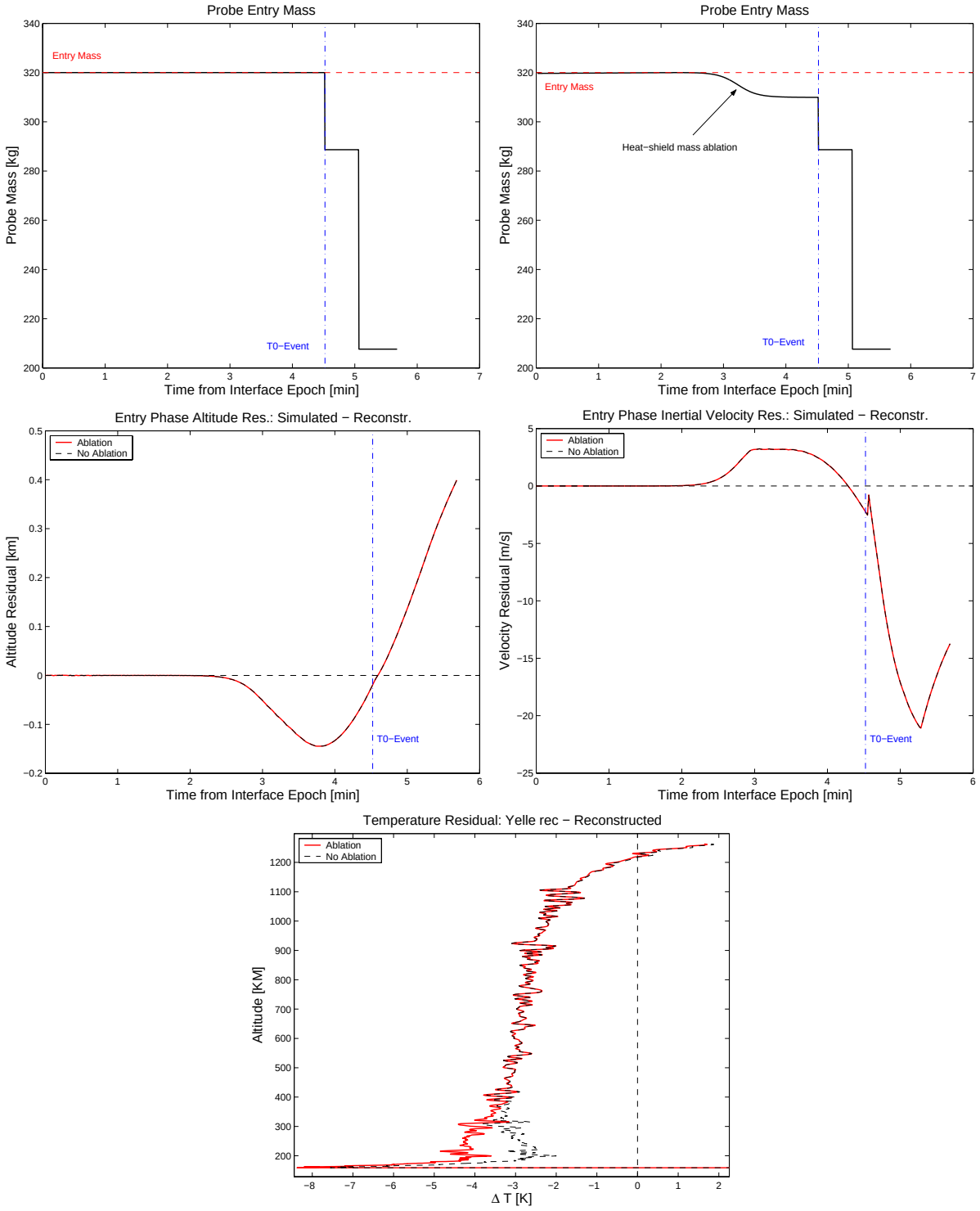

Figure 7.10: *Comparison of entry phase reconstruction using a constant heat-shield mass (left panel) and one that decreases due to heat-shield mass ablation (right panel). Upper panels: probe mass development. The first jump at T_0 is due to the Back Cover release, the second jump is due to the jettison of the heat-shield (FRSS). The middle panels show that the heat-shield mass ablation has no impact on the altitude and descent speed residuals. The lower panel shows the impact on the temperature profile as residuals from the Y97 model. The residuals for the ablation mass simulation are higher as a constant entry mass was used for the computation of the HSDS.*

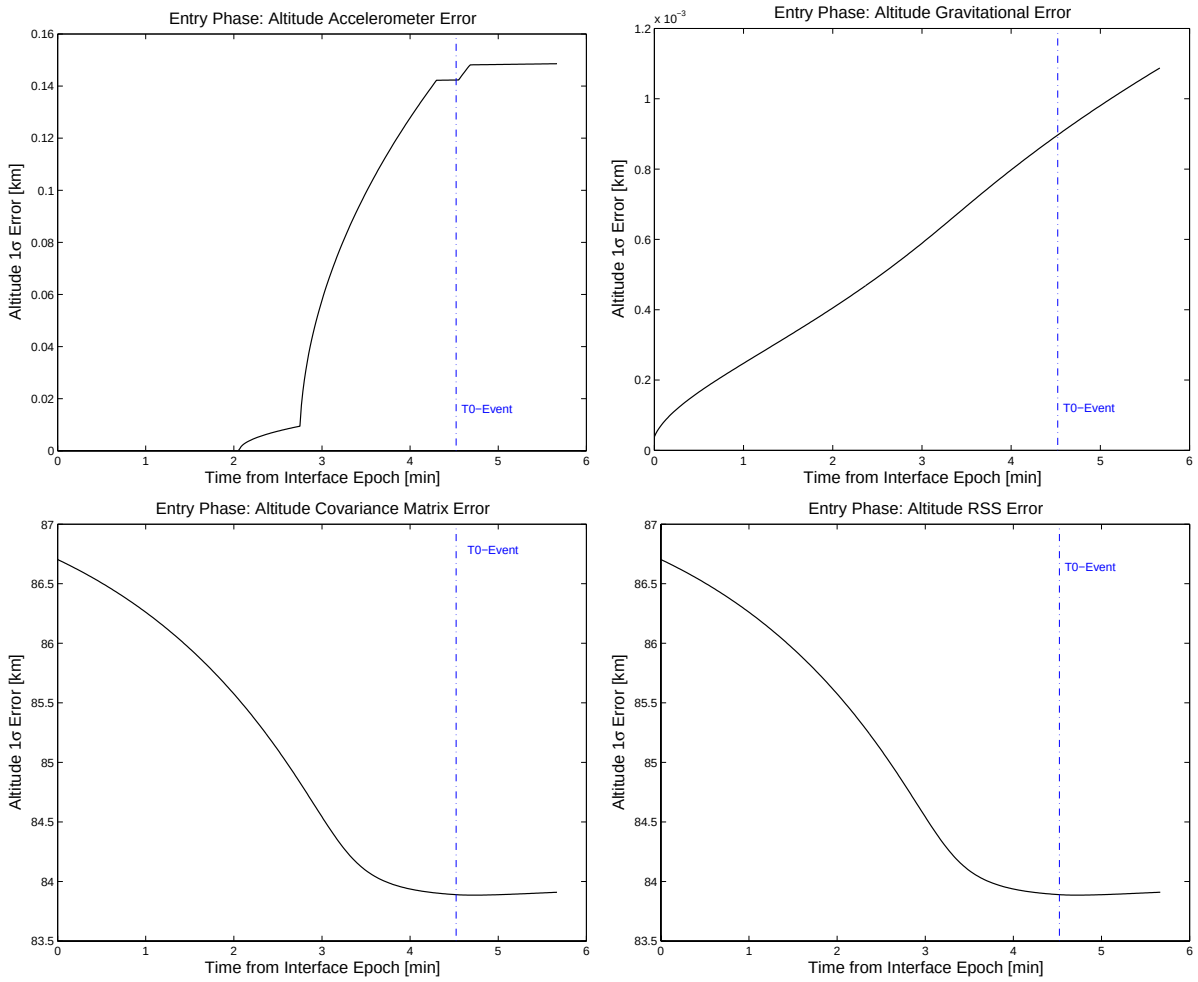

Figure 7.11: *Entry phase altitude 1σ errors: Upper left panel: error contribution from accelerometer error; Upper right panel: error contribution from gravitational force error; Lower left panel: error from covariance matrix propagation; Lower right panel: rss of the three error sources.*

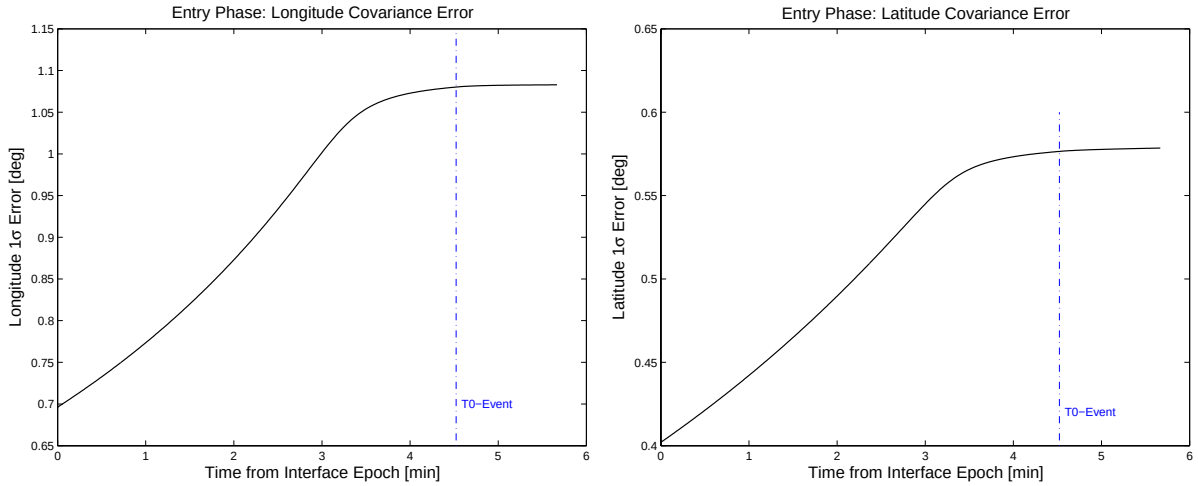

Figure 7.12: *Entry phase longitude and latitude 1σ errors resulting from the propagation of the covariance matrix.*

Chapter 8

Descent Phase Reconstruction

The probe entry phase reconstruction is based primarily on the measurements of the aerodynamic accelerations by the HASI science and the probe engineering accelerometers. Once the parachute sequence starts the accelerations will still be measured but are very likely to be affected by oscillatory motions and swing of the probe parachute system, which will make them inaccurate for the reconstruction of the trajectory. During the descent phase however all the science instruments are sampling data and provide alternative measurements to reconstruct this portion of the trajectory.

In Sec. 8.1 the instruments that will provide data for the descent phase reconstruction are summarized. In the subsequent Sec. 8.2–8.4 the mathematical equations and methodology of the reconstruction effort are provided, and in Sec. 8.5 the descent phase error analysis is outlined.

8.1 Instrument Data for the Descent Phase

HASI Pressure and Temperature Data

The Huygens Atmospheric Structure Instrument (HASI) (Fulchignoni *et al.*, 2002) onboard Huygens is equipped with a dedicated pressure sensor (the *Pressure Profile Instrument*) and two (TEM1 and TEM2) dual-element (Fine and Coarse) platinum resistance thermometers, which will start to sample pressure and temperature measurements at $T_0 + 9.625$ sec. This corresponds to an altitude of $\sim$154.5 km for the nominal descent profile (see lower panel of Fig. 5.1). Note that the heat shield is released at $T_0 + 32.5$ seconds, i.e., an altitude of 152.9 km. Both temperature and pressure measurements need to be corrected for dynamic effects due to the probe velocity. Considering a perfect adiabatic gas one can write the conservation of energy in the form

$$dh + d\left(\frac{v_{rel}^2}{2}\right) = 0 \tag{8.1}$$

where h is the specific enthalpy (i.e., the enthalpy per gas particle) defined as

$$h = \frac{c_s^2}{\gamma - 1} \tag{8.2}$$

c_s is the speed of sound and v_{rel} the flow velocity of the gas. $\gamma = c_p/c_v$ is the ratio of specific heats. Integrating Eq. (8.1) one gets

$$h + \frac{v_{rel}^2}{2} = const \tag{8.3}$$

Taking into account Eq. (8.2) one can write

$$\frac{c_s^2}{\gamma - 1} + \frac{v_{rel}^2}{2} = \frac{c_{s,0}^2}{\gamma - 1} \tag{8.4}$$

and with the definition of the Mach number $Ma = v_{rel}/c_s$ one obtains

$$c_s^2 \left(1 + \frac{\gamma - 1}{2} Ma\right) = c_{s,0}^2 \tag{8.5}$$

where c_s and $c_{s,0}$ are the speed of sound of the moving air (around the probe) and the static air (at the stagnation point) respectively. It is important to note that the temperature and pressure will be measured at the stagnation point and one can therefore write

$$\begin{aligned} c_{s,0}^2 &= \frac{\gamma R}{\mu} T_{\text{meas}} \\ c_s^2 &= \frac{\gamma R}{\mu} T_{\text{stat}} \end{aligned} \tag{8.6}$$

where T_{meas} is the measured temperature value and T_{stat} the corrected one. Substituting Eq. (8.6) into Eq. (8.4) one finally gets (see also Gaborit, 2004a)

$$T_{\text{stat}} = T_{\text{meas}} \left(1 + \frac{K(\gamma - 1)}{2} Ma^2\right)^{-1} \tag{8.7}$$

where K is the so-called recovery factor that defines the fraction of the flow kinetic energy that is converted into heat and results in heating of the measurement sensor and therefore a higher measured temperature. Note that the remaining kinetic energy is also converted into heat but is conducted outward through the sensor boundary layer. K is a sensor design specific value and needs to be known from preflight measurements. For HASI K is assumed to have the value of 1. Using the adiabatic gas equation one can derive the dynamic corrections for the pressure measurements according to

$$\frac{P_{\text{stat}}}{P_{\text{meas}}} = \left(\frac{T_{\text{stat}}}{T_{\text{meas}}}\right)^{\frac{\gamma}{\gamma - 1}} \tag{8.8}$$

where again P_{meas} and P_{stat} define the pressure values at the stagnation point (where they are actually measured by the pressure sensor) and the flow field. Using Eq. (8.7) one can rewrite Eq. (8.8) as

$$P_{\text{stat}} = P_{\text{meas}} \left(1 + \frac{\gamma - 1}{2} Ma^2\right)^{\frac{\gamma}{1 - \gamma}} . \tag{8.9}$$

One can easily see that similar to the temperature measurement the actual pressure will be lower than the measured one. The lower panels of Fig. 5.1 show the (simulated) probe

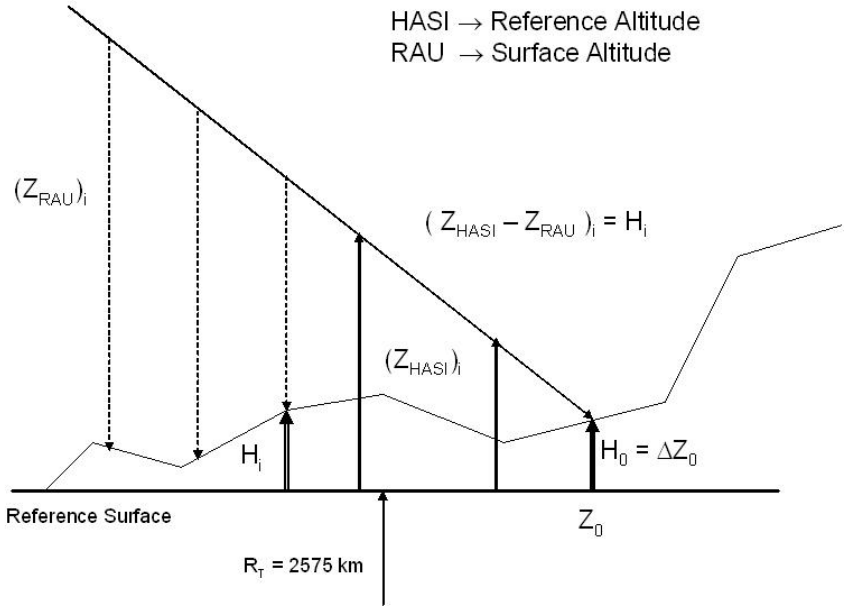

Figure 8.1: *Measurements of the Radar Altimeter Units.*

Mach profile for the entire descent phase. Note that T_0 is initiated at a supersonic probe speed of $Ma \sim 1.4$ whereas the HASI pressure and temperature sampling starts at a subsonic speed of $Ma \sim 0.5$.

GCMS Measurements of the Atmosphere Composition

The conversion process of the measured pressure and temperature data into altitude and descent speed [see Eq. (8.17-8.19)] as well as the dynamic pressure and temperature correction process [Eqs. (8.7) and (8.9)] require the knowledge of the molecular mass μ and the mole fractions of the various atmospheric constituents. The mole fractions of the major constituents will be obtained from measurements by GCMS, which will operate during the entire descent phase. The mean molecular mass of the gas mixture μ can then be derived from

$$\mu = \sum_i f_i \, \mu_i \tag{8.10}$$

where f_i and μ_i are the mole fraction and molecular weight of the ith atmospheric constituent.

SSP Speed of Sound and Impact Measurements

The Acoustic Properties Instrument (API) is part of the Surface Science Package (SSP) and consists of two units, API-V and API-S, which provide measurements of the speed of sound below altitudes of ∼46 km and altitude soundings below altitudes of ∼ 400 m respectively. Furthermore SSP provides an accelerometer (i.e., ACC-I) which is able to measure much higher g-loads than the Huygens Atmospheric Structure Instrument (HASI) accelerometers as it was specifically designed to survive and measure the probe

impact pulse. The deceleration profile of the impact can be used to pin down the impact epoch.

DWE Measurements

The Doppler Wind Experiment (DWE) will initiate the measurements of the zonal wind speed once the probe/orbiter communication link has been established. This is scheduled to start at $T_0 + 45.5$ seconds, which corresponds to an altitude of ∼151.8 km. The zonal wind speed measurement determine the probe longitude drift starting from the initial starting value which can be derived from the probe entry phase reconstruction.

Radar Altimeter Unit Measurements

The two Radar Altimeter Units (RAU) will provide the surface altitude in the final portion of the descent phase (∼20 km downwards). Combining the RAU altitude measurements with the reconstructed HASI descent trajectory provides the altitude profile of the topography (see left panel of Fig. 8.1)

$$H_i = (z_{\mathrm{HASI}} - z_{\mathrm{RAU}}) \tag{8.11}$$

where H_i designates the topography altitude (relative to the 2575 km reference sphere) at the measurement epoch t_i. Note that the knowledge of the surface topography close to the impact point would give an estimation of the starting altitude error uncertainty Δz_0 in the reverse reconstruction mode.

DISR Measurements

The Descent Imager and Spectral Radiometer will provide a set of measurements in the form of imaging sequences, which will be processed by the PI team in a dedicated effort to yield altitude, descent speed, and probe position. The results of this effort will serve as a cross-check of the reconstructed DTWG trajectory. Furthermore DISR will measure the Solar Zenith Angle (SZA), which is defined as the separation angle between the local probe vertical and the Sun position vector.The SZA will help to constrain the probe longitude and longitude drift.

8.2 Altitude and Descent Speed Reconstruction

The conversion from measured atmospheric pressure P and temperature T into altitude z and descent speed v_{desc} is based on two fundamental physical principles, the law of hydrostatic equilibrium,

$$dP = -g\,\rho\,dz \tag{8.12}$$

and the equation of state for a real gas (see Sec. 4.6 for detailed derivation)

$$\frac{P\,\mu}{\rho\,R\,T} = \zeta \tag{8.13}$$

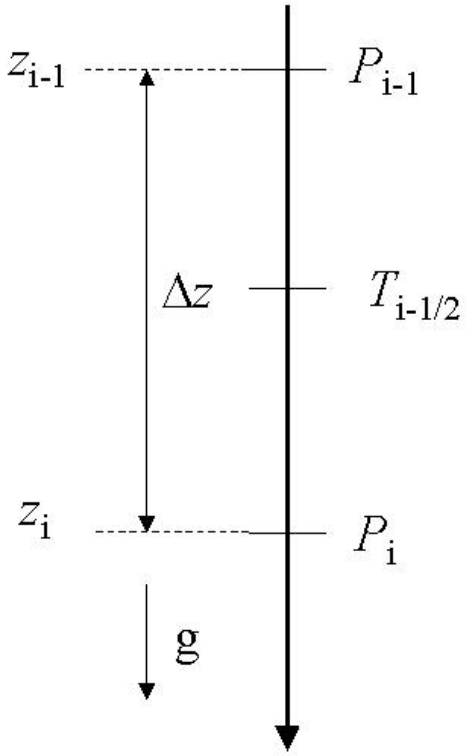

Figure 8.2: *Derivation of the descent altitude and speed from the measured atmospheric pressure gradient and temperature.*

where dP is the incremental change in atmospheric pressure, g is the local acceleration of gravity, ρ is the atmospheric pressure density, dz is a small change in altitude (i.e., radial position), R is the universal gas constant (8314.3 J/kmol/K), μ is the mean molecular mass (kg/kilomole), T is the temperature, and ζ is the compressibility factor that takes into account the deviation of the gas behavior from an ideal gas. Dividing Eq. (8.12) by an incremental time dt, a relationship between the time rate of change in altitude and the time rate of change in pressure results

$$\frac{dP}{dt} = -g\,\rho\,\frac{dz}{dt} \tag{8.14}$$

Writing Eq. (8.13) in terms of density ρ and substituting into Eq. (8.14) provides an expression for the descent velocity

$$v_{\text{desc}} = \frac{dz}{dt} = -\frac{1}{g}\,\frac{R\,T\,\zeta}{\mu}\,\frac{1}{P}\,\frac{dP}{dt} \tag{8.15}$$

Multiplying Eq. (8.15) by dt and integrating on both sides yields

$$\int_{z_{i-1}}^{z_i} dz = -\frac{1}{g}\,\frac{R\,T\,\zeta}{\mu}\,\int_{P_{i-1}}^{P_i}\,\frac{1}{P}\,dP \tag{8.16}$$

and finally

$$\boxed{\Delta z = (z_i - z_{i-1}) = -\frac{1}{g}\,\frac{R\,T_{i-1/2}\,\zeta}{\mu}\,\ln\left(\frac{P_i}{P_{i-1}}\right)} \tag{8.17}$$

The temperature value is considered to be constant in the altitude interval Δz and taken as the mean value, i.e., $T_{i-1/2} = \frac{1}{2}(T_i + T_{i-1})$. If the speed of sound c_s is directly measured one can also use the relation

$$c_s = \sqrt{\frac{\gamma\, R\, T}{\mu}} \tag{8.18}$$

to rewrite Eq. (8.17) in the form

$$\boxed{\Delta z = (z_i - z_{i-1}) = -\frac{1}{g}\,\frac{c_s^2\,\zeta}{\gamma}\,\ln\left(\frac{P_i}{P_{i-1}}\right)} \tag{8.19}$$

where γ is the ratio of specific heats, which needs to be calculated for the given gas mixture according to

$$\gamma = \frac{c_p}{c_v} = \frac{\sum_k\, f_k\, c_{p,k}}{\sum_k\, f_k\, c_{v,k}} \tag{8.20}$$

where f_k is the mole fraction of the kth gas component with the corresponding specific heats $c_{p,k}$ and $c_{v,k}$. Starting from an initial altitude z_0 the final altitude can be derived by simple addition of all the altitude intervals Δz

$$z_i = z_0 + \sum_i \Delta z_{i-1} \tag{8.21}$$

Note that for a positive pressure gradient (i.e., $P_i > P_{i-1}$), Δz will be negative according to Eq. (8.17) and the probe is descending. For a negative pressure gradient (i.e., $P_i > P_{i-1}$), Δz is positive and the probe is ascending. Assuming a constant descent velocity for the descent interval Δz the descent velocity can be approximated from Eq. (8.15)

$$v_{\text{desc}} \approx \frac{\Delta z}{\Delta t} \tag{8.22}$$

8.3 Longitude Drift Reconstruction

DWE Zonal Wind Speed Measurements

Equations (8.17) and (8.22) provide only the probe altitude and descent speed. The deviation from the initial probe longitude φ_0 at the beginning of the descent phase due the zonal wind speed can be derived from the following relation

$$v_{\text{drift}}(t_i) = \omega\,(R_T + z_i)\,\cos\lambda_0 = \dot{\varphi}\,(R_T + z_i)\,\cos\lambda_0 \tag{8.23}$$

where v_{drift} is the probe drift due to zonal wind, ω the rotation velocity (i.e., the time derivative of the longitude coordinate φ), R_T the radius of the planet, λ_0 the probe initial latitude, and z_i again the probe altitude above the reference surface at epoch t_i. For the time interval $\Delta t \equiv t_i - t_{i-1}$ one can approximate the longitude drift as

$$\dot{\varphi} = \frac{d\varphi}{dt} \approx \frac{\Delta\varphi_i}{\Delta t} = \frac{\varphi_i - \varphi_{i-1}}{\Delta t} = \frac{v_{\text{drift}}}{(R_T + z_i)\,\cos\lambda_0} \tag{8.24}$$

Rewriting Eq. (8.24) yields

$$\Delta\varphi_i = \frac{v_{\text{drift}}}{(R_T + z_i)\,\cos\lambda_0}\,\Delta t \tag{8.25}$$

Starting from the initial longitude φ_0 at the epoch t_0 the integration of Eq. (8.25) provides the final longitude φ_f at epoch t_f from

$$\varphi_f(t_f) = \varphi_0 + \sum_{i=0}^{t_f} \Delta\varphi_i \Delta t_i \tag{8.26}$$

DISR Solar Zenith Angle Measurements

The reconstruction of the probe longitude drift from the measured DISR Solar Zenith Angle (SZA) requires the knowledge of the sub-solar longitude and latitude coordinates Λ_S and δ_S. The probe (planetographic) west longitude Φ can the be derived from (Allison *et al.*, 2004)

$$\Phi = \Lambda_S - H_S \tag{8.27}$$

with H_S given by

$$\cos H_S = \frac{\cos \text{SZA} - \sin\Theta\,\sin\delta_S}{\cos\Theta\,\cos\delta_S} \tag{8.28}$$

where Θ is the probe (planetographic) latitude, which can be considered as constant during the entire probe descent phase.

8.4 Reconstruction Strategies

Forward and Reverse Mode

The reconstruction of the probe descent phase requires the specification of an initial altitude z_0 and the corresponding 1σ uncertainty Δz_0. The altitude reconstruction from pressure and temperature measurements requires the specification of an initial altitude value z_0 in Eq. (8.21), which can be estimated using the results of the entry phase reconstruction. A possible way to decrease the initial uncertainty is to start the reconstruction from the surface integrating upwards assuming z_0=0 and an error Δz_0, which represents the topography elevation at the impact site. The time of impact will be measured very accurately from both the HASI and the SSP accelerometers. The algorithm was therefore implemented with the capability to perform the descent phase reconstruction in the so called "reverse" mode, which starts at the surface and ends at the first measurement of the HASI atmosphere measurements.

Dynamic Corrections Mode

It is important to note that the dynamic correction process of both temperature and pressure measurements require the knowledge of the Mach number [see Eq. (8.9) and (8.7)]. The Mach number itself however depends on the descent speed of the probe,

which is an output of the reconstruction process itself. The dynamic sensor correction is therefore an iterative process that starts using uncorrected measurements to provide a first estimation of the descent speed.

Pressure and Speed of Sound Mode

The reconstruction of the altitude and descent speed can be done either from the measured HASI pressure and temperature data or from the HASI pressure data combined with the SSP speed of sound measurements. Note that the speed of sound profile will only cover the final portion of the descent (∼50 km down to the surface). The two different reconstruction strategies are referred to as *Pressure Mode* and *Speed of Sound Mode* respectively.

8.5 Descent Phase Error Analysis

Assuming a variable z is calculated from a set of measurements x_i, i.e., $z = f(x_i)$ with $(i = 1..N)$, and each of these independent measurements is affected by an error $\sigma(x_i)$, then $\sigma(z)$ is given by the law of error propagation

$$\sigma^2(z) = \sum_{i=1}^{N} \left(\frac{\partial f}{\partial x_i} \right)^2 \sigma^2(x_i) \tag{8.29}$$

Altitude and Descent Speed Error

The altitude z is determined via a simple addition of the altitude intervals Δz [see Eqs. (8.17-8.21)]. If the error of each altitude interval $\sigma(\Delta z_i)$ at every reconstruction step Δt_i can be considered to be independent and therefore uncorrelated, the altitude error at the time t_i can be calculated in a root-sum-square fashion from

$$\sigma(z_i)^2 = \sum_{i=1}^{N-1} \sigma(\Delta z_i)^2 + \sigma(z_0)^2 \tag{8.30}$$

where $\sigma(z_0)$ is the error of the initial altitude z_0. If the altitude and descent speed is derived from pressure and temperature data according to Eq. (8.17) then the error of Δz_i can be determined by

$$\sigma^2\left(\Delta z_i\right) = \left(\frac{\partial \Delta z_i}{\partial T} \right)^2 \sigma^2(T) + 2 \left(\frac{\partial \Delta z_i}{\partial P_i} \right)^2 \sigma^2(P_i) + \left(\frac{\partial \Delta z_i}{\partial g} \right)^2 \sigma^2(g) + \left(\frac{\partial \Delta z_i}{\partial \mu} \right)^2 \sigma^2(\mu) \tag{8.31}$$

with

$$\begin{aligned} \frac{\partial \Delta z_i}{\partial T} &= -\frac{R\,\zeta}{\mu\,g} \ln\left(\frac{P_i}{P_{i-1}} \right) \\ \frac{\partial \Delta z_i}{\partial P_i} &= -\frac{R\,T\,\zeta}{\mu\,g} \frac{1}{P_i} \end{aligned}$$

$$\begin{aligned} \frac{\partial \Delta z_i}{\partial g} &= \frac{R\,T\,\zeta}{\mu\,g^2}\,\ln\left(\frac{P_i}{P_{i-1}}\right) \\ \frac{\partial \Delta z_i}{\partial \mu} &= \frac{R\,T\,\zeta}{\mu^2\,g}\,\ln\left(\frac{P_i}{P_{i-1}}\right) \end{aligned} \tag{8.32}$$

If the altitude and descent speed are derived from pressure and speed of sound measurements, then the error of Δz_i is determined by

$$\sigma^2\left(\Delta z_i\right) = \left(\frac{\partial \Delta z_i}{\partial c_s}\right)^2 \sigma^2(c_s) + 2\left(\frac{\partial \Delta z_i}{\partial P_i}\right)\sigma^2(P_i) + \left(\frac{\partial \Delta z_i}{\partial g}\right)^2 \sigma^2(g) \tag{8.33}$$

with

$$\begin{aligned} \frac{\partial \Delta z_i}{\partial c_s} &= -\frac{2\,c_s\,\zeta}{\gamma\,g}\,\ln\left(\frac{P_i}{P_{i-1}}\right) \\ \frac{\partial \Delta z_i}{\partial P_i} &= -\frac{c_s^2\,\zeta}{g\,\gamma}\,\frac{1}{P_i} \\ \frac{\partial \Delta z_i}{\partial g} &= \frac{c_s^2\,\zeta}{\gamma\,g^2}\,\ln\left(\frac{P_i}{P_{i-1}}\right) \end{aligned}$$

Note that the error of the compressibility factor ζ, the universal gas constant R, and the ratio of specific heats γ was neglected. With the simplified calculation of the gravitational constant g using the relation

$$g = \frac{GM}{r^2}\,, \tag{8.34}$$

where $r = (z + R_T)$ is the distance of the probe from the planet center and R_T the radius of Titan, $\sigma(g)$ can be calculated by

$$\sigma(g) = \frac{1}{r^2}\left(\sigma^2(GM) + \frac{4\,GM^2}{r^2}\,\sigma^2(r)\right)^{1/2} \tag{8.35}$$

with $\sigma^2(r) = \sigma^2(z) + \sigma^2(R_T)$. As a sufficient approximation, $\sigma(z)$ can be used from the previous iteration step. The descent velocity can be calculated by dividing Eq. (8.17) through the time step Δt_i

$$v_{\mathrm{desc}} = \frac{\Delta z_i}{\Delta t_i}\,. \tag{8.36}$$

Neglecting the measurement error in Δt_i the corresponding error $\sigma(v_{\mathrm{desc}})$ can be obtained by

$$\sigma(v_{\mathrm{desc}}) = \frac{\sigma(\Delta z_i)}{\Delta t} \tag{8.37}$$

Longitude Drift Error (DWE)

The error propagation for the longitude φ_i can be derived from Eq. (8.26) according to the law of error propagation

$$\sigma(\varphi_i)^2 = \sigma(\varphi_0)^2 + \sum_i \sigma(\Delta\,\varphi_i)^2 \tag{8.38}$$

Assuming no error in the time interval Δt, $\sigma(\Delta\varphi_i)$ can be calculated according to

$$\sigma(\Delta\varphi_i) = \left(\frac{\partial\Delta\varphi_i}{\partial\dot{\varphi}_i}\right)\,\sigma(\dot{\varphi}_i) = \sigma(\dot{\varphi}_i)\,\Delta t \tag{8.39}$$

with

$$\sigma^2(\dot{\varphi}_i) = \left(\frac{\partial\dot{\varphi}_i}{\partial v_{\text{drift}}}\right)^2 \sigma^2(v_{\text{drift}}) + \left(\frac{\partial\dot{\varphi}_i}{\partial z_i}\right)^2\,\sigma^2(z_i) + \left(\frac{\partial\dot{\varphi}}{\partial\lambda_0}\right)^2\,\sigma^2(\lambda_0)\ . \tag{8.40}$$

The partial derivatives in Eq. (8.40) are found to be

$$\begin{aligned}
\frac{\partial\dot{\varphi}_i}{v_{\text{drift}}} &= \frac{1}{(R_T + z_i)\,\cos\lambda_0} \\
\frac{\partial\dot{\varphi}_i}{\partial z_i} &= -\frac{v_{\text{drift}}}{(R_T + z_i)^2\,\cos\lambda_0} \\
\frac{\partial\dot{\varphi}_i}{\partial\lambda_0} &= \frac{v_{\text{drift}}\,\sin\lambda_0}{(R_T + z_i)\,\cos\lambda_0^2}
\end{aligned} \tag{8.41}$$

Longitude Drift Error (SZA)

For the derivation of the longitude drift error using the DISR SZA angle it is assumed that the subsolar longitude and latitude coordinates Λ_S and δ_S have no error. Applying the law of error propagation to Eq. (8.27) and Eq. (8.28), $\sigma^2(\Phi)$ can be found from

$$\sigma^2(\Phi) = \left(\frac{\partial H_S}{\partial\text{SZA}}\right)^2\,\sigma^2(\text{SZA}) + \left(\frac{\partial H_S}{\partial\Theta}\right)^2\,\sigma^2(\Theta) \tag{8.42}$$

with the partial derivatives given by

$$\begin{aligned}
\frac{\partial H_S}{\partial\text{SZA}} &= -(1-\cos H_S)^{-\frac{1}{2}}\,\frac{\sin\text{SZA}}{\cos\Theta\,\cos\delta_S} \\
\frac{\partial H_S}{\partial\Theta} &= (1-\cos H_S)^{-\frac{1}{2}}\,\frac{\tan\delta_S}{\cos\Theta^2}
\end{aligned} \tag{8.43}$$

Chapter 9

Descent Phase Test Cases

In the descent phase test case campaign the outlined reconstruction algorithm (see Chap. 8) is applied to the HSDS v1.5 simulated sensor output.

The sensor output from the various instruments relevant for the descent phase reconstruction are characterized by significant measurement noise, which decreases the quality of the reconstruction effort and in some cases makes it impossible. A data smoothing algorithm as introduced in Sec. 5.2 is therefore applied to smooth the input data before it is used in the reconstruction algorithm. The amount of smoothing is defined by the span, which defines the number of data points that are averaged to replace each measurement point. The higher this number the smoother the measurement profiles gets, but the tradeoff is the loss of measurement resolution and the potential danger to lose fine scale features of the profile. The right smoothing span therefore requires some experimentation in order to achieve the best trade-off. Table 9.1 provides an overview of the smoothing spans used for the various instrument sensors. Both the noise and the no noise instrument datasets were used in the test campaign, which provided the opportunity to assess the decrease in reconstruction quality due to instrument noise.

The test cases were grouped into three categories: 1) the reconstruction of the probe altitude and descent speed from the measurements of the physical properties of the atmosphere (Sec. 9.1); 2) the reconstruction of the probe longitude drift from wind and solar zenith angle measurements (Sec. 9.2); 3) the reconstruction of the probe elevation using radar altimeter and sounder measurements (Sec. 9.3).

9.1 Altitude and Descent Speed

Descent Test Case 0 (DTC0) is the simplest of the altitude and descent phase test cases with the various sensor combinations outlined in Table 9.2. It is the only test case in that campaign that uses the dynamically corrected HASI pressure and temperature data. It was therefore not necessary to apply the internal dynamical correction procedure. No speed of sound measurements from the SSP-APIV sensors are incorporated and the reconstruction is done according to Eq. (8.17). Fig. 9.1 shows the altitude (left panel) and descent velocity (right panel) residuals of the reconstruction effort. The reconstruction was done in *reverse mode* (starting from the surface with an initial altitude of 0 km at the measured impact time up to the first point of pressure and temperature measurement), which implies a constant increase in the altitude residual profile up to $\sim$0.75 km. Apart

Instrument Sensor	Smoothing Span
HASI-TEM (uncorr.)	71
HASI-TEM (corr.)	71
HASI-PPI (uncorr.)	151
HASI-PPI (corr.)	151
GCMS-N_2	101
GCMS-CH_4	101
GCMS-Ar	101
SSP-APIV	81
DWE	151
RAU-1	no smoothing
RAU-2	no smoothing

Table 9.1: *Overview of the applied smoothing spans [$2N + 1$ in Eq. (5.1)] for the moving average filtering algorithm (see Sec. 5.2). No smoothing was required for the RAU-1 and RAU-2 datasets.*

from the continuous increase the altitude residuals show oscillations with an amplitude of about 0.05 to 0.1 km. These oscillations can also be seen in the form of a zig-zag behavior with the same frequency as the oscillations in the altitude residuals. From the oscillation frequency one can derive the corresponding altitude step by multiplying with the corresponding velocity at the given altitude. With a decreasing descent velocity (from about 180 m/s down to only 5 m/s prior to impact) and an increasing oscillation frequency one gets more or less constant altitude steps on the order of 2 km. This corresponds very well to the altitude steps in the Y97 input data file, which was used for the computation of the HSDS v1.5 (M. Perez, private communication). One can therefore conclude that the oscillations in the altitude as well as the descent velocity residuals arise very likely from the limited accuracy of the input data and can therefore be considered as an artifact of the HSDS and not a malfunction of the reconstruction algorithm itself.

Fig. 9.2 shows the altitude and descent velocity residuals for DTC1, DTC2, and DTC3. Note that the same oscillations and zig-zag can be observed in all three test case results.

DTC1 uses the exact same sensor combination as DTC0 but is based upon pressure and temperature input data that have not been corrected for dynamic effects. Furthermore DTC1 did not apply any sensor correction algorithm. The reconstruction results are shown in the upper panels of Fig. 9.2. As the dynamic effects on sensors are proportional to the descent velocity one can observe high residuals at the beginning of the descent and at about 20 minutes past interface epoch when the main parachute is released[1]. The altitude residuals at the beginning of the descent phase reconstruction go up to 20 km. The main parachute release can also be seen in the descent velocity residuals as a sudden jump in the residuals up to about 30 m/s. At the beginning of the descent phase the descent residuals go up to 1300 m/s. Both the altitude and descent velocity residuals are extremely high, which makes the need for a dynamic sensor correction evident.

[1]The release of a parachute produces a sudden increase in descent velocity up to the time the chute is released and fully inflated.

Test Case	TEM (UC)	TEM (C)	PPI (UC)	PPI (C)	MF.	APIV	IMPACT	Noise	DC.
DTC0	No	Yes	No	Yes	Yes	No	Yes	No	No
DTC1	Yes	No	Yes	No	Yes	No	Yes	No	No
DTC1_N	Yes	No	Yes	No	Yes	No	Yes	Yes	No
DTC2	Yes	No	Yes	No	Yes	No	Yes	No	Yes
DTC2_N	Yes	No	Yes	No	Yes	No	Yes	Yes	Yes
DTC3	No	No	Yes	No	No	Yes	Yes	No	Yes
DTC3_N	No	No	Yes	No	No	Yes	Yes	Yes	Yes

Table 9.2: *Summary of test cases for the probe descent phase altitude and descent speed. Sensors: TEM = HASI temperature, PPI = HASI pressure, (UC)=uncorrected, (C)=corrected, MF. = GCMS mole fractions, APIV = SSP speed of sound, IMPACT = probe impact time from HASI or SSP accelerometer (in the HSDS v1.5 both the SSP and the HASI impact time measurements are identical), DC = dynamic sensor correction; note that for the noise cases a data smoothing algorithm according to Table 9.1 has been applied.*

The dynamic sensor corrections are applied in DTC2 (see middle panels of Fig. 9.2) for both the pressure and the temperature input data according to Eq. (8.7) and Eq. (8.9). This clearly decreases the residuals at the beginning of the descent (from more than 20 km down to 13 km for the reconstructed altitude and from 1300 m/s down to 100 m/s for the descent speed) but still implies a fairly high deviation from the actual trajectory. The peak at the time of the main parachute release is comparable to DTC1, which implies that the dynamic sensor correction algorithm was not effective during this period. One can see that the dynamic flow during period of high relative flow velocity introduces a systematic error that cannot very effectively be removed. This has to be taken into account in the interpretation of the reconstructed descent trajectory.

In DTC3 the SSP-APIV sensor (speed of sound measurements) is used, which can replace the HASI temperature measurement in the lower part of the descent.[2] The trajectory reconstruction is then performed according to Eq. (8.19). The DTC3 results are shown in the lower panels of Fig. 9.2 with the crossing of the 100 mbar threshold indicated by the dashed vertical line. As the no noise versions of the HSDS was used for DTC1–3 one can see no difference (as expected) between DTC3 and DTC2, which is a clear indication that the the reconstruction procedure according to Eq. (8.19) was correctly implemented.

DTC1_N, DTC2_N, and DTC3_N have the exact same sensor combination as DTC1, DTC2, and DTC3 respectively, but are based on the noisy version of the HSDS. A moving average smoothing filter was applied to the input data with the corresponding smoothing spans given in Table 9.1. Comparing Fig. 9.3 to Fig. 9.2 it can be seen that even after the smoothing of the input data the remaining noise has a clear impact on the reconstruction quality. The maximum altitude residual increases from 20 km to more than 50 km for DTC1_N and from 13 km to more than 35 km for DTC2_N and DTC3_N. It can be

[2]SSP-APIV will measure the speed of sound only at atmospheric pressures higher than 100 mbar. In the HSDS trajectory the 100 mbar threshold is reached at about 50 minutes past interface epoch which corresponds to an altitude of ∼175 km (see Sec. 5.1).

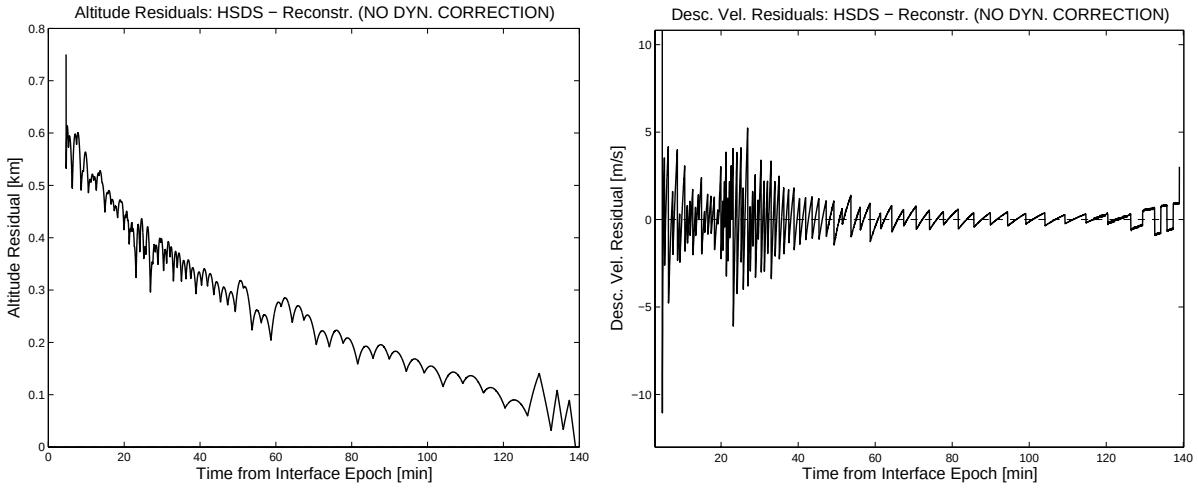

Figure 9.1: ***DTC0:*** *Left panel: altitude residuals (i.e., HSDS simulated trajectory minus reconstructed one); Right panel: descent velocity residuals .*

seen that the descent velocities are very sensitive to both the oscillations in the altitude residuals which are due to the interpolation error from the Y97 atmosphere input tables (see discussion in DTC0) and the oscillations in the input data that is related to the remaining measurement noise after the smoothing procedure.

The final portion in this section deals with the evaluation of the altitude and descent speed error according to Eq. (8.31) and Eq. (8.33). In both relations the pressure errors $\sigma(P_i)$ are taken into account even if the altitude and descent speed are calculated from the ratio of two subsequent pressure measurements. This is due to the fact that even if any systematic error would cancel out in the derivation of each altitude step Δz_i this would not necessarily hold for random errors. It has be taken into account that random errors (in theory) can change in any time interval Δt no matter how short it is. However, the pressure measurements in the noise test cases are treated with a moving average filter with a span of 151 data points (i.e., 151 subsequent measurement values are averaged to replace one data point). For a PPI sampling rate of 2/2.3 Hz, 151 data points correspond to a time span of about 131 seconds. The time step dt of the descent reconstruction algorithm [Eq. (8.15)] is only 1 second and therefore a lot shorter than the smoothing time span. One can therefore consider the pressure error as being constant in the time interval dt and neglect it in the error propagation evaluation.

Fig. 9.4 shows the error propagation for the altitude (left) and descent speed (right) profile for DTC2_N and DTC3_N. A continuous increase in both the altitude and the descent velocity errors (which are derived from the altitude increments) can be seen. The altitude error reaches its maximum value of about 15 km at the end of the reconstruction effort (which corresponds to the start of the descent phase due to the reverse reconstruction mode). The descent speed errors reach a very high value of more than 400 m/s and show very strong oscillations. Keeping in mind that the DTC2_N and DTC3_N test cases differ solely with respect to the use of the SSP speed of sound data below the 100 mbar threshold it is very interesting to note that no major difference in the error propagation profiles can be seen. According to this result it could be concluded that the SSP speed of sound

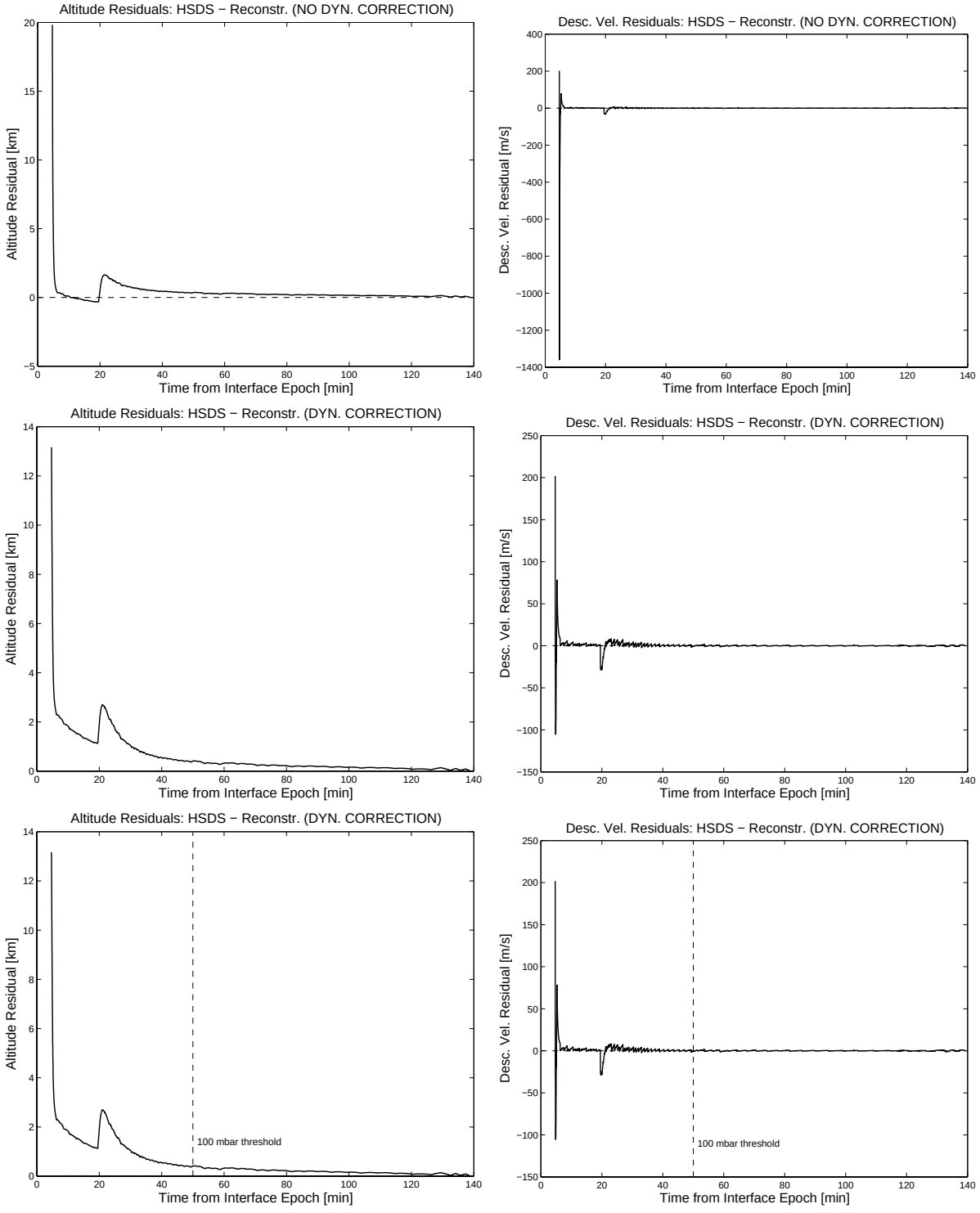

Figure 9.2: ***DTC1*** *(upper panels),* ***DTC2*** *(middle panel), and* ***DTC3*** *(lower panel) results. The left panels show the altitude residuals (i.e., HSDS simulated trajectory minus reconstructed one) and the right panels the residuals in descent velocity. DTC1 did not apply the dynamic sensor correction procedure that was applied in DTC2 and DTC3.*

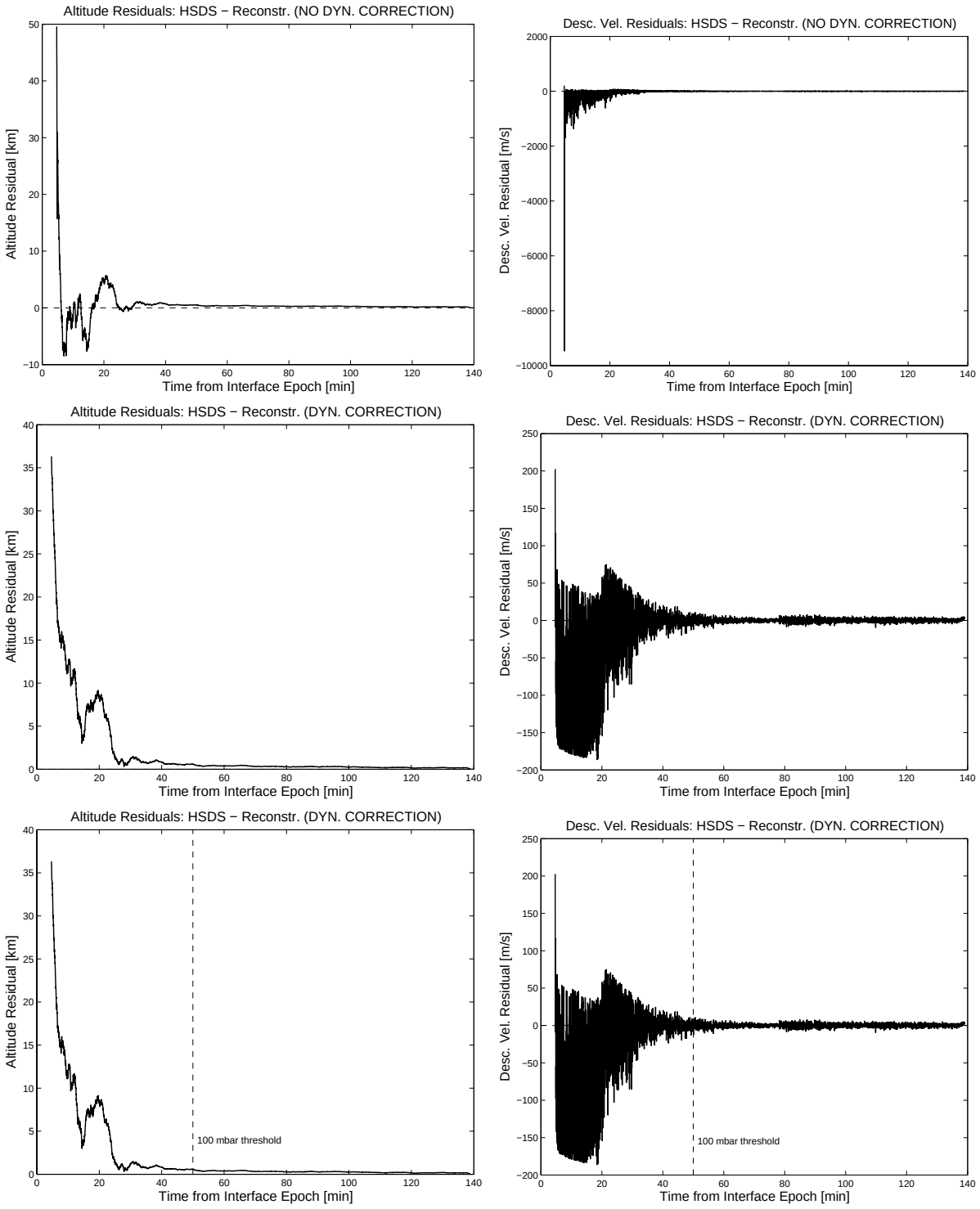

Figure 9.3: ***DTC1_N*** *(upper panels),* ***DTC2_N*** *(middle panels), and* ***DTC3_N*** *(lower panels) results. The left panels show the altitude residuals (i.e., HSDS simulated trajectory minus reconstructed one) and the right panels the residuals in descent velocity. DTC1 is the only test case that did not apply dynamic sensor corrections.*

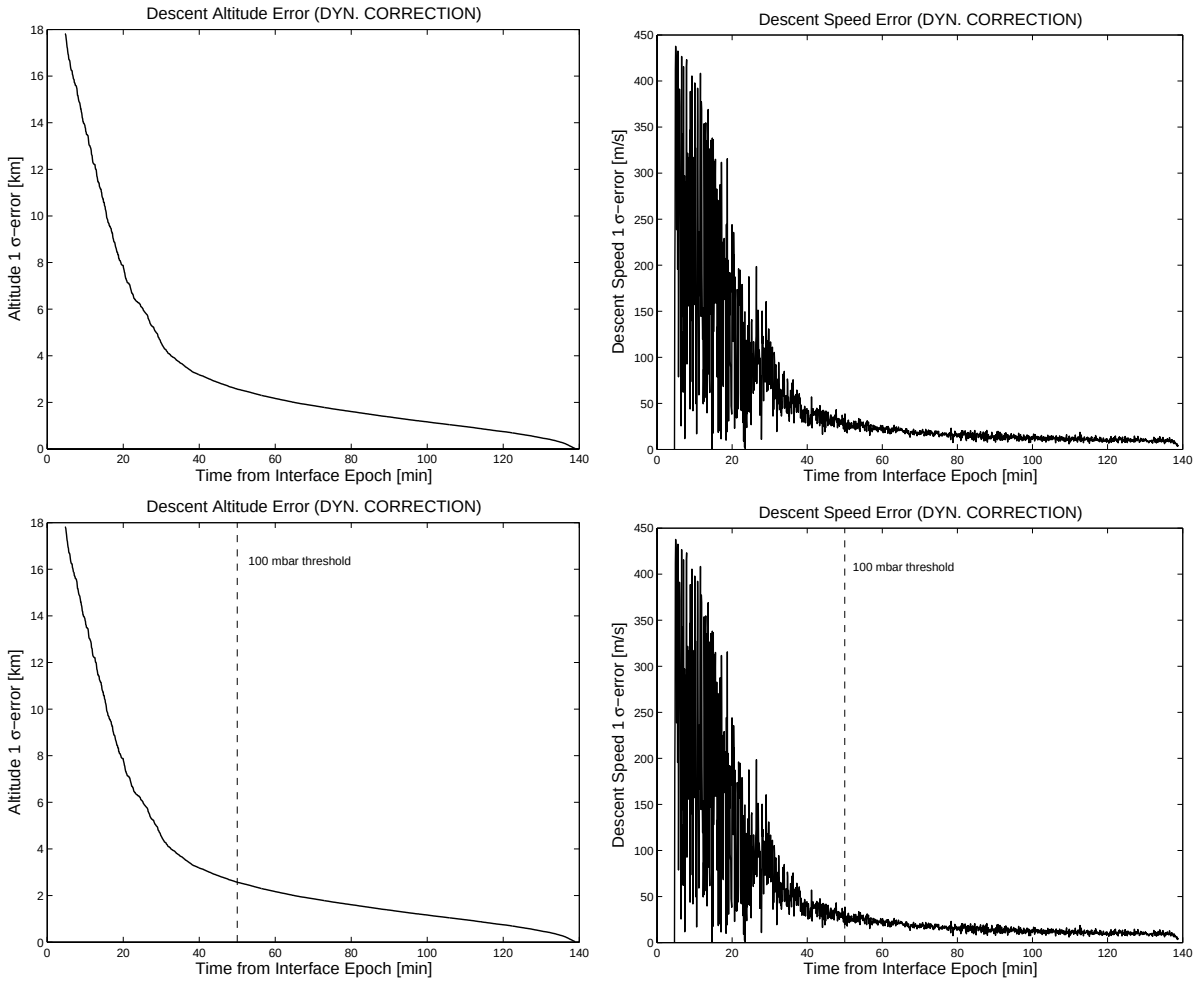

Figure 9.4: ***DTC2_N*** *(upper panels), and* ***DTC3_N*** *(lower panels) error propagation. The dashed line in the lower panels designates the 100 mbar threshold below which SSP speed of sound measurements are used.*

measurements serve primarily as an additional means (e.g., in terms of a backup in case HASI temperature measurements fail or are corrupt) to reconstruct the trajectory but will not necessarily provide a higher confidence.

9.2 Longitude Drift

Table 9.3 summarizes the test case campaign for the probe longitude drift reconstruction, which aims to assess the capability of the longitude reconstruction algorithm from both the DWE zonal wind speed (LDTC1 and LDTC1_N) and the DISR Solar Zenith Angle (SZA) measurements (LDTC2 and LDTC2_N). It is important to note that the synthetic DISR SZA dataset does not reflect any probe oscillations due to parachute dynamics as they are very complex to simulate and can therefore be considered as an ideal dataset. Recall from Eq. (8.23) that the longitude drift reconstruction from zonal wind speed measurements require an initial longitude and latitude value $\varphi_0 = \varphi(t_0)$ and $\lambda_0 = \lambda(t_0)$ at integration starting time t_0. Furthermore the probe descent altitude profile is required, which can be obtained from a previous reconstruction effort as performed in Sec. 9.1. Finally the uncertainties $\Delta\varphi_0$ and $\Delta\lambda_0$ need to be provided for the longitude drift error estimation [see Eq. (8.39)].

Test Case	DWE data	DISR SZA data	Noise	Smoothing
LDTC1	Yes	No	No	No
LDTC1_N	Yes	No	Yes	151 points
LDTC2	No	Yes	No	No
LDTC2_N	No	Yes	Yes	10 points

Table 9.3: *Summary of test cases for the probe descent phase longitude reconstruction. Assumptions for all test cases:* h_0*=152.036 km,* $\varphi_0 = 162.688°$, $\lambda_0 = 10.6°$, $\Delta\varphi_0 = 0°$, *and* $\Delta\lambda_0 = 0.2°$. *The altitude profile was taken from DTC3_N. For LDTC1_N and LDTC2_N the input data were smoothed using a 151 and 10 points moving average filter, respectively (see Sec. 5.2).*

Fig. 9.5 shows the longitude residuals (HSDS trajectory minus reconstructed) for the longitude reconstruction effort based on the DWE zonal wind measurements for both the noise and no noise datasets. The noise dataset was smoothed with a moving average filter (LDTC1_N) with a span of 151 data points. As the reconstruction process is an integrating process starting from an initial assessment φ_0 (which was directly taken from the HSDS trajectory), the residuals increase during the reconstruction process and reach a maximum of -0.14 degree at the time of probe impact. It should be kept in mind however that this value corresponds only to the algorithm internal error built up and does not include the error of the initial longitude uncertainty. The -0.14 degree can therefore be considered as a lower boundary for the longitude offset at probe impact. Comparing the longitude residuals of LDTC1 and LDTC1_N it can be clearly seen that the noise of the zonal wind measurements (which were of course reduced due to the smoothing) did not have an impact the longitude drift reconstruction.

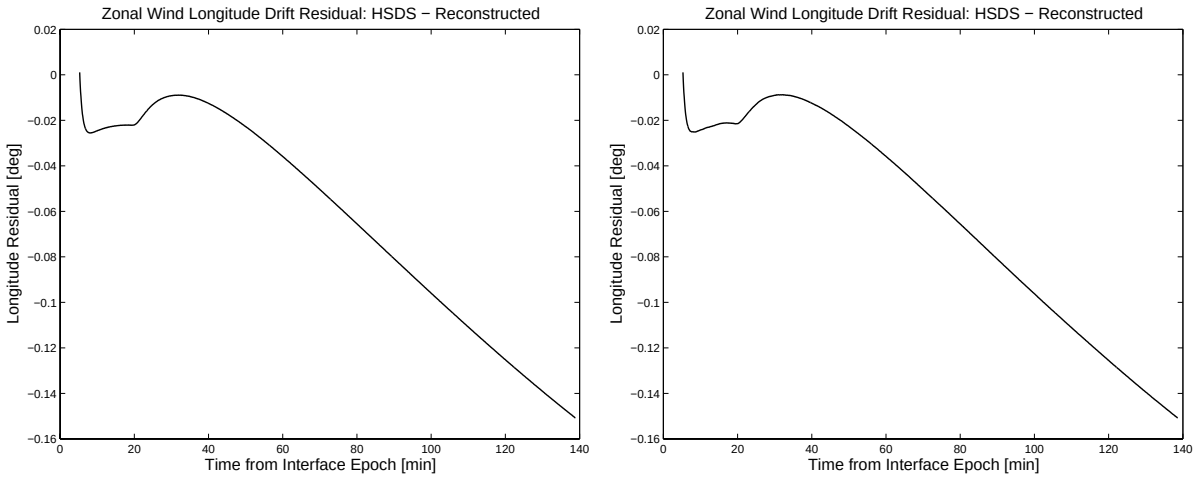

Figure 9.5: ***LDTC1 and LDTC1_N:*** *longitude residuals for the longitude drift reconstruction based on the DWE zonal wind speed measurements.*

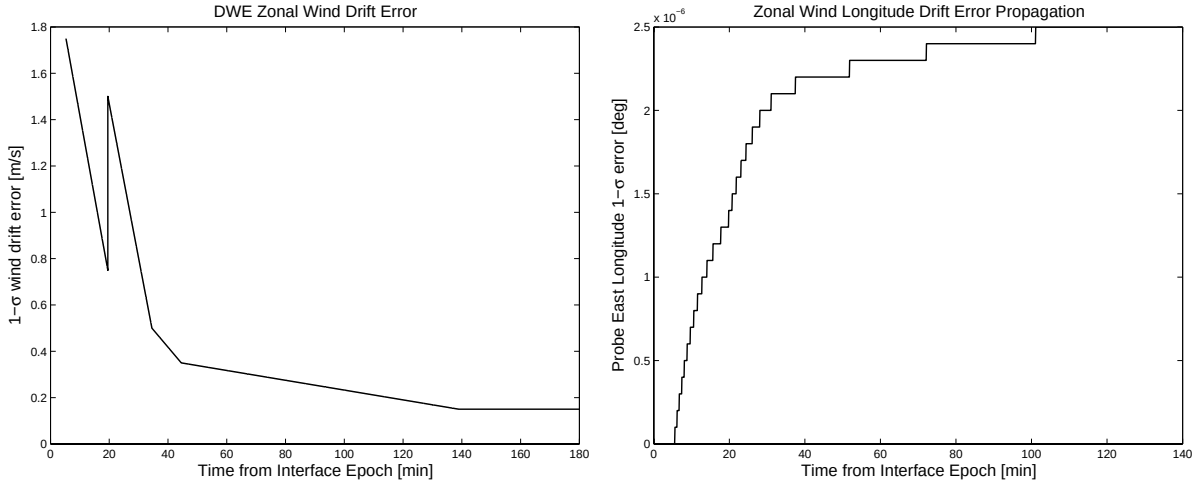

Figure 9.6: *Left panel: DWE zonal drift velocity error; Right panel: 1σ error propagation for the probe longitude drift due to zonal wind for the simulation of LDTC1_N.*

The error of the longitude drift reconstruction depends on the error of the initial longitude estimation φ_0 at the beginning of the drift reconstruction [$\sigma(\varphi_0)$=1.5 deg]. Furthermore the error increases at each integration step by the error of the longitude drift $\sigma(\Delta\varphi_i)$ according to Eq. (8.38). The latter is given by Eq. (8.39) and depends on the error of the zonal probe drift $\sigma(v_{\text{drift}})$ (shown in the left panel of Fig. 9.6), the error of the altitude profile reconstruction $\sigma(z_i)$, and finally the error of the initial latitude estimation $\sigma(\lambda_0)$. The error will therefore increase starting from $\sigma(\varphi_0)$. The simulation results show that the increase above $\sigma(\varphi_0)$ (shown in the right panel of Fig. 9.6) is very minor (lower than 2.5E-6 deg) and the longitude drift error can therefore be considered as constant having the value of $\sigma(\lambda_0)$.

Fig. 9.7 shows the longitude drift residuals from the reconstruction effort using the DISR solar zenith angle (SZA) for the no noise (LDTC2, see left upper panel) and noise (LDTC2_N, right upper panel). It can be seen that the no noise dataset implies very low residuals, which means that the SZA reconstruction methodology is very accurate. Even if the noise in the SZA input data increases the residuals significantly they remain below 0.02 deg. Recall again that the actual SZA flight data will be affected by oscillatory motions due to the complicated parachute dynamics. This has however not been considered in the current version of the HSDS. The evaluation of the LDTC2_N error propagation (see Eq. (8.42) and the lower panel of Fig. 9.7) shows a steady increase from about 0.17 to 0.23 deg at the point of impact.

9.3 Surface Topography

The last part of the descent phase test campaign is related to the reconstruction of the surface topography using three different instrument datasets (i.e., the two radar altimeter units RAU1 and RAU2, and the SSP sounder) and the reconstructed descent phase altitude with respect to the 2575 km reference sphere. Note that all three instruments will only provide data in the very final part of the descent (i.e., 30 km downwards). Table 9.4 provides an overview of the test case terminology and the sensor combinations.

TOPTC1 and TOPTC2 simulate the surface topography reconstruction using the RAU1 and RAU2 data respectively. It is important to point out that the radar altimeter units will very likely not provide useful data throughout their entire altitude range of operation. This stems from the fact that they have to lock on to the transmitted and reflected signal. The ability to lock on the reflected signal however depends on a variety of conditions (e.g., surface reflectiveness, the topography itself, etc.). It is therefore likely that the RAU data will have gaps of useless data points, which have to be cut out from the input data file. This was simulated in the synthetic dataset RAU input files. Fig. 9.8 shows the input raw data file (left panel) and the same data after the gaps have been cut out (right panel).

Fig. 9.9 shows the reconstructed surface topography using the simulated measurements from RAU1 (left panel) and RAU2 (right panel). The input data assumed that both instruments would achieve a lock on the reflected signal from about 30 km down to about 45 m above the surface (the RAU units will not be able to stay in lock down to the surface impact as they will very likely saturate). Comparing those two profiles to the simulated profile that was used for the creation of the HSDS (see lower panel of Fig. 5.11) it can be seen that the reconstruction process was successful. It should be kept in mind that

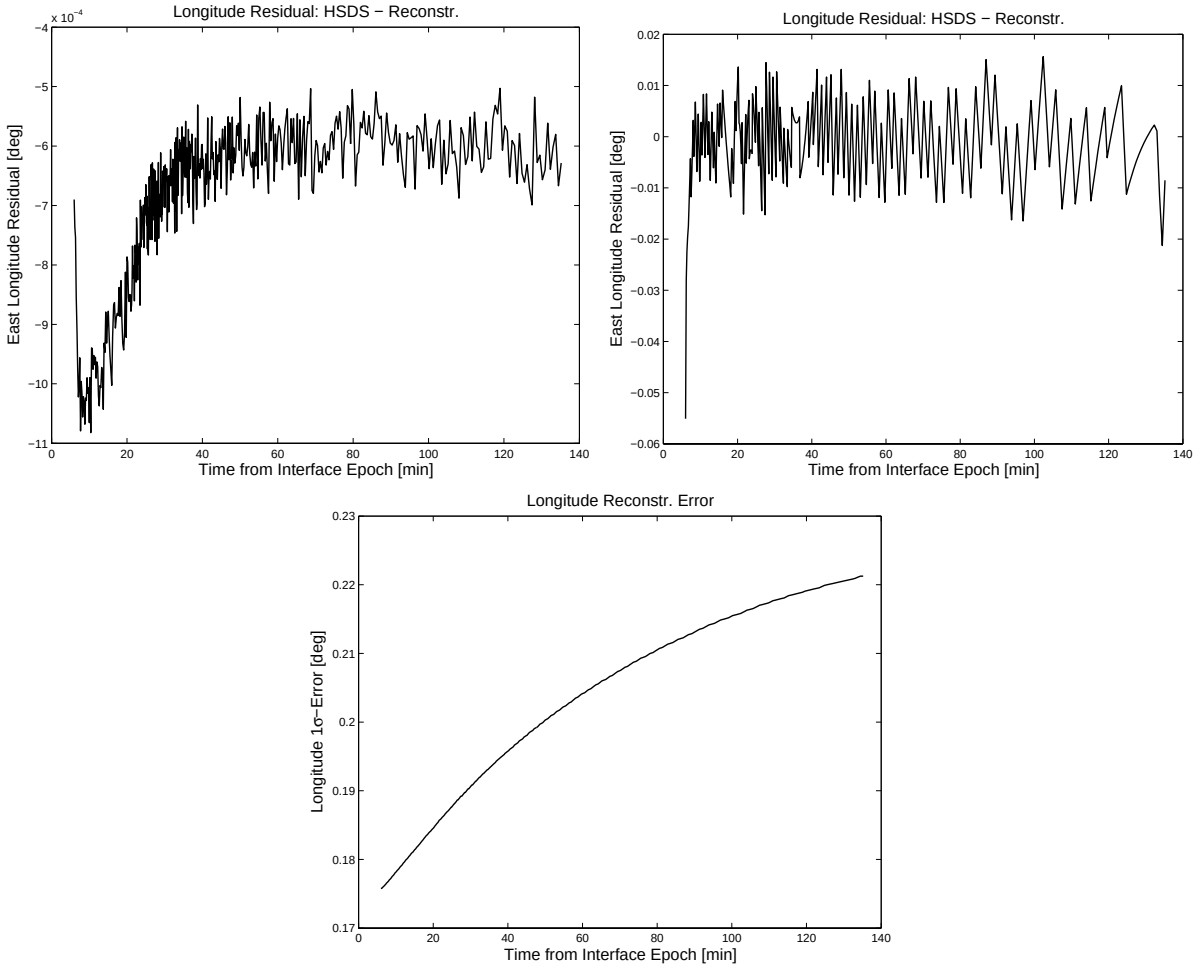

Figure 9.7: *Longitude drift residuals for* ***LDTC2*** *(upper left panel) and* ***LDTC2_N*** *(upper right) panel. Lower panel: 1σ error propagation for the LDTC2_N simulation.*

the topography reconstruction from RAU or acoustic sounder measurements require the reconstructed altitude profile from the atmosphere measurements [see Eq. (8.11)]. In all three cases TOPTC1, TOPTC2, and TOPTC3 the altitude profile from DTC3_N is used. The accuracy of the surface topography therefore depends on the following points:

- The data gaps from the RAU or the acoustic sounder measurements due to loss of lock during the descent. The RAU data gaps could be partially compensated for by combining the data from the two redundant units.
- The precision of the altitude profile reconstructed from atmosphere parameters.
- The precision (performance) of the radar altimeter units or the acoustic sounder measurements which depends on both the instrument dependent measurement noise and the surface properties itself (e.g., surface reflectivity, surface roughness, slope etc.).

Fig. 9.10 shows the TOPTC3 reconstruction results. The upper left panel shows the SSP-APIS input data that cover only the very last ∼234 m of the descent phase. The reconstructed surface topography is shown in the right panel. The lower panel shows that the RAU-1, RAU-2, and the SSP-APIS topography profiles overlap each other in the altitude range of 234 – 45 m.

Test Case	RAU1	RAU2	SSP-APIS
TOPTC1	Yes	No	No
TOPTC2	No	Yes	No
TOPTC3	No	No	Yes

Table 9.4: *Summary of test cases for the surface topography reconstruction.*

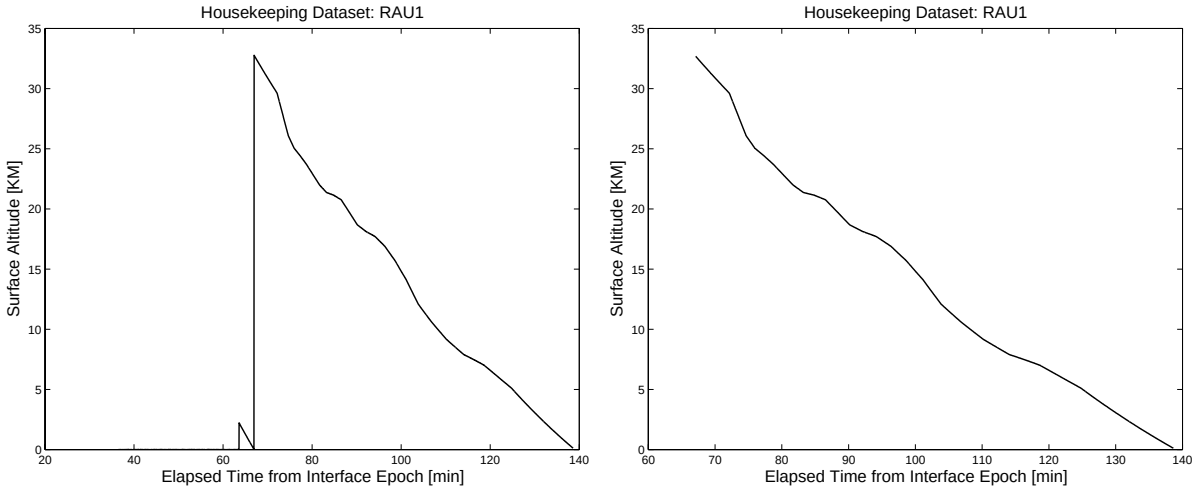

Figure 9.8: *Radar Altimeter Unit altitude measurements in raw version (left) and after the data cutting procedure.*

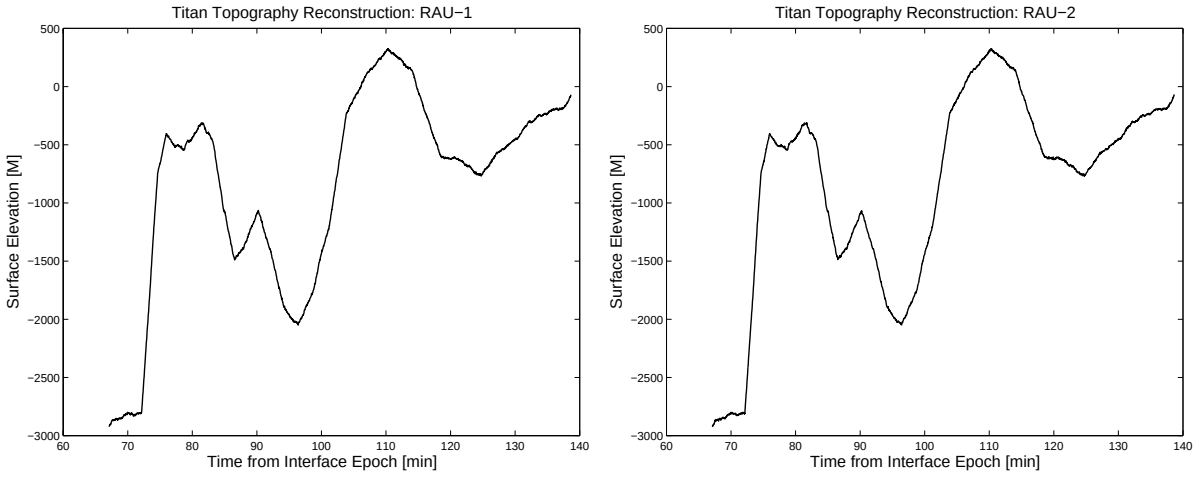

Figure 9.9: ***TOPTC1*** *and* ***TOPTC2*** *radar reconstructed surface topography files.*

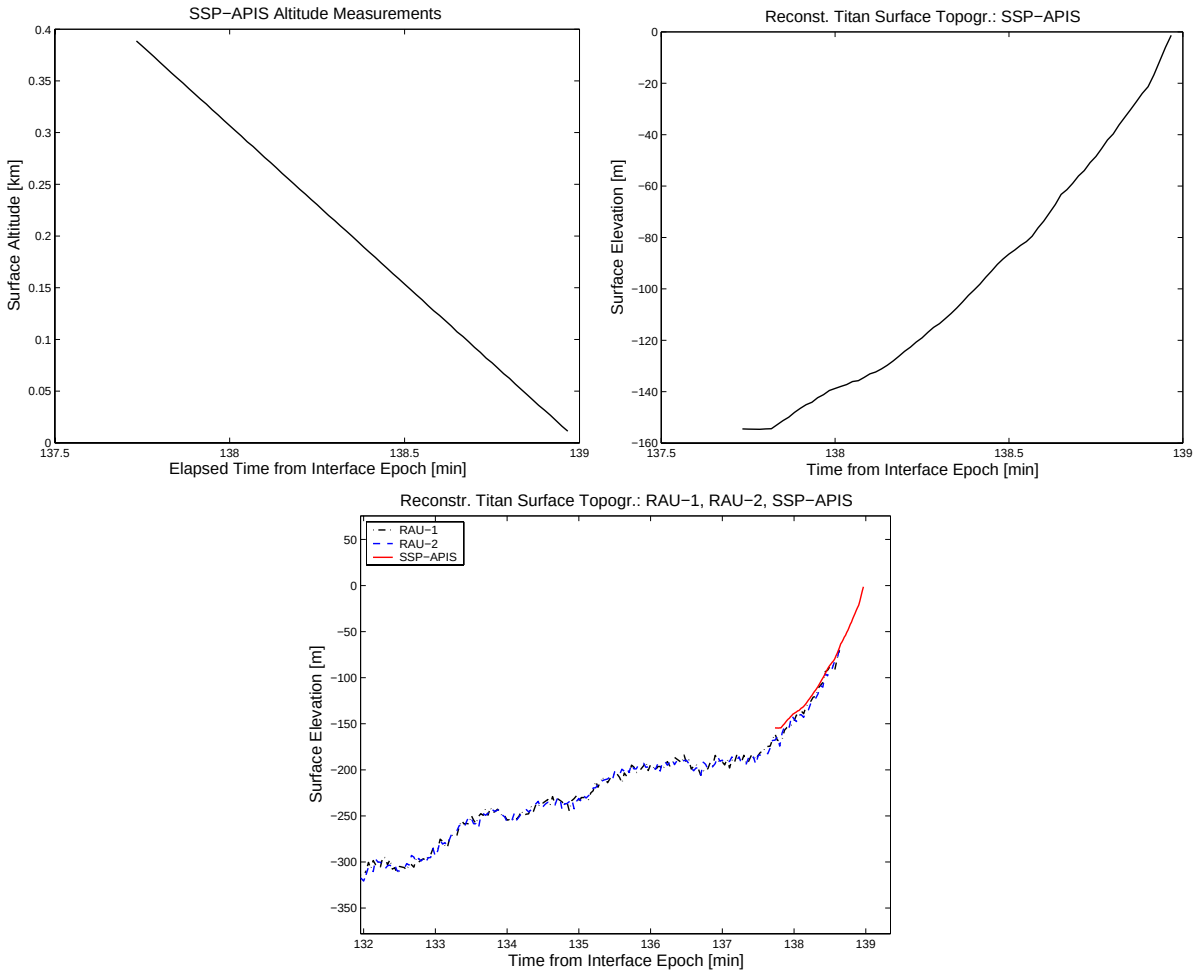

Figure 9.10: *SSP-APIS sounder measurements (upper left panel) starting from an altitude of 234 m and surface topography reconstruction from* ***TOPTC3*** *(upper right panel). The lower panel shows an overlay of the reconstructed topography profile from RAU-1, RAU-2, and SSP-APIS measurements.*

Chapter 10

Entry and Descent Phase Fitting

The reconstruction of the Huygens trajectory is done in two separate efforts that are based on different sets of input data, i.e., the entry phase and the descent phase reconstruction (see Chap. 6 and Chap. 8 respectively). It is therefore possible (and even likely) that the two portions of trajectories do not match together at the end of the entry and the beginning of the descent phase. As there is only one correct trajectory this results is unsatisfactory. A possibility to reduce the gap between the two portions is to develop and implement a methodology that adjusts certain parameters of motion (e.g., the spacecraft initial conditions which are normally provided together with their uncertainties from an a priori orbit determination process) in their respective range of uncertainty.

A standard method to approach this problem is to implement a statistical trajectory estimation algorithm like a least-squares, sequential batch, or *Kalman* filter, which provides a means to assess the amount of correction needed in order to minimize the residuals between the two trajectory portions. The application of any of these filters requires that the reconstruction of both trajectory portions could be performed to an extent that allows them to overlap each other. In this overlap region one can then form the residuals in both altitude and descent speed which then enter into the filter.

10.1 Formulation of the Least-Squares Problem

The basic idea of least-squares estimation as applied to orbit determination is to find the trajectory and the model parameters for which the sum of the squares of the differences between the modeled observations and the actual measurements become as small as possible, or, in other words, a trajectory which best fits the observations in a least-squares of the residual sense (see Fig. 10.1). In a real world each measurement is affected by a specific measurement error. A weighting factor can therefore be applied to each residual and it is the rss of the weighted residuals which is minimized.

In this specific case the reconstructed entry trajectory is considered to be the reference trajectory, given by the time dependent state vector

$$\vec{x}(t) = \begin{pmatrix} \vec{r}(t) \\ \vec{v}(t) \end{pmatrix} \tag{10.1}$$

which is a 6-dimensional vector comprising the spacecraft position $\vec{r}$ and velocity $\vec{v}$ vectors. The time evolution $\vec{y}$ is governed by the equations of motion, which can be expressed by

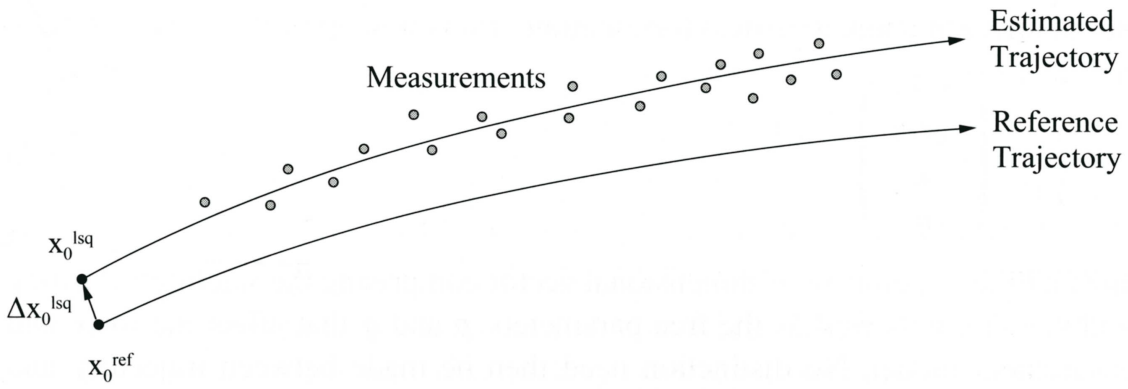

Figure 10.1: *Least-squares orbit determination. The parameters of a reference trajectory are corrected to find the trajectory which best fits the observations in a least-squares of the residual sense (Montenbruck and Gill, 2000).*

an ordinary differential equation in the form of (see Eq. 6.4)

$$\vec{y} = \dot{\vec{x}} = f(t, \vec{x}) \tag{10.2}$$

and an initial value

$$\vec{x}_0 = \vec{x}(t_0) \tag{10.3}$$

In the overlap area of the entry and descent phase one obtains the observation vector $\vec{o}$, which comprises the descent phase altitude Z and descent speed $\dot{Z}$

$$\vec{o} = \begin{pmatrix} Z \\ \dot{Z} \end{pmatrix} \tag{10.4}$$

From the entry phase reconstruction one obtains the calculated or modeled observation vector $\vec{c}$, which is a function of the reconstructed entry phase trajectory

$$\vec{c} = \begin{pmatrix} z \\ \dot{z} \end{pmatrix} \tag{10.5}$$

where z and $\dot{z}$ are the (entry phase) altitude and descent speed. The calculated vector $\vec{c}$ is derived from the integrated (entry) reference trajectory, which can be expressed as

$$c_i(t_i) = g_i(t_i, \vec{x}(t_i)) = h_i(t_i, \vec{x}_0) \tag{10.6}$$

g_i denotes the calculated observation vector at t_i as a function of the instantaneous state $\vec{x}(t_i)$, whereas h_i denotes the same value as a function of the initial state $\vec{x}_0$ at the reference epoch t_0. The differences of the actual observations and the calculated (modeled) ones can be expressed as residuals

$$\vec{\rho} = \vec{o} - \vec{c} \tag{10.7}$$

The least-squares orbit determination problem can now be defined as finding the state $\vec{x}_0^{\,\mathrm{lsq}}$ that minimizes the loss function

$$\chi^2(\vec{x}_0) = \vec{\rho}^T \, \vec{\rho} \tag{10.8}$$

which is the squared sum of the residuals ρ_i for a given set of observations o_i. In order to avoid a non-unique determination of $\vec{x}$ it is assumed that the number of observations n is at least equal to the number of unknowns m.

Linearization and Normal Equations

The practical solution of the least-squares orbit determination problem is complicated by the fact that $\vec{h}$ is usually a highly non-linear function of the unknown vector $\vec{x}_0$, which makes it difficult or impossible to locate the minimum of the loss function without additional information. As mentioned above, an approximate value $\vec{x}_0{}^{\rm apr}$ of the actual epoch state is often known and can be used to simplify the least-squares problem considerably. Linearizing[1] $\vec{h}$ around the reference state $\vec{x}_0^{\rm ref}$ yields

$$\vec{h}(\vec{x}_0) \approx \vec{h}(\vec{x}_0^{\rm ref}) - \frac{\partial \vec{h}}{\partial \vec{x}_0}(\vec{x}_0 - \vec{x}_0^{\rm ref}) \tag{10.9}$$

which is initially given by $\vec{x}_0^{\rm apr}$, the residual vector can be approximated by

$$\begin{aligned} \vec{\rho} &= \vec{o} - \vec{h}(\vec{x}_0) \\ &\approx \vec{o} - \vec{h}(\vec{x}_0^{\rm ref}) - \frac{\partial \vec{h}}{\partial \vec{x}_0}(\vec{x}_0 - \vec{x}_0^{\rm ref}) \\ &= \Delta\vec{\rho} - \vec{H}\,\Delta\vec{x}_0 \; . \end{aligned} \tag{10.10}$$

Here

$$\Delta\vec{x}_0 = \Delta x_0 - \vec{x}_0^{\rm ref} \tag{10.11}$$

denotes the difference between $\vec{x}_0$ and the reference state, while

$$\Delta\vec{\rho} = \vec{o} - \vec{h}(\vec{x}_0^{\rm ref}) \tag{10.12}$$

denotes the difference between the actual observation and the observation predicted from the reference trajectory. Furthermore, the Jacobian

$$\mathbf{H} = \left.\frac{\partial \vec{h}(\vec{x}_0)}{\partial \vec{x}_0}\right|_{\vec{x}_0 = \vec{x}_0^{\rm ref}} \tag{10.13}$$

gives the partial derivatives of the modeled observations with respect to the state vector at the reference epoch t_0. Eq. (10.10) provides a prediction of the measurement residual after applying a correction $\Delta\vec{x}_0$ to the reference state and recomputing the modeled observations $\vec{h}$. The orbit determination problem is now reduced to the linear least-squares problem of finding $\Delta\vec{x}_0^{\rm lsq}$ such that

$$\chi^2(\Delta\vec{x}_0) = (\Delta\vec{\rho} - \mathbf{H}\,\Delta\vec{x}_0)^T \, (\Delta\vec{\rho} - \mathbf{H}\,\Delta\vec{x}_0) \, , \tag{10.14}$$

[1] The term "linearize" stems from the truncation of a Taylor Series after its linear term.

i.e., the predicted loss function after applying a correction $\Delta\vec{x}_0$ becomes a minimum. If the Jacobian has full rank m (i.e., the columns of $\mathbf{H}$ are linearly independent) this minimum is uniquely determined by the condition that the partial derivatives of J with respect to $\Delta\vec{x}_0$ vanish, and the solution of the linear least-squares problem may be written as

$$\Delta\vec{x}_0^{\,\mathrm{lsq}} = (\mathbf{H}^T\,\mathbf{H})^{-1}\,(\mathbf{H}^T\,\Delta\vec{\rho}) \tag{10.15}$$

using standard techniques for positive linear systems of equations. The matrix $\mathbf{H}^T\,\mathbf{H}$ is an m-dimensional symmetric square matrix, which is also known as the normal equations matrix. Due to the non-linearity of $\vec{h}$, the simplified loss function differs slightly from the rigorous one and the value

$$\vec{x}_0^{\,\mathrm{lsq}} = \vec{x}^{\,\mathrm{ref}} + \Delta\vec{x}_0^{\,\mathrm{lsq}} \tag{10.16}$$

determined so far is not yet the exact solution of the orbit determination problem. It may however be further improved in an iterative process by substituting each time the linear least-squares solution $\Delta\vec{x}_0^{\,\mathrm{lsq}}$ for the reference value $\vec{x}_0^{\,\mathrm{ref}}$.

Weighting

The algorithm developed so far suffers from the fact that all observations are treated equally, even though the observation vector $\vec{o}$ is generally composed of different measurement types. The accuracy of each measurement type may, however, easily be accounted for by weighting all observations with the inverse of the mean measurement error σ_i, i.e., by replacing the residuals ρ_i with the normalized residuals

$$\rho\prime_i = \frac{1}{\sigma_i}\rho_i = \frac{1}{\sigma}[o_i - h_i(\vec{x}_0)] \tag{10.17}$$

Here σ_i should consider the total expected error in the measurement due to both random noise and systematic error. Introducing the weighting matrix

$$\mathbf{W} = \mathrm{diag}(\sigma_1^{-2}, ..., \sigma_n^{-2}) \tag{10.18}$$

the solution of the weighted least-squares problem may be written as

$$\Delta\vec{x}_0^{\,\mathrm{lsq}} = (\mathbf{H}^T\,\mathbf{W}\,\mathbf{H})^{-1}\,(\mathbf{H}^T\,\mathbf{W}\,\Delta\vec{\rho}) \tag{10.19}$$

Estimation with a priori Information

Aside from the approximate state $\vec{x}_0^{\,\mathrm{apr}}$ that is required to start the least-squares orbit determination, some information on the accuracy of this value is often available. In order to incorporate the *a priori* covariance $\mathbf{P}_0^{\,\mathrm{apr}}$ into the least-squares estimation the so-called *information matrix* was introduced, which is the inverse of the covariance matrix

$$\mathbf{\Lambda} = \frac{1}{\mathbf{P}_0^{\,\mathrm{apr}}}\,. \tag{10.20}$$

The solution of the weighted least-squares problem with *a priori* knowledge can be written as (cf. Montenbruck and Gill, 2000)

$$\Delta\vec{x}_0^{\,\mathrm{lsq}} = (\mathbf{\Lambda} + \mathbf{H}^T\,\mathbf{W}\,\mathbf{H})^{-1}\,(\mathbf{\Lambda}\,\Delta\,\vec{x}_0^{\,\mathrm{apr}} + \mathbf{H}^T\,\mathbf{W}\,\Delta\vec{z}) \tag{10.21}$$

The covariance $\mathbf{P}_0$ after the trajectory estimation is furthermore related to the *a priori* covariance and the measurement information matrix by

$$(\mathbf{P}_0)^{-1} = (\mathbf{P}_0^{\mathrm{apr}})^{-1} + (\mathbf{H}^T\,\mathbf{W}\,\mathbf{H})\,. \tag{10.22}$$

10.2 Variational Equations

The Jacobian $\mathbf{H}$ at the time t_i given by Eq. (10.13) can be rewritten

$$\mathbf{H}_i = \frac{\partial\vec{h}_i}{\partial\vec{x}_0^{\,\mathrm{ref}}} = \mathbf{G}_i \cdot \mathbf{\Phi}(t_i, t_0)\,. \tag{10.23}$$

$\mathbf{G}_i$ is the partial derivative matrix

$$\mathbf{G}_i = \frac{\partial\vec{g}_i}{\partial\vec{x}_i^{\,\mathrm{ref}}} \tag{10.24}$$

where $\vec{g}$ is calculated from the reference trajectory vector $\vec{x}_i^{\,\mathrm{ref}}$ at the instant t_i. $\mathbf{\Phi}_i$ is the *state transition matrix* that describes the change of the spacecraft position and velocity vector at a given epoch t due to the changes in the initial condition vector at the initial epoch t_0. For a six dimensional state vector

$$\vec{y} = \begin{pmatrix} \vec{r}(t) \\ \vec{v}(t) \end{pmatrix} \tag{10.25}$$

$\mathbf{\Phi}$ can be written as

$$\mathbf{\Phi}(t, t_0) = \frac{\partial\mathbf{y}(t)}{\partial\mathbf{y}(t_0)} = \begin{pmatrix} \frac{\partial y_1(t)}{\partial y_1(t_0)} & \cdots & \frac{\partial y_1(t)}{\partial y_6(t_0)} \\ \vdots & \ddots & \vdots \\ \frac{\partial y_6(t)}{\partial y_1(t_0)} & \cdots & \frac{\partial y_6(t)}{\partial y_6(t_0)} \end{pmatrix} \tag{10.26}$$

and can be calculated from the numerical integration of the *Variational Equations*, which are derived from the the fact that $\vec{y}$ obeys the first-order differential equation

$$\frac{d\,\vec{y}(t)}{dt} = f(t, \vec{y}) = \begin{pmatrix} \vec{v}(t) \\ \vec{a}(t, \vec{r}, \vec{v}) \end{pmatrix} \tag{10.27}$$

and

$$\begin{aligned} \frac{\partial}{\partial\vec{y}(t_0)}\,\frac{d\,\vec{y}(t)}{dt} &= \frac{\partial f(t, \vec{y}(t))}{\partial\vec{y}(t_0)} \\ &= \frac{\partial f(t, \vec{y}(t))}{\partial\vec{y}(t)} \cdot \frac{\partial\vec{y}(t)}{\partial\vec{y}(t_0)} \end{aligned} \tag{10.28}$$

Knowing that

$$\frac{\partial}{\partial \vec{y}(t_0)} \frac{d\,\vec{y}(t)}{dt} = \frac{d}{dt} \frac{\partial \vec{y}(t)}{\partial \vec{y}(t_0)}\,, \tag{10.29}$$

$\mathbf{\Phi}$ may be obtained from the set of first order differential equations (the Variational Equations)

$$\frac{d}{dt}\mathbf{\Phi}(t,t_0) = \frac{\partial f(t,\vec{y}(t))}{\partial \vec{y}(t)} \cdot \mathbf{\Phi}(\mathbf{t},\mathbf{t_0}) \tag{10.30}$$

or

$$\frac{d}{dt}\mathbf{\Phi}(t,t_0) = \begin{pmatrix} \mathbf{0}_{3\times3} & \mathbf{1}_{3\times3} \\ \frac{\partial \vec{a}(\vec{r},\vec{v},t)}{\partial \vec{r}(t)} & \frac{\partial \vec{a}(\vec{r},\vec{v},t)}{\partial \vec{v}(t)} \end{pmatrix}_{6\times6} \cdot \mathbf{\Phi}(t,t_0) \tag{10.31}$$

Eq. (10.31) can be solved by numerical integration together with the equations of motion, given the initial condition $\mathbf{\Phi}(t_0,t_0) = \mathbf{1}_{6\times6}$ and the partial derivatives of the total acceleration vector $\vec{a}$ with respect to the spacecraft position $\vec{r}$ and velocity $\vec{v}$.

10.3 Partial Derivatives

The total spacecraft acceleration vector is given by

$$\vec{a} = \vec{a}_g + \vec{a}_{\mathrm{Ad}} \tag{10.32}$$

with the gravitational force acceleration $\vec{a}_g$ and the aerodynamic acceleration $\vec{a}_{\mathrm{Ad}}$ (see Eq. (6.5)). The partial derivatives of $\vec{a}$ with respect to the position vector $\vec{r}$ are given by

$$\frac{\partial \vec{a}}{\partial \vec{r}} = \frac{\partial \vec{a}_g}{\partial \vec{r}} + \frac{\partial \vec{a}_{\mathrm{Ad}}}{\partial \vec{r}}\,, \tag{10.33}$$

and the partial derivatives of $\vec{a}$ with respect to the velocity vector $\vec{v}$ are simply

$$\frac{\partial \vec{a}}{\partial \vec{v}} = \frac{\partial \vec{a}_{\mathrm{Ad}}}{\partial \vec{v}} \tag{10.34}$$

as the term $\partial \vec{a}_g/\partial \vec{v}$ vanishes. $\partial \vec{a}_g/\partial \vec{r}$ can be obtained from the relation

$$\begin{aligned} \frac{\partial a_{g,i}}{\partial r_n} &= \frac{G\,M_0}{|\vec{r}|^3}\left(3\,\frac{r_i\,r_n}{|\vec{r}|^2} - \delta_{in}\right) + \\ &+ \sum_j \frac{G\,M_j}{(p_{j,i}-r_i)^3}\left(\frac{3\,(p_{j,i}-r_i)\,(p_{j,n}-r_n)}{(p_{j,i}-r_i)^2} - \delta_{in}\right) + \\ &+ \frac{\partial U}{\partial r_i\,\partial r_n} \end{aligned} \tag{10.35}$$

where the subscripts $i = (1,...,3)$ and $n = (1,...,3)$ designate the rectangular component of the acceleration or position vector and the subscript j identifies the perturbing planet. The first term in Eq. (10.35) stems from the central (primary) body gravity, the second term from the perturbing body gravity, and the third term from the flattening perturbation of the central body. The Kronecker symbol $\delta_{in} = 1$ if $i = n$, otherwise $\delta_{in} = 0$. From

Eq. (6.12) the partial derivatives of the gradient of the flattening disturbing function U can be easily derived and are given in Appendix A.1.

Starting from the basic expression

$$\vec{a}_{\mathrm{Ad}} = -\frac{1}{2}\, C_D\, \frac{A}{m}\, \rho\, |\vec{v}_{\mathrm{rel}}|\, \vec{v}_{\mathrm{rel}} \tag{10.36}$$

from the acceleration due to atmospheric drag the partial derivatives with respect to the spacecraft velocity can be derived (see also Appendix A.3)

$$\frac{\partial \vec{a}_{\mathrm{Ad}}}{\partial \vec{v}} = -\frac{1}{2}\, C_D\, \frac{A}{m}\, \rho\, \left(\frac{\vec{v}_{\mathrm{rel}}\, \vec{v}_{\mathrm{rel}}^{T}}{|\vec{v}_{\mathrm{rel}}|} + |\vec{v}_{\mathrm{rel}}|\, \vec{1} \right) \tag{10.37}$$

where C_D is the drag coefficient, A is the cross-sectional area, m is the mass of the spacecraft, ρ is the atmospheric density, and $\vec{v}_{\mathrm{rel}}$ is the relative velocity between the spacecraft and the atmosphere [see Eq. (6.19)]. It is important to note that $\vec{v}_{\mathrm{rel}}\, \vec{v}_{\mathrm{rel}}^{T}$ designates a dyadic and not a scalar product (see Appendix A.3). The partial derivatives with respect to position involve a direct term describing the atmospheric density variation as well as a minor contribution from the changing atmospheric wind velocity:

$$\frac{\partial \vec{a}_{\mathrm{Ad}}}{\partial \vec{r}} = -\frac{1}{2}\, C_D \frac{A}{m}\, |\vec{v}_{\mathrm{rel}}|\, \vec{v}_{\mathrm{rel}} \frac{\partial \rho}{\partial \vec{r}} - \frac{1}{2}\, C_D\, \frac{A}{m}\, \rho \left(\frac{\vec{v}_{\mathrm{rel}}\, \vec{v}_{\mathrm{rel}}^{T}}{|\vec{v}_{\mathrm{rel}}|} + |\vec{v}_{\mathrm{rel}}|\, \mathbf{1} \right) \frac{\partial \vec{v}_{\mathrm{rel}}}{\partial \vec{r}}\,. \tag{10.38}$$

From Eq. (6.19) one can see that the partial derivatives of the relative velocity are given by

$$\frac{\partial \vec{v}_{\mathrm{rel}}}{\partial \vec{r}} = \frac{\partial \vec{v}}{\partial \vec{r}} - \frac{\partial}{\partial \vec{r}} (\vec{\omega}_p \times \vec{r}) - \frac{\vec{v}_w}{\partial \vec{r}}\,. \tag{10.39}$$

where the first term vanishes. Introducing the cross-product matrix

$$\mathbf{X}(\vec{\omega}) = \begin{pmatrix} 0 & -\omega_z & +\omega_y \\ +\omega_z & 0 & -\omega_x \\ -\omega_y & +\omega_x & 0 \end{pmatrix} \tag{10.40}$$

one can rewrite the second term

$$\frac{\partial}{\partial \vec{r}} (\vec{\omega}_p \times \vec{r}) = \mathbf{X}(\vec{\omega}_p)\,. \tag{10.41}$$

The wind velocity vector can be expressed (in the inertial planet centered Q-frame) as

$$\vec{v}_w = \frac{v_w}{(r_x^2 + r_y^2)^{1/2}} \begin{pmatrix} -r_x \\ +r_y \\ 0 \end{pmatrix} \tag{10.42}$$

and the partial derivatives of the wind velocity vector with respect to the spacecraft position (again in Q-frame) can therefore be easily derived and are also provided in Appendix A.2. Using the partial derivatives with respect to the velocity vector $\vec{v}$ from Eq. (10.37) one can now rewrite Eq. (10.39)

$$\frac{\partial \vec{a}_{\mathrm{Ad}}}{\partial \vec{r}} = -\frac{1}{2} C_D \frac{A}{m} |\vec{v}_{\mathrm{rel}}| \, \vec{v}_{\mathrm{rel}} \frac{\partial \rho}{\partial \vec{r}} - \frac{\partial \vec{a}_{\mathrm{Ad}}}{\partial \vec{v}} \mathbf{X}(\vec{\omega}_p) \tag{10.43}$$

Here $\partial\rho/\partial\vec{r}$ describes the dependence of the atmospheric density on the spacecraft location, which can be expressed with respect to the spacecraft altitude z

$$\frac{\partial \rho}{\partial \vec{r}} = \frac{\partial \rho}{\partial z} \cdot \frac{\partial z}{\partial \vec{r}} \ . \tag{10.44}$$

and $\partial z/\partial\vec{r}$ is given by Eq. (10.48). One can see that the computation of the transition matrix from the variational equations requires the knowledge of the spacecraft mass[2], the drag coefficient C_D, and the atmospheric density ρ. The atmospheric density profile can be derived from the spacecraft accelerometer measurements during the entry phase, C_D is interpolated as function of the aerodynamic regime from the existing pre-flight aerodynamic database (see Appendix C).

The partial derivative matrix $\mathbf{G}$ [see Eq. (10.24)] is a 2×6 matrix consisting of the partial derivatives of the modelled observations with respect to the reference trajectory vector $\vec{y}$

$$\mathbf{G} = \begin{pmatrix} \frac{\partial z}{\partial \vec{r}} & \frac{\partial z}{\partial \vec{v}} \\ \\ \frac{\partial \dot{z}}{\partial \vec{r}} & \frac{\partial \dot{z}}{\partial \vec{v}} \end{pmatrix} \tag{10.45}$$

with z and $\dot{z}$ as the modeled altitude and descent speed which can be derived from the state vector $\vec{y}$ by

$$z = (y_1^2 + y_2^2 + y_3^2)^{1/2} - R_p = |\vec{r}| - R_P \tag{10.46}$$

and

$$\frac{dz}{dt} = \dot{z} = \frac{1}{|\vec{r}|} (y_1 \cdot \dot{y}_1 + y_2 \cdot \dot{y}_2 + y_3 \cdot \dot{y}_3) \tag{10.47}$$

where R_p is the radius of the planet. The partial derivatives of z and $\dot{z}$ with respect to the position vector $\vec{r}$ are given by the following relations respectively

$$\frac{\partial z}{\partial \vec{r}} = \frac{\vec{r}}{|\vec{r}|} \tag{10.48}$$

and

$$\frac{\partial \dot{z}}{\partial \vec{r}} = \frac{|\vec{r}| \cdot \dot{\vec{r}}^T - |\dot{\vec{r}}| \cdot \vec{r}^T}{|\vec{r}|^2} \tag{10.49}$$

where

$$|\dot{\vec{r}}| = \frac{1}{|\vec{r}|} (y_1 \cdot \dot{y}_1 + y_2 \cdot \dot{y}_2 + y_3 \cdot \dot{y}_3) \ . \tag{10.50}$$

[2]The spacecraft mass m is time dependent, i.e., $m = m(t)$, due to the heat-shield ablation during the hypersonic entry phase, the heat-shield separation and the deployment and release of the various parachutes during the descent phase.

The partials of z with respect to the velocity vector $\vec{v}$ vanish and the corresponding partials of $\dot{z}$ are given by

$$\frac{\partial \dot{z}}{\partial \vec{v}} = \frac{\vec{r}^T}{|\vec{r}|} \tag{10.51}$$

Chapter 11

Trajectory Fitting Test Cases

In this Chapter the trajectory fitting algorithm as described in Chap. 10 is tested. The computational flow of the trajectory matching process is schematically shown in Fig. 11.1. The entry phase is first reconstructed from the nominal HSDS initial conditions and the probe accelerometer measurements providing the altitude and descent speed profiles. In parallel to the integration of the equations of motion, the system transition matrix is propagated by integration of the Variational Equations (see Chap. 6). From the reconstructed entry phase altitude and descent speed profiles one can then compute the residuals to the corresponding parameters from the descent phase (this requires of course an overlap of the two trajectory portions). The trajectory portion mismatch can then be expressed as χ^2, i.e., the squared sum of altitude and descent speed residuals [see Eq. (10.8)]. Using the system transition matrix and the calculated residuals the trajectory fitting algorithm proposes a correction to the initial state vector that can then be used in a subsequent iteration for a new reconstruction of the probe entry phase. A decrease of the trajectory mismatch (expressed by the χ^2 value) in the subsequent iteration means that the trajectory fitting algorithm has been successful and the iterative correction process has converged.

In all the trajectory fitting test cases the optimum sensor combination for the entry phase (i.e., HASI X-servo, Y-piezo, and Z-piezo in the no noise version like ETC1) was used. For the descent phase the combination of the corrected HASI pressure and temperature (no-noise) data, as well as the GCMS mole fraction, the SSP speed of sound and SSP impact accelerometer data were used. To assess the match of the entry phase and descent phase using the nominal HSDS state vector both trajectory portions are shown together with the HSDS reference trajectory in Fig. 11.2. One can see that the entry phase merges very well with the descent phase. The altitude and descent speed residuals in the overlapping region stay below $\sim$1.3 km and 10^{-02} m/s respectively.

11.1 Trajectory Fitting Test Case 1

In our first test case (i.e. FIT_TC1) we modify only the position related part of the state vector and keep the velocities from the HSDS state vector. Table 11.1 provides the nominal HSDS probe state vector at the interface epoch and altitude (1270 km above Titan's surface) and the corresponding 1σ uncertainties. Furthermore the modified state vector that is used for FIT_TC1 is provided together with the introduced bias (expressed

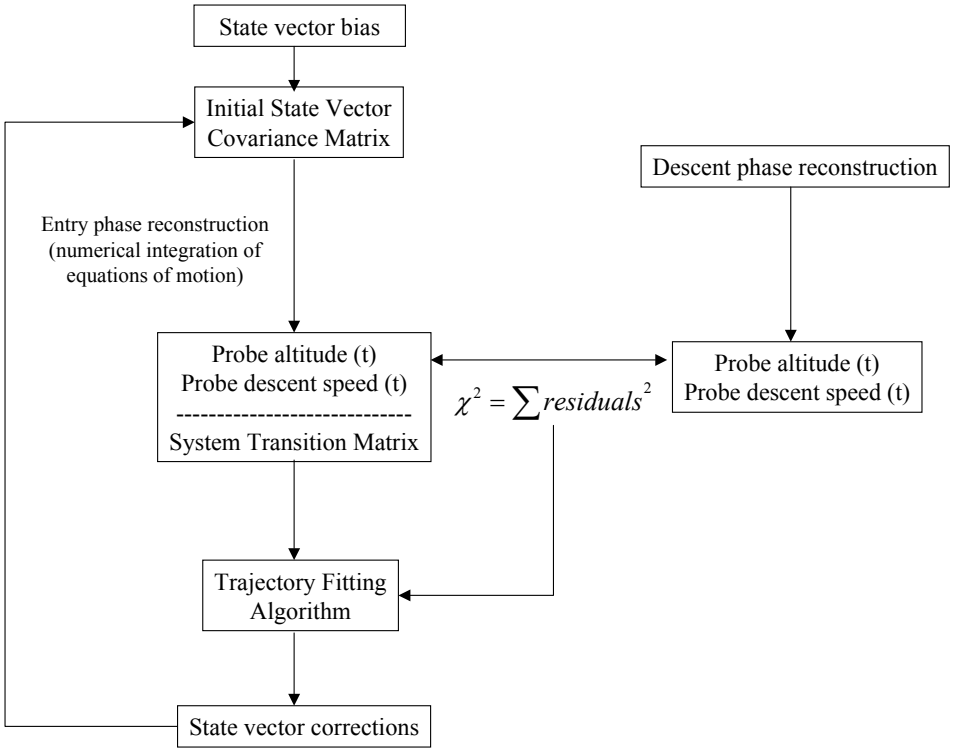

Figure 11.1: *Computational flow of the trajectory fitting process. See text for detailed explanation.*

as fraction of 1σ uncertainties). The comparison of entry and descent phase trajectory is shown in the upper panels of Fig. 11.3 (the left upper panel zooms into the first minute past interface epoch). One can see that the biased FIT_TC1 state vector starts at an initial altitude of 1290 km instead of the nominal 1270 km. In the right upper panel of Fig. 11.3 one can readily see that the FIT_TC1 trajectory shows a significant mismatch to the descent phase trajectory. Table 11.2 provides the corresponding quantitative residuals in altitude and descent velocity for the first 8 altitude and velocity values taken from the descent phase.

Applying the trajectory fitting algorithm (using the *a priori* covariance matrix provided in the HSDS) according to Eq. (10.21) one obtains corrections for the initial state vector values, which have to be added to the biased vector in order to get the new state vector. These are listed together with the new (corrected) state vector in Table 11.3. The new state vector starts at an altitude which deviates from the nominal by less than 2 km as shown in the left lower panel of Fig. 11.3. The lower right panel of Fig. 11.3 shows the trajectory match of the reconstructed entry trajectory using the corrected state vector. One can see the corrected vector implies a much better match of the two trajectory portions. The corresponding altitude and descent speed residuals are listed in Table 11.4. The altitude differences remain below 1.5 km.

	HSDS (JPL040225)	HSDS 1σ	Bias	Modified State
x	-1.312458638E+02	3.920909191E+01	-0.2σ	-1.390876822E+02
y	-3.824933072E+03	9.296961868E+01	-0.2σ	-3.843526996E+03
z	-3.697321588E+02	1.340085253E+01	-0.5σ	-3.764325851E+02
v_x	-2.346112519E+00	3.571847510E-03	0	-2.346112519E+00
v_y	5.539336275E+00	8.932350759E-03	0	5.539336275E+00
v_z	4.588600223E-01	1.773649315E-03	0	4.588600223E-01

Table 11.1: *Comparison of the nominal probe initial state vector and corresponding uncertainties as provided in the HSDS to the biased vector as used for* ***FIT_TC1****. The interface epoch is January 14, 2005 09:00:00.000 ET. Units are in km and km/s respectively.*

Time [min]	Z [km]	$Z - z$ [km]	$\dot{Z} - \dot{z}$ [m/s]
4.7527	155.40893	-20.969	-3.928
4.8360	154.53744	-21.065	0.050
4.9194	153.82772	-21.115	2.896
5.0027	153.22591	-21.136	4.788
5.0861	152.70007	-21.137	6.177
5.1694	152.23116	-21.129	6.996
5.2527	151.80901	-21.120	7.714
5.3361	151.42121	-21.084	2.245

Table 11.2: *Residuals (descent phase - entry phase) of the reconstructed altitude and descent speed in the overlapping portion of the trajectory for the* ***FIT_TC1*** *biased initial conditions. The time is given in minutes relative to the interface epoch. Note that the capital letters Z and $\dot{Z}$ are used for the altitude and descent speed of the descent phase (those values are considered as the "observations" in the sense of an orbit determination problem) and the small letters z and $\dot{z}$ for the corresponding values derived from the spacecraft accelerometer integration.*

	Proposed correction	New vector
x	-1.203604485E+00	-1.400829554E+02
y	1.782880402E+00	-3.818931457E+03
z	2.577154740E+00	-3.930807402E+02
vx	1.852832527E-03	-2.342796259E+00
vy	-4.353817527E-03	5.532487358E+00
vz	-3.601446425E-04	4.596527203E-01

Table 11.3: ***FIT_TC1*** *proposed state vector corrections and corrected state vectors. Units are [km] and [km/s].*

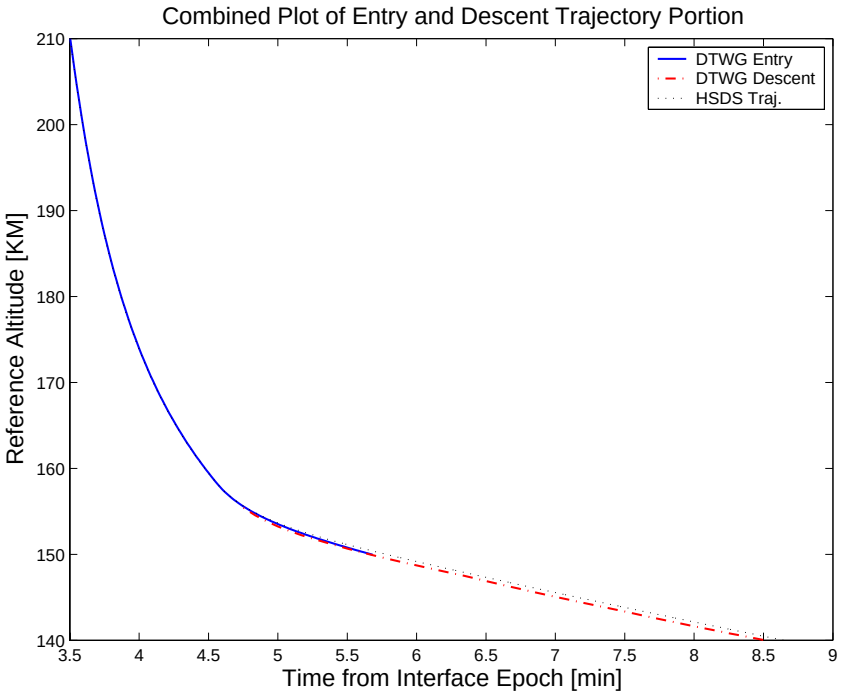

Figure 11.2: *Comparison of reconstructed entry phase and descent phase portion with the HSDS simulated trajectory. The entry phase reconstruction used the initial state vector as provided in the HSDS.*

11.2 Trajectory Fitting Test Case 2

In the second trajectory fitting test case both the initial position and velocity vector are biased as shown in Table 11.5. As expected, this implies even higher residuals than those of FIT_TC1 (see Table 11.6). The upper panel of Fig. 11.1 depicts the overlay of the reconstructed entry and descent trajectories to the simulated HSDS reference trajectory (dotted line). Applying the fitting algorithm according to Eq. (10.21) one obtains the first set of corrections which are listed in Table 11.7. The subsequent entry trajectory reconstruction based on the corrected state vector from Table 11.7 decreases the residuals significantly as shown in the lower panel of Fig. 11.1. The residuals after the first correction process are given in Table 11.8.

Applying the trajectory fitting algorithm a second time one obtains the state vector corrections as listed in Table 11.9. Redoing the reconstruction with the new state vector from Table 11.9 one obtains even lower residuals as shown in the upper panel of Fig. 11.2. The lower panel of Fig. 11.2 shows the χ^2 values for 48 input observations (i.e., 24 altitude and 24 descent speed residuals) as function of the number of iterations of the trajectory fitting algorithm. One can clearly see that the χ^2 values decrease with every iteration, which means that the trajectory fitting process converged very well.

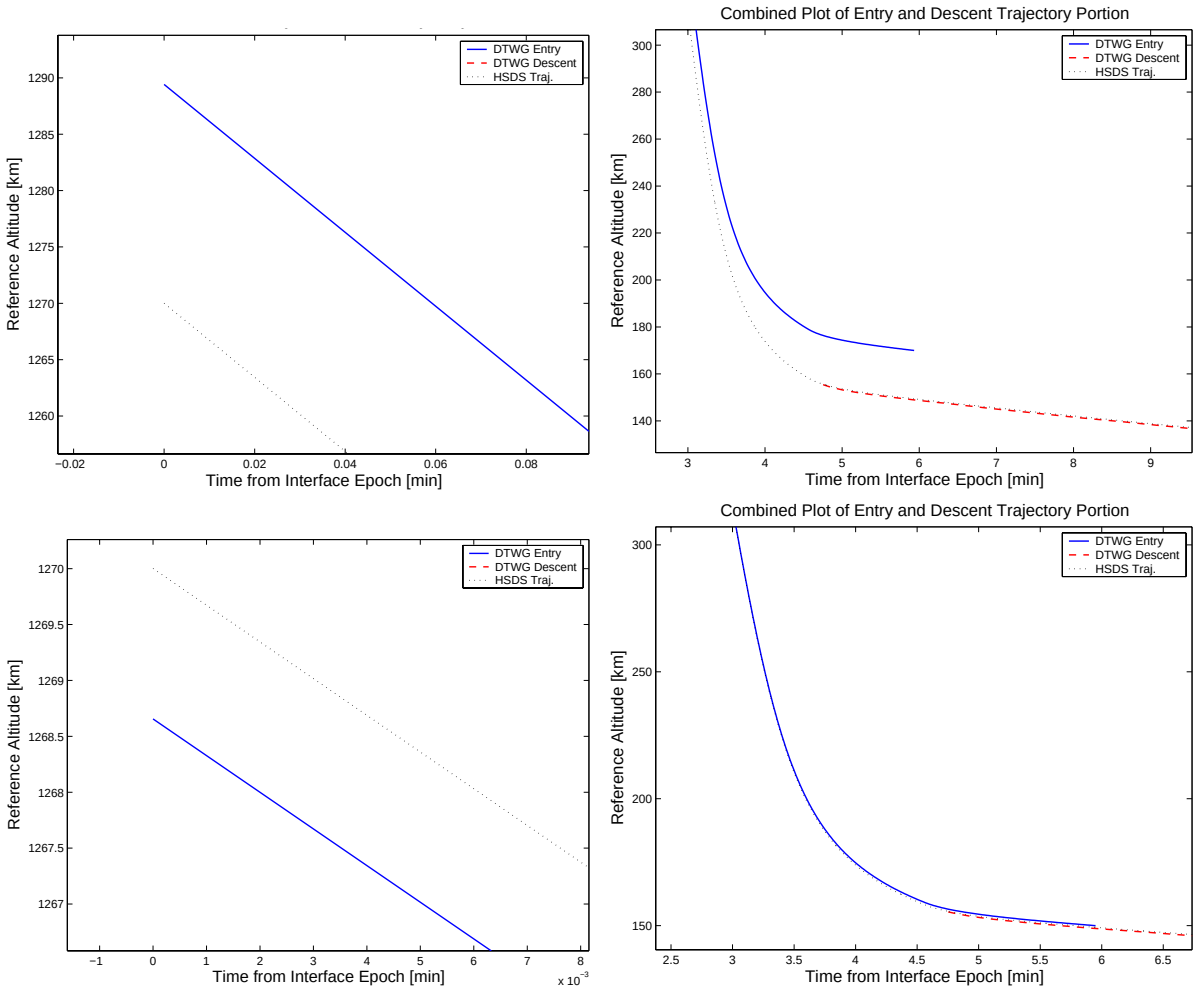

Figure 11.3: *Upper panels: comparison of entry and descent phase trajectory portions using the biased FIT_TC1 initial state vector. The left upper panel zooms into the first minute from initial epoch and clearly shows the altitude difference between the biased and the nominal HSDS position vector. Lower panels: same as upper panels but after using the corrected state vector as proposed from the trajectory fitting algorithm.*

Time [min]	Z [km]	$Z - z$ [km]	$\dot{Z} - \dot{z}$ [m/s]
4.7527	155.40893	-1.087	-3.803
4.8361	154.53744	-1.182	2.605
4.9194	153.82772	-1.230	3.190
5.0027	153.22591	-1.249	5.163
5.0861	152.70007	-1.249	6.633
5.1694	152.23116	-1.238	7.532
5.2527	151.80901	-1.216	8.330
5.3361	151.42121	-1.187	2.948

Table 11.4: ***FIT_TC1*** *residuals (descent phase - entry phase) of the reconstructed altitude and descent speed in the overlapping portion of the trajectory after the* ***first iteration*** *of the trajectory fitting algorithm.*

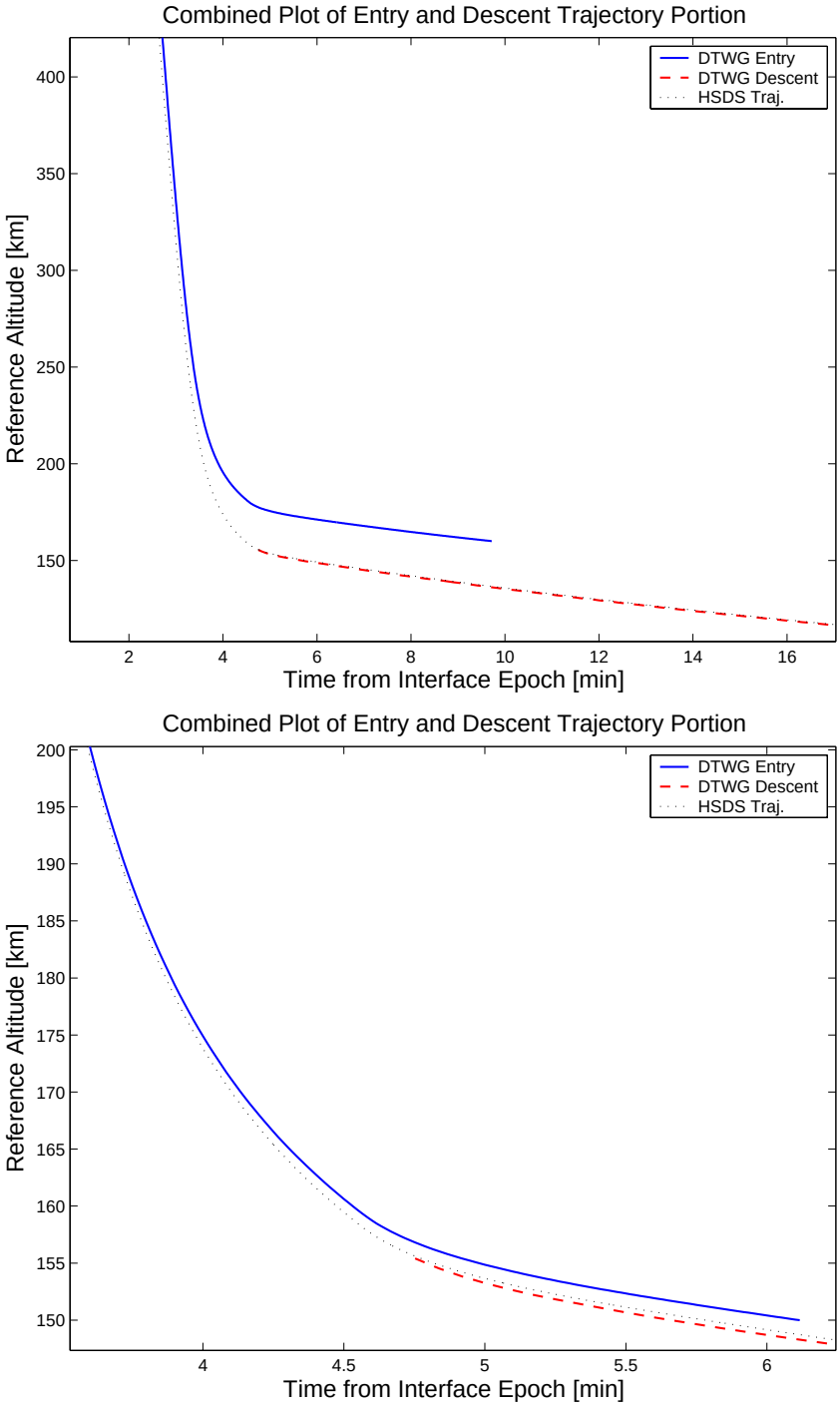

Figure 11.4: *Comparison of the entry phase trajectory using the biased* ***FIT_TC2*** *state vector (upper panel) and after application of the corrections in Table 11.7.*

	HSDS (JPL040225)	HSDS 1σ	Bias	Modified State
x	-1.312458638E+02	3.920909191E+01	-0.2σ	-1.390876822E+02
y	-3.824933072E+03	9.296961868E+01	-0.2σ	-3.843526996E+03
z	-3.697321588E+02	1.340085253E+01	-0.5σ	-3.764325851E+02
v_x	-2.346112519E+00	3.571847510E-03	$+0.5\sigma$	-2.344326595E+00
v_y	5.539336275E+00	8.932350759E-03	-0.5σ	5.5348701E+00
v_z	4.588600223E-01	1.773649315E-03	$+0.5\sigma$	4.59746847E-01

Table 11.5: *Comparison of the nominal probe initial state vector and corresponding uncertainties as provided in the HSDS to the biased vector as used for* ***FIT_TC2****. The interface epoch is January 14, 2005 09:00:00.000 ET. Units are in km and km/s respectively.*

Time [min]	Z [km]	$Z - z$ [km]	$\dot{Z} - \dot{z}$ [m/s]
4.7527	155.40893	-22.072	-7.939
4.8361	154.53744	-22.188	-3.994
4.9194	153.82772	-22.257	-1.178
5.0027	153.22591	-22.297	6.831
5.0861	152.70007	-22.320	2.040
5.1694	152.23116	-22.333	2.825
5.2527	151.80901	-22.335	3.509
5.3361	151.42121	-22.330	-1.993

Table 11.6: *Residuals (descent phase - entry phase) of the reconstructed altitude and descent speed in the overlapping portion of the trajectory for the* ***FIT_TC2*** *biased initial conditions. The time is given in minutes relative to the interface epoch. Note that the capital letters Z and $\dot{Z}$ are used for the altitude and descent speed of the descent phase (those values are considered as the "observations" in the sense of an orbit determination problem) and the small letters z and $\dot{z}$ for the corresponding values derived from the spacecraft accelerometer integration.*

	Proposed correction	New vector
x	1.036123175E+00	-1.380515590E+02
y	2.319775270E+01	-3.820329243E+03
z	-1.733993919E+01	-3.937725243E+02
vx	1.410112271E-03	-2.342916483E+00
vy	-2.442758010E-03	5.532427342E+00
vz	1.051270033E-03	4.607981170E-01

Table 11.7: ***FIT_TC2*** *proposed state vector corrections and corrected state vectors. Units are [km] and [km/s].*

Time [min]	Z [km]	$Z - z$ [km]	$\dot{Z} - \dot{z}$ [m/s]
4.7527	155.40893	-1.398	-7.648
4.8361	154.53744	-1.513	-3.618
4.9194	153.82772	-1.580	-7.201
5.0027	153.22591	-1.619	1.224
5.0861	152.70007	-1.638	2.663
5.1694	152.23116	-1.647	3.531
5.2527	151.80901	-1.645	4.298
5.3361	151.42121	-1.637	-1.114

Table 11.8: *Residuals (descent phase - entry phase) of the reconstructed altitude and descent speed in the overlapping portion of the trajectory for the* ***FIT_TC2*** *after applying corrections (first iteration) specified in Table 11.7 to the nominal state vector.*

	Proposed correction	New vector
x	-4.796161577E-01	-1.385311752E+02
y	1.349445787E+00	-3.818979797E+03
z	5.217993901E+00	-3.885545304E+02
vx	1.817415363E-03	-2.341099068E+00
vy	-4.374303833E-03	5.528053038E+00
vz	-5.153095604E-04	4.602828074E-01

Table 11.9: ***FIT_TC2*** *probe state vector corrections and new state vector after the second iteration of the fitting algorithm. Units are [km] and [km/s].*

Time [min]	Z [km]	$Z - z$ [km]	$\dot{Z} - \dot{z}$ [m/s]
4.7527	155.40893	-0.721	-10.145
4.8361	154.53744	-0.855	-0.745
4.9194	153.82772	-0.941	-4.570
5.0027	153.22591	-0.999	-2.648
5.0861	152.70007	-0.104	-1.233
5.1694	152.23116	-0.107	-3.919
5.2527	151.80901	-0.108	0.350
5.3361	151.42121	-0.120	-5.085

Table 11.10: *Residuals (descent phase - entry phase) of the reconstructed altitude and descent speed in the overlapping portion of the trajectory for the* ***FIT_TC2*** *after applying corrections (second iteration) specified in Table 11.9 to the nominal state vector.*

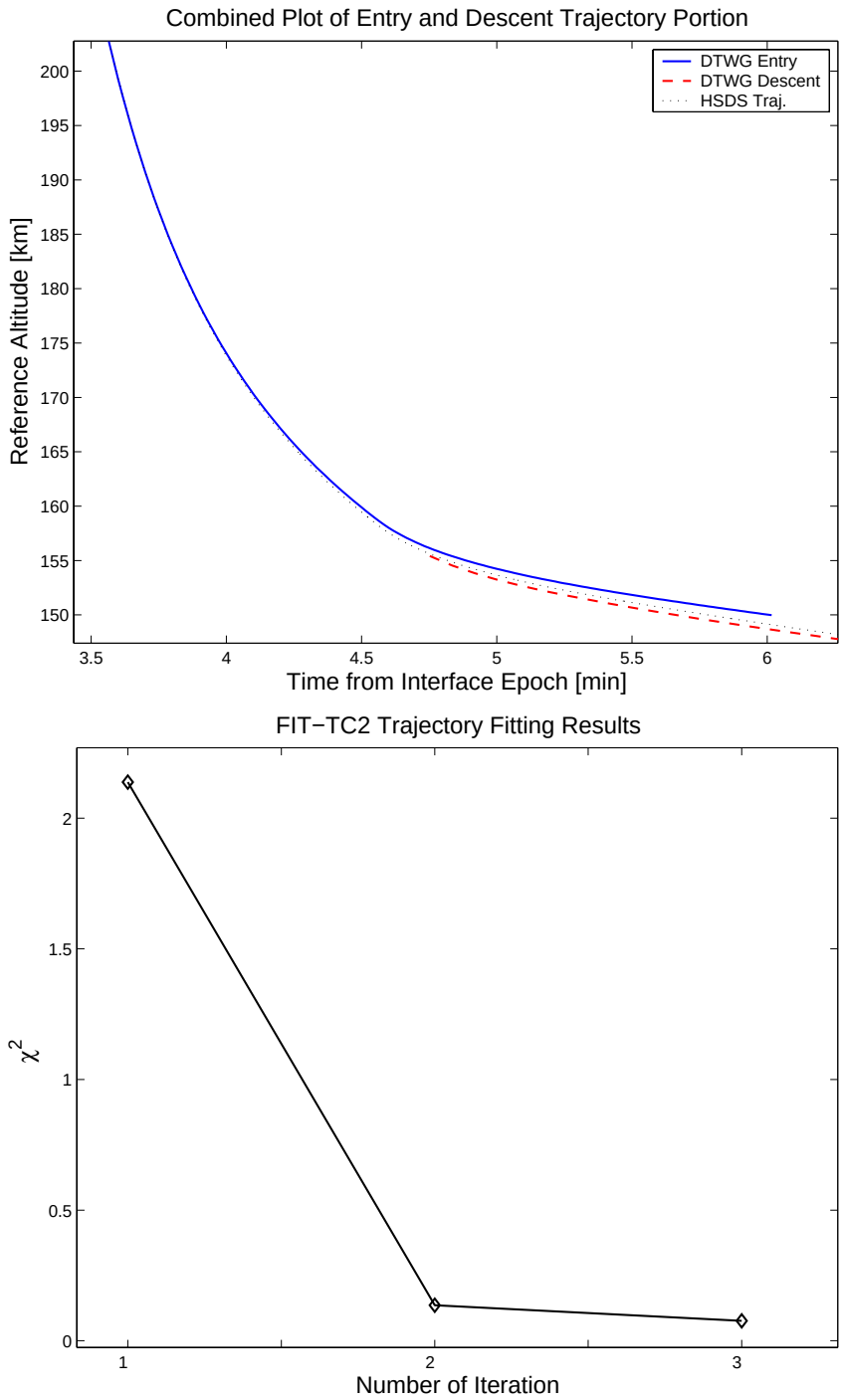

Figure 11.5: *Upper panel: comparison of the entry phase trajectory using the biased* ***FIT_TC2*** *state vector after applying the state vector corrections as listed in Table 11.9. Lower panel: FIT_TC2 χ^2 for 48 input observations (i.e., 24 altitude and 24 descent speed residuals) as a function of the number of iterations of the trajectory fitting algorithm.*

Chapter 12

Mars Pathfinder Reconstruction

In this Chapter the entry phase reconstruction algorithm (see Chapter 6) is applied to real flight data from the Mars Pathfinder spacecraft. Section 12.1 provides 12.2 an overview of the Pathfinder mission and the spacecraft measurements that are relevant for the trajectory reconstruction. The trajectory reconstruction results are presented in Section 12.3 and compared to previous efforts. Section 12.4 presents the results of the atmosphere reconstruction effort.

12.1 Pathfinder Mission Overview

Mars Pathfinder (MPF) was one of the first two missions launched under NASA's new Discovery Program. The mission was designed to demonstrate a low-cost, reliable system for entering the Martian atmosphere and placing a lander safely on the surface of Mars. Pathfinder also carried a science payload that returned data on Mars' atmosphere, meteorology, geology and morphology, and the elemental composition of rocks and soil near the lander (Golombek *et al.*, 1999).

The Mars Pathfinder spacecraft entered the Martian atmosphere directly from an Earth-to-Mars interplanetary transfer trajectory with an inertial velocity of 7.26 km/s. With the release of the cruise stage at 30 minutes prior to entry, the ability to propulsively control the spacecraft was lost. The entry vehicle was spin-stabilized with a roll rate of 2.0 rpm, and the vehicle spin axis was aligned so that the angle of attack with respect to the relative wind at the atmospheric interface (defined at a radius of 3522.2 km) would be near zero nominally. The entry vehicle mass was 585.3 kg, and the hypersonic continuum ballistic coefficient was 63.1 kg/m^2.

The spacecraft Entry, Descent, and Landing (EDL) sequence (see upper panel of Fig. 12.1) comprised the use of the aeroshell (i.e., forebody heatshield and aftbody backshell) during the entry phase, a parachute for the descent phase, a set of three solid rockets (initiated by the radar altimeter unit), and an airbag system for the final part of the descent and the impact on the surface.

The Pathfinder aeroshell consisted of a forebody heatshield and an aftbody backshell (see lower panel of Fig. 12.1). The aeroshell diameter was 2.65 m, and the forebody shape was a Viking- heritage 70 deg half-angle sphere-cone with a nose radius of 0.6638 m and a shoulder radius of 0.0662 m. The forebody ablative material was SLA-561V, with a uniform thickness of 19.05 mm. SLA-561V is a silicon-based ablator, which consists

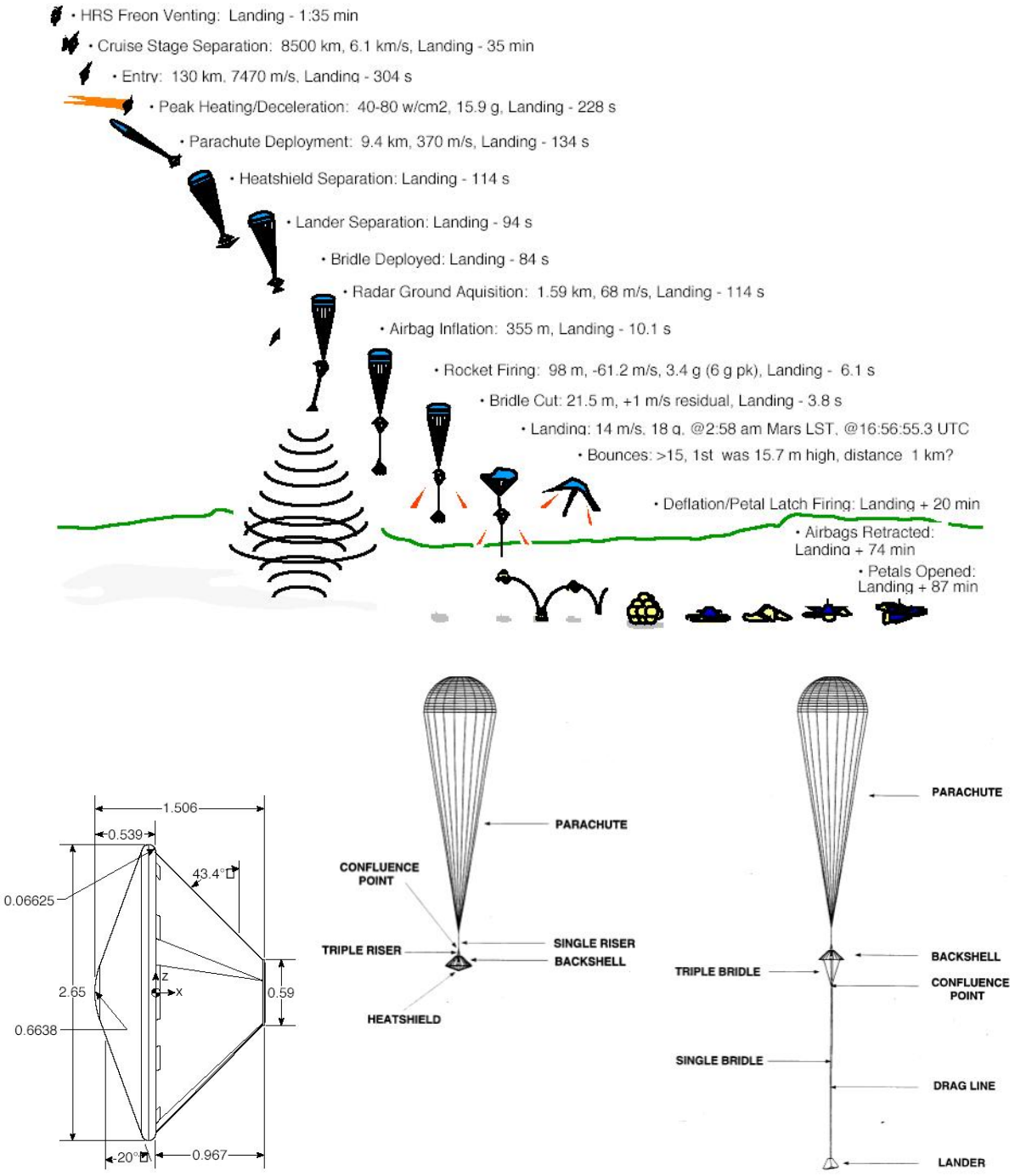

Figure 12.1: *Upper panel: MPF entry, descent, and landing sequence; Lower left: Pathfinder Aeroshoell; Lower right: Pathfinder parachutes (Spencer* et al.*, 1998).*

consists of a mixture of silicone, silica microballoons, corks, and silica glass fibers. The mixture is injected into a reinforcing phenolic honeycomb. The backshell was thermally protected with a silicon-based ablator (SIRCA) developed at Ames Research Center. The heatshield mass was 64.4 kg, and the backshell mass was 56.9 kg (Spencer *et al.*, 1998).

The Pathfinder parachute was a modified Viking-heritage disk-gap-band design, developed by Pioneer Aerospace. The parachute canopy was made of Dacron, with Kevlar suspension lines. The Project requirement for peak dynamic pressure at parachute deployment was 703 N/m^2, although parachute drop tests had indicated that dynamic pressures over 800 N/m^2 were within the design capability. The total parachute mass was 17.5 kg. The stowed parachute and suspension lines were packaged within an overpack, or container, which in turn was inserted into a deployment canister. Deployment was achieved through use of a mortar assembly, which was initiated by an electroexplosive device.

12.2 Discussion of Accelerometer Measurements

Two sets of three orthogonally-positioned Allied Signal QA-3000 accelerometer heads each provided 3-axis acceleration measurements during entry. One set of accelerometers was part of the Atmospheric Structure Investigation/Meteorology (ASI/MET) experiment (Schofield *et al.*, 1997; Seiff *et al.*, 1997). The ASI/MET accelerometers were range switched during the entry trajectory to provide increased resolution. Dynamic ranges of 16 mg, 800 mg and 40 g were used. Changes in gain state were commanded by an onboard data management subsystem, which monitored the magnitude of the decelerations during the EDL sequence. The ASI/MET accelerometers were aligned parallel to the entry vehicle coordinate system axes. The second set of accelerometers was used as the primary input for the parachute deployment algorithm. This set of engineering accelerometers was oriented such that two of the sensor heads were canted at ± 45 deg to the entry vehicle Z-axis (the longitudinal axis) in the Y-Z plane, and the third accelerometer head was aligned with the X-axis. No Inertial Measurement Unit or gyros were used. The science accelerometers were all within 15 mm of the spacecraft Z-axis and within 155 mm of the center of mass (CM) of the vehicle during its entry phase configuration, which was along the Z-axis to high accuracy. The close proximity of the CM and the Z-axis to the entry vehicle's symmetry axis ensured that the measurements of the axial accelerations were largely free of signal due to the vehicle motions about the CM.

Time-ordered acceleration data showing key events during the Pathfinder entry, as measured by the ASI/MET accelerometers, are shown in Figures 12.2 and 12.3. These figures are presented in time segments starting at the atmospheric entry interface and extending beyond touchdown. The upper two panels of Fig. 12.2 present the initial 40 s of the entry trajectory starting at the time, which corresponds to the entry interface radius of 3352.2 km. The normal acceleration (second panel) is the RSS of the two accelerometers normal to the axial acceleration (first panel). The axial accelerometer shows the acceleration disturbance created when the instrument detects an automatic uprange condition. This spurious spike in the data is also seen on the subsequent figures. The normal acceleration disturbance, at about 29 sec., is attributed to the removal of the Kapton thermal shield that protected the probe during the interplanetary cruise phase.

The lower two panels of Fig. 12.2 show the continuation of the accelerometer data from 40 to 180 sec. The axial accelerometer range changes to its maximum value of 40 g

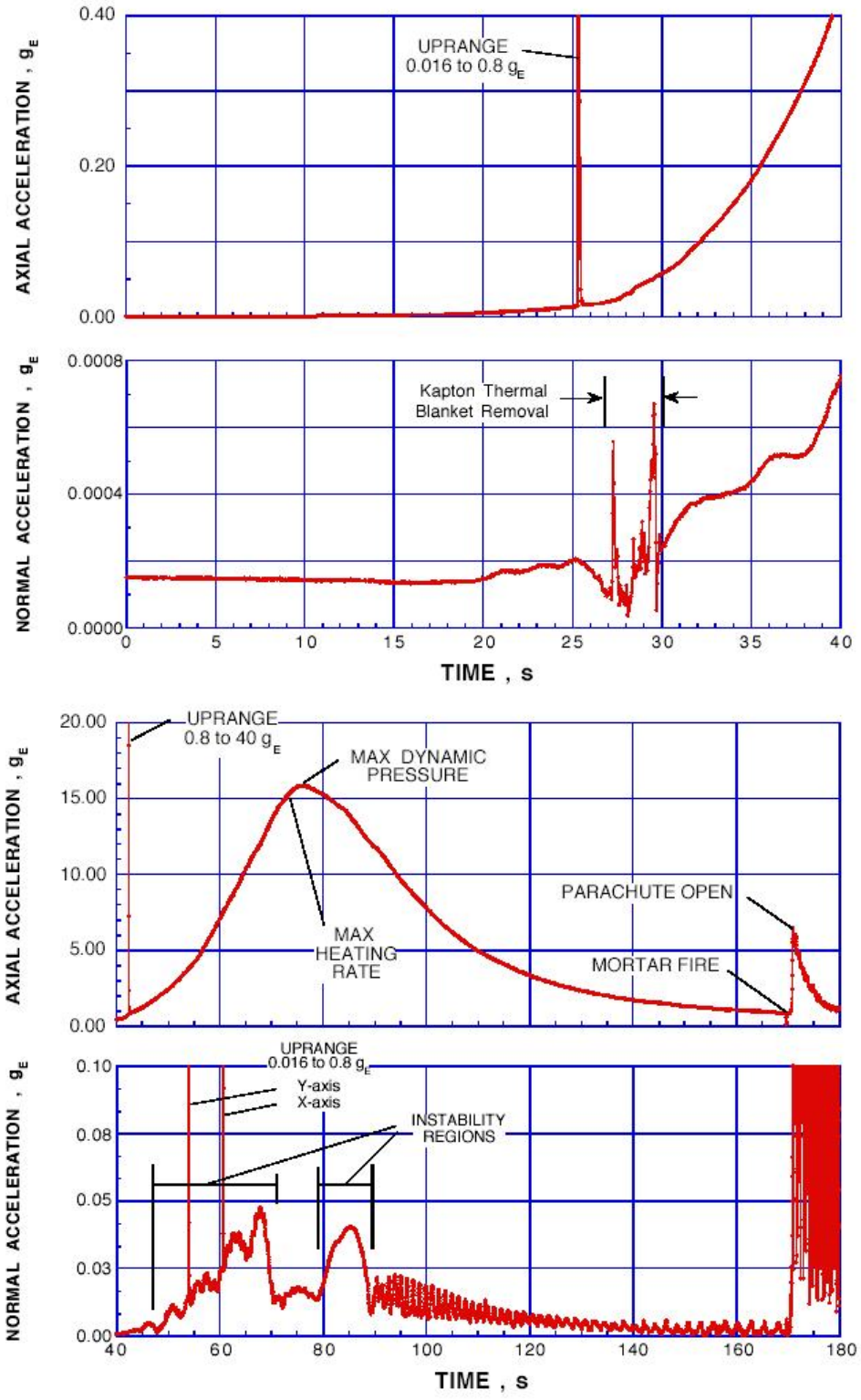

Figure 12.2: *Mars Pathfinder axial and normal acceleration for the first 180 sec. relative to the time that corresponds to the entry interface radius of 3352.2 km (Spencer* et al.*, 1998).*

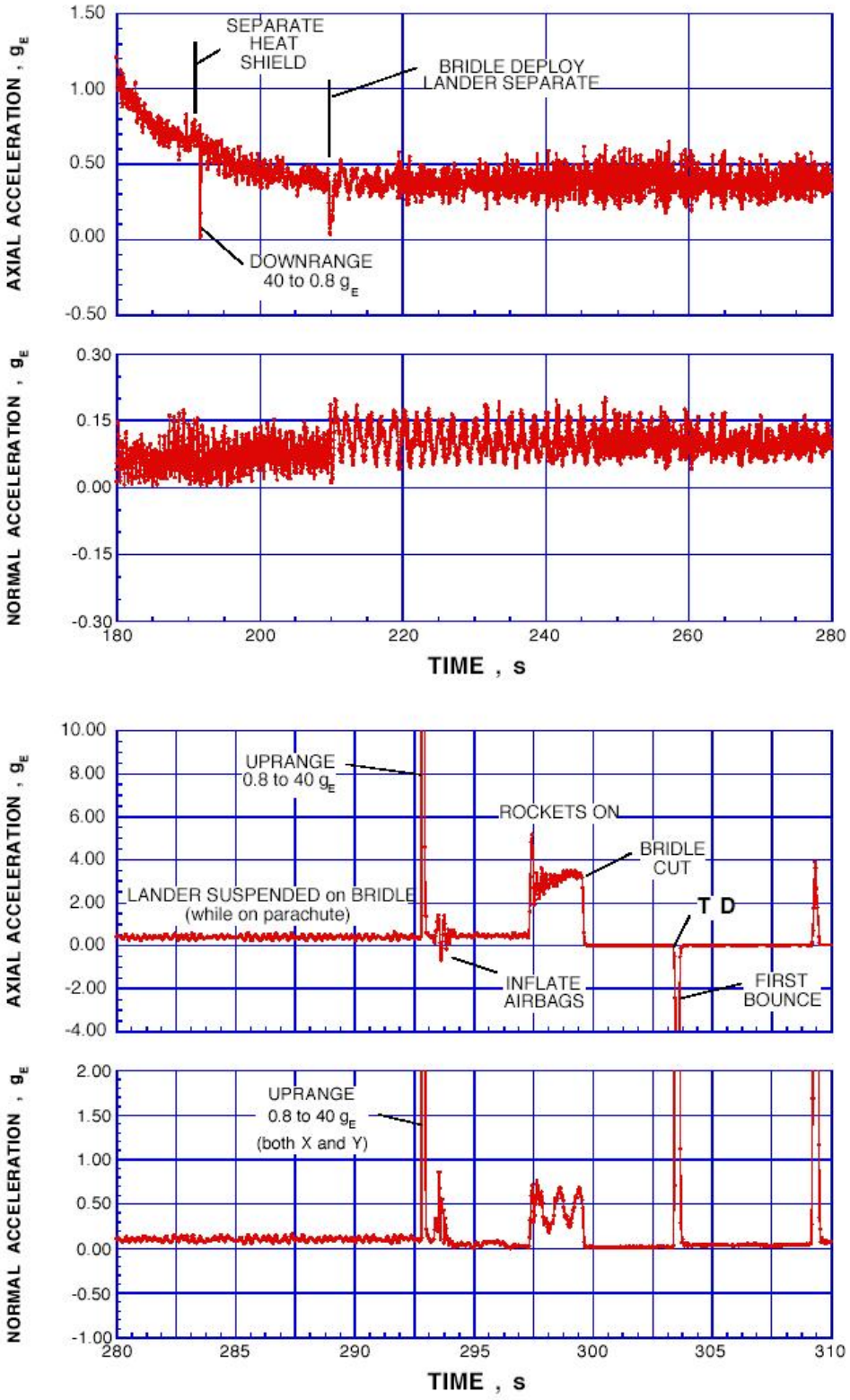

Figure 12.3: *Mars Pathfinder axial and normal acceleration from 180 – 310 sec. relative to the time that corresponds to the entry interface radius of 3352.2 km (Spencer* et al.*, 1998).*

(full scale) at about 44 sec. A short time later, both the Y-axis and X-axis accelerometers are automatically upranged to their next range level (0.8 g). The axial accelerometer shows the key events of: (1) maximum dynamic pressure, which closely corresponds to the maximum acceleration of 16.1 g, (2) firing of the pyrotechnic devise, which jettisons the parachute canister (labeled as mortar fire), and (3) the 6.2 g shock induced when the chute opens.

The upper two panels of Fig. 12.3 show a continuation of this data during the parachute phase of the mission for a time period covering 180 sec. to 280 sec. from the atmospheric interface. The axial accelerometer shows the automatic down range to its next lowest scale of 0.8 g. Also seen are the separation of the heatshield and the separation of the lander onto a 20 m bridle as discussed earlier. At this time, there is a corresponding shift in the normal accelerations. This is expected since the spacecraft center of gravity has shifted significantly, providing an additional small but spurious centripetal input into the accelerometers (which are not located exactly at the center of gravity).

The lower two panel of Fig. 12.3 show the remaining portion of the parachute phase down to airbag impact, including the first bounce on the surface of the planet, 280 sec. to 310 sec. past the atmospheric entry interface. Both the axial and normal accelerometers are forced to go to full scale (40 g) in anticipation of landing. The uprange signature of the instrument is clearly seen in the figure. Shortly thereafter, the airbags are inflated, and then the Rocket Assisted Deceleration (RAD) system is ignited. Note that a small component of the thrust appears in the normal direction. While the rockets are providing the retarding force, the bridle, from which the lander is suspended, is cut and the lander free- falls to the surface and begins to bounce. The first bounce spike due to impact with the surface is indicated.

A summary of the MPF EDL sequence events and their timing with respect to the entry interface epoch was provided by Spencer *et al.* (1998) and shown in Table 12.1. The ASI/MET accelerometer measurements and the reconstructed trajectory together with the derived atmospheric properties are available on the PDS volume MPAM_0001, which is online at http://atmos.nmsu.edu/PDS/data/mpam_0001/.

12.3 Trajectory Reconstruction

Entry State Vector

The best entry state vector solution was obtained from the pre-entry trajectory utilized range and Doppler data collected from 4 February 1997, to 4 July 1997 at 15:36 UTC. Tracking data after 15:36 UTC was judged unusable since at that time the spacecraft had switched from coherent to non-coherent tracking, which reduced the precision of the data (Vaughan *et al.*, 1998). However, this non-coherent Doppler data was later utilized in conjunction with onboard accelerometer and other spacecraft-based data. The results of this solution were used to update and predict the conditions at the atmosphere entry point, which was defined to occur at a radial distance of 3522.2 km. Table 12.2 provides the entry state resulting from this orbit solution as provided by Vaughan *et al.* (1998) and used by Spencer *et al.* (1998). Table 12.3 provides the same state vector transformed into a planet-centered EME2000 reference system.

EDL Sequence Event	Time from Entry [sec.]
Entry Interface (Radius=3522.2 km)	0
Thermal Blanket Removal (begin)	27.2
Max Heat Rate	73.2
Max Dynamic Pressure	76.1
Mortar Fire	169.6
Parachute Open	170.9
Heatshield Separation	190.3
Bridle Deploy (Lander Sep.)	209.6
Inflate Airbags (begin)	293.3
Rocket Ignition	297.3
Bridle Cut	299.5
Touchdown (1st Bounce)	303.4
Last Recorded Bounce	258.4
Last Data Record	359.3

Table 12.1: *Mars Pathfinder EDL sequence events as provided by Spencer* et al. *(1998)*

Parameter	Orbit Determination Estimate
Epoch	4-JUL-1997, 16:51:50.482 UTC
Radial Distance	3522.2 km
Areocentric Latitude	22.6303 deg
Longitude	338.1691 deg
Inertial Flight Path Angle	-14.0610 deg
Inertial Velocity	7.2642 km/s
Inertial Flight Path Azimuth	253.1479 deg

Table 12.2: *Mars Pathfinder estimated entry state from orbit determination. A planetary radius of R_P=3522.2 km is assumed.(Spencer* et al.*, 1998)*

	Orbit Determination Estimate
x	1360.62662662080D+00
y	-3176.82807430583D+00
z	-679.964270556047D+00
vx	-7.16847147687223D+00
vy	-1.15739189422690D+00
vz	0.205091024784583D+00

Table 12.3: *Mars Pathfinder entry state from Table 12.2 transformed into Mars centered EME2000 reference system.*

Previous Reconstruction Efforts

The Mars Pathfinder entry and descent trajectory was independently reconstructed by Magalhães *et al.* (1999), Spencer *et al.* (1998), and more recently by Withers *et al.* (2003). The Magalhães *et al.* (1999) reconstructed trajectory is provided in the Planetary Data System (PDS) volume MPAM_0001 together with the initial state vector, which differs from that used by Spencer *et al.* (1998)[1]. An independent reconstruction effort was done by Spencer *et al.* (1998) which is based on the combination of accelerometer, altimeter, and ground-based measurements of received frequency using sequential filtering and smoothing techniques. The Spencer *et al.* (1998) initial state vector is given in Table 12.2 and was also used for this reconstruction effort.

Accelerometer Data Preprocessing

The Mars pathfinder accelerometer measurements are provided in the PDS volume in the /edl_erdr directory. The file /edl_erdr/r_sacc_ s.tab contains the dataset with the highest sampling rate (i.e., 32 Hz). Accelerations need to be multiplied by a reference value for the Earths gravity, 9.795433 ms^{-}2.

One x-axis data point is 0.0, a clear outlier from the neighbouring data points. One z-axis data point is also 0.0 and an outlier. These are mentioned in Magalhães *et al.* (1999) and Withers *et al.* (2003) but not in the file /document/edler_ ds.htm. These were replaced with an interpolation from neighbouring data points. There are also about 10 data points in the y-axis data that are zero. However, these are consistent with neighbouring data points and have not been modified.

The accelerometers have several different gain states. The gain state of each accelerometer changed several times during atmospheric entry. When an accelerometer changes gain state, there is a brief acceleration pulse that is an artifact of the electronic time constant of the sensor (see spikes in Fig. 12.2 and Fig. 12.3). From calibration studies as discussed in Magalhães *et al.* (1999) the time constant for the transients was far less than one second and the effects of the transients were generally undetectable within about 1 second of the gain change. The values in the transient were therefore replaced by interpolation between the values acquired before the gain change and the values acquired about 1 second after the gain change.

Trajectory Reconstruction Results

The MPF entry and descent trajectory was reconstructed by integration of the equations of motion. To account for the effects of gravity, a gravity model was used that includes the first zonal harmonic coefficient ($J2$=1.960E-03) in the normalized spherical harmonic expansion of the gravity field. The aerodynamic drag was taken from the PDS 32 Hz axial accelerometer measurement file. The initial state vector was taken from Spencer *et al.* (1998) after transforming it into a Mars centered EME2000 system.

[1]The initial conditions provided in the PDS and published by Magalhães *et al.* (1999) are very likely inconsistent with the PDS archived trajectory. This problem was already discussed by Withers *et al.* (2003) and could be confirmed in this work. The Magalhães *et al.* (1999) state vector was therefore not used in further reconstruction efforts.

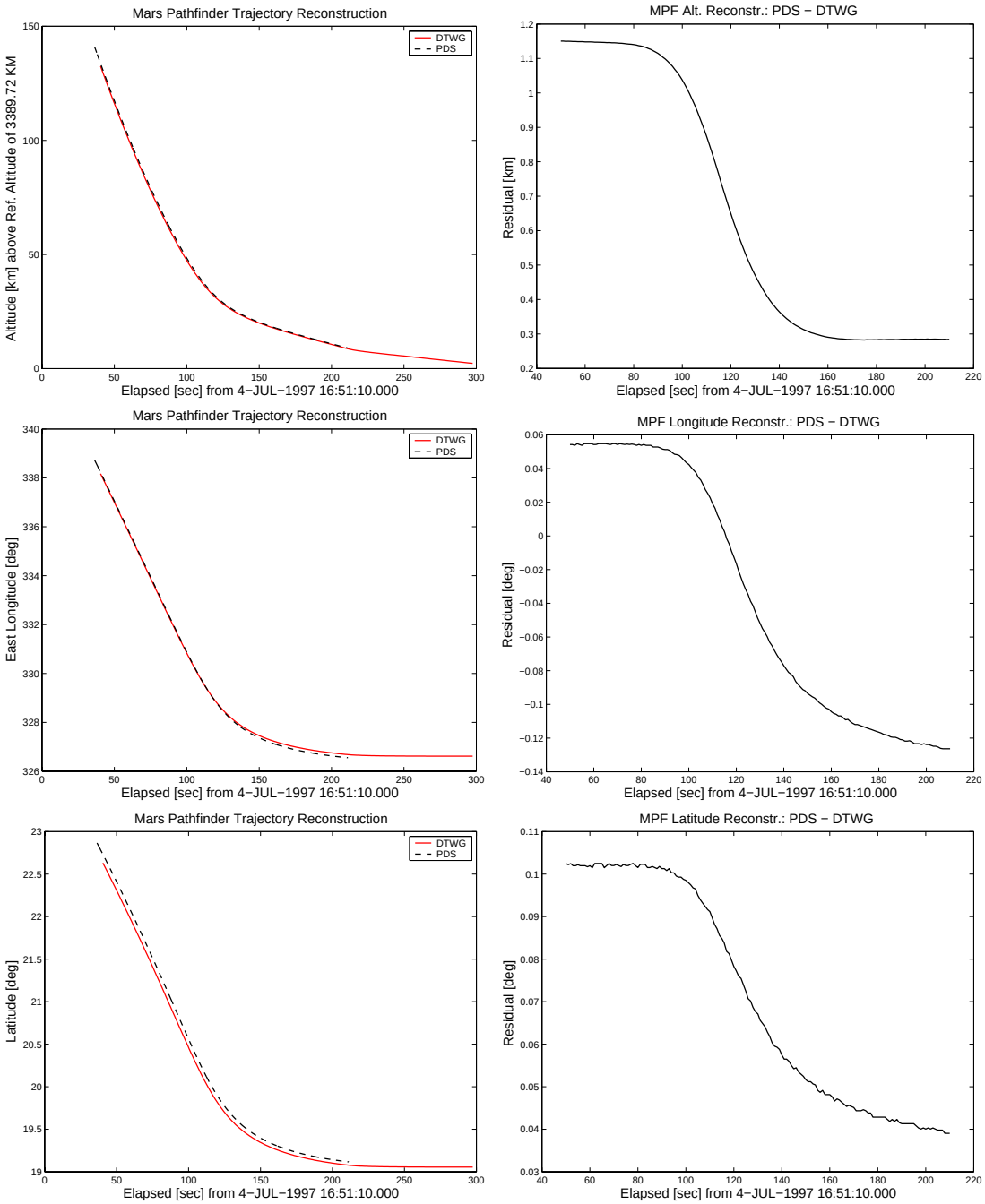

Figure 12.4: *Pathfinder trajectory reconstruction results. The left panel show an overlay of the reconstructed trajectory onto the PDS archived one. The right panels show the residuals (PDS minus reconstructed) in the overlapping region.*

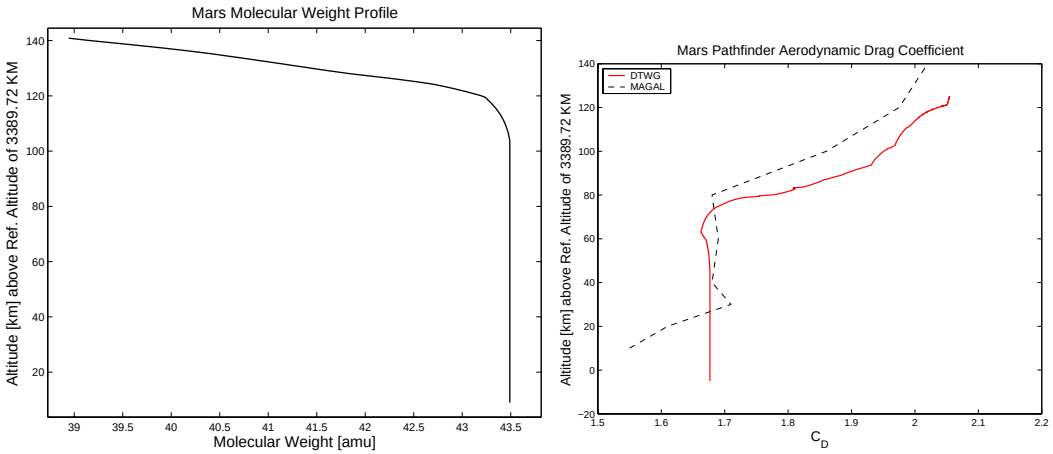

Figure 12.5: *Left panel: Mars molecular weight profile; Right panel: interpolated MPF drag coefficient.*

Method	E. Long. [deg]	Latitude [deg]
DTWG effort	326.62	19.05
Landmark recogniton	326.45	19.33
Radiometric tracking	326.48	19.28
PDS archive	326.48	19.09

Table 12.4: *Comparison of MPF landing site as obtained from this reconstruction effort (DTWG reconstruction), the PDS archive position (Magalhães* et al.*, 1999), and the position derived from radiometric tracking and landmark recognition (Golombek* et al.*, 1997).*

Fig. 12.4 compares the results of this effort (solid line) to the PDS archived one (dashed line) from Magalhães *et al.* (1999). The left panels overlay the trajectories and the right panels show the corresponding residuals (PDS minus reconstruction). The altitude residuals decrease from slightly more than 1 km down to only 300 m (about 10 km prior to landing). The longitude residuals increase from about 0.05 deg up to - 0.13 deg and the latitude residuals decrease from 0.1 down to 0.04 deg. The residuals are within the order of magnitude of the entry state uncertainties (Vaughan *et al.*, 1998).

Table 12.4 compares the MPF landing point coordinates of this reconstruction effort to the Magalhães *et al.* (1999) position as well as the coordinates derived from landmark recognition and lander radiometric tracking and provided by Golombek *et al.* (1997). One can see that the differences in all cases are lower than 0.2 deg in longitude and 0.3 deg in latitude.

12.4 Atmospheric Structure Reconstruction

The methodology to reconstruct the atmospheric properties from spacecraft accelerometer is described in detail in Sec. 6.6. First the atmospheric density profiles was derived from

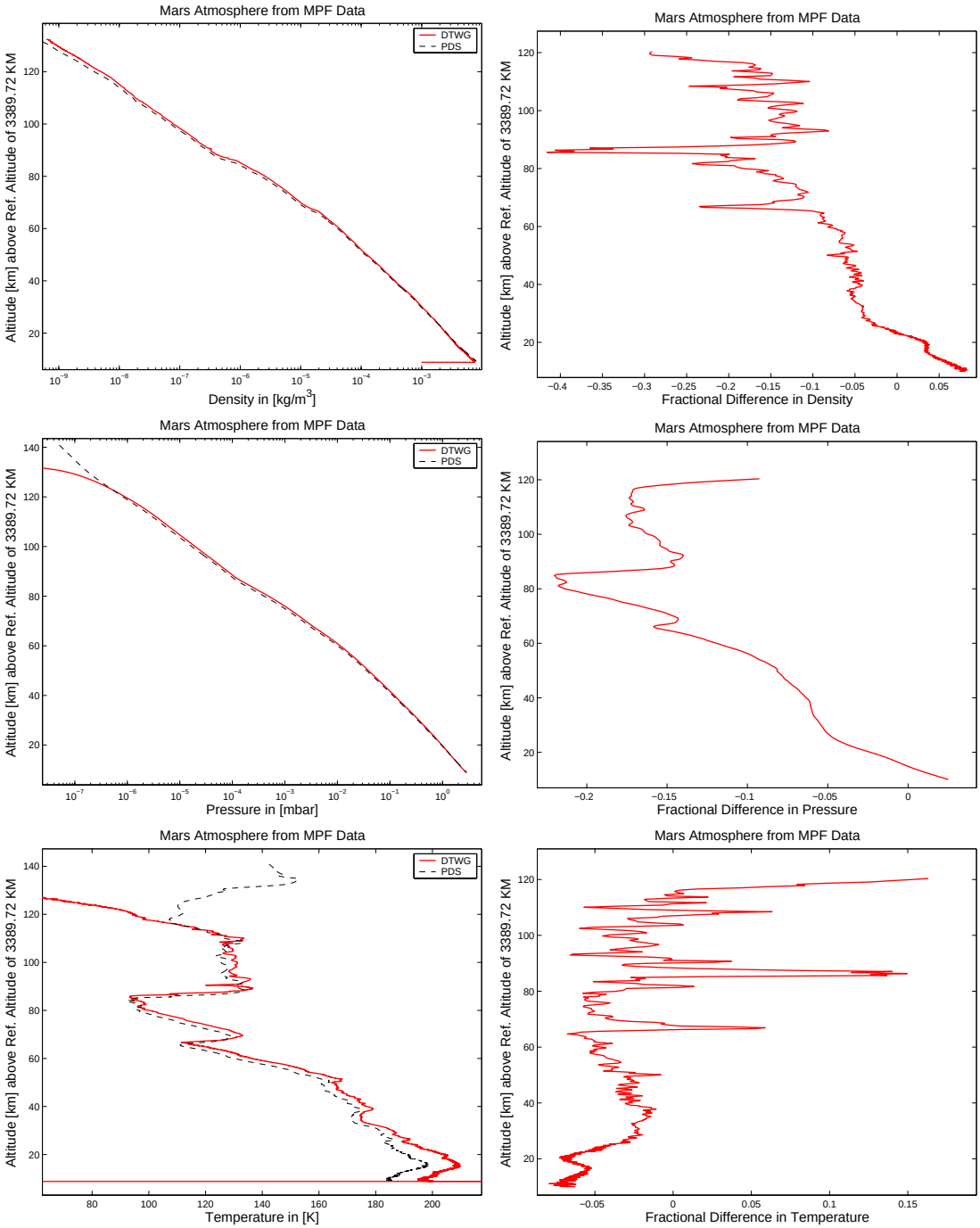

Figure 12.6: *Mars Atmosphere properties reconstructed from MPF entry accelerometer measurements. The left panels show an overlay of the reconstructed and the PDS archived profiles and the right panels show the corresponding fractional differences (relative mutual deviations).*

the probe accelerometer measurements [see Eq. (6.21)]. This required the knowledge of the probe mass, cross-sectional area, relative velocity, and the drag coefficient. During the entry phase, the total mass of the Pathfinder entry vehicle was $m = 585.3$ kg and its area was $A = 5.526$ m^2. These values are considered to remain constant during the entire entry phase. The relative velocity was taken from the trajectory reconstruction effort as described in the previous section. The drag coefficient of the probe varies during the entry, and this variation was accounted for iteratively using the aerodynamic database from Moss *et al.* (1998). The drag coefficient was interpolated as a function of the angle-of-attack α and hard sphere Knudsen number $Kn_{\infty,HS}$ and is shown in the right panel of Fig. 12.5.

As a second step the atmospheric pressure profile was reconstructed by integrating the equation of hydrostatic equilibrium and using an initial pressure estimation of $p_0 = 3.9532 \times 10^{-7}$ mbar (this value was taken from the PDS archived reconstructed atmosphere for an altitude of 124.58 km) as a boundary condition [see Eq. (6.25)].

Finally the temperature profile was derived from the reconstructed density and pressure profile according to Eq. (6.26). This required the knowledge of the molecular mass as function of altitude. For the temperature reconstruction effort the Martian atmosphere was considered as being well mixed below an altitude of 100 km having a mean molecular weight of 43.49 amu. This value is based on Viking Lander mass spectrometer measurements (Owen *et al.*, 1976). At higher altitudes photodissociation and diffusive separation lead to a gradient with altitude of the mean molecular weight. The variation of the molecular mass with pressure was modeled based on the Viking 1 Upper Atmosphere Mass Spectrometer results (Nier and McElroy, 1977; Seiff and Kirk, 1977) and is shown in the left panel of Fig. 12.5.

The reconstructed atmosphere properties are shown in Fig. 12.6 and compared to those from Magalhães *et al.* (1999) (labeled as "PDS"). The left panels show an overlay of the density, pressure, and temperature profiles and the right panels show the corresponding fractional differences (i.e., the relative mutual deviation of the reconstructed and the PDS profile). The density and pressure profiles are consistent within the range of 20%. The temperature profile is consistent to about 5%. In all three profiles sudden jumps at about 85 and 65 km can be seen, which were also reported by Withers *et al.* (2003). These jumps coincide with the altitudes of changes in the accelerometer gain states. A possible explanation could therefore be that Magalhães *et al.* (1999) used a different interpolation technique in their data preprocessing.

12.5 Attitude Reconstruction

The spacecraft attitude was reconstructed from the ratio of the measured normal and axial accelerations using the preflight aerodynamic database as published by Moss *et al.* (1998) (see Appendix C).

The left panel of Fig. 12.7 shows the ratio of normal and axial acceleration as a function of elapsed time from the interface epoch. The right panel shows the reconstructed angle-of-attack profile. Those results can be compared to Fig. 12.8 that shows the corresponding profiles as published by Spencer *et al.* (1998). One can see that the two acceleration ratios differs slightly, which indicates that the Spencer *et al.* (1998) input data might have been differed from the one that was finally published on the PDS. One can also see

the spikes from the accelerometer gain state change in the Spencer *et al.* (1998) data, which where removed prior to this reconstruction effort. The angle-of-attack profile of this reconstruction effort shows slightly lower values but reproduces well the overall shape as shown in the Spencer plot. The difference in the angle-of-attack might (apart from a different acceleration input dataset) also be due to the use of a different version of the MPF aerodynamic dataset.

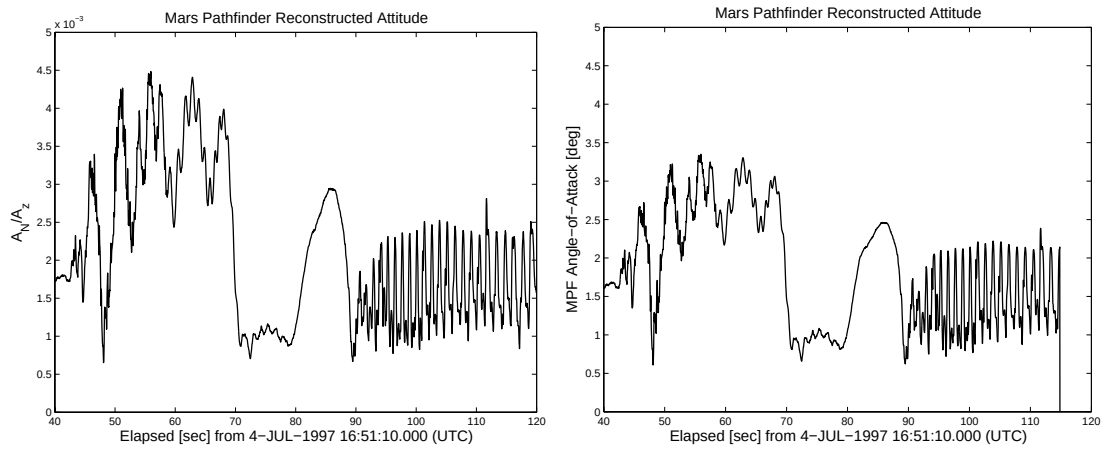

Figure 12.7: *Pathfinder entry phase attitude reconstruction. The left panel shows the ratio of normal to axial accelerations and the right panel depicts the reconstructed angle-of-attack.*

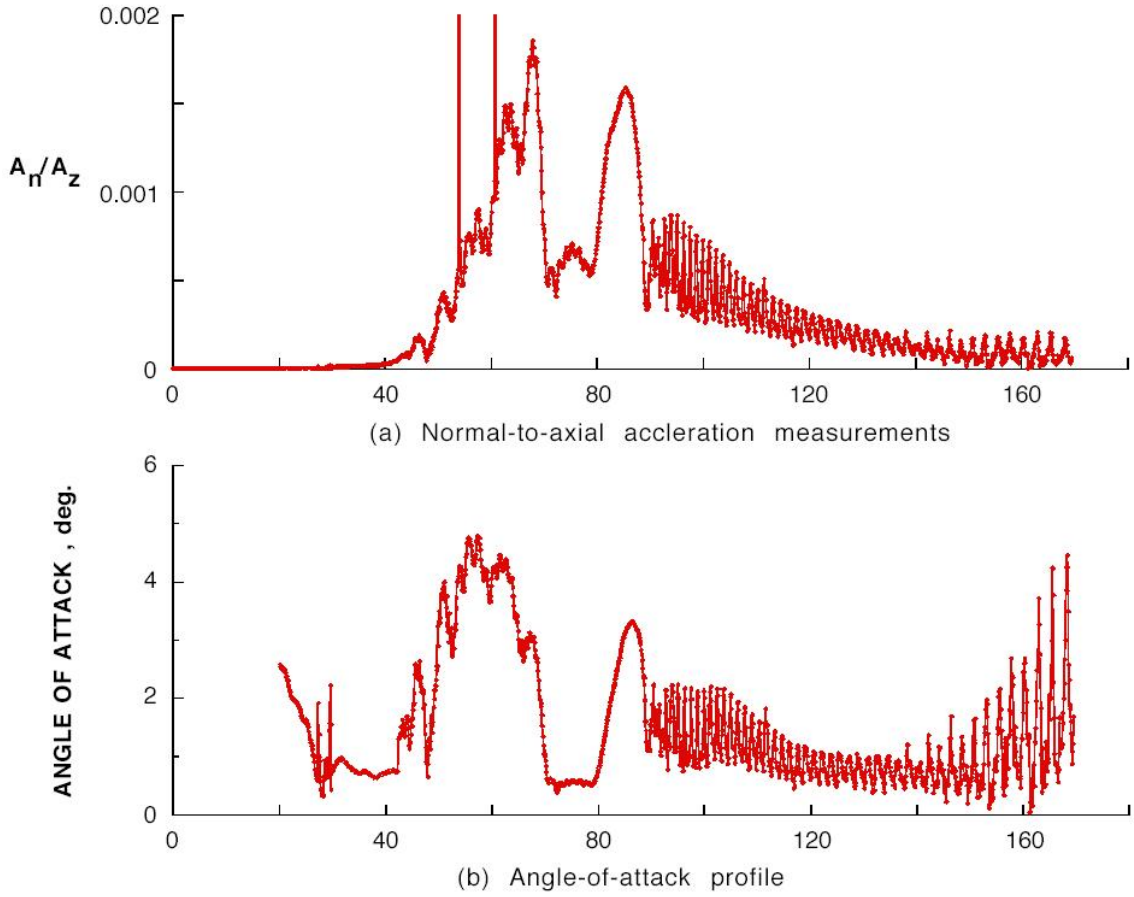

Figure 12.8: *Pathfinder entry phase attitude reconstruction from Spencer* et al. *(1998).*

Chapter 13

Concluding Remarks

Huygens is the first planetary probe that entered Titan's atmosphere and descended down to the planet's surface. The reconstruction of its entry and descent trajectory is therefore an important task for both the proper scientific interpretation of all the sampled data and the assessment of the probe entry descent and landing system. The probe trajectory as well as Titan's upper atmosphere can be reconstructed from the various measurements of the engineering and scientific payload. A reconstruction methodology was developed, implemented, and successfully applied to a simulated probe dataset, which is representative of the actual flight data in terms of sampling time, resolution, and dynamic sensor behavior.

The entry phase test campaign clearly showed that the implemented algorithm is capable of reconstructing the entry phase trajectory based on the measured HASI X-servo accelerations. In case of a failure of this sensor, the HASI X-piezo measurement can be used as a backup, and a reasonably good reconstruction result still be achieved. A trajectory reconstruction that is entirely based on the probe engineering accelerometer (CASU) however implies a significant decrease in accuracy due to the limited measurement range ($10g$) of this instrument. The reconstruction strategy could in this case be enhanced by replacing the missing accelerometer measurements beyond 10 g with a simulated profile, which however was not explicitly developed nor implemented in this work. It could furthermore be shown that a proper estimation of wind speed for altitude ranges where no direct DWE measurements are available contributes significantly to the accuracy of trajectory reconstruction. Even if the high altitude winds will only be known to a limited extent from Cassini and Earth-based remote sensing, it is better to take into account the best available estimation rather than ignoring the winds alltogether. The upper atmosphere density, pressure, and temperature profiles were also successfully reconstructed from the probe accelerometer measurements. It was found that the integrated pressure profile is mainly sensitive to the initial pressure value at altitudes higher than 1100 km. Care should therefore be taken in any scientific interpretation of the reconstructed pressure and temperature profiles higher than 1100 km. The change of the probe entry mass due to heat-shield ablation will not be directly measured (the Huygens heat-shield is not equipped with ablation sensors) and has been simulated using a simple ablation mass model. It could be shown that the mass change will affect the results of the atmosphere reconstruction in an altitude range from 200–350 km, and can result in temperature differences up to 3 K.

The descent phase test campaign showed that data smoothing due to instrument noise plays a significant role. However, care must be taken in choosing the right smoothing span. The choice of a very small span would not achieve the proper amount of data smoothing; a high span however could lead to a loss in time resolution of the input data. Span numbers for the various instrument datasets are proposed in Table 9.1. The limited sampling rate of the model input atmosphere that was used for the computation of the synthetic dataset caused oscillatory deviations from the actual trajectory which could be seen in the reconstructed altitude and descent speed of all test cases. These deviations have been analyzed and are very likely an artifact of the input data and should therefore not be present in the reconstruction results from the actual flight data. Simulated pressure and temperature data were used in two versions, one that ignored the effects of the relative flow on the sensors and another one that was modified in order to simulate this effect. From the latter dataset it could be shown that the deviation of pressure and temperature measurements due to dynamic effects has a significant impact on the reconstructed trajectory. The reconstruction efforts based on this dataset therefore included a correction due to dynamic effects before the actual reconstruction was done. It could be shown that the dynamic correction process increased the accuracy but could not fully compensate the dynamic sensor effects. These effects can therefore be considered as a systematic error in the descent phase reconstruction process. The probe longitude drift was successfully reconstructed from both the DWE zonal wind and the DISR Solar Zenith Angle measurements.

A significant effort was put into the development of a statistical trajectory estimation algorithm providing the capability to adjust the initial spacecraft state vector at 1270 km altitude in order to achieve a best match of the entry and descent phase reconstructed trajectory portions. The algorithm was tested by introducing an artificial bias into the entry state vector and as a result a mismatch of the entry and descent trajectory portions was artificially created. An iterative process using a least-squares algorithm with *a priori* knowledge converged and provided a proper correction to the state vector. The actual probe entry state vector is only known with a limited accuracy. The trajectory fitting algorithm therefore provides an important tool to decrease this uncertainty.

The Mars Pathfinder entry and descent trajectory as well as the angle-of-attack profile were reconstructed from the 3-axis science accelerometer measurements, which are archived on the Planetary Data System. The results are consistent with previous reconstruction efforts and therefore provide an additional validation of the developed reconstruction algorithm.

Appendix A

Partial and Vector Derivatives

A.1 Partial Derivatives of the Flattening Function U

From Eq. 6.12 the mixed partial derivatives of $\vec{\nabla}U$ are given by the relations

$$\begin{aligned}
\frac{\partial^2 U}{\partial r_2\,\partial r_1} &= \frac{\kappa}{|\vec{r}|^4}\left\{\frac{\partial \sin\Theta}{r_2}\left(15\,\sin\Theta\frac{r_1}{|\vec{r}|}-3\,\cos\alpha\,\cos\delta\right)-5\frac{r_1\,r_2}{|\vec{r}|^3}\,\chi(\Theta)+12\,\sin\Theta\,\cos\alpha\,\cos\delta\,\frac{r_2}{|\vec{r}|^2}\right\}\\
\frac{\partial^2 U}{\partial r_3\,\partial r_1} &= \frac{\kappa}{|\vec{r}|^4}\left\{\frac{\partial \sin\Theta}{r_3}\left(15\,\sin\Theta\frac{r_1}{|\vec{r}|}-3\,\cos\alpha\,\cos\delta\right)-5\frac{r_1\,r_3}{|\vec{r}|^3}\,\chi(\Theta)+12\,\sin\Theta\,\cos\alpha\,\cos\delta\,\frac{r_3}{|\vec{r}|^2}\right\}\\
\frac{\partial^2 U}{\partial r_3\,\partial r_2} &= \frac{\kappa}{|\vec{r}|^4}\left\{\frac{\partial \sin\Theta}{r_3}\left(15\,\sin\Theta\frac{r_2}{|\vec{r}|}-3\,\sin\alpha\,\cos\delta\right)-5\frac{r_2\,r_3}{|\vec{r}|^3}\,\chi(\Theta)+12\,\sin\Theta\,\sin\alpha\,\cos\delta\,\frac{r_3}{|\vec{r}|^2}\right\}
\end{aligned} \tag{A.1}$$

and the diagonal partial derivatives of $\vec{\nabla}U$ by

$$\begin{aligned}
\frac{\partial^2 U}{\partial^2 r_1} &= \frac{\kappa}{|\vec{r}|^4}\left\{\frac{\partial \sin\Theta}{r_1}\left(15\,\sin\Theta\frac{r_1}{|\vec{r}|}-3\,\cos\alpha\,\cos\delta\right)+\chi(\Theta)\,\zeta(r_1)+12\,\sin\Theta\,\cos\alpha\,\cos\delta\,\frac{r_1}{|\vec{r}|^2}\right\}\\
\frac{\partial^2 U}{\partial^2 r_2} &= \frac{\kappa}{|\vec{r}|^4}\left\{\frac{\partial \sin\Theta}{r_2}\left(15\,\sin\Theta\frac{r_2}{|\vec{r}|}-3\,\sin\alpha\,\cos\delta\right)+\chi(\Theta)\,\zeta(r_2)+12\,\sin\Theta\,\sin\alpha\,\cos\delta\,\frac{r_2}{|\vec{r}|^2}\right\}\\
\frac{\partial^2 U}{\partial^2 r_3} &= \frac{\kappa}{|\vec{r}|^4}\left\{\frac{\partial \sin\Theta}{r_3}\left(15\,\sin\Theta\frac{r_3}{|\vec{r}|}-3\,\sin\delta\right)+\chi(\Theta)\,\zeta(r_3)+12\,\sin\Theta\,\sin\delta,\frac{r_3}{|\vec{r}|^2}\right\}
\end{aligned} \tag{A.2}$$

with

$$\frac{\partial^2 U}{\partial r_i\,\partial r_n}=\frac{\partial^2 U}{\partial r_n\,\partial r_i} \tag{A.3}$$

The constant κ and the function $\chi(x)$ are given by Eq. 6.13 and Eq. 6.14 respectively. The function $\zeta(r_i)$ is given by

$$\zeta(r_i)=\left(\frac{1}{|\vec{r}|}-\frac{5\,r_i^2}{|\vec{r}|^3}\right) \tag{A.4}$$

A.2 Partial Derivatives of the Wind Velocity Vector

The partial derivatives of the wind velocity vector $\vec{v}_w$ in the planet centered (inertial) Q-frame are given by

$$\begin{aligned} \frac{\partial v_w(x)}{\partial r_x} &= \frac{v_w\, r_x\, r_y}{(r_x^2 + r_y^2)^{3/2}} \\ \frac{\partial v_w(x)}{\partial r_y} &= \frac{v_w\, r_y^2}{(r_x^2 + r_y^2)^{3/2}} \\ \frac{\partial v_w(x)}{\partial r_z} &= 0 \end{aligned} \tag{A.5}$$

$$\begin{aligned} \frac{\partial v_w(y)}{\partial r_x} &= \frac{v_w}{(r_x^2 + r_y^2)^{1/2}} - \frac{v_w\, r_x^2}{(r_x^2 + r_y^2)^{3/2}} \\ \frac{\partial v_w(y)}{\partial r_y} &= -\frac{v_w\, r_x\, r_y}{(r_x^2 + r_y^2)^{3/2}} \\ \frac{\partial v_w(y)}{\partial r_z} &= 0 \end{aligned} \tag{A.6}$$

$$\frac{\partial v_w(z)}{\partial r_i} = 0 \tag{A.7}$$

A.3 Vector Derivatives

Derivative of Velocity Vector Product

Let the velocity vector be given by

$$\vec{v} = (v_x, v_y, v_z) \tag{A.8}$$

then the corresponding vector norm is

$$|\vec{v}| = (v_x^2 + v_y^2 + v_z^2)^{1/2} \tag{A.9}$$

and the velocity vector derivative of its norm by

$$\frac{\partial |\vec{v}|}{\partial \vec{v}} = \frac{\vec{v}}{|\vec{v}|} \tag{A.10}$$

The derivative of the product of $\vec{v}$ and its norm $|\vec{v}|$ is given by

$$\frac{\partial}{\partial \vec{v}} \left(|\vec{v}| \cdot \vec{v} \right) = \frac{\partial |\vec{v}|}{\partial \vec{v}}\, \vec{v} + |\vec{v}|\, \frac{\partial \vec{v}}{\partial \vec{v}} \tag{A.11}$$

This can be further simplified to

$$\frac{\partial}{\partial \vec{v}} \left(|\vec{v}| \cdot \vec{v} \right) = \frac{\vec{v}\, \vec{v}^T}{|\vec{v}|} + |\vec{v}|\, \mathbf{1} \tag{A.12}$$

Dyadic Vector Product

The dyadic vector product of a row vector

$$\vec{v} = (v_x, v_y, v_z) \tag{A.13}$$

and a column vector

$$\vec{v}^T = \begin{pmatrix} v_x \\ v_y \\ v_z \end{pmatrix} \tag{A.14}$$

is a 3×3 matrix $\mathbf{A}$ given by

$$\mathbf{A} = \vec{v} \otimes \vec{v}^T = \begin{pmatrix} v_x v_x & v_x v_y & v_x v_z \\ v_y v_x & v_y v_y & v_y v_z \\ v_z v_x & v_z v_y & v_z v_z \end{pmatrix} \tag{A.15}$$

Appendix B

Time Systems

This Appendix should give some basic explanations about the different time systems used in fundamental astronomy. For more detail the reader is referred to Moyer (1981a), Moyer (1981b) and Seidelmann (1992).

International Atomic Time (TAI)

International Atomic Time (TAI) is based upon the atomic second as defined by the "oscillation of the undisturbed cesium atom." Atomic time is simply a count of atomic seconds that have occurred since the astronomically determined instant of midnight January 1, 1958 00:00:00 at the Royal Observatory in Greenwich, England. Atomic time is kept by the International Earth Rotation Service (IERS, formally the Bureau International L'Heure) in Paris, France. The National Bureau of Standards and the U.S. Naval Observatory set their clocks by the clock maintained by the IERS.

Coordinated Universal Time UTC

Coordinated Universal Time is a system of time keeping that gives a name to each instant of time of the TAI system. These names are formed from the calendar date and time of day that is used in daily affairs. They consist of 6 components: year, month, day, hour, minutes and seconds. The year, month and day components are the normal calendar year month and day that appear on wall calendars. The hours component may assume any value from 0 through 23. The minutes component may assume any value from 0 to 59. The seconds will usually (but not always) range from 0 to 59.999... . The hour-minute-second string "00:00:00" is midnight and is the first instant of the calendar day specified by the first three components of the UTC time.

The names given to TAI instants by the UTC system are governed by the Earth's rotation. Ideally, UTC strings having hours, minutes and seconds components all zero should correspond to Greenwich midnight as determined by the observations of the transits of stars (the time system known as UT1). However, since the rotation of the Earth is not uniform, this ideal cannot be realized. The difference between Greenwich midnight observed astronomically and UTC midnight is almost never zero. However, to keep the difference from becoming too large, UTC is occasionally adjusted so that the difference

between the two midnights never exceeds .9 seconds. Thus from a knowledge of UTC one can always compute UT1 to better than 1 second accuracy.

When Greenwich UT1 midnight lags behind UTC midnight by more than 0.7 seconds the IERS will announce that a leap second will be added to the collection of UTC names. This leap second has traditionally been added after the last "normal" UTC name of December 31 or June 30. Should Greenwich UT1 midnight run ahead of UTC midnight by more than 0.7 seconds the IERS will announce a negative leap second. In this case one of the usual UTC hours-minutes-seconds triples will be missing from the list of UTC names. Since 1972 when leap seconds and the UTC system were introduced, a negative leap second has not occurred.

Barycentric Dynamical Time / Ephemeris Time

Ephemeris time is the uniform time scale represented by the independent variable in the differential equations that describe the motions of the planets, sun and moon. There are two forms of ephemeris time: *Barycentric Dynamical Time* (TDB) and *Terrestrial Dynamical Time* (TDT). Although they represent different time systems, these time systems are closely related.

Barycentric Dynamical Time (TDB) is used when describing the motion of bodies with respect to the solar system barycenter. TDB is believed to be in agreement with the time that would be kept by an atomic clock located at the solar system barycenter. A comparison of the times kept by a clock at the solar system barycenter with a TDB clock on earth would reveal that the two clocks are in close agreement but that they run at different rates at different times of the year. This is due to relativistic effects. Note that in the NAIF Toolkit ephemeris time (ET) is interpreted as TDB. This has also been adapted for the NASA/ESA interface time. Ephemeris time is given in terms of elapsed seconds with respect to the reference epoch J2000 (12:00 January 1, 2000=JD2451545.0).

Terrestrial Dynamical Time (TDT) is used when describing motions of objects near the earth. As far as measurements have been able to detect, TDT and TAI change at the same rate. Thus the difference between TDT and TAI is a constant. It is defined to be 32.184 seconds. At the zero point of TAI, TDT has a value of 32.184.

Appendix C

Aerodynamic Databases

C.1 Huygens Preflight Aerodynamic Database

The Huygens aerodynamic database was obtained from both dedicated wind tunnel campaigns and theoretical results from Computational Fluid Dynamics (CFD) codes (Schipper, 2002, and references cited therein). The test campaigns focussed on module scale tests and were executed between 1991 and 1995 with tests in the subsonic, transonic, and supersonic regions. The campaign provided static and dynamic characteristics of the Huygens entry and descent module shapes. Hypersonic behavior has been assessed through shape comparison.

The full database comprises both static and dynamic coefficients for the Huygens entry and the descent module, and static coefficients for the Huygens parachute system. Here only the entry module coefficients are reported, as they are relevant for the upper atmosphere reconstruction based on the spacecraft accelerometer measurements. The entry module database provides the following static coefficients as functions of angle-of-attack (AOA) and Mach number Ma:

- force coefficients including axial force C_A, drag force C_D, lift force C_L, and normal and lateral force coefficients C_N;
- moment coefficients including pitch and yaw moments C_m;
- pressure coefficient C_{PB}.

The database furthermore contains the following dynamic coefficients:

- pitching moment coefficients;
- damping in pitch coefficients C_{mq}.

Note that the knowledge of the damping in the pitch coefficient is sufficient to assess the entry module dynamic stability. All the listed coefficients are provided as function of AOA (in the range from 0 – 90 deg) and Ma (in the range from 0 – 99) by Schipper (2002). Fig. C.1 depicts the normal and axial coefficients (upper panels) and its ratio (lower panel) for Mach numbers up to 7.15.

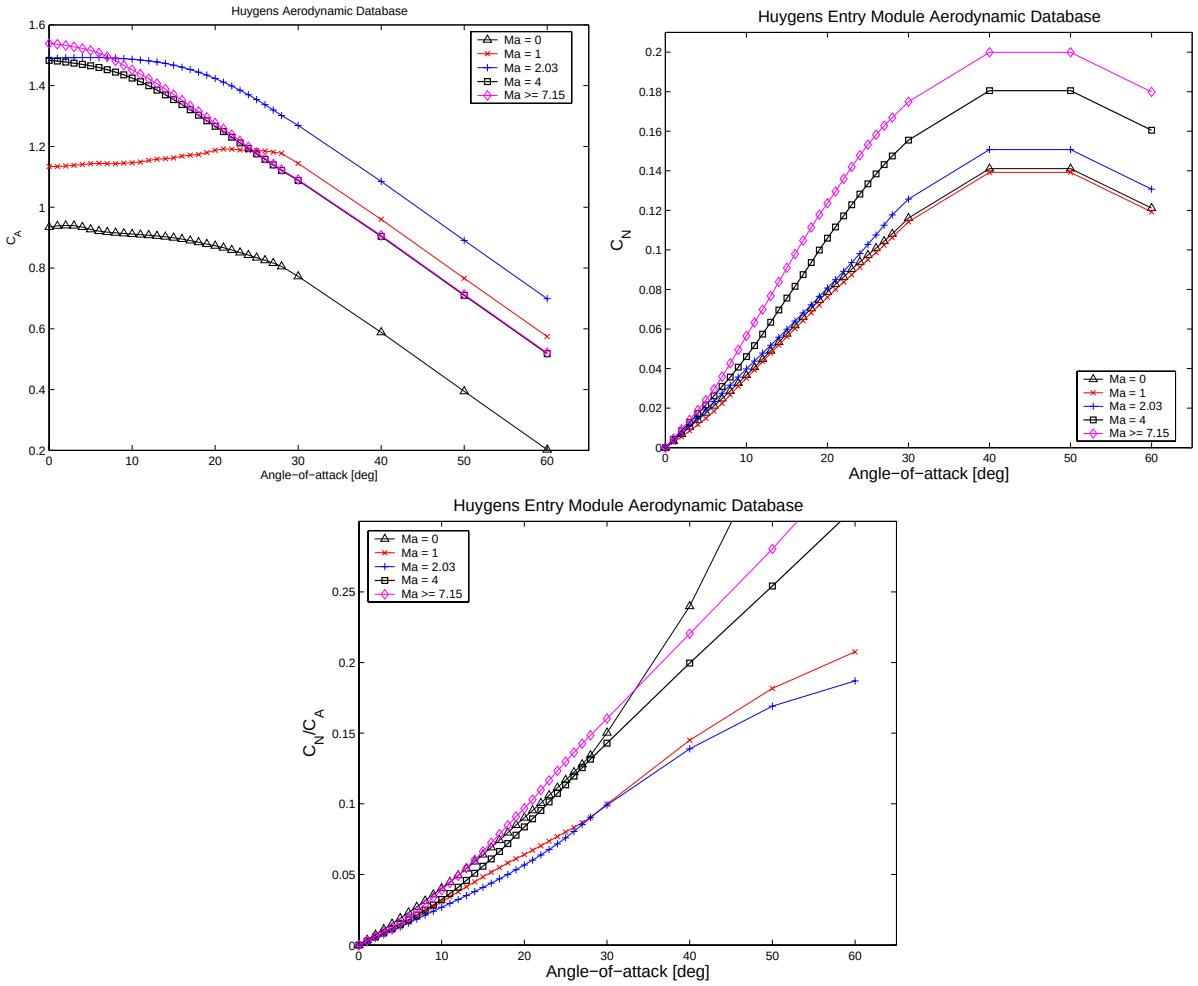

Figure C.1: *Axial force coefficient C_A (upper left), normal force coefficient C_N (upper right), and ratio C_A/C_N (lower panel) of the Huygens entry module.*

C.2 Pathfinder Preflight Aerodynamic Database

The Mars Pathfinder aerodynamic database is described and provided in Moss *et al.* (1998). This database was derived from computation results of direct simulation Monte Carlo (DSMC) and free molecular/Newtonian codes. The coefficients are provided as function of the hard sphere Knudsen number, $Kn_{\infty,HS}$, and the probe angle-of-attack (AOA). Note that a constant molecular diameter of 4.64×10^{-10} m was assumed for the CO_2/N_2 gas. Consequently the Knudsen number is the inverse of the freestream density ρ_∞ and is defined as $Kn_{\infty,HS} = 2.8351 \times 10^{-8}/\rho_\infty$. Fig. C.2 shows the axial and normal force coefficients C_A and C_N in the upper panels. The lower panels show the drag coefficient C_D (left panel) and the C_N/C_A ratio (right panel).

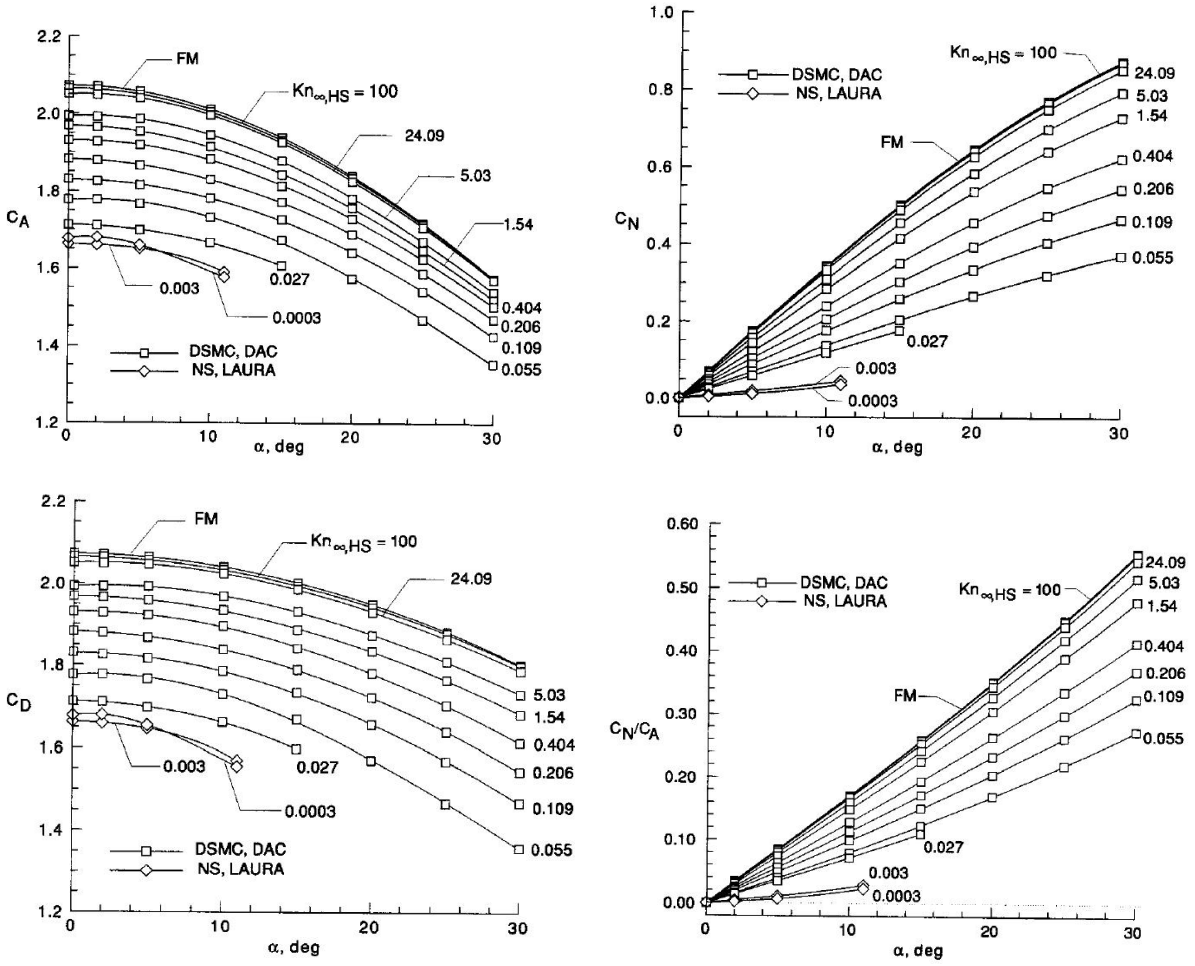

Figure C.2: *Axial force coefficient C_A (upper left), normal force coefficient C_N (upper right), drag coefficient (lower left), and ratio C_A/C_N of the Mars Pathfinder entry module (Moss* et al.*, 1998).*

C.3 Cartesian to Latitudinal Error Conversion

The conversion of a cartesian state vector $\vec{r} = x_i = (x, y, z)$ (given in a planet-centered rotating reference system) into latitudinal coordinates (i.e., altitude, latitude, and east longitude) is done using the transformation

$$\begin{aligned} x &= r\,\cos\lambda\,\cos\varphi \\ y &= r\,\cos\lambda\,\sin\varphi \\ z &= r\,\sin\lambda \end{aligned} \tag{C.1}$$

The inverse transformation is given by

$$\begin{aligned} r &= (x^2 + y^2 + z^2)^{1/2} \\ \varphi &= \arctan\left(\frac{y}{x}\right) \\ \lambda &= \arctan\left(\frac{z}{\sqrt{x^2 + y^2}}\right) \end{aligned} \tag{C.2}$$

The error of the latitudinal coordinates can be derived from the errors of the cartesian position vector according to

$$\begin{aligned} \sigma(r)^2 &= \sum_i \left(\frac{\partial r}{\partial x_i}\right)^2 \sigma(x_i)^2 \\ \sigma(\varphi)^2 &= \sum_i \left(\frac{\partial \varphi}{\partial x_i}\right)^2 \sigma(x_i)^2 \\ \sigma(\lambda)^2 &= \sum_i \left(\frac{\partial \lambda}{\partial x_i}\right)^2 \sigma(x_i)^2 \end{aligned} \tag{C.3}$$

with the partial derivatives given by

$$\frac{\partial r}{\partial x_i} = \frac{x_i}{|\vec{r}|}\,, \tag{C.4}$$

$$\begin{aligned} \frac{\partial \varphi}{\partial x} &= -\frac{y}{x^2 + y^2} \\ \frac{\partial \varphi}{\partial y} &= \frac{1}{x + \frac{y^2}{x}} \\ \frac{\partial \varphi}{\partial z} &= 0\,, \end{aligned} \tag{C.5}$$

and

$$\begin{aligned}
\frac{\partial \lambda}{\partial x} &= \frac{-z\,x}{(x^2+y^2)^{3/2}+z^2\,(x^2+y^2)^{1/2}} \\
\frac{\partial \lambda}{\partial y} &= \frac{-z\,y}{(x^2+y^2)^{3/2}+z^2\,(x^2+y^2)^{1/2}} \\
\frac{\partial \lambda}{\partial y} &= \frac{1}{(x^2+y^2)^{1/2}+\frac{z^2}{(x^2+y^2)^{1/2}}}\,.
\end{aligned} \tag{C.6}$$

Appendix D

The HSDS 260504 Event File

```
begintext

*******************************************************
HUYGENS PROBE INITIAL CONDITIONS AND EVENT FILE *
*******************************************************

According to:  "HUYGENS - DTWG Experimenter to DTWG Interface
Control Document " Issue 7, Rev.  6, May 2004 Section 5

begindata

Delivery_File_Description = ( 'HUYGENS +'
' SYNTHETIC DATA SET +'
'VER. 1.4')
begintext

Predicted Interface Time (ET).

begindata

Interface_Time = ( @14-JAN-2005-09:00:00.000)

begintext

     Probe position (km) and velocity (km/s) vectors
in Titan-centered, EME2000 coordinates at the
predicted interface time.

begindata

Probe_State = ( -1.312458638E+02,
-3.824933072E+03,
-3.697321588E+02,
-2.346112519E+00,
5.539336275E+00,
4.588600223E-01 )

begintext

Saturnian system gravitational constant (GM) in km3/s2.

begindata

Estimate_Saturn_GM = ( 3.794062976E+07 )

begintext

Titan gravitational constant (GM) in km3/s2.

begindata

Estimate_Titan_GM = ( 8.978200000E+03 )

begintext

Full 14 x 14 knowledge covariance matrix mapped at the predicted
interface time.  Ordered as probe state (Xp,Yp,Zp,DXp,DYp,DZp),
orbiter state (Xo,Yo, Zo,DXo,DYo,DZo), Saturnian system GM, the
Titan GM.

begindata

Cov_Matrix = ( 1.537352888589838E+03, 3.479670578873070E+03, -2.840046297735558E+02,
-1.389006908822917E-01, 3.319298895701578E-01, 6.205492395134900E-02,
8.710872652069688E+02, 1.823026624859702E+03, -3.220435656244631E+02,
4.243691924186593E-04, 8.293441764525419E-03, 1.597977680386113E-04,
-3.055685615748513E+01, 7.813061331872737E-01,
3.479670578873070E+03, 8.643349996730927E+03, -7.011270255199345E+02,
-3.270227369377572E-01, 8.301192932327996E-01, 1.544529102679520E-01,
2.084525099385429E+03, 4.446175690512405E+03, -7.954496388012716E+02,
```

```
1.132923842650727E-03, 2.010946997786566E-02, 4.117211280592018E-04,
-9.800737847173602E+01, 2.231318147917456E+00,
-2.840046297735558E+02, -7.011270255199345E+02, 1.795828485584980E+02,
2.642688267520124E-02, -6.561939635212416E-02, -1.939960178051532E-02,
-2.832497302518869E+02, -6.203551772862969E+02, 1.246679321179621E+02,
-1.689651722819217E-04, -2.813773776674066E-03, -8.164856044829701E-05,
8.236889302479417E+00, -3.134479454939063E-01,
-1.389006908822917E-01, -3.270227369377572E-01, 2.642688267520124E-02,
1.275809463754104E-05, -3.129029240559664E-05, -5.826191579031357E-06,
-8.039965773809918E-02, -1.695947500134435E-01, 3.010419379849304E-02,
-4.097443678544482E-08, -7.696327496888744E-07, -1.509322718821726E-08,
3.241383397961811E-03, -7.828889482519122E-05,
3.319298895701578E-01, 8.301192932327996E-01, -6.561939635212416E-02,
-3.129029240559664E-05, 7.978689008891384E-05, 1.474139699251994E-05,
1.981625155304882E-01, 4.229742894772123E-01, -7.556386801070049E-02,
1.082195679989559E-07, 1.912400332784275E-06, 3.906247836255645E-08,
-9.450648444922299E-03, 2.175023320582403E-04,
6.205492395134900E-02, 1.544529102679520E-01, -1.939960178051532E-02,
-5.826191579031357E-06, 1.474139699251994E-05, 3.145831894178856E-06,
4.355044019847844E-02, 9.384580684401057E-02, -1.755065488723923E-02,
2.468428856326683E-08, 4.248613809761639E-07, 1.074568218251989E-08,
-1.807185727699651E-03, 4.814169536133546E-05,
8.710872652069688E+02, 2.084525099385429E+03, -2.832497302518869E+02,
-8.039965773809918E-02, 1.981625155304882E-01, 4.355044019847844E-02,
8.972360116727701E+03, 1.914244919022266E+04, -2.441584287545779E+02,
5.355593324225808E-03, 8.496789042320170E-02, -4.833562942764848E-03,
-3.500366869289047E+01, 8.768999959008937E-01,
1.823026624859702E+03, 4.446175690512405E+03, -6.203551772862969E+02,
-1.695947500134435E-01, 4.229742894772123E-01, 9.384580684401057E-02,
1.914244919022266E+04, 6.213347839630608E+04, -1.464700707475713E+03,
3.490963454538498E-02, 2.647826688742190E-01, -1.379917482906250E-02,
-9.226994903173909E+01, 2.236125081712133E+00,
-3.220435656244631E+02, -7.954496388012716E+02, 1.246679321179621E+02,
3.010419379849304E-02, -7.556386801070049E-02, -1.755065488723923E-02,
-2.441584287545779E+02, -1.464700707475713E+03, 4.675320472433761E+03,
-1.317654430475594E-03, -7.275911835853433E-03, -9.936403272175525E-03,
1.216488347019632E+01, -4.081536754710693E-01,
4.243691924186593E-04, 1.132923842650727E-03, -1.689651722819217E-04,
-4.097443678544482E-08, 1.082195679989559E-07, 2.468428856326683E-08,
5.355593324225808E-03, 3.490963454538498E-02, -1.317654430475594E-03,
2.919327149834648E-08, 1.427883066124538E-07, -6.341867005195039E-09,
-4.478643551104608E-05, 1.289148593920510E-06,
8.293441764525419E-03, 2.010946997786566E-02, -2.813773776674066E-03,
-7.696327496888744E-07, 1.912400332784275E-06, 4.248613809761639E-07,
8.496789042320170E-02, 2.647826688742190E-01, -7.275911835853433E-03,
1.427883066124538E-07, 1.132711793632363E-06, -5.661897103212482E-08,
-2.911031133448807E-04, 9.825885009288610E-06,
1.597977680386113E-04, 4.117211280592018E-04,-8.164856044829701E-05,
-1.509322718821726E-08, 3.906247836255645E-08,1.074568218251989E-08,
-4.833562942764848E-03, -1.379917482906250E-02,-9.936403272175525E-03,
-6.341867005195039E-09, -5.661897103212482E-08,2.645223195225744E-08,
-1.643553435210967E-05, 5.936556414333761E-07,
-3.055685615748513E+01, -9.800737847173602E+01, 8.236889302479417E+00,
3.241383397961811E-03, -9.450648444922299E-03, -1.807185727699651E-03,
-3.500366869289047E+01, -9.226994903173909E+01, 1.216488347019632E+01,
-4.478643551104608E-05, -2.911031133448807E-04, -1.643553435210967E-05,
1.580823131836584E+03, -9.731175250944245E-02,
7.813061331872737E-01, 2.231318147917456E+00, -3.134479454939063E-01,
-7.828889482519122E-05, 2.175023320582403E-04, 4.814169536133546E-05,
8.768999959008937E-01, 2.236125081712133E+00, -4.081536754710693E-01,
1.289148593920510E-06, 9.825885009288610E-06, 5.936556414333761E-07,
-9.731175250944245E-02, 7.941743932606013E-02 )

begintext

Titan related physical constants, i.e.,
- Pole right ascension [deg]
- Pole declination [deg]
- Pole prime meridian numbers as defined in [RD.1]
Davies et.  al, 1996, "Report
- Longitude Axis
- Titan radius
- Titan J2 harmonic coefficient

begindata

BODY606_POLE_RA = ( 36.41 -0.036 0.  )
BODY606_POLE_DEC = ( +83.94 -0.004 0.  )
BODY606_PM = ( 189.64 +22.5769768 0.  )
BODY606_LONG_AXIS = ( 0.  )
BODY606_J2 = ( 0.0D0 )

begintext

The following important events [all in ET seconds past J2000] are
required for the quality control and consistency check of the
reconstructed trajectory:
  - S0 detection


- T0 detection
- G-switch epochs
- Main parachute deploy
- Heat shield (FRSS) release
- Stabilizing chute deploy
```

```
- DISR cover ejection
- HASI boom deployment
- GCMS cover ejection
- ACP cover ejection
- RAU1 lock
- RAU2 lock
- RAU1 unlock
- RAU2 unlock

begindata

S0_EVENT= (158965464.9798)
T0_EVENT= (158965471.3548)
GSW_EVENT= (0.00)
MAIN_CH_EVENT= (158965473.8548)
FRSS_EVENT= (158965503.8548)

DISR_COV_EVENT= (158965537.6048)
HASI_BOOM_EVENT= (158965521.0098)
GCMS_INLET_COV_EVENT= (158965521.3548)
GCMS_OUTLET_COV_EVENT= (158965529.4798)
ACP_COV_EVENT= (158965504.2298)
DROGUE_CH_EVENT= (158966371.3548)

RAU1_LOCK_1= (158967386.4798)
RAU2_LOCK_1= (158967386.4798)
RAU1_UNLOCK_1= (00000.00)
RAU2_UNLOCK_1= (00000.00)
```

D.1 Symbols and Abbreviations

$\vec{a}$ ... total acceleration

$\vec{a}_{\rm g}$ ... gravitational acceleration

$\vec{a}_{\rm Ad}$ ... aerodynamic acceleration

a_D, a_L ... drag and lift accelerations

a_N, a_A ... normal and axial accelerations

a_{s1}, a_{s2}, a_{s3} ... accelerations in spacecraft frame

A ... cross sectional aerea

$\vec{c}$ ... vector containing z and $\dot{z}$

c_s ... speed of sound

C_N, C_A ... normal and axial aerodynamic force coefficients

C_L, C_D ... aerodynamic lift and drag coefficient

$\vec{F}_{\rm Ad}$ ... aerodynamic force vector

g ... gravitational acceleration of unity mass

$\mathbf{G}_i$ ... Jacobian of the calculated (modeled) measurement vector with respect to the reference state vector at the measurement epoch t_i

G ... gravitational constant G=6.67259(85)E-11 N m^2 kg^{-2}

J_k ... coefficient of the kth zonal harmonic

m or m_s ... spacecraft mass

M_0 ... mass of primary body

M_j ... mass of jth perturbing body ($j = 1...N$)

Ma ... Mach number

$\vec{M}_{\rm Ad}$ ... moment of aerodynamic force vector $\vec{F}_{\rm Ad}$

$\vec{o}$ ... vector containing Z and $\dot{Z}$

P ... atmospheric pressure

$\vec{p}_j$ ... rectangular position vector of jth perturbing body $j = (1 \cdots N)$

P_k ... Legendre polynoms of degree k

$\mathbf{P}_0^{\rm apr}$ ... a priori covariance matrix at epoch t_0

$\mathbf{r}$ ... $= (r_1, r_2, r_3)$: rectangular position vector in the planet centered EME2000 coordinate system

$\mathbf{r\prime}$ ... $= (r_1\prime, r_2\prime, r_3\prime)$: rectangular position vector in the planet centered equatorial coordinate system (Q-System)

R ... universal (molar) gas constant R=8.31451 J/K/mole

$R_{\rm P}$ ... planetary radius; Titan: $R_{\rm P} = (2575 \pm 2)$ km, Mars: $R_{\rm P}$=(3389.92 $\pm$ 0.04) km

t ... time epoch (nominally in Ephemeris Time)

T ... atmospheric temperature (in K)

U ... gravitational flattening potential function

$\vec{v}$ ... rectangular velocity vector (in EME2000 system)

$\vec{v}_w$ ... wind velocity vector (in EME2000 system)

$\vec{v}_{\rm rel}$ ... relative flow velocity vector (i.e., relative velocity vector between spacecraft and atmosphere)

$\mathbf{W}$ ... weighting matrix of the measurements at the measurement epoch t_i: $W = {\rm diag}(\sigma_1^{-2}, \cdots, \sigma_n^{-2})$

$\vec{y}$ ... $= (y_1, ..., y_6) = (\vec{r}, \vec{v})$: probe state vector (in EME2000 system)

Z ... reconstructed altitude from probe *descent* phase

$\dot{Z}$ ... reconstructed descent speed from probe *descent* phase

z ... reconstructed altitude from probe *entry* phase

$\dot{z}$ ... reconstructed descent speed from probe *entry* phase

$\mathbf{0}_{n\times m}$ ... null matrix of dimension $n \times m$

$\mathbf{1}_{n\times m}$ ... n-dimensional identity matrix

$(\cdots)_{n\times m}$ ... matrix $(\cdots)$ has dimension $n \times m$

α ... angle of attack

α_0, δ_0 ... right ascension and declination of the planet's north pole

Θ ... spherical latitude

$\mathbf{\Lambda}$ ... information matrix

ω_{P} ... angular velocity vector of the planet

γ ... ratio of specific heats c_p/c_v

δ_{in} ... Kronecker symbol: $\delta_{in} = 1$ for $i = n$ otherwise $\delta_{in} = 0$

ρ ... atmospheric density

$\vec{\rho}$ ... $= \vec{o} - \vec{c}$

σ ... standard deviation of instrument measurement

Φ_i ... state transition matrix at epoch t_i: $\Phi_i \equiv \partial \mathbf{y}_i / \partial \mathbf{y}_{i-1}$

ASI ... Atmospheric Structure Investigation

BC ... Back Cover

CASU ... Central Acceleration Sensor Unit

CFD ... Computational Fluid Dynamics

CM ... Center of Mass

DISR ... Descent Imager and Spectral Radiometer

DM ... Descent Module

DTAT ... Descent Trajectory Analysis Tool

DTWG ... Descent Trajectory Working Group

DWE ... Doppler Wind Experiment

EDL ... Entry, Descent, and Landing

EME 2000 ... Earth Mean Equator at the reference epoch J2000

ET ... Ephemeris Time

FRSS ... Front Shield Subsystem

GCMS ... Gas Chromatograph and Mass Spectrometer

HASI ... Huygens Atmospheric Structure Instrument

HASI-ACC ... HASI Accelerometer Subsystem

HASI-PPI ... HASI Pressure Profile Instrument

HASI-TEM ... HASI temperature sensor

HGA ... High Gain Antenna

HK ... Housekeeping data

HRTF ... Huygens Recovery Task Force

HSDS ... Huygens Synthetic Dataset

IAU ... International Astronomical Union

MLI ... Multi Layer Insulation

MPF ... Mars Pathfinder

NAIF ... Navigation and Ancillary Information Facility

NAV ... Navigation

ODM ... Orbiter Delay Maneuver

ODT ... Orbiter Delay Time

PI ... Principal Investigator

PDS ... Planetary Data System

PRL ... Probe Relay Link

PRM ... Periapsis Raise Maneuver

PSE ... Probe Support Equipment

PST ... ESA/ESTEC Project Scientist Team

PWA ... Permittivity, Wave, and Altimetry Instrument

RAU ... Radar Altimeter Unit

RASU ... Radial Acceleration Sensor Unit

RSS or rss ... root of the summed squares

RUSO ... Receiving Ultrastable Oscillator

SSP ... Surface Science Package

SSP-APIV ... SSP speed of sound instrument

SSP-APIS ... SSP acoustic sounder instrument

SOI ... Saturn Orbit Insertion

SZA ... Solar Zenith Angle

TDB ... Barycentric Dynamical Time

TUSO ... Transmitter Ultrastable Oscillator

UTC ... Coordinated Universal Time

Y97 ... Yelle (1997) Titan atmosphere model

Bibliography

Allison, M., D. H. Atkinson, M. K. Bird, and M. G. Tomasko 2004. Titan zonal wind corroboration via the Huygens DISR solar zenith angle measurement. In *ESA SP-544: Planetary Probe Atmospheric Entry and Descent Trajectory Analysis and Science*, pp. 125–+.

Atkinson, D., and B. Kazeminejad 2004. Report of the Huygens Descent Trajectory Working Group. Technical Report Revision 3, Univ. of Idaho.

Bauer, S. J., and H. Lammer 2004. *Planetary Aeronomy*. Springer.

Belló-Mora, M., and M. Sánchez-Nogales 2000. Huygens Entry and Descent Software Development Final Report. Technical Report GMV-HUYGENS-FR, GMV.

Bird, M. K., R. Dutta-Roy, M. Heyl, M. Allison, S. W. Asmar, W. M. Folkner, R. A. Preston, D. H. Atkinson, P. Edenhofer, D. Plettemeier, R. Wohlmuth, L. Iess, and G. L. Tyler 2002. The Huygens Doppler Wind Experiment - Titan Winds Derived from Probe Radio Frequency Measurements. *Space Sci. Rev.* **104**, 613–640.

Broadfoot, A. L., B. R. Sandel, D. E. Shemansky, S. K. Atreya, T. M. Donahue, H. W. Moos, J. L. Bertaux, J. E. Blamont, J. M. Ajello, and D. F. Strobel 1977. Ultraviolet spectrometer experiment for the Voyager mission. *Space Sci. Rev.* **21**, 183–205.

Castillo, A., and M. Sánchez-Nogales 2004. Huygens Descent Trajectory Analysis Tool. Technical Report HUY-ESOC-ASW-TN-1002-TOS-OFH, Deimos Space S.L., Madrid, Spain.

Clausen, K. C., H. Hassan, M. Verdant, P. Couzin, G. Huttin, M. Brisson, C. Sollazzo, and J.-P. Lebreton 2002. The Huygens Probe System Design. *Space Sci. Rev.* **104**, 155–189.

Coustenis, A., and B. Bezard 1995. Titan's atmosphere from Voyager infrared observations. 4: Latitudinal variations of temperature and composition. *Icarus* **115**, 126–140.

Coustenis, A., B. Bezard, and D. Gautier 1989. Titan's atmosphere from Voyager infrared observations. I - The gas composition of Titan's equatorial region. *Icarus* **80**, 54–76.

Davies, M. E., V. K. Abalakin, M. Bursa, J. H. Lieske, B. Morando, D. Morrison, P. K. Seidelmann, A. T. Sinclair, B. Yallop, and Y. S. Tjuflin 1995. Report of the IAU/IAG/COSPAR Working Group on Cartographic Coordinates and Rotational Elements of the Planets and Satellites: 1995. *Celestial Mechanics and Dynamical Astronomy* **63**, 127–148.

Desai, P. N., R. C. Blanchard, and R. W. Powell 2004. Entry trajectory and atmosphere reconstruction methodologies for the Mars Exploration Rover

mission. In *ESA SP-544: Planetary Probe Atmospheric Entry and Descent Trajectory Analysis and Science*, pp. 213–220.

Dymond, J. H., and E. B. Smith 1992. *The Virial Coefficients of Pure Gases and Mixtures, a Critical Compilation*. Oxford University Press, Oxford.

European Space Agency 2001. Probe Delivery and Orbiter High Gain Antenna Pointing Operational Interface Document. Technical Report HUY-SYST-SC-ICD-1001-TOS-OFH, European Space Agency.

Flasar, F. M., R. E. Samuelson, and B. J. Conrath 1981. Titan's atmosphere - Temperature and dynamics. *Nature* **292**, 693–698.

Fulchignoni, M., F. Angrilli, G. Bianchini, A. Bar-Nun, M. A. Barucci, W. Borucki, M. Coradini, A. Coustenis, F. Ferri, R. J. Grard, M. Hamelin, A. M. Harri, G. W. Leppelmeier, J. J. Lopez-Moreno, A. M. McDonnel, C. McKay, F. M. Neubauer, A. Pedersen, G. Picardi, V. Pirronello, R. Prijola, R. Rodrigo, C. Schwingenschuh, A. Seiff, H. Svedhem, E. Thrane, V. Vanzani, G. Viskonti, and J. Zarnecki 1997. The Huygens Atmospheric Structure Instrument. In *ESA SP-1177: Huygens Science, Payload and Mission*, pp. 163+.

Fulchignoni, M., F. Ferri, F. Angrilli, A. Bar-Nun, M. A. Barucci, G. Bianchini, W. Borucki, M. Coradini, A. Coustenis, P. Falkner, E. Flamini, R. Grard, M. Hamelin, A. M. Harri, G. W. Leppelmeier, J. J. Lopez-Moreno, J. A. M. McDonnell, C. P. McKay, F. H. Neubauer, A. Pedersen, G. Picardi, V. Pirronello, R. Rodrigo, K. Schwingenschuh, A. Seiff, H. Svedhem, V. Vanzani, and J. Zarnecki 2002. The Characterisation of Titan's Atmospheric Physical Properties by the Huygens Atmospheric Structure Instrument (Hasi). *Space Sci. Rev.* **104**, 397–434.

Gaborit, V. 2004a. *Modèles et méthodes expérimentlaes qui supportent une mission spatiale: reconstruction de la trajectoire d'une sonde dans une atmosphère planétaire*. Ph. D. thesis, Université de Paris VII.

Gaborit, V. 2004b. Procedure development for the trajectory reconstruction of a probe descending in a planetary atmosphere: application to Galileo and HASI balloon tests. In *ESA SP-544: Planetary Probe Atmospheric Entry and Descent Trajectory Analysis and Science*, pp. 151–162.

Golombek, M. P., N. T. Bridges, H. J. Moore, S. L. Murchie, J. R. Murphy, T. J. Parker, R. Rieder, T. P. Rivellini, J. T. Schofield, A. Seiff, R. B. Singer, P. H. Smith, L. A. Soderblom, D. A. Spencer, C. R. Stoker, R. Sullivan, N. Thomas, S. W. Thurman, M. G. Tomasko, R. M. Vaughan, H. Wänke, A. W. Ward, and G. R. Wilson 1999. Overview of the Mars Pathfinder Mission: Launch through landing, surface operations, data sets, and science results. *J. of Geophys. Res. 104*(13), 8523–8554.

Golombek, M. P., R. A. Cook, T. Economou, W. M. Folkner, A. F. C. Haldemann, P. H. Kallemeyn, J. M. Knudsen, R. M. Manning, H. J. Moore, T. J. Parker, R. Rieder, J. T. Schofield, P. H. Smith, and R. M. Vaughan 1997. Overview of the Mars Pathfinder Mission

and Assessment of Landing Site Predictions. *Science* **278**, 1743–+.

Hubbard, W. B., et al. 1993. The occultation of 28 SGR by Titan. *Astronomy and Astrophysics* **269**, 541–563.

Huygens Implementation Team 2004. Huygens Mission Operations Plan. Technical Report HUY-OPS-PL-1001-TOS-OFH, ESA/JPL. Ver. 1.

Huygens Recovery Task Force 2001. HRTF- Final Report. Technical Report HUY-RP-12241, ESA/NASA.

Israel, M. C. J.-F. B. G., S. W. H. Niemann, W. Riedler, M. Steller, F. Raulin, and D. Coscia 2002. Huygens Probe Aerosol Collector Pyrolyser Experiment. *Space Sci. Rev.* **104**, 435–466.

Kazeminejad, B. 2000. Orbit Calculation of Thebe (J-14) by Numerical Integration and Analytical Theories. Technical report, Master Thesis, Karl-Franzens University Graz, Austria.

Kazeminejad, B. 2002. Analysis and Optimization of the Recovered ESA Huygens Mission. Technical report, Master Thesis, Graz University of Technology, Austria.

Kazeminejad, B. 2004. Experimenter to DTWG Interface Control Document. Technical Report HUY-DTWG-IF-0001, ESA Technical Note.

Kazeminejad, B., and D. H. Atkinson 2002. Huygens Probe Imaging Analysis. Technical Report Ver. 1, Space Research Institute, Austrian Academy of Sciences.

Kazeminejad, B., J.-P. Lebreton, M. K. Bird, and D. H. Atkinson 2002. Titan wind effects on the descent trajectory of the ESA Huygens probe. In *ESA SP-514: Earth-like Planets and Moons*, pp. 191.

Kazeminejad, B., M. Pérez-Ayúcar, J.-P. Lebreton, M. Sanchez-Nogales, M. Belló-Mora, N. Strange, D. Roth, L. Popken, K. Clausen, and P. Couzin 2004. Simulation and analysis of the revised Huygens probe entry and descent trajectory and radio link modelling. *Planet. Space Sci.* **52**, 799–814.

Kerzhanovich, V. V. 1977. Mars 6 - Improved analysis of the descent module measurements. *Icarus* **30**, 1–25.

Kostiuk, T., K. E. Fast, T. A. Livengood, T. Hewagama, J. J. Goldstein, F. Espenak, and D. Buhl 2001. Direct measurement of winds of Titan. *Geophys. Res. Lett.* **28**, 2361–2364.

Krasnov, N. F. 2000. *Aerodynamics of Bodies of Revolution*. American Elsevier Publishing Company, Inc., New York, c1970.

Lebleu, D. 2003. Entry and Descent Performance Report for Yelle and Gravity Wave Models, Issue 01, Rev. A. Technical Report HUY.ASP.HIT.RE.0005, Alcatel Space.

Lebreton, J.-P. 2001. Engineering Titan Zonal Wind Model revisited: The HRTF Titan Zonal Wind Model. Technical report, European Space Agency.

Lebreton, J.-P. 2003. Titan Atmosphere Model Evolution, Issue 01. Technical Report HUY-RP-79, ESA/ESTEC RSSD/SCI-SB.

Lebreton, J.-P., and D. L. Matson 2002. The Huygens Probe: Science, Payload and Mission Overview. *Space Sci. Rev.* **104**, 59–100.

Lellouch, E., A. Coustenis, D. Gautier, F. Raulin, N. Dubouloz, and C. Frere 1989. Titan's atmosphere and

hypothesized ocean - A reanalysis of the Voyager 1 radio-occultation and IRIS 7.7-micron data. *Icarus* **79**, 328–349.

Lellouch, E., and D. M. Hunten 1987. Titan atmosphere engineering model. Technical Report ESLAB 87/199, ESA Space Science Department.

Lellouch, E., D. M. Hunten, G. Kockarts, and A. Coustenis 1990. Titan's thermosphere profile. *Icarus* **83**, 308–324.

Lindal, G. F., G. E. Wood, H. B. Hotz, D. N. Sweetnam, V. R. Eshleman, and G. L. Tyler 1983. The atmosphere of Titan - an analysis of the Voyager 1 radio occultation measurements. *Icarus* **53**, 348–363.

Lorenz, R. D. 1994. *Exploring the Surface of Titan*. Ph. D. thesis, University of Kent at Canterbury, UK.

Lunine, J. I., F. M. Flasar, and M. Allison 1991. Huygens probe wind drift: science issues and recommendations, Internal Report to the Huygens Project.

Magalhães, J. A., J. T. Schofield, and A. Seiff 1999. Results of the Mars Pathfinder atmospheric structure investigation. *J. Geophys. Res.* **104**, 8943–8956.

Matson, D. L., L. J. Spilker, and J. Lebreton 2002. The Cassini/Huygens Mission to the Saturnian System. *Space Sci. Rev.* **104**, 1–58.

Montenbruck, O., and E. Gill 2000. *Satellite Orbits: Models, Methods, Application*. Berlin ; New York : Springer.

Moss, J., R. C. Blanchard, R. G. Wilmoth, and R. D. Braun 1998. Mars Pathfinder Rarefied Aerodynamics: Computations and Measurements. *AIAA 98-0298*.

Moyer, T. D. 1981a. Transformation from Proper Time on Earth to Coordinate Time in Solar System Barycentric Space-Time Frame of Reference - Part Two. *Celestial Mechanics* **23**, 57+.

Moyer, T. D. 1981b. Transformation from proper time on earth to coordinate time in solar system barycentric space-time frame of reference. I. II. *Celestial Mechanics* **23**, 33–68.

NASA-JPL 1996. Cassini Orbiter Functional Requirements Book: Mechanical Configuration Requirements. Technical Report 699-205-CAS-3-180, ESA/NASA. Rev B.

Niemann, H. B., S. K. Atreya, S. J. Bauer, K. Biemann, B. Block, G. R. Carignan, T. M. Donahue, R. L. Frost, D. Gautier, J. A. Haberman, D. Harpold, D. M. Hunten, G. Israel, J. I. Lunine, K. Mauersberger, T. C. Owen, F. Raulin, J. E. Richards, and S. H. Way 2002. The Gas Chromatograph Mass Spectrometer for the Huygens Probe. *Space Sci. Rev.* **104**, 553–591.

Nier, A. O., and M. B. McElroy 1977. Composition and structure of Mars' upper atmosphere - Results from the neutral mass spectrometers on Viking 1 and 2. *J. Geophys. Res. 82*(11), 4341–4349.

Owen, T., K. Biemann, J. E. Biller, A. L. Lafleur, D. R. Rushneck, and D. W. Howarth 1976. The atmosphere of Mars - Detection of krypton and xenon. *Science* **194**, 1293–1295.

Pérez-Ayúcar, M., O. Witasse, J.-P. Lebreton, B. Kazeminejad, and D. H. Atkinson 2004. A simulated dataset of the Huygens mission. In *ESA*

SP-544: Planetary Probe Atmospheric Entry and Descent Trajectory Analysis and Science, pp. 343.

Peterson, V. L. 1965. Analysis of the errors associated with the determination of planetary atmosphere structure from measured accelerations of an entry vehicle. Technical Report NASA-TR-R-225, NASA Ames Research Center, California, USA.

Schipper, A. 2002. Huygens aerodynamic databases. Technical Report HUY.ASPI.HIT.TN.0006, Alcatel Space.

Schipper, A. 2003. Cassini-Huygens Recovery Mission Integrated Data Link Report. Technical Report HUY-RP-83, Alcatel Space.

Schofield, J. T., J. R. Barnes, D. Crisp, R. M. Haberle, S. Larsen, J. A. Magalhaes, J. R. Murphy, A. Seiff, and G. Wilson 1997. The Mars Pathfinder Atmospheric Structure Investigation/Meteorology. *Science* **278**, 1752–+.

Seal, D. 2004. Cassini Saturn Arrival Mission Description. Technical Report PD 699-100, Rev. O, Supplement, NASA Jet Propulsion Laboratory.

Seidelmann, P. K. 1992. *Explanatory Supplement to the Astronomical Almanac*. Published by University Science Books, 648 Broadway, Suite 902, New York, NY 10012, 1992. Completely revised and rewritten, edited by Seidelmann, P. Kenneth.

Seiff, A., and D. B. Kirk 1977. Structure of the atmosphere of Mars in summer at mid-latitudes. *J. Geophys. Res. 82*(11), 4364–4378.

Seiff, A., D. B. Kirk, T. C. D. Knight, J. D. Mihalov, R. C. Blanchard, R. E. Young, G. Schubert, U. von Zahn, G. Lehmacher, F. S. Milos, and J. Wang 1996. Structure of the Atmosphere of Jupiter: Galileo Probe Measurements. *Science* **272**, 844–845.

Seiff, A., D. B. Kirk, R. E. Young, R. C. Blanchard, J. T. Findlay, G. M. Kelly, and S. C. Sommer 1980. Measurements of thermal structure and thermal contrasts in the atmosphere of Venus and related dynamical observations - Results from the four Pioneer Venus probes. *J. Geophys. Res. 85*(14), 7903–7933.

Seiff, A., D. E. Reese, S. C. Sommer, D. B. Kirk, E. E. Whiting, and H. B. Niemann 1973. PAET: An Entry Probe Experiment in the Earth's Atmosphere. *Icarus* **18**, 525–+.

Seiff, A., J. E. Tillman, J. R. Murphy, J. T. Schofield, D. Crisp, J. R. Barnes, C. Labaw, C. Mahoney, J. D. Mihalov, G. R. Wilson, and R. Haberle 1997. The atmosphere structure and meteorology instrument on the Mars Pathfinder lander. *J. of Geophys. Res.* **102**, 4045–4056.

Smith, G. R., D. F. Strobel, A. L. Broadfoot, B. R. Sandel, D. E. Shemansky, and J. B. Holberg 1982. Titan's upper atmosphere - Composition and temperature from the EUV solar occultation results. *J. of Geophys. Research* **87**, 1351–1359.

Spencer, D. A., R. C. Blanchard, S. W. Thurmann, R. D. Braun, C.-Y. Peng, and P. H. Kallemeyn 1998. Mars Pathfinder Atmospheric Entry Reconstruction. Technical Report AAS 98-146, NASA.

Steiner, G., and S. J. Bauer 1990. Molecular and eddy diffusion in the atmo-

sphere of Titan. *Annales Geophysicae* **8**, 473–476.

Strange, N. 2001. T2001-01 Preliminary Reference Trajectory Delivery. Technical Report 312/01.E-011, NASA/JPL.

Strobel, D. F., and B. Sicardy 1997. Gravity Wave and Wind Shear Models. In *ESA SP-1177: Huygens: Science, Payload and Mission*, pp. 299.

Strobel, D. F., M. E. Summers, and X. Zhu 1992. Titan's upper atmosphere - Structure and ultraviolet emissions. *Icarus* **100**, 512–526.

Tomasko, M. G., D. Buchhauser, M. Bushroe, L. E. Dafoe, L. R. Doose, A. Eibl, C. Fellows, E. M. Farlane, G. M. Prout, M. J. Pringle, B. Rizk, C. See, P. H. Smith, and K. Tsetsenekos 2002. The Descent Imager/Spectral Radiometer (DISR) Experiment on the Huygens Entry Probe of Titan. *Space Sci. Rev.* **104**, 469–551.

Tomasko, M. G., L. R. Doose, P. H. Smith, R. A. West, L. A. Soderblom, M. Combes, B. Bézard, A. Coustenis, C. deBergh, E. Lellouch, J. Rosenqvist, O. Saint-Pé, B. Schmitt, U. H. Keller, N. Thomas, and F. Gliem 1997. The Descent Imager/spectral Radiometer Aboard Huygens. In *ESA SP-1177: Huygens Science, Payload and Mission*, pp. 109+.

Vaughan, R. M., P. H. Kallemeyn, D. Spencer, and R. D. Braun 1998. Navigation Flight Operations for Mars Pathfinder. Technical Report AAS 98-145, AAS/AIAA Space Flight Mechanics Meeting, Monterey, CA, February 9-11.

Vervack, R. J., B. R. Sandel, and D. F. Strobel 2004. New perspectives on Titan's upper atmosphere from a reanalysis of the Voyager 1 UVS solar occultations. *Icarus* **170**, 91–112.

Withers, P., M. C. Towner, B. Hathi, and J. C. Zarnecki 2003. Analysis of entry accelerometer data: A case study of Mars Pathfinder. *Planet. Space Sci.* **51**, 541–561.

Yelle, R. V., D. F. Strobell, E. Lellouch, and D. Gautier 1997. The Yelle Titan Atmosphere Engineering Models. In *ESA SP-1177: Huygens Science, Payload and Mission*, pp. 243.

Zarnecki, J. C., M. R. Leese, J. R. C. Garry, N. Ghafoor, and B. Hathi 2002. Huygens' Surface Science Package. *Space Sci. Rev.* **104**, 593–611.